

INFORMATION TO USERS

This manuscript has been reproduced from the microfilm master. UMI films the text directly from the original or copy submitted. Thus, some thesis and dissertation copies are in typewriter face, while others may be from any type of computer printer.

The quality of this reproduction is dependent upon the quality of the copy submitted. Broken or indistinct print, colored or poor quality illustrations and photographs, print bleedthrough, substandard margins, and improper alignment can adversely affect reproduction.

In the unlikely event that the author did not send UMI a complete manuscript and there are missing pages, these will be noted. Also, if unauthorized copyright material had to be removed, a note will indicate the deletion.

Oversize materials (e.g., maps, drawings, charts) are reproduced by sectioning the original, beginning at the upper left-hand corner and continuing from left to right in equal sections with small overlaps. Each original is also photographed in one exposure and is included in reduced form at the back of the book.

Photographs included in the original manuscript have been reproduced xerographically in this copy. Higher quality 6" x 9" black and white photographic prints are available for any photographs or illustrations appearing in this copy for an additional charge. Contact UMI directly to order.

UMI[®]

Bell & Howell Information and Learning
300 North Zeeb Road, Ann Arbor, MI 48106-1346 USA
800-521-0600

Three-Dimensional Modeling of Various Slab and Thin-Strip Twin-Roll Casting Processes

Seyed Hossein Seyedein

Department of Mining and Metallurgical Engineering
McGill University
Montreal, Canada

A thesis submitted to the Faculty of Graduate Studies and Research
in partial fulfillment of the requirements for the degree of
Doctor of Philosophy.

© Seyed Hossein Seyedein

July, 1997



National Library
of Canada

Acquisitions and
Bibliographic Services

395 Wellington Street
Ottawa ON K1A 0N4
Canada

Bibliothèque nationale
du Canada

Acquisitions et
services bibliographiques

395, rue Wellington
Ottawa ON K1A 0N4
Canada

Your file Votre référence

Our file Notre référence

The author has granted a non-exclusive licence allowing the National Library of Canada to reproduce, loan, distribute or sell copies of this thesis in microform, paper or electronic formats.

The author retains ownership of the copyright in this thesis. Neither the thesis nor substantial extracts from it may be printed or otherwise reproduced without the author's permission.

L'auteur a accordé une licence non exclusive permettant à la Bibliothèque nationale du Canada de reproduire, prêter, distribuer ou vendre des copies de cette thèse sous la forme de microfiche/film, de reproduction sur papier ou sur format électronique.

L'auteur conserve la propriété du droit d'auteur qui protège cette thèse. Ni la thèse ni des extraits substantiels de celle-ci ne doivent être imprimés ou autrement reproduits sans son autorisation.

0-612-37023-2

ABSTRACT

This numerical modeling study consists of two main parts. The first part is related to the simulation of industrial scale continuous slab casting systems, while the second part deals with the simulation of a twin-roll thin-strip casting process. In the first part, a numerical investigation was conducted for exploring the steady state transport phenomena of coupled turbulent flow, heat transfer and macroscopic solidification in a continuous stainless steel slab caster. The numerical model is based on a generalized transport equation applicable to all the three regions, namely liquid, mushy and solid, which exist in a slab caster. The turbulence effects on the transport equations were taken into account using a low-Reynolds number $k - \varepsilon$ turbulence model. The solidification of molten steel was modeled through the implementation of the popular enthalpy-porosity and/or continuum modeling techniques. A control volume based finite-difference scheme was used to discretize the modeled equations on a staggered grid arrangement. The resulting algebraic equations were solved simultaneously within the context of a SIMPLE-based iterative methodology. A series of simulations was carried out to investigate the effects of the casting speed, the delivered superheat, the immersion depth of the twin-ported submerged entry nozzle (SEN) and mold wall heat extraction rate on the velocity and temperature distributions and on the extent of the solidified and mushy regions on the narrow and broad faces of the caster.

Next, the model was further developed to take into account two other important aspects of the continuous casting processes, namely electromagnetic flow control and bubble gas injection. For the electromagnetic part, the continuum model equations were coupled with Maxwell equations and were solved simultaneously to study the usefulness of five different commercially used electromagnetic braking (EMBR) configurations in continuous slab casting processes. The predicted results showed that the minimum thickness of the solidifying shell at the mold exit increases due to the application of the EMBR devices and should allow the steel industries to increase the casting speed and

productivity of the process. In addition, the quality of the cast may be improved as a result of the enhancement of the inclusion removal rate in the mold.

In a separate effort, the program was further advanced by incorporating the multiphase continuum model for simulating the argon gas bubble injection via the submerged entry nozzle (SEN) into the mold. The coupling of gas dispersion with the other transport phenomena in the model made it possible to study the entrapment of the gas bubbles in the solidifying shell. The predicted results from this study showed that the flow pattern and temperature distribution were significantly influenced by the bubble injection especially in the upper part of the mold. The gas bubbles with smaller sizes were found to travel deeper towards the narrow face of the slab and spread wider in the mold. The smaller gas bubbles showed more susceptibility for entrapment.

In the second part, a numerical study was carried out to investigate the two-dimensional turbulent flow, heat transfer and macroscopic solidification in a twin-roll thin-strip casting machine. The arbitrary nature of the computational domain was accounted for through the use of a non-orthogonal boundary-fitted coordinate (BFC) system on a staggered grid. In the course of this study, the BFC scheme was modified in such a way that enabled the model to simulate the twin-roll caster for relatively very thin strip thicknesses. The developed code was later used to study the sensitivity of the model parameters such as Darcy coefficient and turbulent viscosity modification factor in the mushy region as well as the effect of the casting parameters such as casting speed, roll gap thickness, inlet nozzle width and inlet superheat on the thin-strip twin-roll casting operations.

RÉSUMÉ

Cette étude de modélisation numérique comporte deux parties principales. La première est relative à la simulation de coulées continues de plaque de type industriel. La seconde partie traite la simulation du procédé de coulée à deux cylindres de bandes fines. Dans une première partie, une investigation numérique a été conduite pour étudier l'état permanent des phénomènes de transport relatifs à un flux turbulent, au transfert de chaleur et à la solidification macroscopique dans une plaque d'acier inoxydable coulée en continu. Le modèle numérique est basé sur une équation de transport généralisée applicable aux trois domaines existant dans une plaque coulée, c'est à dire le liquide, le solide et le mélange liquide/solide. Les effets des turbulences sur les équations de transport ont été pris en considération par l'utilisation d'un modèle turbulent à nombre de Reynolds faible $k - \varepsilon$. La modélisation de la solidification d'acier en fusion a été réalisée via l'utilisation des modèles enthalpie/porosité et/ou d'un modèle continu. Le volume étudié est découpé en éléments finis, permettant ainsi de discrétiser les équations. Celles-ci ont été résolues simultanément par simples itérations. Une série de simulations a été réalisée pour étudier l'effet de la vitesse de coulée, de la chaleur dégagée, de la profondeur d'immersion des deux goupilles d'entrée de gaz et de la vitesse d'extraction de chaleur par les parois du moule sur la distribution des vitesses et des températures et sur l'étendue des régions solidifiées et des régions liquide/solide pour les faces situées sur la largeur et la longueur du produit coulé.

Ensuite, le modèle a été amélioré de façon à prendre en compte deux autres aspects importants des procédés de coulée continue, à savoir le contrôle du flux électromagnétique et l'injection de bulles de gaz. Pour la partie électromagnétique, les équations du modèle continu ont été couplées aux équations de Maxwell. Elles ont été résolues pour étudier l'efficacité de cinq différentes configurations de ralentisseurs électromagnétiques (EMBR) utilisés dans l'industrie de la coulée continue. Les résultats ont montré que l'épaisseur minimum des plaques à la sortie du moule augmente grâce à l'utilisation des appareils EMBR. Ceci devrait permettre aux aciéries d'augmenter les cadences de production ainsi que la productivité. En outre, la qualité du produit coulé

devrait être améliorée en raison de l'augmentation de la vitesse d'extraction des inclusions depuis la masse liquide.

Dans une autre partie le programme a été amélioré en introduisant le modèle continu multiphase de façon à simuler l'injection de bulles d'argon via les goupilles d'entrée immergées dans la masse liquide. Le couplage de la dispersion de gaz avec d'autres phénomènes de transport a permis d'étudier l'emprisonnement du gaz dans la structure solidifiée. Les résultats ont montré que la forme du flux et la distribution des températures sont influencées par l'injection des bulles, et ce surtout, pour le liquide contenu dans la partie supérieure du moule. Il a aussi été montré les bulles de gaz de plus faible taille voyagent plus profondément vers la partie la moins épaisse de la plaque et vont aussi plus loin dans le liquide contenu dans le moule. Les bulles les plus petites sont celles qui restent le plus facilement emprisonnées.

Dans une seconde partie, une étude numérique concernant le flux turbulent à deux dimensions, le transfert de chaleur et la solidification macroscopique pour la coulée continue à doubles cylindres a été poursuivie. La nature arbitraire du domaine à étudier a été prise en compte via l'utilisation d'un découpage non orthogonal et d'un système de transformation des coordonnées de référence arbitraire (BFC). A ce stade de l'étude, le système BFC a été employé pour pouvoir simuler la coulée la coulée à doubles cylindres pour des bandes de relativement faibles épaisseurs. Le code de calcul été utilisé pour étudier la sensibilité de paramètres du modèle (coefficient de Darcy, facteur de viscosité turbulente dans la région solide/liquide) ainsi que les paramètres de coulée comme la vitesse de coulée, l'espacement des rouleaux, la profondeur des injecteurs d'entrée et l'arrivée de chaleur sur les opérations de coulée continue à doubles cylindres.

ACKNOWLEDGMENTS

I would like to express my deep appreciation to my thesis supervisor, Professor M. Hasan for recommending this topic of research and for his constant guidance, encouragement and support during the course of this work. His invaluable suggestions which arose from many long discussions throughout the course of this research and the time spent in reviewing the manuscript are all well acknowledged.

I am also very grateful to Prof. M. Hasan, Prof. A. Ray and Prof. R. Baliga for their excellent teaching of courses related to computational methods in fluid flow and heat transfer.

Thanks are also due to Prof. M. Weber and Prof. A. S. Mujumdar for their valuable course on heat and mass transfer.

I am also thankful to Prof. R. I. L. Guthrie for teaching me the technology of steel making.

I am also indebted to anonymous reviewers of *International Journal of Heat and Mass Transfer*, *Numerical Heat Transfer* and *Canadian Metallurgical Quarterly* for their detailed review of the part of the materials presented in Chapters 2, 6 and 7 of this study.

I am also thankful to Mr. Arnaud Tronche who provided me with the French translation of the abstract.

This work could not have been attempted without the understanding, patience and continuous encouragement of my wife, Tayebeh Bayati. Her sacrifices were great.-my deep appreciation to her and my children, Mohammad Moeen and Mohammad Mahdi.

I would like to express my heartfelt thanks to my late father for his ever-lasting support, to my mother and parents in-laws for their understanding, moral support and endless patience.

Last, but far from least, I would like to extend my appreciation to the Ministry of Culture and Higher Education of the Islamic Republic of Iran for making my post-graduate studies possible.

TABLE OF CONTENTS

ABSTRACT.....	i
RÉSUMÉ.....	iii
ACKNOWLEDGEMENTS.....	v
TABLE OF CONTENTS.....	vi
LIST OF FIGURES.....	xii
LIST OF TABLES.....	xxii

CHAPTER 1

INTRODUCTION

1.1 Continuous Slab Casting Processes.....	1-1
1.2 Near Net Shape Casting.....	1-5
1.3 Prior Studies in Modeling Complexities.....	1-8
1.4 Objectives.....	1-13
1.5 Thesis Outline.....	1-13
References.....	1-16

CHAPTER 2

3-D SIMULATION OF COUPLED TURBULENT FLUID FLOW AND SOLIDIFICATION FOR CONTINUOUS STEEL SLAB CASTERS

2.1 Introduction and Prior Studies.....	2-1
2.2 Mathematical Formulation.....	2-4
2.2.1 Assumptions in Modeling.....	2-5
2.2.2 Modeling of Various Aspects Involved.....	2-6
2.2.2.1 Turbulent Modeling	2-6
- Two-Equation Low-Re $k - \varepsilon$ model.....	2-8

2.2.2.2 Solidification Modeling.....	2-9
2.2.2.3 Modeling of Fluid Flow in the Mushy Region.....	2-11
2.2.3 Boundary Conditions.....	2-13
2.2.4 Non-Dimensionalization of the Formulation.....	2-14
2.5 Numerical Solution.....	2-17
2.6 Results and Discussions.....	2-19
2.7 Concluding Remarks.....	2-26
Nomenclature.....	2-28
References.....	2-30

CHAPTER 3

MOLD HEAT EXTRACTION RATE EFFECTS ON THE 3-D TURBULENT TRANSPORT PHENOMENA IN CONTINUOUS STEEL SLAB CASTERS

3.1 Introduction.....	3-1
3.2 Literature Survey.....	3-3
3.3 Mathematical Formulation.....	3-5
3.4 Results and Discussion.....	3-10
3.5 Concluding Remarks.....	3-16
Nomenclature.....	3-18
References.....	3-20

CHAPTER 4

THE EFFECT OF DC MAGNETIC FIELD ON THE 3-D FLOW HEAT TRANSFER AND SOLIDIFICATION STUDIES IN THE CONTINUOUS CASTING MOLD

4.1 Introduction.....	4-1
4.1.1 History of MHD.....	4-2

4.1.2 In-Mold Electromagnetic Stiring.....	4-3
4.1.3 In-Mold Electromagnetic Braking.....	4-4
4.1.4 Principle of MHD Phenomena.....	4-4
4.2 Literature Review.....	4-5
4.3 Mathematical Formulation of MHD.....	4-11
4.3.1 Electric and Magnetic Aspects.....	4-11
4.3.2 Fluid Mechanic Aspects.....	4-13
4.4 MHD Equations for Continuous Slab Casting	4-14
4.4.1 Non-Dimensionalization of the MHD Parameters.....	4-15
4.4.2 Boundary Conditions.....	4-16
4.5 Solution Method.....	4-16
4.6 Results and Discussion.....	4-18
4.6.1 Effect of Magnetic Field Configuration.....	4-19
4.6.2 Effect of Magnetic Field Density.....	4-23
4.6.3 Effect of Electric Field Consideration.....	4-23
4.6.4 Effect of Magnetic Field on Mushy Region Solidification.....	4-24
4.6.5 Effect of Magnetic Field on Inclusion Distributions.....	4-25
4.6.6 Electric Current Density and Lorentz Force.....	4-27
4.7 Concluding Remarks.....	4-28
Nomenclature.....	4-30
References.....	4-32

CHAPTER 5

THE EFFECT OF ARGON GAS INJECTION ON THE 3-D FLOW HEAT TRANSFER AND SOLIDIFICATION STUDIES IN THE CONTINUOUS SLAB CASTING OPERATION

5.1 Introduction.....	5-1
5.2 Literature Review.....	5-2

6.4 Numerical Solution.....	6-16
6.5 Results and Discussion.....	6-18
6.5.1 Flow Pattern.....	6-18
6.5.2 Heat Transfer.....	6-20
6.6 Concluding Remarks.....	6-22
Nomenclature.....	6-24
References.....	6-26

CHAPTER 7

COUPLED TURBULENT FLOW, HEAT TRANSFER AND MACROSCOPIC SOLIDIFICATION IN A VERTICAL TWIN- ROLL THIN-STRIP CASTER

7.1 Introduction.....	7-1
7.2 Mathematical Modeling.....	7-2
7.2.1 Turbulent Modeling.....	7-3
7.2.2 Solidification Modeling.....	7-3
7.2.3 Complex Geometry Treatment.....	7-5
7.2.4 Boundary Conditions.....	7-6
7.3 Numerical Solution.....	7-7
7.4 Results and Discussion.....	7-8
7.4.1 Darcy Coefficient Effect.....	7-8
7.4.2 Turbulent Viscosity Modification Effect.....	7-12
7.4.3 Casting Profile Effect.....	7-15
7.5 Concluding Remarks.....	7-15
Nomenclature.....	7-17
References.....	7-19

CHAPTER 8

SUMMARY AND CONCLUDING REMARKS

8.1	Conclusions.....	8-1
8.2	Contributions to Knowledge.....	8-6
8.3	Recommendations for Future Work.....	8-7

List of Figures

Figure

- 1.1 The schematic diagram of a typical continuous slab caster.
- 1.2 Process routes for the production of steel sheet products.
- 1.3 The schematic diagram of a typical pilot-scale twin-roll caster.

- 2.1. A schematic view of the caster's domain modeled along with grid distributions and coordinates system used.
- 2.2. Two-dimensional arrangement of the staggered control volumes.
- 2.3. Computational flow chart of the 3-D turbulent fluid flow, heat transfer and solidification code.
- 2.4. Computed results at the vertical centrally symmetric plane paralleled to the wide face for a casting speed of 0.02 m/sec and 26° C superheat; (a) velocity vectors, (b) liquidus and solidus isotherms, (c) temperature contours.
- 2.5. Computed results at the vertical centrally symmetric plane paralleled to the wide face for a casting speed of 0.015 m/sec and 26° C superheat; (a) velocity vectors, (b) liquidus and solidus isotherms, (c) temperature contours.
- 2.6. 3-D surface plot of the velocity vectors for a casting speed of 0.015 m/sec and 26° C superheat; (a) the complete solution domain, (b) enlarged view of the top domain.
- 2.7. Comparison of solidified shell thickness predicted in this study (for case B) with experimental data from Nakato et al. (1984).
- 2.8. 3-D surface contour plot of non-dimensional turbulent viscosity for a casting speed of 0.015 m/sec and 26° C superheat.
- 2.9. Contours of solidus and liquidus temperatures at various transverse cross-sectional planes (Y-Z planes) for a casting speed of 0.02 m/sec and 26° C superheat.

- 2.10. Contours of solidus and liquidus temperatures at various transverse cross-sectional planes (Y-Z planes) for a casting speed of 0.015 m/sec and 26° C superheat.
- 2.11. Computed results at the vertical centrally symmetric plane paralleled to the wide face for a casting speed of 0.015 m/sec and 16° C superheat; (a) velocity vectors, (b) liquidus and solidus isotherms, (c) temperature contours.
- 2.12. Computed results at the vertical centrally symmetric plane paralleled to the wide face for a casting speed of 0.015 m/sec , 26° C superheat and $\text{SEN}=23\text{ cm}$; (a) velocity vectors, (b) liquidus and solidus isotherms, (c) temperature contours.
- 2.13. Contours of solidus and liquidus temperatures at various transverse cross-sectional planes (Y-Z planes) for a casting speed of 0.015 m/sec , 26° C superheat and $\text{SEN}=23\text{ cm}$.

- 3.1. 3-D surface plot of the velocity vectors for a casting speed of 0.02 m/sec , 26° C superheat and $\gamma = 1.1\text{ kW/m}^2\text{ K}$ (type A B.C.); (a) the complete solution domain, (b) enlarged view of the top domain.
- 3.2. Computed results of velocity vectors at the vertical centrally symmetric plane paralleled to the wide face for a casting speed of 0.02 m/sec and 26° C superheat; (a) for solidification with type A boundary condition, (b) flow without considering solidification.
- 3.3. Computed results of velocity vectors at the vertical centrally symmetric plane paralleled to the wide face for a casting speed of 0.02 m/sec , 26° C superheat and various thermal boundary conditions at the mold walls; (a) type A, (b) type B, and (c) type C.
- 3.4. 3-D surface contour plot of non-dimensional turbulent viscosity for a casting speed of 0.02 m/sec and 26° C superheat and various thermal boundary conditions at the mold walls; (a) type A, (b) type B, and (c) type C.

- 3.5. Contours of solidus and liquidus temperatures at the vertical centrally symmetric plane paralleled to the wide face for a casting speed of 0.02 m/sec , 26° C superheat and various thermal boundary conditions at the mold walls; (a) type A, (b) type B, and (c) type C.
- 3.6. Contours of solidus and liquidus temperatures for a transverse cross-sectional plane (Y-Z plane) at the exit of the mold for three types of thermal boundary conditions at the mold walls; (a) type A, (b) type B, and (c) type C.
- 3.7. Contours of solidus and liquidus temperatures for a transverse cross-sectional plane (Y-Z plane) at the exit of the submold region ($3m$ below meniscus) for three types of thermal boundary conditions at the mold walls; (a) type A, (b) type B, and (c) type C.
- 3.8. Superheat temperature contours at the vertical centrally symmetric plane paralleled to the wide face for a casting speed of 0.02 m/sec , 26° C superheat and various thermal boundary conditions at the mold walls; (a) type A, (b) type B, and (c) type C.
- 3.9. Computed surface temperatures for the transverse planes at the exit of the mold and submold regions for type A thermal boundary condition.
- 3.10. Computed surface temperatures for the transverse planes at the exit of the mold and submold regions for type B thermal boundary condition.
- 3.11. Computed surface temperatures for the transverse planes at the exit of the mold and submold regions for type C thermal boundary condition.
- 3.12. Comparison of solidified shell thickness predicted in this study (type B thermal boundary condition used) with experimental data from Lait et al. (1974).
- 3.13. Comparison of the predicted surface temperature profile with Lait et als' various one-dimensional models' predictions.

- 4.1. Magnetohydrodynamic flow in a duct (Hartmann flow).
- 4.2. A schematic diagram of type A-EMBR design for continuous slab casters.

- 4.3. Application of level magnetic field (LMF) in the continuous slab casters; type C-EMBR with LMF located under the nozzle, type B-EMBR with LMF located at the meniscus (although not shown here).
- 4.4. A schematic diagram of type D-EMBR design for continuous slab casters.
- 4.5. A schematic diagram of type E-EMBR design for continuous slab casters.
- 4.6. 2-D velocity field for a conventional continuous slab caster without magnetic field; (a) wide symmetry plane, (b) parallel wide plane at half thickness, (c) wide plane near the broad face.
- 4.7. 2-D velocity field for a typical continuous slab caster with type A-EMBR; (a) wide symmetry plane, (b) parallel wide plane at half thickness, (c) wide plane near the broad face.
- 4.8. 2-D velocity field for a typical continuous slab caster with type B-EMBR; (a) wide symmetry plane, (b) parallel wide plane at half thickness, (c) wide plane near the broad face.
- 4.9. 2-D velocity field for a typical continuous slab caster with type C-EMBR; (a) wide symmetry plane, (b) parallel wide plane at half thickness, (c) wide plane near the broad face.
- 4.10. 2-D velocity field for a typical continuous slab caster with type D-EMBR; (a) wide symmetry plane, (b) parallel wide plane at half thickness, (c) wide plane near the broad face.
- 4.11. 2-D velocity field for a typical continuous slab caster with type E-EMBR; (a) wide symmetry plane, (b) parallel wide plane at half thickness, (c) wide plane near the broad face.
- 4.12. 2-D velocity vectors at various transverse cross-sectional planes for a continuous slab caster with type A-EMBR; (a) 2.6 cm depth, (b) 18.4 cm depth, (c) 34.1 cm depth, (d) 55 cm depth.
- 4.13. 2-D velocity vectors at various transverse cross-sectional planes for a continuous slab caster with type B-EMBR; (a) 2.6 cm depth, (b) 18.4 cm depth, (c) 34.1 cm depth, (d) 55 cm depth.

- 4.14. 2-D velocity vectors at various transverse cross-sectional planes for a continuous slab caster with type C-EMBR; (a) 2.6 cm depth, (b) 18.4 cm depth, (c) 34.1 cm depth, (d) 55 cm depth.
- 4.15. 2-D velocity vectors at various transverse cross-sectional planes for a continuous slab caster with type D-EMBR; (a) 2.6 cm depth, (b) 18.4 cm depth, (c) 34.1 cm depth, (d) 55 cm depth.
- 4.16. 2-D velocity vectors at various transverse cross-sectional planes for a continuous slab caster with type E-EMBR; (a) 2.6 cm depth, (b) 18.4 cm depth, (c) 34.1 cm depth, (d) 55 cm depth.
- 4.17. 3-D surface plot of the velocity vectors for a conventional continuous slab caster without EMBR.
- 4.18. 3-D surface plot of the velocity vectors for a typical continuous slab caster with type E-EMBR and 0.1 tesla magnetic flux density.
- 4.19. 3-D surface plot of the velocity vectors for a typical continuous slab caster with type E-EMBR and 0.2 tesla magnetic flux density.
- 4.20. 3-D surface plot of the velocity vectors for a typical continuous slab caster with type E-EMBR and 0.3 tesla magnetic flux density.
- 4.21. 3-D surface plot of the velocity vectors for a typical continuous slab caster with type E-EMBR, 0.3 tesla magnetic flux density and without electric field consideration.
- 4.22. Contours of solidus and liquidus temperatures at various transverse cross-sectional planes (Y-Z planes) for a conventional continuous slab caster without an EMBR device.
- 4.23. Contours of solidus and liquidus temperatures at various transverse cross-sectional planes (Y-Z planes) for a typical continuous slab caster with type E-EMBR device and 0.3 tesla magnetic flux density.
- 4.24. Effect of magnetic flux density on the minimum thickness of the solidified shell at the mold exit of a continuous slab caster with type E-EMBR device.

- 4.25. Effect of magnetic flux density on distribution of the inclusions with 0.28 mm diameter in the wide symmetry plane of a continuous slab caster with type E-EMBR device; (a) 0 tesla, (b) 0.1 tesla, (c) 0.2 tesla, (d) 0.3 tesla.
- 4.26. Effect of inclusion size on distribution of the inclusions in the wide symmetry plane of a continuous slab caster with type E-EMBR device, 0.3 tesla magnetic flux density and various inclusion diameters; (a) 0.235 mm, (b) 0.255 mm, (c) 0.285 mm.
- 4.27. Predicted induced current density vectors for various faces paralleled to the wide symmetry plane of a caster with type E-EMBR and 0.3 tesla magnetic flux density; (a) wide symmetry plane, (b) the surface at the half-thickness, (c) the surface close to the broad face.
- 4.28. Predicted Lorentz force vectors for various faces paralleled to the wide symmetry plane of a caster with type E-EMBR and 0.3 tesla magnetic flux density; (a) wide symmetry plane, (b) the surface at the half-thickness, (c) the surface close to the broad face.
- 4.29. A schematic diagram of the proposed design of EMBR (type E-EMBR) for continuous slab casters.

- 5.1. 3-D surface plot of the velocity vectors and gas volume fraction for a continuous slab caster operating with the condition used by Bessho et al. (1991); (a) velocity field, (b) gas volume fraction distribution.
- 5.2. Predicted liquid velocity profiles in the water modeling operating with the condition used by Bessho et al. (1991); (a) present study, (b) Bessho's prediction.
- 5.3. Predicted gas volume fraction distributions in the water modeling operating with the condition used by Bessho et al. (1991); (a) present study, (b) Bessho's prediction.
- 5.4. A comparison between predicted gas volume fraction distributions in the present study and those obtained numerically and experimentally by Bessho et al. (1991) for water modeling.

- 5.5. 3-D surface plot of the velocity vectors for a continuous slab caster at various conditions; (a) with solidification and without gas injection, (b) with gas injection and without solidification, (c) with both solidification and gas injection.
- 5.6. 3-D surface plot of gas volume fraction contours for a continuous slab caster; (a) without solidification, (b) with solidification.
- 5.7. Effect of argon gas bubble size on 3-D surface plot of velocity vectors for a continuous slab caster with inlet injection rate of 11% and various bubble size; (a) 1 mm, (b) 2 mm, (c) 3 mm.
- 5.8. Effect of argon gas bubble size on 3-D surface plot of gas volume fraction contours for a continuous slab caster with inlet injection rate of 11% and various bubble size; (a) 1 mm, (b) 2 mm, (c) 3 mm.
- 5.9. Gas volume fraction contours in the various cross-sectional planes of a continuous slab caster with 11% gas injection rate and 3 mm bubble size.
- 5.10. Gas volume fraction contours in the various cross-sectional planes of a continuous slab caster with 11% gas injection rate and 1 mm bubble size.
- 5.11. Effect of argon gas injection rate on 3-D surface plot of velocity vectors for a continuous slab caster with bubble size of 3 mm and various inlet gas injection rate; (a) 11%, (b) 16%, (c) 22%.
- 5.12. Effect of argon gas injection rate on 3-D surface plot of gas volume fraction contours for a continuous slab caster with 3 mm bubble size and various gas injection rate; (a) 11%, (b) 16%, (c) 22%.
- 5.13. Contours of solidus and liquidus temperatures at various transverse cross-sectional planes (Y-Z planes) for a conventional continuous slab caster without gas injection.
- 5.14. Contours of solidus and liquidus temperatures at various transverse cross-sectional planes (Y-Z planes) for a continuous slab caster with gas injection rate of 11% at inlet and bubble size of 3 mm.
- 6.1. A schematic configuration of a vertical twin-roll casting machine.

- 6.2. Blocked-off region for complex geometry of twin-roll caster in Cartesian domain.
- 6.3. Grid layout in the physical domain and its transformation into the rectangular coordinate system; (a) physical domain, (b) computational domain.
- 6.4. Velocity components in physical and computational domains; (a) physical domain, (b) computational domain.
- 6.5. Computational flow diagram for 2-D BFC code.
- 6.6. Location of the velocity components for a typical control volume.
- 6.7. Effect of grid number on the u-component velocity profile at a depth of 0.12 m across the cross-section of the cavity for $t = 10 \text{ mm}$ and $u_r = 1 \text{ m/s}$.
- 6.8. Effect of grid number on the turbulent kinetic energy profile at a depth of 0.12 m across the cross-section of the cavity for $t = 10 \text{ mm}$ and $u_r = 1 \text{ m/s}$.
- 6.9. Effect of the roll gap thickness on the velocity field for $u_r = 1 \text{ m/s}$; (a) $t = 4 \text{ mm}$, (b) $t = 10 \text{ mm}$, (c) $t = 20 \text{ mm}$.
- 6.10. Comparison of the velocity profile for a constant gap thickness ($t = 10 \text{ mm}$) and different roll speeds; (a) $u_r = 1 \text{ m/s}$, (b) $u_r = 2 \text{ m/s}$, (c) $u_r = 3 \text{ m/s}$.
- 6.11. Comparison of the non-dimensional turbulent viscosity for $u_r = 1 \text{ m/s}$ and different gap thicknesses; (a) $t = 4 \text{ mm}$, (b) $t = 10 \text{ mm}$, (c) $t = 20 \text{ mm}$.
- 6.12. Comparison of the non-dimensional turbulent viscosity for $t = 10 \text{ mm}$ and different roll speeds; (a) $u_r = 1 \text{ m/s}$, (b) $u_r = 2 \text{ m/s}$, (c) $u_r = 3 \text{ m/s}$.
- 6.13. Effect of the roll gap thickness on the turbulent kinetic energy for a constant roll speed, $u_r = 1 \text{ m/s}$; (a) $t = 4 \text{ mm}$, (b) $t = 10 \text{ mm}$, (c) $t = 20 \text{ mm}$.
- 6.14. Effect of the inlet superheat on the isotherm curves for $t = 10 \text{ mm}$ and $u_r = 1 \text{ m/s}$; (a) $SH = 10^\circ \text{C}$, (b) $SH = 20^\circ \text{C}$, (c) $SH = 30^\circ \text{C}$.
- 6.15. Comparison of the temperature contours for different roll speeds, $t = 10 \text{ mm}$ and $SH = 30^\circ \text{C}$; (a) $u_r = 1 \text{ m/s}$, (b) $u_r = 2 \text{ m/s}$, (c) $u_r = 3 \text{ m/s}$.
- 6.16. Effect of the roll gap thickness on the temperature profiles for $u_r = 2 \text{ m/s}$ and $SH = 20^\circ \text{C}$; (a) $t = 4 \text{ mm}$, (b) $t = 10 \text{ mm}$, (c) $t = 20 \text{ mm}$.

- 6.17. Nu_t distribution along the roll surface for $t = 10 \text{ mm}$, $SH = 10^\circ \text{C}$ and different roll speeds.
- 6.18. Variation of the Nu_t along the roll surface for $u_r = 1 \text{ m/s}$ and different gap thicknesses.
- 6.19. Variation of the Nu_t along the roll surface for $u_r = 2 \text{ m/s}$ and different gap thicknesses.
- 6.20. Variation of the Nu_t along the roll surface for $u_r = 3 \text{ m/s}$ and different gap thicknesses.
- 7.1. Various conditions for solidification progressing in a twin-roll casting machine; (a) unstable and exerts mechanical force on the rolls, (b) stable, (c) unstable and leads to breakout.
- 7.2. Effect of grid number on the u-component velocity profile at a depth of 0.12 m across the cross-section of the cavity for $t = 4 \text{ mm}$ and $u_r = 1 \text{ m/s}$.
- 7.3. Effect of grid number on the turbulent kinetic energy profile at a depth of 0.12 m across the cross-section of the cavity for $t = 4 \text{ mm}$ and $u_r = 1 \text{ m/s}$.
- 7.4. Effect of C_0 value on the velocity field for $u_r = 1 \text{ m/s}$ and $t = 4 \text{ mm}$; (a) $C_0 = 0$, (b) $C_0 = 200$, (c) $C_0 = 400$, (d) $C_0 = 800$, (e) $C_0 = 1600$, (f) $C_0 = 3200$.
- 7.5. Effect of C_0 value on the solidus and liquidus contours for $u_r = 1 \text{ m/s}$ and $t = 4 \text{ mm}$; (a) $C_0 = 0$, (b) $C_0 = 200$, (c) $C_0 = 400$, (d) $C_0 = 800$, (e) $C_0 = 1600$, (f) $C_0 = 3200$.
- 7.6. Effect of C_0 value on the superheat isotherms for $u_r = 1 \text{ m/s}$ and $t = 4 \text{ mm}$; (a) $C_0 = 0$, (b) $C_0 = 200$, (c) $C_0 = 400$, (d) $C_0 = 800$, (e) $C_0 = 1600$, (f) $C_0 = 3200$.
- 7.7. Comparison of the non-dimensional turbulent viscosity contours for $t = 4 \text{ mm}$, $u_r = 1 \text{ m/s}$, and different C_0 value; (a) $C_0 = 0$, (b) $C_0 = 1600$, (c) $C_0 = 3200$.
- 7.8. Effect of C_0 value on the temperature profile on a horizontal cross-sectional plane at a depth of 0.12 m from the top.

- 7.9. Effect of C_0 value on the temperature profile on a horizontal cross-sectional plane at a depth of $0.25\ m$ from the top.
- 7.10. Effect of C_0 value on the temperature profile on a horizontal cross-sectional plane at exit (depth of $0.385\ m$ from the top).
- 7.11. Effect of various turbulent viscosity modification factors on the velocity distribution for $C_0 = 1600$; (a) $f_m = 1$, (b) $f_m = \sqrt{g_t}$, (c) $f_m = g_t^2$.
- 7.12. Effect of various turbulent viscosity modification factors on liquidus and solidus temperatures for $C_0 = 1600$; (a) $f_m = 1$, (b) $f_m = \sqrt{g_t}$, (c) $f_m = g_t^2$.
- 7.13. Effect of various turbulent viscosity modification factors on temperature distributions for $C_0 = 1600$; (a) $f_m = 1$, (b) $f_m = \sqrt{g_t}$, (c) $f_m = g_t^2$.
- 7.14. Effect of various turbulent viscosity modification factors on the temperature profile on a horizontal cross-sectional plane at exit (depth of $0.385\ m$ from the top).
- 7.15. Predicted results for a nozzle width of $12\ mm$, roll-gap of $3\ mm$, $C_0 = 1600$ and $f_m = 1$; (a) velocity vectors, (b) liquidus and solidus temperatures, (c) temperature contours.
- 7.16. Predicted results for a nozzle width of $12\ mm$, roll-gap of $4\ mm$, $C_0 = 1600$ and $f_m = 1$; (a) velocity vectors, (b) liquidus and solidus temperatures, (c) temperature contours.

List of Tables

Tables	Page
1.1 Key technologies supporting the continuous casting process.....	1-3
2.1 Coefficients and empirical constants of low-Re $k-\varepsilon$ turbulent mode developed by Launder and Sharma.....	2-10
2.2 Summary of the non-dimensional governing equations for Launder and Sharma version of the low-Re $k-\varepsilon$ turbulent model.....	2-16
2.3. Thermophysical properties of steel, geometrical parameters and heat transfer coefficients used for the simulation.....	2-20
3.1. Summary of the adopted boundary conditions.....	3-9
3.2. The various types of energy boundary conditions in the mold for stainless steel slab casters.....	3-10
3.3. Thermophysical properties of stainless steel and geometrical parameter used for the simulations.....	3-12
4.1. Summary of the non-dimensional governing equations.....	4-17
4.2. Thermophysical properties of steel, electromagnetic condition and geometrical parameters used for the simulation.....	4-20
5.1. Summary of the non-dimensional governing equations.....	5-8
5.2. Thermophysical properties of steel, casting conditions and geometrical parameters used for the simulation.....	5-11
6.1. The empirical constants for low-Re $k-\varepsilon$ turbulent model of Launder and Sharma.....	6-10
6.2. Physical properties of stainless steel and the geometrical parameter used for the calculations.....	6-18
7.1. Summary of the adopted boundary conditions.....	7-7
7.2. Physical properties of stainless steel and the geometrical parameter used for the calculations.....	7-9

INTRODUCTION

1.1 Continuous Slab Casting Processes

The process of the continuous casting is credited to the first trial of the continuous casting of steel performed by H. Bessemer in 1846. Bessemer's original machine was a top feeding twin-roll caster designed for producing iron and steel sheets directly from the molten metal. Although he received a patent for his process, due to numerous technical difficulties at that time, he could not proceed with his idea. However, for several decades, his idea played a significant role in many research efforts carried out in many different parts of the world.

The 1947 trial of the continuous casting machine of Junghans from former West Germany was the first application of the continuous casting process to steel (Wolf 1992). He initiated the series of research and inventions of key technologies of today's continuous casting process, such as: open-ended water-cooled mold, mold oscillation, mold lubrication and submerged nozzle.

The first commercialized continuous casting process for the steel industries was established in the 1950's. This industrial continuous casting process could not surpass the traditional ingot casting for the following couple of decades. From the 1970's onward, a rapid and steady growth of the continuous casting process was achieved in the industrialized countries. The gradual domination of the continuous casting process in steel production is mainly due to the advantages of this process over the conventional ingot casting processes, such as:

- 1) High productivity; the time required for producing slab from molten steel is 30 to 60 *min* in continuous casting processes compared to 1-2 days in ingot casting-primary rolling processes.
- 2) Yield; a continuous casting process possesses 96 to 99% yield from molten metal to slab, while an ingot casting-primary rolling process has 80 to 90% yield.
- 3) Energy saving; a continuous casting process only expends 1/2 to 1/4 of the energy required in an ingot casting-primary rolling process.
- 4) Labor saving; the labor work in one shift for an ingot casting process is 20 to 30 persons, while it decreases to almost one third for a continuous casting process.
- 5) Space requirement saving; the plant floor space in a continuous casting process decreases to one third or less compared to that of an ingot casting process.
- 6) High quality; the quality of steel cast and its homogeneity in a continuous casting process are better than that presently achievable by an ingot casting process.

All these success were achieved with the support of various key technologies developed to modify and make the process more efficient and controllable. Table 1.1 represents the key technologies supporting the continuous casting processes.

For the development of the continuous casting process, a variety of designs of continuous casters have been used in industries. These designs originated with the vertical type which was replaced by more efficient types such as: bow, vertical-bending and low-head types. A schematic diagram of a typical continuous slab caster is provided in Fig. 1.1. Casting machines may differ in size, capacity, shape, number of strands and other design characteristics but they all perform some common basic operations as follows:

The process of casting starts with feeding of molten steel from tundish into the open-end water-cooled mold through a submerged bifurcated nozzle. The casting speed is determined by the rate at which liquid metal is supplied. This is done by installing of slide gates, stopper rods or sometimes both at the bottom of the tundish. The primary function of the mold in a continuous casting operation is to extract sufficient heat from the steel to form a solidified shell at the mold exit. This solid layer should be thick enough to hold the liquid steel without bulging or breaking. On the hot surface of the mold, i.e., the

mold/steel interface, the solidifying shell shrinks away from the wall due to the volumetric contraction of steel as it undergoes solidification, and an air-gap is formed. The air-gap

Table 1.1 Key technologies supporting the continuous casting process.

Ladle	Steel weight control
	Slag carryover detection
Tundish	Steel weight control
	Continuous steel feeding
	Temperature measurement
	Steel heating
Mold	Automatic start and stop
	Steel level control
	Breakout prediction
	Steel flow control (electromagnetic stirring and control)
	On-line width and taper control
	Mold oscillation control
Secondary cooling zone	Secondary cooling control (air-mist)
	Strand surface temperature control
	Roll gap measurement and control
	Spray nozzle clogging detection
	Casting speed control
	Electromagnetic stirring
	Compression casting
	Hot slab width measurement
	Strand soft reduction control

and its evolution as described by Samarasekera and Brimacombe (1979) provides the largest resistance to heat flow in the system. On the other hand, the ferro-static pressure

from above is enough to reduce the air-gap and even contacts the solidified shell to the mold wall for a longer period of time.

The other important aspects related to the operation of the mold are oscillation and lubrication which can be done by rapeseed oils or low-melting powders. These functions in the mold have made it possible to continuously cast steel at rates high enough to make the operation more profitable than conventional ingot casting.

The argon gas bubble injection through a submerged nozzle is another interesting phenomenon in the mold operation. In fact, today, argon gas bubbles are blown into the immersion nozzle in almost all of the continuous slab caster machines in order to prevent nozzle clogging. The reason for nozzle clogging can be related to the reactions which usually occur in the nozzle due to the natural sucking of air through cracks, pores or joints in the nozzle walls. The reoxidation products such as alumina associated with these reactions may either deposit on the nozzle walls and cause clogging, or enter into the mold in the form of inclusions. The inclusions penetrated into the mold can be trapped by the moving solidifying shell and create surface or internal defects of the product. One of the undesired consequences of argon gas bubble injection is their entrapment by the solidifying shell and the formation of blow-holes in the slab. The presence of blow-holes deteriorates the quality of steel sheet especially as the strip passes through the annealing processes. In order to prevent such defects, the motion and distribution of the argon gas bubbles in the mold must be controlled.

One of the recent and important innovations in controlling the steel flow in the mold is the application of the magnetohydrodynamics (MHD) in the mold. In the usual continuous casting machine for slabs, the steel flow which is discharged from the submerged entry nozzle impinges on to the narrow face of the slab and, by thinning the mushy and solid layers developing on this face, increases the breakout possibility. On the other hand, the inlet jet flow after impinging on to the narrow face produces two strong upper and lower recirculation flows. The lower recirculation flow, which penetrates downward along the narrow face of the slab, may carry non-metallic inclusions and gas bubbles deep into the caster. Therefore, the control of jet flow leaving the submerged

entry nozzle is a critical step in the technology of mold control. In this regard, the magnetohydrodynamic techniques are designed and applied to the continuous casting process to operate as a brake against the liquid jet stream in the mold for further improvement of casting capability. MHD has also been used for the purpose of electromagnetic stirring in the mold for homogenizing and improving the internal quality of cast steel.

The other section of the continuous casting machine is the spray zone or secondary cooling zone which is located immediately below the mold. The function of the spray zone is to continue to extract heat from the solidifying section after it leaves the mold. Due to the thermal resistance of the solidified shell, if a too high cooling rate is imposed at the slab surface in the secondary cooling zone, it results in an overcooled surface temperature rather than growth of the solidification which may yield to the appearance of high thermal stresses within the shell.

Due to the technical limitation in increasing the casting speed in a conventional continuous casting machine, and also for reducing the operating and capital costs in continuous slab casting, a new competitive field of research in casting has been evolving by developing and implementing various near net shape casting processes.

1.2 Near Net Shape Casting

Commercialization of a near net shape casting process would be one of the major challenges for the next generation of the continuous casting processes. The principle of a near net shape casting process is the direct conversion of the molten steel nearer to final flat product sizes (or near net shape) thereby bypassing the intermediate steps of thick slab casting, conditioning, reheating, roughing, hot rolling and cold rolling. It is customary to classify the process routes for different technologies as shown in Fig. 1.2, according to the cast product thickness.

- I. Thin slab, ranging from 30 to 80 *mm* in thickness and 1500 to 2000 *mm* in width. The as-cast thin slab could be directly fed, without conditioning, into a hot-strip finishing mill.
- II. Strip or thin sheet, from 3 to 20 *mm* thick and 1200 to 1500 *mm* wide. The aim is to make these as-cast sections suitable for direct cold rolling into strip. This route not only eliminates the need for costly conventional hot-strip mill, but also offers the possibility of producing new alloy steels in strip form.
- III. Thin strip, ranging from 0.5 to 3 *mm* in thickness and up to 1200 *mm* in width. This process requires minor cold rolling operation to produce thin strip.
- IV. Foils, whose thickness is around 20 μm to 500 μm and up to 300 *mm* wide. It produces a final net-shape flat products without processing through the hot and cold strip mill.

Conversion of cast steel into final shape (near net shape casting) should have considerable advantages over the conventional continuous casting process, including:

- a) Lower demands for energy, operational personnel and maintenance, by directly rolling thin sections into final products, thereby eliminating the intermediate steps such as cooling, scarfing and dressing, roughing in thin slab processing and additional eliminating of hot rolling and cold rolling in strip casting processing;
- b) Production in smaller tonnage in various steel grades and quality;
- c) Flexibility in producing varying coil width and weights to meet customer requirements;
- d) Lower operating costs and capital investment due to fewer plant components in a more compact arrangement than in the conventional facilities. It has been estimated that by employing thin slab caster and strip caster, the production costs of sheet metal can be reduced by one-third and three quarters, respectively, compared to conventional continuous casting; and
- e) Less space requirement, due to the omission of the intermediate storage, inspection and conditioning of intermediate products.

Due to the aforementioned advantages, the new trend in continuous casting research was initiated at the beginning of the 1980's in USA, Europe, Australia and Japan. Despite significant efforts and relative success achieved till now, none has succeeded in commercialization of the near net shape casting except for the thin slab casting process. Thin slab is now commercially produced with a number of different casting machines capable of producing commercial quality strip (Cramb, 1996; Brimacombe and Samarasekera, 1994).

Among different strip and thin strip casting processes, the twin-roll caster development has dominated thin strip casting in recent years due to its high productivity.

Today, numerous pilot-scale twin-roll casters (Fig. 1.3) have been installed worldwide and many researchers have put significant effort into their developments. Both thick strip (around 25 mm thick), that needs some hot working, and strip (around 5 mm thick), which can be directly cold rolled, are the kinds of semi-products targeted by this technology (Grosjean et al., 1993; Cook et al., 1990). The basic principle of the twin-roll caster operation (Fig. 1.3) is that liquid metal is fed from the top using a submerged refractory shroud. The two rolls have rotational axes located in the same horizontal plane; they are generally made of high conductivity copper alloy, water cooled; a constant gap between them is maintained by pressure cylinders. A constant height of liquid melt is maintained automatically or semi-automatically in the mold region so that the rolls are wet along a certain angle, usually around 40° . The withdrawal of the strip is carried out by the twin rolls themselves for the strip thicknesses of 5 mm or less. The mold volume is shut off on the sides by refractory plates which are tightly applied against the rolls. Since it is very important to control the start-up period and also the steady-state casting conditions carefully, in most of the designs a computer control system takes charge of the most critical operations. The basic effective parameters in the operation are the steel level in the mold, the roll speed, the torque on the driving shaft, the roll separating force, water temperature in and out of the rolls, liquid steel temperature in the tundish and in the mold, etc. As seen, the twin-roll casting process involves quite complicated control problems because of its poor stability with respect to heat and mass flow within the mold and the

difficulty of controlling the kissing (nip) point of the solidifying shells on the roll. Stable casting conditions can only be obtained if a uniform solidification is completed in the very vicinity of the kissing point between rolls, otherwise either a negative or a positive segregated central region is formed. In addition, if solidification is completed before reaching the minimum clearance point between the rolls, then deformation of the solid will occur if operation is under the fixed gap. Another parameter affecting the stability of the operation is temperature across the width of the section which is required to be kept almost constant in order to get uniform shell thickness. This can be achieved only with a uniform feed and excellent temperature and composition control during the operation.

In both continuous slab casting and twin-roll casting processes, the transport phenomena play a significant role in their operation. In the continuous casting process there are still key technology improvements, such as steel flow control in the mold, bubble injection effects, magnetohydrodynamic break and electromagnetic stirring, to be correctly implemented and understood. In the twin-roll casting processes, to attain successful operation and control solidification rate, a better understanding of all aspects of transport phenomena such as turbulent fluid flow, heat transfer and solidification, etc. is required. Mathematical and physical modeling, as well as experimental observations on real casting processes, can be used as the basic tools in such understandings. However, the experimental studies in real process involving solidification are much more expensive and sometimes impossible. Thus, a comprehensive mathematical model of a real caster machine seems to be required for gaining sufficient knowledge for the improvement of the caster mold and for the design and operation of more sophisticated continuous casting machines.

1.3 Prior Studies and Modeling Complexities

The modeling of both continuous slab casters and twin-roll strip casters, which is the subject of this study, involves coupled turbulent fluid flow, heat transfer and phase change phenomena. These phenomena individually have received considerable attention

among the various researchers over the past 25 years. Generally, the progress in the continuous casting modeling critically depends on the evolution and development of the modeling method for these individual aspects. A brief review of the basic concepts of the modeling of these phenomena, in the context of metallurgical applications, has been discussed in the present section. This survey includes a review of: (1) heat conduction in phase change problems, (2) convection phase change problems, and (3) turbulence transport in phase change problems.

As far as the numerical phase-change studies are concerned, Poirier and Salcudean (1988) have reviewed a number of numerical methods which are available for modeling of heat conduction phase change in liquid metals. The various modeling approaches for phase change problems, such as apparent heat capacity, effective heat capacity, explicit enthalpy, post iterative enthalpy method, enthalpy source based and semi-analytical methods were discussed and their relative advantages and disadvantages were analyzed. Another review paper, which is devoted to the numerical investigations of conduction phase change heat transfer problems, has been presented by Voller et al. (1990a). In this paper, the applications of the various finite difference and finite element methods in solidification processes were explained and compared.

The enthalpy method, which has been used widely in phase-change problems, was first proposed by Shamsundar and Sparrow (1975). They used the enthalpy method in conjunction with an implicit finite difference scheme for the solidification process of a phase change material with a distinct freezing point (pure material). In 1981 Voller and Cross (1981) applied an implicit finite difference scheme as well as various explicit schemes to calculate enthalpy and temperature fields for various phase change problems. In 1983, Voller and Cross (1983) extended the enthalpy method to continuously track the phase change front in one-dimensional solidification problems. Later, Voller (1985) proposed a new technique of enthalpy formulation in order to analyze the situation in which the phase change takes place over a range of temperature. An application of this technique was made to the case of a binary alloy and led to the approximation of solidification parameters such as the rate of growth of the mushy region.

The majority of the previous investigations were concerned with the phase change problems in which conduction was the principal mechanism of heat transfer. It is only in the 1980's that the effect of convection has been taken into account while modeling phase-change heat transfer problems. It seems that Gartling (1980) and Morgan (1981) were among the first investigators who considered convection terms in phase-change problems and employed the simple approach of fixing velocities to zero in a computational cell whenever the nodal latent heat of the cell was less than a predetermined value. The simulation of motion in the mushy region was considered by making viscosity as a function of nodal latent heat. This approach formed the basis of the variable viscosity method for modeling the mushy region phase change problems which was used later by Voller et al. (1985), and Salcudean and Abdullah (1988). Two investigators who have made significant contributions in the convection phase-change modeling are Voller and Prakash (1987). These authors developed a fixed grid enthalpy method to solve the convection-diffusion controlled mushy region phase change problems. The phase change material in their study was not pure and in order to simulate fluid motion in the mushy region, they used the Darcy source approach, which is conventionally used for porous medium. They used also the Carman-Koseny (1937) equation to relate the permeability to the liquid fraction in the mushy region. In the enthalpy-porosity approach, the velocities in the solid region turn automatically to zero or any other predetermined value.

Recently, the enthalpy-porosity method has been successfully extended by many investigators to model mushy zone solidification. Voller et al. (1990b) investigated a number of alternative approaches to account for the nature of the mushy region. Sinha et al. (1992) developed the enthalpy-porosity method for anisotropic porous medium and accounted for the property variations in the presence of dendritic phase change. While modeling solidification of a pure material, Lee and Tzong (1991) applied the enthalpy formulation for a phase change material which is characterized by a high jump of thermal diffusivity at the discrete interface. Rostami et al. (1992) modified the enthalpy approach to account for rapid melting and solidification.

Another successful method for convection diffusion phase change problems was developed by Bennon and Incropera (1987). Their formulation was generally developed from the description of the transport behavior and the volume averaging techniques based on the classical mixture theory. Their resultant equations were a consistent set of equations governing the conservation of mass, momentum, energy and species. This kind of formulation is generally considered unsuitable for addressing discrete phase change problems.

Although flows in liquid metal processing operations are often turbulent and recirculatory in nature, a very few investigators have considered the effect of turbulence in their studies. Asai and Szekely (1975) applied the one-equation turbulence model (Kolmogorov-Prandtl model) for a two-dimensional modeling of a continuous billet casting system. A less than satisfactory agreement between measurements and predictions in their study clearly reveals the weakness of the one-equation turbulence model in the calculation of the flow field of such processes.

Flint (1990) reported the use of the standard high-Reynolds $k - \epsilon$ model for the simulation of a continuous slab caster. The application of this turbulence model requires a separate wall function approximation at the vicinity of the solid boundary. In a separate work by Huang et al. (1992) the standard high Reynolds $k - \epsilon$ model and associated near wall functions proposed by Launder and Spalding (1974) were implemented to the 2-D and 3-D simulation of a continuous slab casting system. This study has been carried out for a single phase material, and interactions among liquid, mushy and solid phases have not been appropriately considered. The standard high-Re $k - \epsilon$ turbulent model was also used by Murthy et al. (1988), Prescott and Incropera (1995) and Li (1996) for different metallurgical problems. However, all of these investigators, except Prescott and Incropera, simplified the phenomena to a single-phase problem. Generally, in the solidification processes being modeled using the standard high-Re $k - \epsilon$ turbulent model, the implementation of the near wall functions at the liquid-solid interface is difficult since the interface is unknown a priori.

Farouk et al. (1992), Murakami et al. (1993), Shyy et al. (1993) and Aboutalebi et al. (1995) used the low Reynolds $k - \varepsilon$ turbulence models in the numerical simulation of coupled fluid flow and solidification of different casting systems. The low-Re turbulence $k - \varepsilon$ models do not need any wall functions and, moreover, those versions which do not require the explicit distance from the wall can be easily implemented in modeling solidification processes.

The other complexity associated with turbulent phase-change problems which involves mushy region development is how to combine the mushy fluid flow modeling and turbulent modeling. Since it is believed that the turbulent energy decays in the mushy region, one way of modeling this aspect is by putting a damping term in the turbulent kinetic energy equation applicable only in the mushy region and the other way is by applying a damping factor in the calculation of the turbulent viscosity for the mushy region. Aboutalebi et al. (1995) used a damping term for the turbulent kinetic energy equation similar to the Darcy term used in the momentum equation. The damping factor was considered to be a function of porosity of the mushy region. Shyy et al. (1993) used a turbulent viscosity modification factor for the mushy region and allowed the turbulent viscosity to decay in the mushy region with a square root function of the liquid fraction.

Concerning other phenomena used for continuous slab casting systems, such as gas blown to the caster and electromagnetic braking for flow control, there are only a few studies which have modeled these phenomena for the continuous slab casters, however without considering the solidification heat transfer. A detailed review of these investigations as well as those specifically related to the continuous slab casting or twin-roll strip casting modeling will be presented in the relevant chapters.

On the basis of the existing literature related to the continuous casting processes, one can make the following observations:

- 1) The implementation of the turbulence model in the liquid-solid region, especially in the presence of mushy zone solidification phase change, is still a challenge to be tackled.
- 2) Most of the previous studies of the slab casting systems are related to either one or two dimensions or unrealistic modeling in the third dimension. To model a real continuous slab

casting system, a three-dimensional study of the fully coupled momentum, energy and solidification is required.

3) There are only a few simplified studies related to the implementation of argon gas bubble injection and electromagnetic brake or flow control in the continuous casting modeling. None of these works even considered the mushy solidification effect in modeling.

4) The specific problem of the twin-roll casting process requires a more fundamental study with regard to the sensitivity of the process modeling parameters.

1.4 Objectives

The main objective of the present work is to develop a general comprehensive model and the associated computer codes for solving momentum, energy, turbulent quantities and Maxwell equations governing electromagnetic field which can handle the following problems:

- i) 3-D, steady state, incompressible flow problems.
- ii) The mushy region solidification phase change problems.
- iii) Gas bubble injection simulation with and without mushy region solidification.
- iv) Flow control problems using electromagnetic forces.

Next, a program will be implemented to simulate a typical continuous slab casting system and the predictions of the model will be compared with experimental measurements available.

The other objective of this work is to model a thin-strip twin-roll casting process. For this part a separate code will be developed to solve the associated transport equations and accommodate the arbitrariness in the geometry of the caster.

1.5 Thesis Outline

This study is presented in the seven subsequent chapters. Each chapter is almost complete in itself and contains its own relevant introduction, prior studies, mathematical formulation, solution method, results and discussion, references and nomenclature.

Chapter 2 deals with the 3-D numerical modeling of coupled turbulent flow and solidification of a typical continuous slab casting process. A detailed explanation of the mathematical formulation governing the phenomena taking place in the caster is provided. The closure of this chapter contains model verification and parametric studies on the primary casting conditions such as casting speed, inlet superheat and nozzle submergence depth.

Chapter 3 describes the effect of mold wall heat extraction rate on the flow field and solidification development in the continuous slab casting system.

Chapter 4 is devoted to the simulation of electromagnetic flow control effect on the operation of continuous slab casting processes. In this chapter the Maxwell equations describing the electromagnetic field are explained and how these equations are coupled to the equations concerning the fluid flow and described in Chapter 2 are discussed. The model is then used to evaluate the effect of various commercially used electromagnetic flow control devices or electromagnetic braking systems on the flow characteristics of the molten steel in the mold.

Chapter 5 is concerned with the modeling of the effect of argon gas bubble injection into the mold by rationally varying the parameters associated with a typical continuous slab casting process such as: flow pattern, heat transfer and development of solid and mush layers. The mathematical formulation employed in this chapter is based on the multiphase continuum model. One of the undesired consequences of argon gas blown into the mold, which is to do with their entrapment in the solidifying shell, is also numerically investigated in this chapter.

Chapter 6 presents a thermal fluid flow model for the simulation of turbulent flow and heat transfer in the wedge-shaped pool of the thin-strip twin-roll casting machine. The nonorthogonal body-fitted technique, which is used to tackle the arbitrary geometry, is described here in detail. In addition, the formulated model is implemented through the

development of a numerical code and is subsequently used to study the effect of casting parameters such as roll speed, roll gap thickness and inlet temperature on the flow field and temperature distribution in the pool.

Chapter 7 is concerned with the coupled turbulent fluid flow and macroscopic solidification modeling of a thin-strip twin-roll casting.

Chapter 8 provides overall conclusions, contributions to knowledge and recommendations for future works.

REFERENCES

- Aboutalebi M. R., Hasan M. and Guthrie R. I. L., Coupled turbulent flow, heat and solute transport in continuous casting processes, *Metallurgical Transactions*, Vol. 26B, pp. 731-744, (1995).
- Asai S. and Szekely J., Turbulent flow and its effects in continuous casting, *Ironmaking and Steelmaking*, No. 3, pp. 205-213, (1975).
- Bennon W. D. and Incropera F. P., A continuum model for momentum, heat and species transport in binary solid-liquid phase change systems-I. model formulation. *Int. J. Heat Mass Transfer*, Vol. 30, No. 10, pp. 2161-2170, (1987).
- Bessemer Sir H., British patent No. 11317, (1846).
- Brimacombe J. K. and Samarasekera, I. V., The challenges of thin slab casting, *Iron and Steelmaker*, Vol. 21, No. 11, pp. 29-39, (1994).
- Cook R. D., Furber R. P., Trenty R. F., LTV steel Cleveland works' 84-in. tandem mill modernization, *Iron and Steel Engineer*, Vol. 67, No. 3, pp. 51-56, (1990).
- Carman P. C., Fluid flow through granular beds, *Trans. Inst. Chem. Engrs*, Vol. 15, pp. 150-166, (1937).
- Cramb A.W., Current trend in steel casting for strip, *Melt Spinning, Strip Casting and Slab Casting*, Eds. E. F. Matthys and W. G. Truckner, pp. 1-11, (1996).
- Farouk B., Apelian D. and Kim Y. G., A numerical and experimental study of the solidification rate in a twin-belt caster, *Metallurgical Transaction*, Vol. 23B, pp. 477-492, (1992).
- Flint P. J., A three-dimensional finite difference model of heat transfer, fluid flow and solidification in the continuous slab caster, *ISS 73d Steelmaking Conference Proceedings*, Detroit, MI, March 25-28, pp. 481-490, (1990).
- Gartling D. K., Finite element analysis of convective heat transfer problems with phase change, in K. Morgan et al. (eds.), *Computer Methods in Fluids*, Pentech, London, pp. 257-284, (1980).

- Grosjean J. C., Jacquot J. L., Damasse J. M., Litterscheidt H., Senk D., and Schmitz W., Thin strip casting experiment at Irsid and Thyssen Stahl AG, *Iron & Steelmaker*, Vol. 20, No. 8, pp. 27-32, (1993).
- Huang X., Thomas B. G. and Najjar F. M., Modeling superheat removal during continuous casting of steel slabs, *Metallurgical Transaction*, Vol. 23B, pp. 339-356, (1992).
- Lauder B. E. and Spalding D. B., The numerical computation of turbulent flows, *Comput. Methods in Appl. Mech. Eng.*, Vol. 3, pp. 269-289, (1974).
- Lee S. L. and Tzong R. Y., An enthalpy formulation for phase change problems with a large thermal diffusivity jump across the interface, *Int. J. Heat Mass Transfer*, Vol. 34, No. 6, pp. 1491-1502, (1991).
- Morgan K., A numerical analysis of freezing and melting with convection, *Comp. Methods Appl. Eng.*, Vol. 28, pp. 275-284, (1981).
- Murakami H., Hasan M., and Guthrie R. I. L., Computational study of the transport processes in a twin-roll stainless steel caster, *Proceedings of the International Symposium on Strip Casting, Hot and Cold Working of Stainless Steels*, Eds. N. D. Ryan, A. J. Brown and H. J. McQueen, Quebec City, Quebec, August 1993, pp. 35-52, (1993).
- Poirier D. and Salcudean M., On numerical methods used in mathematical modeling of phase change in liquid metals, *Numerical Heat Transfer*, Vol. 110, PP. 562-570, (1988).
- Rostami A. A., Greif R. and Russo R. E., Modified enthalpy method applied to rapid melting and solidification, *Int. J. Heat Mass Transfer*, Vol. 35, No. 9, pp. 2161-2172, (1992).
- Salcudean M. and Abdullah Z., On the numerical modeling of heat transfer during solidification processes, *Int. J. for Numerical Methods in Engineering*, Vol. 25, No. 2, pp. 445-473, (1988).
- Samarasekera I. V. and Brimacombe J. K., The thermal field in continuous-casting mold, *Canadian Metallurgical Quarterly*, Vol. 18, pp. 251-266, (1979).

- Shamsundar N. and Sparrow E. M., Analysis of multidimensional conduction phase change via the enthalpy model, *ASME J. Heat Transfer*, Vol. 97, pp. 333-340, (1975).
- Shyy W., Pang Y., Hunter G. B., Wei D. Y. and Chen M.-H., Effect of turbulent heat transfer on continuous ingot solidification, *ASME J. of Engineering Materials and Technology*, Vol. 115, pp. 8-16, (1993).
- Sinha S. K., Sundararajan T. and Garg V. K., A variable property analysis of alloy solidification using the anisotropic porous medium approach, *Int. J. Heat Mass Transfer*, Vol. 35, No. 11, pp. 2865-2877, (1992).
- Voller V. and Cross M., Accurate solutions of moving boundary problems using the enthalpy method, *Int. J. Heat Mass Transfer*, Vol. 24, pp. 545-556, (1981).
- Voller V. R., A heat balance integral method for estimating practical solidification parameters, *IMA Journal of Applied Mathematics*, Vol. 35, pp. 223-232, (1985).
- Voller V. R., Markatos N. C. and Cross M., Techniques for accounting for the moving interface in convection diffusion phase change, *Fourth Int. Conf. in Numerical Methods in Thermal Problems*, (Edited by R. W. Lewis and K. Morgan), Swansea, U.K., July 15-18, Vol. 4, pp. 595-609, (1985).
- Voller V. R. and Prakash C., A fixed grid numerical modeling methodology for convection-diffusion mushy region phase-change problems, *Int. J. Heat Mass Transfer*, Vol. 30, No. 8, pp. 1709-1719, (1987).
- Voller V. R., Swaminathan C. R. and Thomas B. G., Fixed grid techniques for phase change problems: A Review, *International Journal for Numerical Methods in Engineering*, Vol. 30, pp. 875-898, (1990a).
- Voller V. R., Brent A. D. and Prakash C., Modeling the mushy region in a binary alloy, *Appl. Math. Modelling*, Vol. 14, pp. 320-326, (1990b).
- Wolf M. M., History of continuous casting, *ISS Steelmaking Conference Proceedings*, Vol. 75, Toronto, Ontario, Canada, April 5-8, pp. 83-137, (1992).

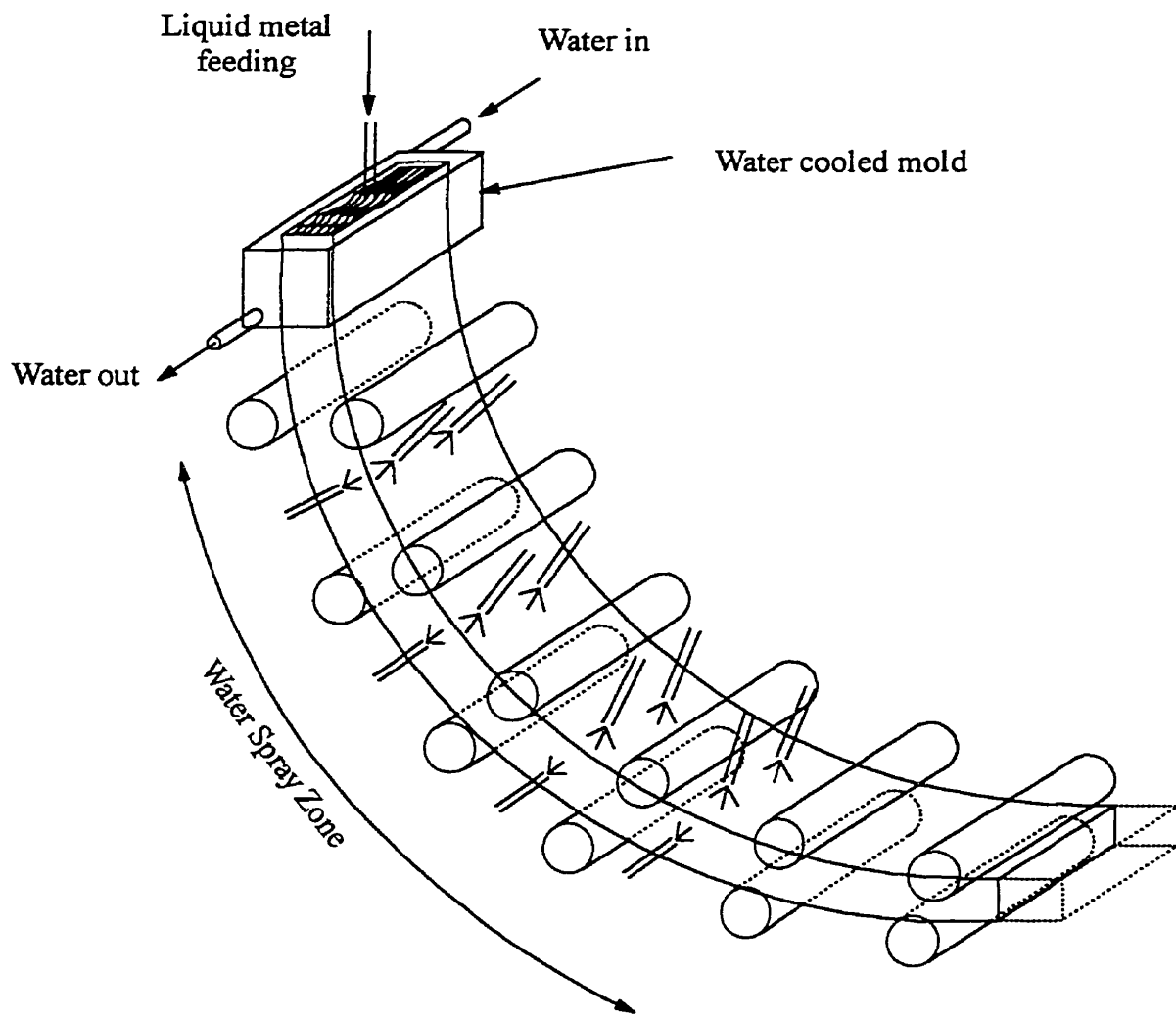


Fig. 1.1. The schematic diagram of a typical continuous slab caster

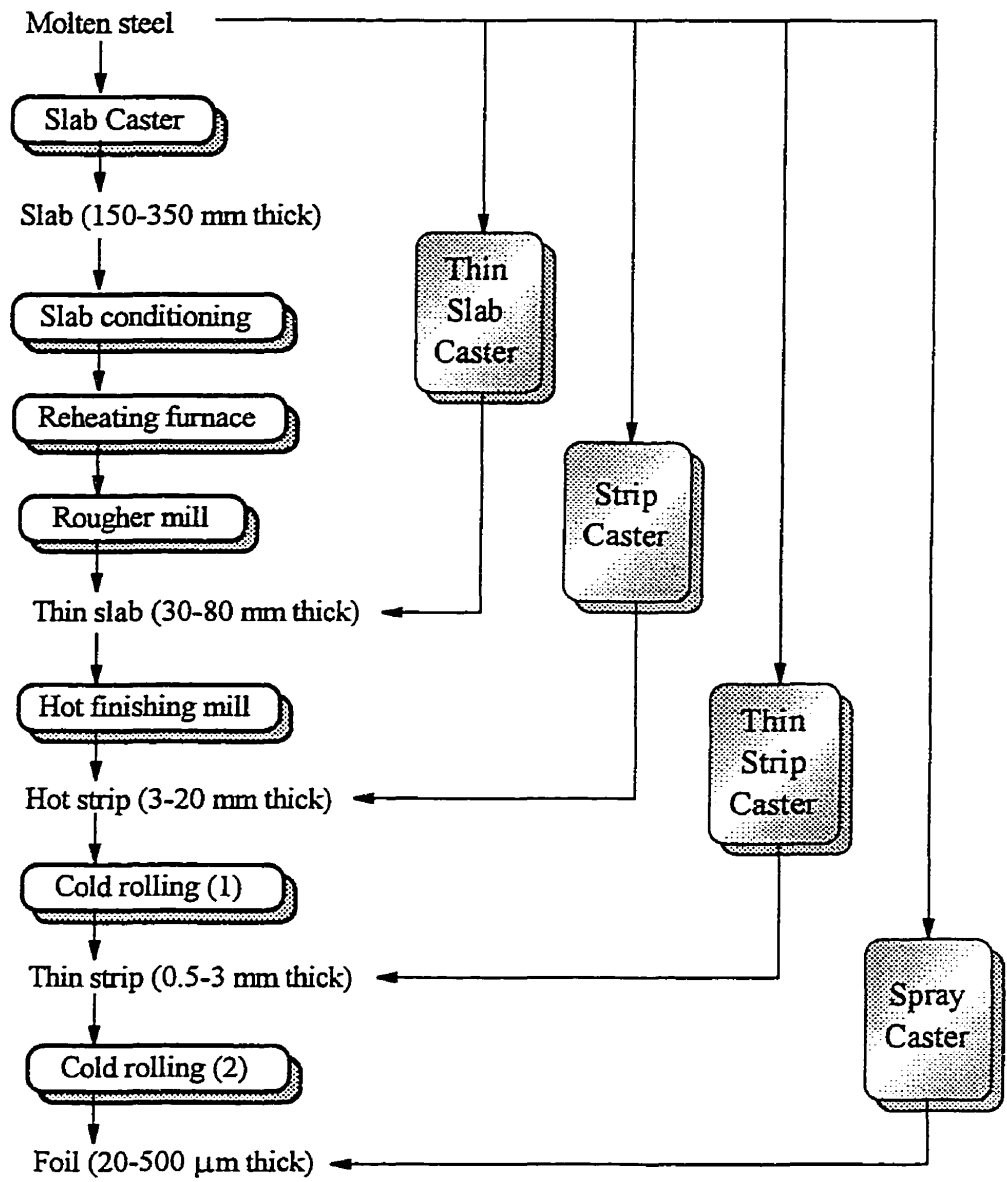


Fig. 1.2. Process routes for the production of steel sheet products.

Pouring ladle

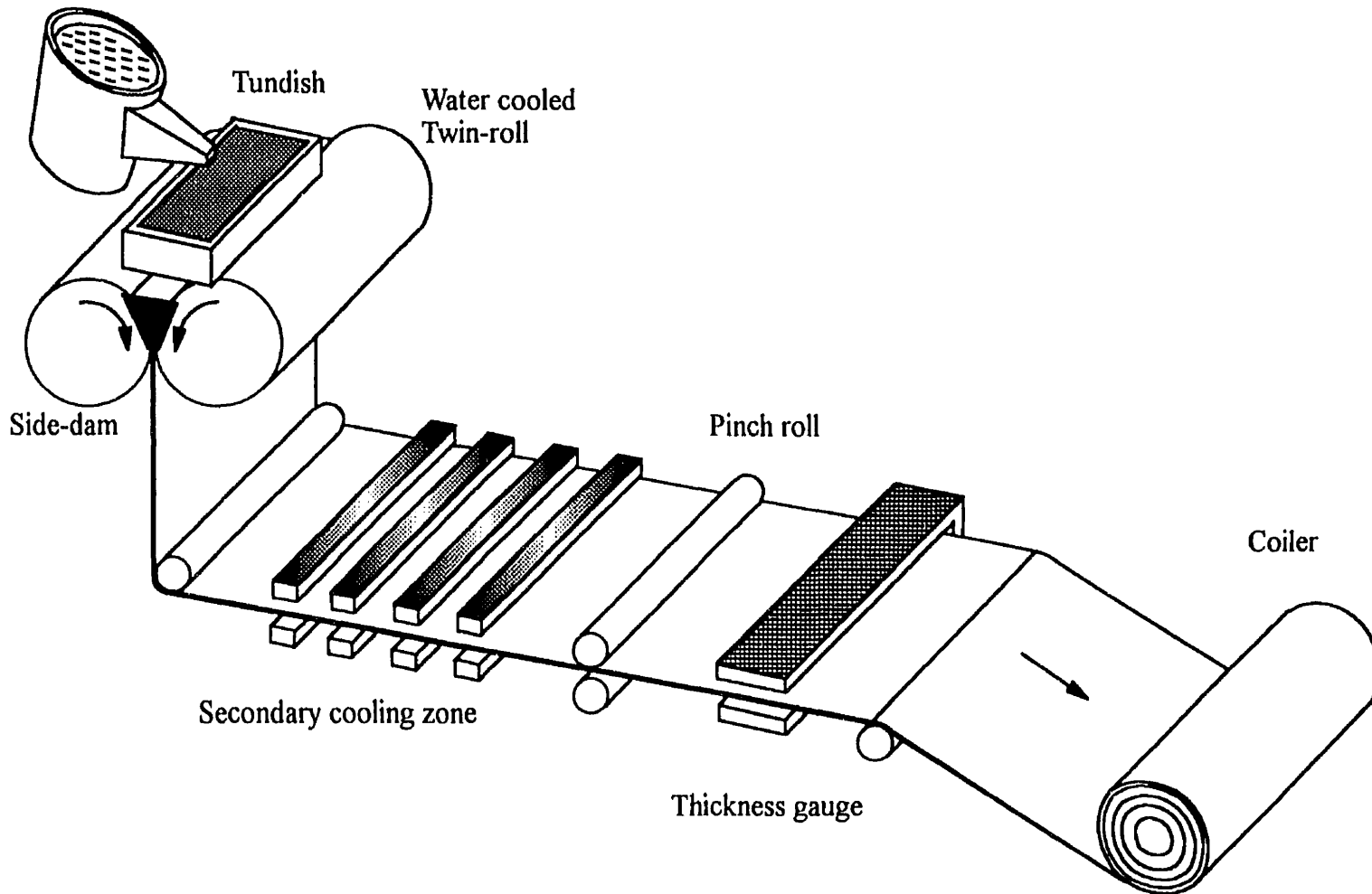


Fig. 1.3. The schematic diagram of a typical pilot-scale twin-roll caster.

3-D SIMULATION OF COUPLED TURBULENT FLUID FLOW AND SOLIDIFICATION FOR CONTINUOUS STEEL SLAB CASTERS

2.1 Introduction and Prior Studies

Over the last two decades, there have been intensive research activities undertaken worldwide related to various aspects of continuous casting (CC) processes for slab, billet and bloom casters. In spite of these studies, an advanced mathematical model, which can enhance the quantitative and qualitative understanding of the process, is still not available. Mathematical models can play a major role in the optimization of the casting parameters, e.g. mold and spray cooling systems. Modeling of a CC process is concerned with the liquid-solid phase change problems in which three-dimensional turbulent convective heat transfer in liquid side has an important effect on the growth of the solidified steel shell. Thus, a realistic model for a CC process should be capable of simulating coupled turbulent fluid flow, heat transfer and solidification.

The solidification modeling studies related to the continuous casting processes can be categorized into two classes; class (I) type models focused only on heat flow and solidification while the class (II) type models have considered the coupled heat and fluid flow with solidification. The studies carried out by Savage and Pritchard (1954), Mizikar (1967), Brimacombe (1976), Sfier and Clumpner (1977), Lait et al. (1974a, 1974b) and Lally et al. (1990) fall into the first category. In these studies the effects of convection were ignored or approximately considered through arbitrary prescriptions of the effective thermal conductivity for the liquid phase. In class (II) models, the fluid flow in the caster

was directly calculated through the solution of Navier-Stokes equations. Although flows in commercial CC processes for liquid steel are often turbulent and recirculatory in nature, a very few number of investigators have taken into account the effect of turbulence in their studies. In this section a brief review of the relevant papers which considered turbulent phenomena in the caster is presented.

Asai and Szekely (1975) considered a two-dimensional model for a continuous billet casting system. The turbulent flow in the liquid zone was modeled using the one-equation turbulence model (Kolmogorov-Prandtl model) and the computations of the flow field within the mushy zone were carried out based on the variable viscosity model. A less satisfactory agreement between measurements and predictions in their study clearly reveals the weakness of the one-equation turbulence model in the calculation of the flow field of a continuous billet caster.

Thomas and co-workers, in a series of papers (1990a, 1990b, 1992), investigated the effect of superheat dissipation on the fluid flow and temperature fields in a continuous-slab casting system. They solved both the 3-D and 2-D governing momentum and energy equations within the liquid pool. These studies did not couple the process of solidification with the fluid flow and heat transfer within the caster. First, the fluid flow and temperature fields were obtained and later the rate of heat transfer at the wall was used in the one-dimensional solidification model in order to find the rate of growth of the solidifying shell. Since these studies were carried out for a single phase material, the interactions among liquid, mushy and solid phases were not appropriately considered.

Flint (1990) reported the results of the heat transfer and fluid flow of the three-dimensional simulation of a continuous slab caster. He utilized a commercial code (PHOENICS) and said to have solved the momentum and enthalpy equations and claimed to have implicitly accounted for the solidification process. He cited that the turbulence behavior of the fluid was modeled using the standard high Reynolds $k-\epsilon$ turbulence model. The application of this turbulence model requires a separate wall function approximation at the vicinity of the solid boundary. In a solidification process, the implementation of the near wall functions at the liquid-solid interface is very difficult since

the interface is unknown a priori. It is not clear from the paper how the wall functions were implemented.

Recently, Choudhary and Mazumdar (1994, 1995) have reported the two-dimensional modeling results of fluid flow, heat transfer and solidification for continuous steel billet casters. One of the major weaknesses of their model is the fact that they have used an empirical bulk effective viscosity expression to calculate the turbulent eddy-diffusivity in the liquid pool and in the mushy region. The used empirical viscosity expression does not have any rational basis as far as the modeling of a continuous casting process is concerned. These authors have also arbitrarily divided the computational domain into a mold and a submold region. In the submold region, the turbulence level was believed to be 50% of the mold region and accordingly the effective viscosity value was reduced by the same percentage point. The authors themselves have clearly stated the weakness of their model in which the differential turbulence model cannot be applied on a zonal basis since appropriate boundary conditions are unknown at the junction of the zones. The modeling approach of these authors, apart from being two-dimensional, cannot be applied to a continuous slab caster because it lacks fundamental basis, especially with respect to the modeling of turbulence phenomena.

Aboutalebi et al. (1995a) carried out a two-dimensional numerical study to model couple turbulent flow, heat transfer and macroscopic solidification in the mold and submold regions of a stainless steel slab caster. In a later work (1995b), these authors extended their coupled turbulent flow and solidification heat transfer model by incorporating the macrosegregation of carbon and taking into account the trajectory of inclusions. They applied their extended model to simulate various transport processes that prevail in round and square billet casters. In both of their works, they applied a modified version of the Launder and Sharma low-Reynolds $k - \varepsilon$ model to analyze the effects of turbulence on transport processes in the liquid and mushy regions. They also employed the enthalpy-porosity method to model fluid flow and solidification in the mushy region. Although the assumption of two-dimensional modeling is applicable for a round billet caster, it limits the applicability of the model for square billet and slab casters. In real

continuous billet and slab casting systems, the transport processes are essentially three-dimensional in nature and a two-dimensional model can therefore predict unsatisfactory results.

On the basis of the above literature survey, it can be said that:

- 1) Most of the previous studies in the modeling of continuous slab casting systems are related to either one or two dimensions. To model a real slab casting system, a three-dimensional study of the fully coupled momentum, energy and solidification is required.
- 2) The implementation of the turbulence model in the liquid-solid region, especially in the presence of mushy zone solidification, is still a challenge to be tackled.

Thus, the study presented in this chapter is concerned with the development of a comprehensive model for the prediction of coupled three-dimensional turbulent flow, heat transfer, and macroscopic solidification in a continuous-slab casting process for steel.

2.2 Mathematical Formulation

In a typical CC machine (as shown in Fig. 1.1) molten steel flows due to gravity from a holding tundish down through a submerged entry nozzle to a water-cooled oscillatory mold. The primary function of the mold is to extract sufficient heat from the steel, so that the solidified shell at the mold exit is thick enough and strong enough to hold the liquid steel without bulging or breaking. As the solidifying strand exits the mold it then enters a spray cooling zone. The function of the spray zone is to continue to extract heat from the solidifying section.

In the present study, a twin-ported submerged entry nozzle (SEN) is considered to be a tube of rectangular cross-section having horizontal outlet ports . The nozzle was considered to be inside the computational domain. As a result, the transport equations for the nozzle zone were simultaneously computed with those applicable for the rest of the domain.

Due to the physical properties of steel in a continuous casting machine and the magnitude of the liquid velocity involved, the fluid flow in this process is essentially in turbulent regime. For example, in continuous casting of a slab with a width of 1.27 m , thickness of 0.25 m and casting speed of 0.02 m/s , the Reynolds number in the nozzle zone with $0.06\text{ m} \times 0.06\text{ m}$ cross-section becomes greater than 100000. Therefore, one of the complexities involved in the simulation of a CC process is that the effect of turbulence on the transport processes must be taken into account. The other complexity involved is the modeling of mushy region solidification in the presence of turbulent recirculating bulk motion of the melt.

2.2.1 Assumptions in Modeling

The following assumptions were made in the formulation of the mathematical model:

1. With respect to the fixed laboratory frame of reference, the casting process is at steady state and can be represented by the steady, three-dimensional turbulent Navier-Stokes and energy transport equations.
2. Molten steel behaves as an incompressible Newtonian fluid.
3. The top surface of the melt is flat and is maintained at a fixed level. The top surface is also covered with a protective slag layer which keeps the surface thermally insulated from the surroundings.
4. The caster is perfectly vertical with respect to the gravitational field and the curvature of the strand is ignored.
5. The effects of mold taper and mold oscillations are not considered.
6. Equilibrium solidification prevails within the caster and there is negligible segregation of solutes.
7. Thermophysical properties of steel are invariant and the density and thermal conductivity of the solid phase are equal to those of the liquid phase.

8. Heat release due to solid-solid transformation (viz., $\delta \rightarrow \gamma$ etc.) is not taken into consideration. Only the evolution of latent heat due to solid-liquid phase change is taken into account.
9. In the mold region equi-axed solidification occurs, while below the mold columnar-dendritic solidification takes place.

2.2.2 Modeling of the Various Aspects Involved

2.2.2.1 Turbulent Modeling

In modeling turbulent flows, the Navier-Stokes equations are assumed to be valid when instantaneous velocities are used rather than the time-averaged velocities. Since mathematics can not handle such instantaneous quantities, they are split into a time average value and a fluctuating term. Using index notation, the time-averaged form of the turbulent transport equations for a *single phase* can be written as:

-Continuity:

$$\frac{\partial(\rho \bar{u}_i)}{\partial x_i} = 0 \quad (2.1)$$

-Momentum equation:

$$\frac{\partial(\rho \bar{u}_i \bar{u}_j)}{\partial x_j} = -\frac{\partial \bar{P}}{\partial x_i} + \frac{\partial}{\partial x_j} \left[\mu \left(\frac{\partial \bar{u}_i}{\partial x_j} + \frac{\partial \bar{u}_j}{\partial x_i} \right) - \overline{\rho u_i' u_j'} \right] \quad (2.2)$$

-Energy equation:

$$\frac{\partial(\rho \bar{u}_j \bar{H})}{\partial x_j} = \frac{\partial}{\partial x_j} \left(K \frac{\partial \bar{T}}{\partial x_j} - \overline{\rho u_j' H'} \right) \quad (2.3)$$

The averaged equations contain the Reynolds stress terms $\overline{\rho u_i' u_j'}$ and the turbulent heat flux $\overline{\rho u_j' H'}$; their determination requires the introduction of a turbulence model.

Most of the general models are based upon the eddy-viscosity approach which were first introduced by Boussinesq at the end of the last century. Accordingly, the Reynolds stress can be rewritten as the function of the turbulent viscosity as:

$$\overline{\rho u_i u_j} = -\mu_t \left(\frac{\partial \bar{u}_i}{\partial x_j} + \frac{\partial \bar{u}_j}{\partial x_i} \right) + \frac{2}{3} \delta_{ij} k \quad (2.4)$$

where μ_t is turbulent viscosity analogous of the molecular viscosity, μ , and $k = \frac{1}{2} \overline{u_i u_i}$ is the turbulent kinetic energy per unit mass and the Kroneiker delta δ_{ij} assumes the following form:

$$\delta_{ij} = \begin{cases} 0 & \text{when } i \neq j \\ 1 & \text{when } i = j \end{cases} \quad (2.5)$$

Similarly, an eddy diffusivity concept is used to relate the turbulent heat flux to the local mean temperature gradient as:

$$\frac{1}{c_p} \overline{\rho u_j H} = -\frac{\mu_t}{\sigma_t} \frac{\partial \bar{T}}{\partial x_j} \quad (2.6)$$

where, σ_t is the turbulent Prandtl number.

Boussinesq's hypothesis does not provide a complete model for turbulence by itself, because there remains the determination of μ_t . Different turbulence models have been presented based on the additional PDE's required for the definition of μ_t . These models can be classified as zero equation models, one equation models, and two equation models.

Two-Equation High-Re $k - \epsilon$ Model

One of the most popular turbulent models is the two-equation $k - \epsilon$ model. The first form of this model was proposed by Harlow and Nakayama (1968). They suggested that:

$$\mu_t = \rho c_\mu \frac{k^2}{\epsilon} \quad (2.7)$$

where ε is the rate of dissipation of turbulent kinetic energy and c_μ is a function of the turbulent Reynolds number which is a constant value for high Reynolds number flows. A detailed derivation of the turbulent dissipation rate and turbulent kinetic energy equations is available in the literature (Warsi 1993). The steady state equations for k and ε in high Reynolds number $k - \varepsilon$ model are as follows:

$$\frac{\partial(\rho\bar{u}_j k)}{\partial x_j} = \frac{\partial}{\partial x_j} \left[\left(\mu_t + \frac{\mu_t}{\sigma_k} \right) \frac{\partial k}{\partial x_j} \right] + \mu_t \left(\frac{\partial \bar{u}_i}{\partial x_j} + \frac{\partial \bar{u}_j}{\partial x_i} \right) \frac{\partial \bar{u}_i}{\partial x_j} - \rho \varepsilon \quad (2.8)$$

$$\frac{\partial(\rho\bar{u}_j \varepsilon)}{\partial x_j} = \frac{\partial}{\partial x_j} \left[\left(\mu_t + \frac{\mu_t}{\sigma_\varepsilon} \right) \frac{\partial \varepsilon}{\partial x_j} \right] - c_1 \mu_t \frac{\varepsilon}{k} \left(\frac{\partial \bar{u}_i}{\partial x_j} + \frac{\partial \bar{u}_j}{\partial x_i} \right) \frac{\partial \bar{u}_i}{\partial x_j} - c_2 \rho \frac{\varepsilon^2}{k} \quad (2.9)$$

This model is especially applicable in the region having high turbulent Reynolds number ($Re_t = \frac{\rho k^2}{\mu \varepsilon}$), and can not be applied for the region very close to the wall which possesses low value of turbulent Reynolds number.

Two-Equation Low-Re $k - \varepsilon$ Model

To extend the standard high-Re $k - \varepsilon$ turbulent model to laminar sublayer close to a solid wall, a low-Re version of this model was initially proposed by Jones and Launder (1972, 1973). In the low-Re $k - \varepsilon$ turbulent model, some additional terms were included in the k and ε equations to account for the effects of viscous diffusion of k and ε and anisotropy due to the wall. This method has been successfully used to predict the laminarization of wall boundary layer flows. In addition to Jones and Launder model, other investigators proposed several different models. In the present study, the low-Re $k - \varepsilon$ turbulent model developed by Launder and Sharma (1974), which was seen to yield better results compared to the different types of low-Re $k - \varepsilon$ models examined by Patel et al. (1985), was employed.

A brief formulation of this model for turbulent kinetic energy and rate of energy dissipation is presented below:

$$\frac{\partial(\rho\bar{u}_j k)}{\partial x_j} = \frac{\partial}{\partial x_j} \left[\left(\mu_l + \frac{\mu_t}{\sigma_k} \right) \frac{\partial k}{\partial x_j} \right] + \mu_t \left(\frac{\partial \bar{u}_i}{\partial x_j} + \frac{\partial \bar{u}_j}{\partial x_i} \right) \frac{\partial \bar{u}_i}{\partial x_j} - \rho(\varepsilon + D_k) \quad (2.10)$$

$$\frac{\partial(\rho\bar{u}_j \varepsilon)}{\partial x_j} = \frac{\partial}{\partial x_j} \left[\left(\mu_l + \frac{\mu_t}{\sigma_\varepsilon} \right) \frac{\partial \varepsilon}{\partial x_j} \right] - c_1 f_1 \mu_t \frac{\varepsilon}{k} \left(\frac{\partial \bar{u}_i}{\partial x_j} + \frac{\partial \bar{u}_j}{\partial x_i} \right) \frac{\partial \bar{u}_i}{\partial x_j} - c_2 f_2 \rho \frac{\varepsilon^2}{k} + E_\varepsilon \quad (2.11)$$

where

$$\mu_t = \rho f_\mu c_\mu \frac{k^2}{\varepsilon} \quad (2.12)$$

The values for E_ε , D_k , f_μ , c_1 , c_2 , c_μ , f_1 , f_2 , σ_k and σ_ε for the Launder-Sharma model are listed in Table 2.1. For more information about the other version of the low-Re $k - \varepsilon$ turbulent models, the readers are referred to Seyedein et al. (1994).

2.2.2.2 Solidification Modeling

The solidification of alloys mostly occurs over a temperature range. Therefore, for a binary-alloy solidification in a continuous casting machine, three distinct regions can be distinguished namely, liquid, solid and mushy regions. In the mushy zone, solid and liquid phases coexist and latent heat of fusion is released during the solidification process. Basically, there are two main approaches for modeling the solidification of pure metal and alloys. They are multiple and single domain methods. In the present study, the solidification was modeled based on the single domain approach which does not require to track the unknown interface. An important feature of the single region formulation is to incorporate the effect of the latent heat release at the solid/liquid interface or mushy region in the energy equation. Among the various fixed domain techniques for taking into account the release of latent heat are: apparent or effective heat capacity methods, and enthalpy based method. The latter approach was adopted in the present work. In this technique, the total enthalpy is decomposed into the sensible and nodal latent heat in the energy equation:

$$H = h + \Delta H \quad (2.13)$$

Table 2.1. Coefficients and empirical constants of low-Re $k-\varepsilon$ turbulent model developed by Launder and Sharma.

parameter	value	parameter	value
E_ε	$\frac{2\mu\mu_t}{\rho} \frac{\partial^2 \bar{U}_i}{\partial x_j \partial x_k} \frac{\partial^2 \bar{U}_i}{\partial x_j \partial x_k}$	c_μ	0.09
D_k	$2\mu \frac{\partial \sqrt{k}}{\partial x_i} \frac{\partial \sqrt{k}}{\partial x_i}$	c_1	1.44
f_μ	$e^{\frac{-3.4}{(1+Re_t/50)^2}}$	c_2	1.92
f_2	$1 - 0.3e^{-Re_t^2}$	σ_k	1.0
f_1	1.0	σ_ε	1.3

where:

$$\int_{h_{ref}}^h dh = \int_{T_{ref}}^T c_p dT \quad (2.14)$$

and for constant c_p , and taking $h_{ref} = 0$ at T_{ref} the sensible heat is $h = c_p(T - T_{ref})$. In order to establish the region of phase change, the latent heat contribution is specified as a function of temperature i.e., $\Delta H = f(T)$.

Since the energy equation is valid for the solid, liquid and mushy regions, the nodal latent heat can be related to the liquid fraction. It becomes zero in the solid phase and equals the latent heat of fusion (ΔH_f) in the liquid phase. In the mushy region, latent heat is assumed to be a linear function (or can be any other function) of liquid fraction as:

$$\Delta H = \Delta H_f f_l \quad (2.15)$$

where f_l is the liquid fraction, which is a function of temperature. The simplest function (linear function) is formulated as follows:

$$f_i = \begin{cases} 1 & \text{when } T \geq T_l, \\ \frac{T - T_s}{T_l - T_s} & \text{when } T_l \geq T \geq T_s, \\ 0 & \text{when } T \leq T_s. \end{cases} \quad (2.16)$$

where T_l is the liquidus temperature, and T_s is the solidus temperature.

The final form of the energy equation is obtained by substituting Eqs. 2.6 and 2.13 into the energy equation (Eq. 2.3):

$$\frac{\partial(\rho\bar{u}_j\bar{h})}{\partial x_j} = \frac{\partial}{\partial x_j} \left[\left(\frac{\mu}{Pr} + \frac{\mu_s}{\sigma_s} \right) \frac{\partial \bar{h}}{\partial x_j} \right] - \frac{\partial(\rho\bar{u}_j\overline{\Delta H})}{\partial x_j} \quad (2.17)$$

The last term in Eq. 2.16 represents the latent heat exchange due to solid-liquid phase change resulting from the turbulent convective flow.

A clarification is needed in the usage of this source term in the present model. One should realize that the present model is based on the assumption that the solid fraction and liquid fraction in the mushy region are moving at the same speed. This assumption can be substantiated by the fact that in a real continuous slab caster, in the upper part, a narrow mushy region seems to develop. This is due to the highly turbulent state of the molten metal from the inlet nozzle flow. In this narrow mushy region, one can assume an equiaxed solidification process to prevail, where an equal velocity in the liquid and solid regions exists. In the lower part of a continuous slab caster, the columnar solidification in the mushy region seems to occur. Due to the decrease in the momentum of the melt, the liquid and solid velocities in the mushy region approach to that of the casting speed. Thus, in the lower part of the caster, one can safely assume that the solid and liquid velocities in the mushy region are equal to the casting speed. On the basis of the above argument, the

general form of the source term $\left(\frac{\partial(\rho\bar{u}_j\overline{\Delta H})}{\partial x_j} \right)$ remains the same and can be said to be

valid for both upper and lower parts of the caster.

2.2.2.3 Modeling of Fluid Flow in the Mushy Region

There are presently two approaches for modeling of fluid flow in a mushy region, i.e., variable viscosity and Darcy source methods. Since the first approach suffers from the lack of information about viscosity in a mushy region, in the present study, the second method was adopted to model fluid flow in the mushy region. In this approach, it is assumed that the flow in the mushy region is governed by Darcy laws for a porous media, i.e.

$$\bar{u}_i = -\frac{K'}{\mu} \left(\frac{\partial P}{\partial x_i} - \rho g_{x_i} \right) \quad (2.18)$$

where, K' is the permeability, which is a function of porosity, or in the case of a mushy region of a binary alloy, a function of liquid fraction. In this method the permeability is defined in such a manner that when liquid fraction decreases, permeability decreases, and forces all the velocities to zero in the case of a stationary solid. Incorporating the diffusive and convective momentum flux terms, one can write the modified Darcy equation in the following form:

$$\frac{\partial(\rho \bar{u}_i \bar{u}_j)}{\partial x_j} = \frac{\partial}{\partial x_j} \left[(\mu_l + \mu_s) \frac{\partial \bar{u}_i}{\partial x_j} \right] - S_{D_i} - \frac{\mu}{K'} (\bar{u}_i - u_i) \quad (2.19)$$

In the above equation, the coefficient μ/K' decreases from a large value in the solid phase to zero in the liquid phase and consequently the Darcy source term vanishes as the liquid fraction becomes one. In order to find a suitable function for the permeability of the mushy zone, one should really consider the physics of the solidification process. A well-known expression for obtaining the permeability as a function of liquid fraction for the mushy region can be deduced from the Carman-Koseny equation as follows:

$$\frac{\mu}{K'} = \frac{C(1-f_l)^2}{f_l^3 + q} \quad (2.20)$$

The value of C in the above equation depends upon the morphology of the porous media and q is a small positive number introduced to avoid division by zero. In the present work, the value of C has been estimated from the expression given by Minakawa

et al. (1987) as $C = 180/d^2$, where d is assumed to be constant and equal to the secondary dendritic arm spacing. The value of d is of the order of 1×10^{-4} m. A large value of C forces the velocity in the solid region ($f_i = 0$) to be equal to the casting speed, u_i .

2.2.3 Boundary Conditions

The schematic of a slab caster representing the computational domain adopted in this work is shown in Fig. 2.1. Using two-fold symmetry, the transport equations have been solved for a quadrant of the system as shown in this figure. The grid layout used in computations is also shown in this figure. The following boundary conditions were applied in this simulation:

Inlet boundary condition

All variables were assumed to have a constant value at the inlet of the nozzle.

$$u = u_{in}, \quad v = w = 0, \quad h = h_{in}, \quad k = 0.01 \times u_{in}^2, \quad \epsilon = c_{\mu} k_{in}^{3/2} / 0.05D \quad (2.21)$$

It is noted that the value of k and ϵ were selected from semi-empirical equations presented by Lai et al. (1986).

Free surface

The normal gradient of all variables were set to zero except the velocity perpendicular to the surface which itself was assumed to be zero.

$$\frac{\partial v}{\partial x} = \frac{\partial w}{\partial x} = \frac{\partial k}{\partial x} = \frac{\partial \epsilon}{\partial x} = \frac{\partial h}{\partial x} = 0 \quad u = 0 \quad (2.22)$$

Symmetry plane

The same boundary conditions as those of free surface, were used here.

$$\text{at x-y symmetry plane: } \frac{\partial u}{\partial z} = \frac{\partial v}{\partial z} = \frac{\partial k}{\partial z} = \frac{\partial \varepsilon}{\partial z} = \frac{\partial h}{\partial z} = 0 \quad w = 0 \quad (2.23)$$

$$\text{at x-z symmetry plane: } \frac{\partial u}{\partial y} = \frac{\partial w}{\partial y} = \frac{\partial k}{\partial y} = \frac{\partial \varepsilon}{\partial y} = \frac{\partial h}{\partial y} = 0 \quad v = 0 \quad (2.24)$$

Outlet

Fully developed conditions were adopted at the outlet, i.e., axial gradients of all dependent variables were assumed to be zero.

$$\frac{\partial u}{\partial x} = \frac{\partial v}{\partial x} = \frac{\partial w}{\partial x} = \frac{\partial k}{\partial x} = \frac{\partial \varepsilon}{\partial x} = \frac{\partial h}{\partial x} = 0 \quad (2.25)$$

Moving walls

The solidified shell at the moving walls were withdrawn with casting speed. Therefore, the following boundary conditions were employed at these faces:

$$u = u_{cs}, \quad v = w = k = \varepsilon = 0, \quad \frac{\partial h}{\partial y} = \frac{\partial h}{\partial z} = -\frac{\gamma}{K}(h_s - h_a), \quad (2.26)$$

where γ is the average heat transfer coefficient between the solid surface and the surrounding. In this study, an averaged heat transfer coefficient was used for the mold region and a different averaged heat transfer coefficient was employed in the submold region. The values of the average heat transfer coefficients were taken from the work of Lally et al. (1990). It is to be noted that in Eq. (2.26) h_s represents the enthalpy at the surface and h_a represents the product of ambient temperature and the specific heat of steel.

2.2.4 Non-Dimensionalization of the Formulation

In order to profit the advantage of generality, the partial differential equations described above were non-dimensionalized using the following dimensionless parameters:

$$\begin{aligned}
X &= \frac{x}{D}, & Y &= \frac{y}{D}, & Z &= \frac{z}{D}, \\
U &= \frac{u}{u_{in}}, & V &= \frac{v}{u_{in}}, & W &= \frac{w}{u_{in}}, \\
P^* &= \frac{P}{\rho_0 u_{in}^2}, & k^* &= \frac{k}{u_{in}^2}, & \varepsilon^* &= \frac{\varepsilon D}{u_{in}^3}, \\
h^* &= \frac{h}{\Delta H_f}, & \Delta H^* &= \frac{\Delta H}{\Delta H_f}, & \mu_i^* &= \frac{\mu_i}{\mu},
\end{aligned} \tag{2.27}$$

where, D is hydraulic diameter of the nozzle, u_{in} is the nozzle's inlet velocity and ΔH_f is the latent heat of fusion. It is noted that in the above equations as well as all subsequent equations all overbars for time-averaged quantities have been dropped for simplicity.

Combination of the turbulent and solidification modeling with the Navier-Stokes equations and applying dimensionless parameters (Eq. 2.27) yield to the general form of the governing equation as follows:

$$\frac{\partial(U_i \Phi^*)}{\partial X_i} = \frac{\partial}{\partial X_i} (\Gamma_\Phi^* \frac{\partial \Phi^*}{\partial X_i}) + S_\Phi^* \quad i = 1, 2, 3 \tag{2.28}$$

The value of Φ^* and associated value of Γ_Φ^* are given in Table 2.2.

Similarly, using dimensionless parameters the non-dimensional form of the boundary conditions becomes:

Inlet boundary condition:

$$U = 1, \quad V = W = 0, \quad h^* = h_{in}^*, \quad k^* = 0.01, \quad \varepsilon^* = c_\mu (0.01)^{3/2} / 0.05 \tag{2.29}$$

Free surface

$$\frac{\partial \mathcal{V}}{\partial X} = \frac{\partial W}{\partial X} = \frac{\partial k^*}{\partial X} = \frac{\partial \varepsilon^*}{\partial X} = \frac{\partial h^*}{\partial X} = 0 \quad U = 0 \tag{2.30}$$

Table 2.2. Summary of the non-dimensional governing equations for Launder and Sharma version of the low-Re $k - \epsilon$ turbulent model.

Equation	Φ^*	Γ_ϕ^*	S_ϕ^*
Continuity	1	0	0
U-momentum	U	$\frac{1}{Re}(1+\mu_t^*)$	$-\frac{\partial P^*}{\partial X} + \frac{\partial}{\partial X_i} \left(\Gamma_\phi^* \frac{\partial U_i}{\partial X} \right) - \frac{A^*}{Re}(U - U_s)$
V-momentum	V	$\frac{1}{Re}(1+\mu_t^*)$	$-\frac{\partial P^*}{\partial Y} + \frac{\partial}{\partial X_i} \left(\Gamma_\phi^* \frac{\partial U_i}{\partial Y} \right) - \frac{A^*}{Re}(V - V_s)$
W-momentum	W	$\frac{1}{Re}(1+\mu_t^*)$	$-\frac{\partial P^*}{\partial Z} + \frac{\partial}{\partial X_i} \left(\Gamma_\phi^* \frac{\partial U_i}{\partial Z} \right) - \frac{A^*}{Re}(W - W_s)$
Kinetic energy	k^*	$\frac{1}{Re} \left(1 + \frac{\mu_t^*}{\sigma_k} \right)$	$\frac{G^*}{Re} - \epsilon^* + \frac{D_k^*}{Re}$
Rate of energy dissipation	ϵ^*	$\frac{1}{Re} \left(1 + \frac{\mu_t^*}{\sigma_\epsilon} \right)$	$\frac{1}{Re} f_1 C_1 G^* \frac{\epsilon^*}{k^*} - C_2 f_2 \frac{\epsilon^{*2}}{k^*} + \frac{E_\epsilon^*}{Re^2}$
Energy	h^*	$\frac{1}{Re} \left(\frac{1}{Pr} + \frac{\mu_t^*}{\sigma_t} \right)$	$-\left(\frac{\partial U \Delta H^*}{\partial X} + \frac{\partial V \Delta H^*}{\partial Y} + \frac{\partial W \Delta H^*}{\partial Z} \right)$

where:

$$Re = \frac{\rho u_{in} D}{\mu}$$

$$G^* = \mu_t^* \left(\frac{\partial U_i}{\partial X_j} + \frac{\partial U_j}{\partial X_i} \right) \frac{\partial U_i}{\partial X_j}, \quad D_k^* = 2 \frac{\partial \sqrt{k^*}}{\partial X_i} \frac{\partial \sqrt{k^*}}{\partial X_i}$$

$$E_\epsilon^* = 2 \mu_t^* \left(\frac{\partial^2 U_i}{\partial X_j \partial X_k} \right) \left(\frac{\partial^2 U_i}{\partial X_j \partial X_k} \right), \quad f_\mu^* = e^{\frac{-3.4}{(1+Re_t^*/50)^2}}, \quad Re_t = Re \frac{k^{*2}}{\epsilon^*}$$

$$\mu_t^* = Re C_\mu f_\mu^* \frac{k^{*2}}{\epsilon^*}, \quad f_1 = 1, \quad f_2 = 1 - 0.3 e^{-Re_t^2}, \quad A^* = \frac{C^*(1-f_1)^2}{f_1^3 + q}$$

$$C_\mu = 0.09, \quad C_1 = 1.44, \quad C_2 = 1.92, \quad \sigma_k = 1.0, \quad \sigma_\epsilon = 1.3, \quad \sigma_t = 0.9$$

Symmetry plane

$$\text{at x-y symmetry plane: } \frac{\partial U}{\partial Z} = \frac{\partial V}{\partial Z} = \frac{\partial k^*}{\partial Z} = \frac{\partial \varepsilon^*}{\partial Z} = \frac{\partial h^*}{\partial Z} = 0 \quad W = 0 \quad (2.31)$$

$$\text{at x-z symmetry plane: } \frac{\partial U}{\partial Y} = \frac{\partial W}{\partial Y} = \frac{\partial k^*}{\partial Y} = \frac{\partial \varepsilon^*}{\partial Y} = \frac{\partial h^*}{\partial Y} = 0 \quad V = 0 \quad (2.32)$$

Outlet

$$\frac{\partial U}{\partial X} = \frac{\partial V}{\partial X} = \frac{\partial W}{\partial X} = \frac{\partial k^*}{\partial X} = \frac{\partial \varepsilon^*}{\partial X} = \frac{\partial h^*}{\partial X} = 0 \quad (2.33)$$

Moving walls

$$U = U_s = u_s/u_{in}, \quad V = W = k^* = \varepsilon^* = 0, \quad \frac{\partial h^*}{\partial Y} = \frac{\partial h^*}{\partial Z} = -\frac{\gamma D}{K}(h_s^* - h_a^*), \quad (2.34)$$

For the sake of simplicity in the subsequent sections superscripts (*) sign from all variables are eliminated, while the variables remain non-dimensional.

2.5 Numerical Solution

The governing equations (Eq. 2.28) associated with the boundary conditions (Eqs. 2.29-2.34) were solved numerically using a control-volume based finite difference method. In this method the whole domain under study is described by a staggered grid system as shown in Fig. 2.2. The scalar quantities (P , k , ε and h) are located at the middle of the scalar control volume shown by the dash line, while the velocity components (u , v and w) are located at the faces of the scalar control volumes and their control volumes are presented by dotted lines. Such a displaced or staggered grid for the velocity components was first used by Harlow and Welch (1965) in their MAC method and has been used in other methods developed by Harlow and co-workers (1968) and Patankar and Spalding (1972). The important advantages of the staggered grid are twofold: firstly, the mass flow rates across the control volume faces can be calculated without any interpolation from adjacent velocities and secondly, the pressure difference between two adjacent grid points

becomes the natural driving forces for the velocity components located between these grid points.

The next step in this numerical solution is to provide the algebraic form of the differential equations at appropriately chosen grid points. This operation is termed “discretization”. Discretized equations are derived by integration of the partial differential equations over each control volume of the domain. A hybrid-scheme, which is a combination of a central difference scheme and a upwind scheme, was used to discretize convection terms. The numerical solution procedure was based on Patankar’s SIMPLE (1980) algorithm for resolving the velocity-pressure coupling in the momentum equations. The algebraic form of the general governing equation obtained from the discretization of Eq. (2.28) can be written as follows:

$$a_P \Phi_P = a_N \Phi_N + a_S \Phi_S + a_E \Phi_E + a_W \Phi_W + a_T \Phi_T + a_B \Phi_B + b_\Phi \quad (2.35)$$

The above discretized equation relates the global value of Φ at the node P to its immediate six neighboring nodes $E, W, N, S, T,$ and B with local production terms. The coefficients $a_E, a_W, a_N, a_S, a_T,$ and a_B are called linking coefficients, which connect each neighbor with the nodal value Φ_P .

The discretized equations were solved iteratively using an implicit relaxation technique and employing the well-known line-by-line TDMA solver until a converged solution was obtained. The iteration loop was terminated when the sum of the residuals for each calculated variable were less than 0.01. The residuals for each variable was defined as follows:

$$R_\Phi = \sum_{\text{all nodes}} \left| a_P \Phi_P - \sum_{nb} a_{nb} \Phi_{nb} - b \right| \quad (2.36)$$

The sequence of operations followed in the present numerical code is given in the form of a flow chart in Fig. 2.3. In order to accelerate the convergence, the governing equations were first solved without invoking solidification by assuming that the temperature at the moving wall is equal to the liquidus temperature. The results obtained from these runs were later used as guessed values for the coupled fluid flow, heat transfer

and solidification runs. In this method, converged solutions of the coupled set of equations were obtained using the underrelaxation factor for energy, turbulent kinetic energy and energy dissipation rate of 0.2 or smaller, while for the other variables underrelaxation factor was as high as 0.5.

Calculations were carried out for a grid size of $30 \times 22 \times 12$ wherein a non-uniform grid was manually distributed with the finer mesh distributions in the vicinity of the solid walls. To verify the algorithm, numerical tests were performed to ensure that the solutions were grid-independent. An increase in the number of the grids from $30 \times 22 \times 12$ to $30 \times 28 \times 19$ resulted in a maximum difference of 6% in the solidified shell thickness at the mold exit. This difference in shell thickness was less than 6% further downstream.

2.6 Results and Discussion

The casting speed and thermophysical properties of stainless steel 304 used in this simulation are given in Table 2.3. All results discussed below are for a 0.34 *m* submergence depth (which is defined as the vertical distance from the meniscus to the center of the outlet ports of the nozzle) of the nozzle unless otherwise stated.

In order to ascertain the effects of the casting speed on the flow patterns and solidification profiles, simulation runs were carried out for two casting speeds viz., 0.02 and 0.015 m/s. Figures 2.4 and 2.5 show the predicted velocity fields, solidus and liquidus isotherms, and temperature contours in three separate plots for the centrally symmetric vertical plane parallel to the wide face of the caster for the aforementioned two casting speeds, respectively. As seen from the velocity fields displayed in these figures, the molten steel, supplied through the submerged entry nozzle, impinges onto the narrow face of the mold. After impingement, the flow is divided into two oppositely directed streams, each of which moves parallel to the narrow face and later forms a large recirculation zone. The upper recirculation flow is confined by the meniscus surface and the wide face of the slab. The lower recirculation flow travels both downstream and towards the wide face of the

slab and a portion of it returns towards the submerged entry nozzle. The flow field in the caster thus can be characterized by the location of the centers of the upper and lower

Table 2.3. Thermophysical properties of steel, geometrical parameters and heat transfer coefficients used for the simulation.

Variable	Case (A)	Case (B)
thermal conductivity (liquid or solid)	$31 \text{ Wm}^{-1} \text{ K}^{-1}$	26
specific heat (liquid or solid)	$700 \text{ Jkg}^{-1} \text{ K}^{-1}$	720
latent heat of fusion	264 kJkg^{-1}	272
liquidus temperature	1454° C	1531
solidus temperature	1400° C	1518
inlet temperature	$1470 - 1490^\circ \text{ C}$	1558
casting speed	$0.01 - 0.02 \text{ ms}^{-1}$	0.0267
viscosity	$0.007 \text{ kgm}^{-1} \text{ s}^{-1}$	0.0055
density	7000 kgm^{-3}	6980
slab width	1.27 m	1.05
mold length	0.75 m	0.6
slab thickness	0.254 m	0.22
nozzle port width	0.058 m	0.056
nozzle port height	0.1 m	0.045
caster length simulated	3.0 m	3.0
nozzle submergence length	$0.34 - 0.23 \text{ m}$	0.1
heat transfer coefficient in the mold region	$1500 \text{ Wm}^{-2} \text{ K}^{-1}$	see Nakato et al. (1984)
heat transfer coefficient in the submold region	$750 \text{ Wm}^{-2} \text{ K}^{-1}$	

recirculation zones and the impingement point. The two turbulent recirculation zones lead to the enhancement of the mass, momentum and energy transport in the upper region of the caster. A comparison of the flow fields for the two different casting speeds shows that an increase in the casting speed results in a minor change of the downward recirculation length. There is, however, a change in the magnitude and shape of the velocity in the axial plane (X-Y plane). For example, the axial velocity profile at around a non-dimensional distance of 20 from the top free surface shows that for the lower casting speed, the velocity profile takes a more uniform shape compared to that seen for the higher casting speed. This signifies that, for a higher casting speed, the effect of the impinging liquid steel on the narrow face of the slab is felt at a greater distance downstream. Moreover, a stronger upward recirculation zone is obtained in the case of a higher casting speed, which leads to an increase of turbulence at the free surface. Figure 2.6a shows the 3-D velocity vectors on the two centrally symmetric planes and the top free surface. An enlarged view of the flow pattern for the upper part of the caster is shown in Fig. 2.6b. From this figure it is seen that the reverse flow under the submerged nozzle is weak, which can be explained from the nullifying effect between the two oppositely directed flows; the downward flow comes from the free surface and the upward flow is supplied by the lower recirculation flow under the nozzle. The velocity fields in Figs. 2.4a and 2.5a also show that, for both cases, the axial velocity is quite uniform in the downstream region and the liquid steel moves vertically downward in the casting direction.

Liquidus (1454°C) and solidus (1400°C) isotherms in the wide symmetry plane for casting speeds of 0.02 and 0.015 m/s are shown in Figs. 2.4b and 2.5b, respectively. From these figures it is seen that a thinner solidifying shell is obtained within the mold for a higher casting speed. The reason for this is that, at a higher casting speed, the dwelling time of the solidifying shell in the mold decreases and the convective heat transfer between the liquid and solidifying shell increases.

In order to verify the modeling of solidification, an additional run, with parameters specified as Case (B) in Table 2.3, was carried out. The parameters for this case were

taken from the experimental work of Nakato et al. (1984). Figure 2.7 compares the solidified shell thickness predicted at the narrow face by the present model with the measured data of Nakato et al. (1984). It is to be noted that the predicted shell presented in this figure is curve-fitted to the data found from the simulation. It can be seen from this figure that for two-thirds of the mold the predicted shell thickness matches the experimental one quite closely. For the last one-third of the mold the shell thickness predicted by our model and the experimental data differs. This discrepancy is due to two factors. First, the experimental data was for a curved mold while our prediction is for a vertical mold. Secondly, although the solidified shell profile on the center of the narrow face along the casting direction was given in Nakato et al.'s (1984) study, neither the experimental heat transfer coefficient nor the experimental heat extraction rate were reported in that paper. In absence of this information we have used in our simulation the standard heat transfer coefficient for the mold region reported by various previous researchers in order to predict the experimental solidified shell profile. In addition to the above, if one considers the measurement uncertainty in Nakato et al.'s (1984) results, the predicted profile in this figure can be said to be in fairly good agreement with the measured solidifying shell.

The effect of the casting speed on the temperature distribution in the liquid region is given in Figs. 2.4c and 2.5c, respectively. In both cases molten steel with $26^{\circ}C$ superheat (difference between the inlet and liquidus temperatures) is introduced into the mold. For a casting speed equal to $0.015\ m/s$, liquid steel loses about $18^{\circ}C$ of its superheat upon impingement onto the narrow face of the slab, while for a casting speed of $0.02\ m/s$ the loss in superheat reduces to $15^{\circ}C$. The available superheat at the impingement area is sufficient enough to remelt the mushy phase, which is seen to develop from the top surface on the mold wall. This phenomenon will be described in greater detail in the relevant section which follows. These figures also show that large temperature gradients develop near the solid-liquid interface, while there exist low temperature gradients in the bulk of the melt due to well mixing from the turbulent convective flows. The variation of the temperature gradient in various parts of the caster is due to the effect

of turbulent flow on the heat transfer mechanism. In the region close to the wall, where the turbulence effect disappears, a high heat transfer rate is the manifestation of a high temperature gradient, while far from the liquid-solid interface, where turbulent thermal diffusivity is dominant, the temperature gradient decreases due to intense turbulent mixing. The highest temperature gradient is seen to form near the impingement area on the narrow face of the mold, which in turn illustrates the region of the highest superheat removal and the lowest solidification rate. From the isotherms in Figs. 2.4c and 2.5c it is seen that, at the bottom of the solution domain for $u_c = 0.015 \text{ m/s}$ the liquid phase almost vanishes, while for the higher casting speed ($u_c = 0.02 \text{ m/s}$) the liquid metal is very close to the liquidus temperature. This can be also attributed to the lower dwelling time of the steel for a higher casting speed.

In order to study quantitatively the level of turbulence in the slab caster process, the non-dimensional turbulent viscosity contours on the free surface and two vertically symmetric planes for a casting speed of 0.015 m/s and 26°C delivered superheat are shown in Fig. 2.8. In this particular case, the turbulent viscosity varies from zero to 1400 times the molecular viscosity. A zero value of the turbulent viscosity appears in the solidified shell as well as on the submerged nozzle walls, and it increases with the increase of the lateral distance from the solid shell into the bulk liquid phase. The highest value of the turbulent viscosity is observed under the nozzle, and decreases by expanding the closed loop contours towards solid walls. Due to the wide variations of turbulent viscosity within the caster and considering the fact that the turbulent viscosity is a flow property, it can be concluded that an *ad hoc* viscosity model, which uses an artificially enhanced melt viscosity, can not be an acceptable modeling approach for the simulation of turbulent flow of molten steel in a continuous-slab casting process.

Figure 2.9 shows the developments of the solidifying shell and mushy region along the wide and narrow faces of the slab caster for a casting speed of 0.02 m/s and 26°C inlet superheat at various transverse cross-sectional planes downstream from the top free surface. At non-dimensional axial distance, $X = 0.3$ (0.026 m from the top) a very thin layer of solidified shell is seen to develop on the mold walls. With the downward distance,

as more heat is extracted through the solidified shell, the thickness of the solid layer as well as the mushy zone progressively increases. The solid layer and the mushy zone each take almost a round shape around the corner of the mold, which is due to the higher heat extraction rate through the two sides of the mold walls, i.e. heat transfer from both of the transverse directions. The wavy shape of the mushy-liquid interface and remelting of a part of the mushy region, especially at the narrow face of the slab at around $X = 3.4$ is due to the impingement of the superheated liquid steel from the inlet nozzle on to the mold wall. The side streams from this inlet flow are responsible for shifting the mushy layer in the direction of the flow. The remelting of the mushy layer reduces the sensible heat of the liquid steel and thus promotes the dissipation of the melt's superheat. It can be seen from these figures that the thickness of the mushy layer at the wide face of the slab caster is maximum at the central symmetric plane. Relatively rapid rate of growth of the solid shell and mushy layer at the center of the wide face, compared to the corresponding growth rate at the wide face close to the narrow side, is due to the fact that the center region is fed essentially by the low superheated melt. This melt comes from the downflow stream of the impinging jet at the narrow face. As the downflow stream moves along the cooled narrow face it loses most of its superheat and moves up through the center of the strand towards the SEN. At further downstream, liquid steel progressively loses its superheat and the growth of the mushy layer on the narrow faces resumes. The decrease of the liquid superheat results in the reduction of the convective heat transfer at the solid-liquid interface, which in turn allows the mushy and solid layers to grow at a faster rate downstream of the strand.

Similar trends in the growth rate of the solidified shell and mushy region as seen in Fig. 2.10 are also observed for a casting speed of 0.015 m/s with an inlet superheat equal to 26° C . Figure 2.10 shows these results in a similar format as Fig 2.9. From this figure, it is observed that liquidus isotherm reaches to the wide symmetry plane ($Z = 0$) at around $X = 6$ below the top free surface and returns back further downstream due to remelting. This location coincides with the small dead zone seen under the nozzle, which is influenced by the recirculatory motion of the superheated liquid steel. Further downstream

from the free surface, since the liquid temperature is close to the liquidus temperature, the liquid phase region diminishes at a faster rate and vanishes at the exit. For this lower casting speed the solidification rate is also higher compared to the higher casting speed.

In order to study the effect of delivered superheat, Fig. 2.11 is plotted for the same set of parameters as Fig. 2.5 except for a superheat of $16^{\circ} C$. A comparison of the Figs. 2.5a and 2.11a shows that there is an insignificant effect on the velocity profile due to a change of superheat of $10^{\circ} C$. This change in superheat does not significantly affect the thickness of the solidifying shell, but it does change the extent of the mushy region, especially at the lower part of the caster.

In order to find the effects of the nozzle submergence depth on the flow, temperature and solidification profiles, the model was run for the same set of parameters as for Fig. 2.5 but with a submergence depth of $0.23\ m$ instead of $0.34\ m$. The results of this simulation are portrayed in Figs. 2.12 and 2.13. A comparison of Figs. 2.12a and 2.5a shows that with the decrease of the immersion depth of the nozzle, the upper counter-clockwise recirculating zone becomes a little stronger while the lower and bigger clockwise recirculating zone becomes weaker. A higher turbulence level at the free surface due to a lower nozzle immersion depth may result in an unwanted entrapment of mold flux within the melt and can significantly affect the quality of the cast. The decrease of the immersion depth results in a corresponding decrease of the impingement point of the jet on the narrow face. A comparison of the liquidus and solidus isotherms in Figs. 2.12b and 2.5b reveals that for a shallower nozzle, the liquid steel dissipates its superheat faster which may be attributed to the higher turbulence mixing in the case of a shallower immersion nozzle. The appearance of the mushy zone across the whole width in the upper part of the submold region is a testimony of the above fact. For a smaller nozzle submergence depth, the liquid steel loses its superheat earlier during its downward flow, a thicker solidified shell is seen to form in the lower part of the caster, which can be seen through a comparison of Figs. 2.10 and 2.13.

2.7 Concluding Remarks

In this study, a three-dimensional control volume based finite-difference model, along with the associated computer code, have been developed to obtain the numerical solution of the coupled turbulent flow, heat transfer and macroscopic solidification in the mold and submold regions of an industrial size continuous caster for steel slabs. A low Reynolds number $k - \epsilon$ model was used to account for the turbulence effects in the liquid metal and an enthalpy-porosity scheme was employed to model solidification of the mushy region. Numerical accuracy of the model was tested by comparing the predicted solid shell with the only known experimentally measured solidified shell thickness for a slab caster. A very good agreement was obtained between the theoretically predicted and experimentally measured solid shell thickness. By rationally varying the parameters, the model is then used to predict the effect of casting speed, delivered superheat and submergence depth of the nozzle on flow pattern, shell thickness and growth rate of the mushy region, and temperature and turbulent viscosity distributions in the liquid and mushy regions within the caster. The model predicts that most of the inlet superheat is removed in or just below the mold. The model also shows the growth, melting and regrowth of the mushy region at the center of the wide face at a level below the inlet jet impingement region on the narrow face within the mold. Results show a relatively rapid rate of growth of the solid shell and mushy region near the center of the wide face compared to the edges. Results also indicate that, except for the vicinity of the jet impingement region, the inlet superheat has minimal effect on the growth rate of the solid shell and mushy layer while the casting speed has the most important effect. Except for the central portion of the strand underneath the nozzle, a 50% increase in the casting speed from 0.01 m/s has shown no change in the turbulence level at the top part of the mold. The nozzle with a smaller submergence depth is seen to enhance the solidification rate, especially in the submold region of the caster. The present study clearly signifies the importance and need for a three-dimensional, conjugate turbulent flow, heat transfer and solidification modeling study for a continuous-slab casting process. Prior modeling studies related to continuous casting processes, which

have employed either *ad hoc* effective thermal conductivity or *ad hoc* effective viscosity approach or have uncoupled the process of solidification from heat transfer and fluid flow, cannot provide realistic results, particularly for a slab caster.

NOMENCLATURE

Symbol	Description
A	Darcy coefficient
α_p, α_{nb}, b	coefficients in the discretized governing equations
c_1, c_2, c_μ	empirical constants for low Reynolds turbulent models
c_p	specific heat
C	morphology constant
D	nozzle hydraulic diameter
D_k	extra dissipation term in k -equation
E_ε	extra generation term in ε -equation
f_1, f_2, f_μ	empirical constants for low Reynolds turbulent models
f_l	liquid fraction
G	turbulent kinetic energy generation in k -equation
h	sensible heat
H	total heat (sensible heat and latent heat)
k	turbulent kinetic energy
K'	permeability
P	Pressure
Pr	laminar Prandtl number
Re	Reynolds number
Re_t	turbulent Reynolds number based on the turbulent quantities
S	source term
S_Φ	source term associated with Φ
T	temperature
T'	fluctuation of temperature
T_{in}	inlet temperature

T_l	liquidus temperature
T_s	solidus temperature
u_i	velocity component in the i-th direction; corresponding to u , v and w
\bar{u}_i	time-average velocity component in i-th direction
u'_i	fluctuation of velocity in i-th direction
u_{in}	inlet velocity
u_s	casting speed

Greek Symbols

ΔH	nodal latent heat
ΔH_f	latent heat of fusion
ε	turbulent kinetic energy dissipation rate
γ	convective heat transfer coefficient
Γ_Φ	diffusion coefficient associated with Φ value
μ	laminar viscosity
μ_e	effective viscosity equal to $\mu + \mu_t$
μ_t	turbulent viscosity
Φ	generalized dependent variable
ρ	mass density
σ_l	laminar Prandtl number
σ_t	turbulent Prandtl number
$\sigma_k, \sigma_\varepsilon$	empirical constants in turbulent model equations

Superscripts

*	non-dimensional variables
—	time-averaged variables
'	fluctuation of variables

References

- Aboutalebi M. R., Hasan M. and Guthrie R. I. L., Numerical study of coupled turbulent flow and solidification for steel slab casters, *Numerical Heat Transfer Part A*, Vol. 28, pp. 279-297, (1995a).
- Aboutalebi M. R., Hasan M. and Guthrie R. I. L., Coupled turbulent flow, heat, and solute transport in continuous casting processes, *Metallurgical & Materials Trans.*, Vol. 26B, pp. 731-744, (1995b).
- Asai S. and Szekely J., Turbulent flow and its effects in continuous casting, *Ironmaking and Steelmaking*, Vol. 3, pp. 205-213, (1975).
- Asai S. and Szekely J., Turbulent flow and its effects in continuous casting, *Ironmaking and Steelmaking*, Vol. 3, pp. 205-213, (1975).
- Brimacombe J. K., Design of continuous casting machines based on a half-flow analysis: state-of-the-art review, *Canadian Metallurgical Quarterly*, Vol. 15, No. 2, pp. 163-175, (1976).
- Choudhary S. K. and Mazumdar D., Mathematical modeling of fluid flow, heat transfer and solidification phenomena in continuous casting of steel, *Steel Research*, Vol. 66, No. 5, pp. 199-205, (1995).
- Flint P. J., A three-dimensional finite difference model of heat transfer, fluid flow and solidification in the continuous slab caster, *Steelmaking Conference Proceedings*, pp. 481-490, (1990).
- Harlow F. H. and Nakayama P. I., Transport of turbulence energy decay rate, *Los Alamos Sci. Lab., Report LA-3854*, University of California, (1968).
- Harlow F. H. and Welch J. E., Numerical calculation of time-dependent viscous incompressible flow of fluid with free surface, *Phys. Fluids*, Vol. 8, pp. 2182-2189, (1965).
- Huang X., Thomas B. G. and Najjar F. M., Modelling superheat removal during Continuous casting of steel slabs, *Metall. Trans.*, Vol. 23B, pp. 339-356, (1992).

- Jones W. P. and Launder B. E., The prediction of laminarization with two-equation model of turbulence, *Int. J. Heat and Mass Transfer*, Vol. 15, pp. 301-313, (1972).
- Jones W. P. and Launder B. E., The calculation of low-Reynolds-number phenomena with a two-equation model of turbulence, *Int. J. Heat and Mass Transfer*, Vol. 16, pp. 1119-1130, (1973).
- Lai K. Y. M., Salcudean M., Tanaka S. and Guthrie R. I. L., Mathematical modelling of flows in large tundish systems in steelmaking, *Metall. Trans.*, Vol. 17B, pp. 449-459, (1986).
- Lait J. E., Brimacombe J. K. and Weinberg F., Mathematical modeling of heat flow in the continuous casting of steel, *Ironmaking and Steelmaking*, Vol. 1, No. 2, pp. 90-97, (1974).
- Lally B., Biegler L. and Henein H., Finite difference heat transfer modelling for continuous casting, *Metall. Trans.*, Vol. 21B, pp. 761-770, (1990).
- Launder B. E., and Sharma B. I., Application of the energy dissipation model of turbulence to the calculation of flow near a spinning disc, *Letters in Heat and Mass Transfer*, Vol. 1, pp. 131-138, (1974).
- Minakawa S., Samarasekera I. V. and Weinberg F., Centerline porosity in plate castings, *Metall. Trans.*, Vol. 16B, pp. 245-255, (1987).
- Mizikar E. A., Mathematical heat transfer model for solidification of continuously cast steel slabs, *Trans. TMS-AIME*, Vol. 239, pp. 1747-1753, (1967).
- Nakato H., Ozawa M., Kinoshita K., Habu Y. and Emi T., Factors affecting the formation of shell and longitudinal cracks in mould during high speed continuous casting of slabs, *Trans. Iron Steel Inst. Japan*, Vol. 24, No. 11, pp. 957-965, (1984).
- Patankar S. V., *Numerical Heat Transfer and Fluid Flow*, Hemisphere publishing co., Washington, D.C., (1980).
- Patankar S. V. and Spalding D. B., A calculation procedure for heat, mass and momentum transfer in three-dimensional parabolic flows, *Int. J. of Heat Mass Transfer*, Vol. 15, pp. 1787-1806, (1972).

- Patel V. C., Wolfgang R. and Scheuerer J., Turbulence models for near-wall and low-Reynolds-number flows: A review, *AIAA Journal*, Vol. 23, No. 9, pp. 1308-1319, (1985).
- Savage J. and Pritchard W. H., *Journal of Iron and Steel Institute*, Vol. 178, pp. 267-277, (1954).
- Seyedein S. H., Hasan M. and Mujumdar A. S. J., Modelling of a single confined turbulent slot jet impingement using various $k-\varepsilon$ turbulence models, *Applied Mathematical Modelling*, Vol. 18, No. 10, pp. 526-537, (1994).
- Sfier A. A. and Clumpner J. A., Continuous casting of cylindrical ingots, *Journal of Heat Transfer*, pp. 29-34, (1977).
- Thomas B. G., Mika L. J. and Najjar F. M., Simulation of fluid flow inside a continuous slab-casting machine, *Metall. Trans.*, Vol. 21B, pp. 387-400, (1990a).
- Thomas B. G., Najjar M. F. and Mika L. J., The removal of superheat from continuous casting moulds, *F. Weinberg Int. Symp. on Solidification Processing, 29th CIM Conference, Hamilton*, pp. 131-145, (1990b).
- Warsi Z. U. A., *Fluid Dynamics Theoretical and Computational Approaches*, CRC Press, Inc., Florida, (1993).

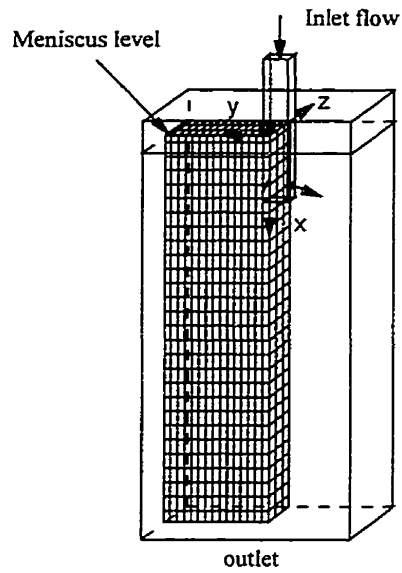
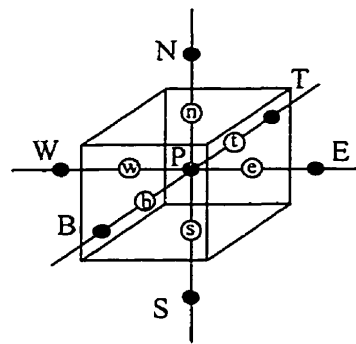
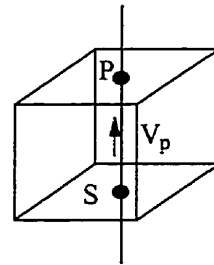


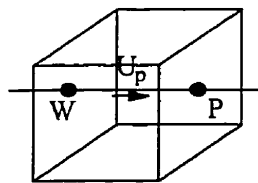
Fig. 2.1. A schematic view of the caster's domain modeled along with grid distributions and coordinate system used.



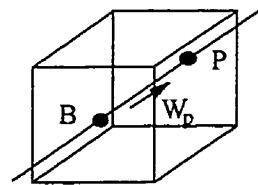
Scalar control volume



V-velocity control volume



U-velocity control volume



W-velocity control volume

Fig. 2.2. Three-dimensional arrangement of the staggered control volumes.

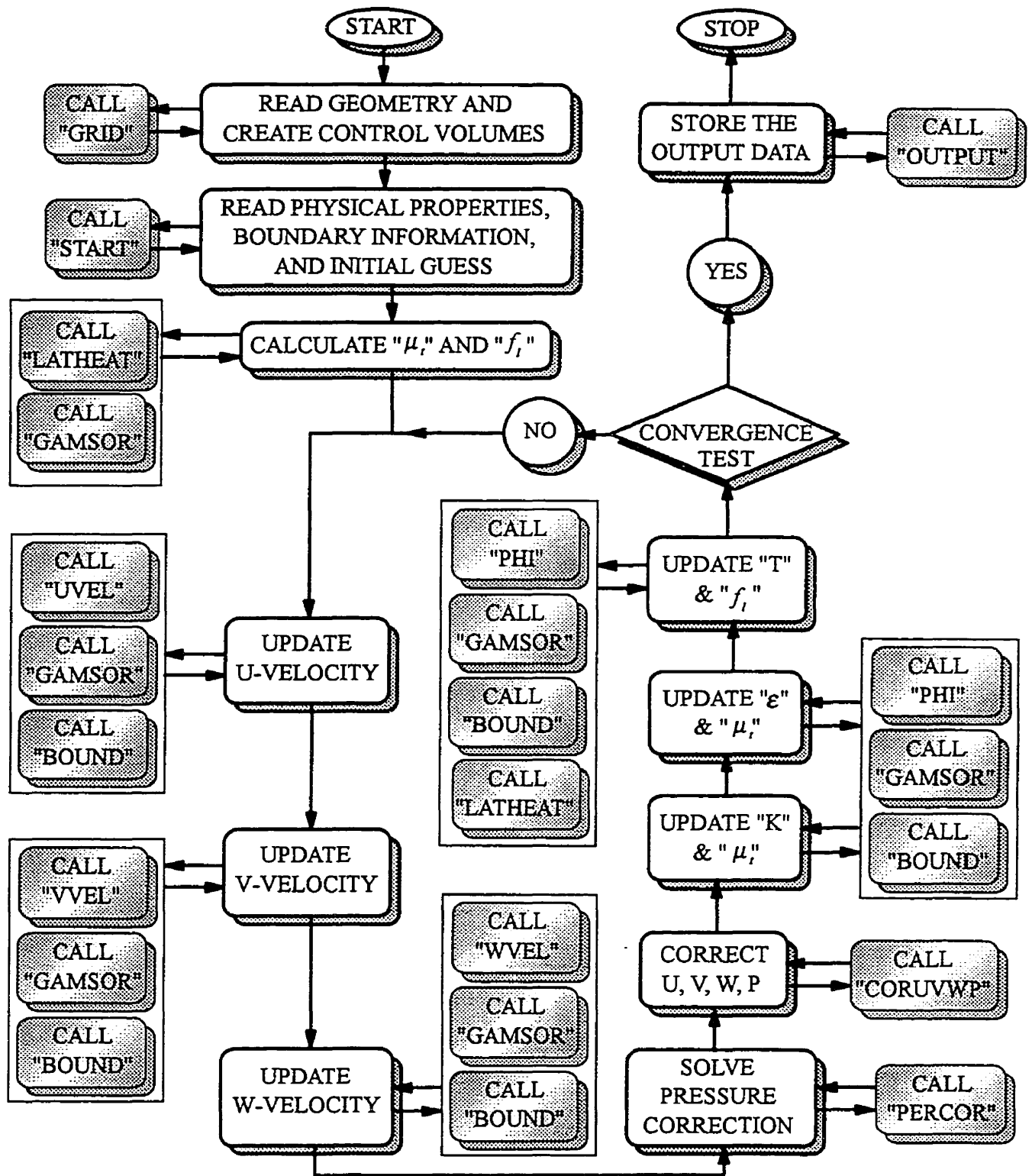


Fig. 2.3. Computational flow chart of the 3-D turbulent fluid flow, heat transfer and solidification code.

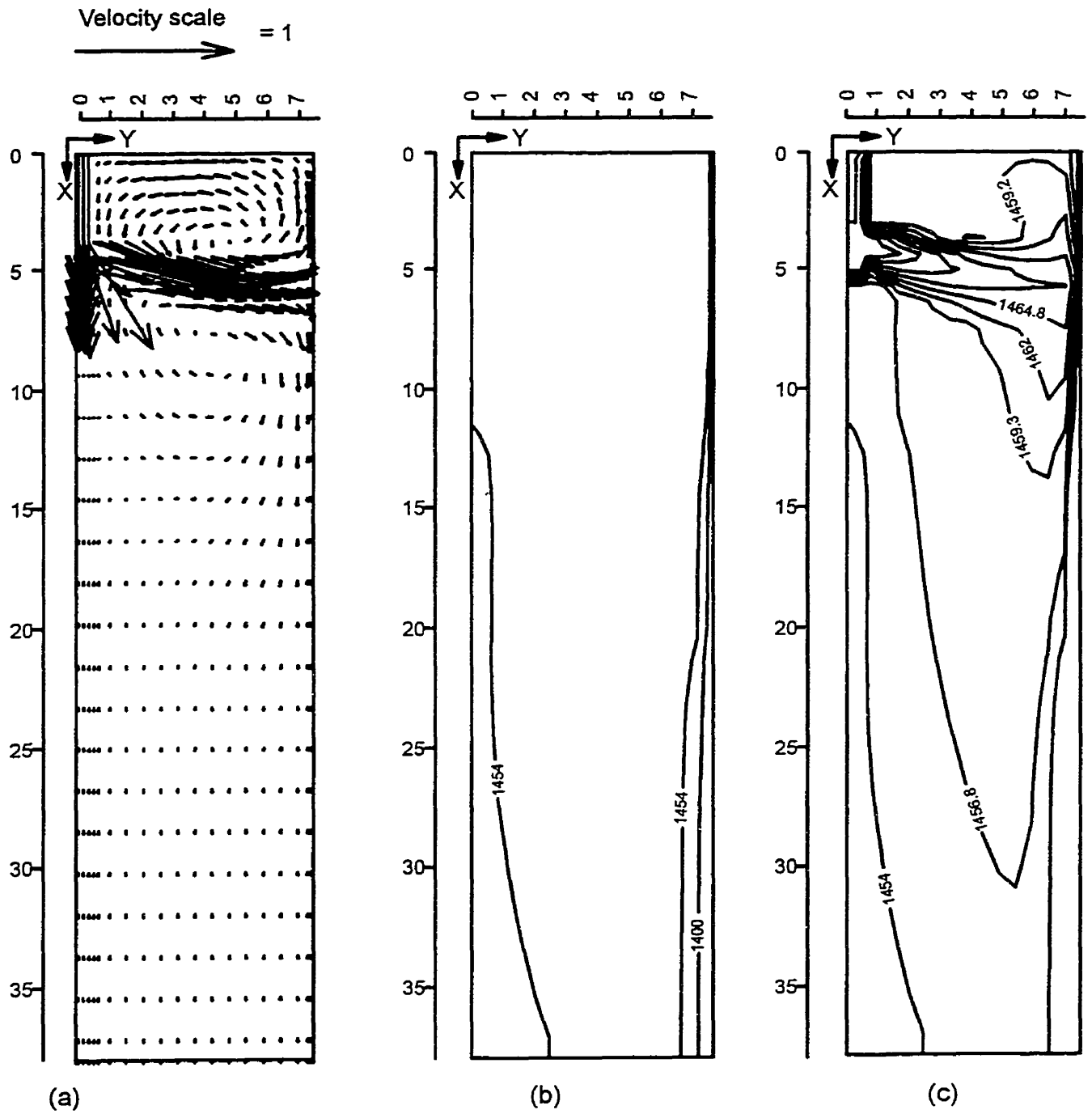


Fig. 2.4. Computed results at the vertical centrally symmetric plane paralleled to the wide face for a casting speed of 0.02 m/sec and 26°C superheat; (a) velocity vectors, (b) liquidus and solidus isotherms, (c) temperature contours.

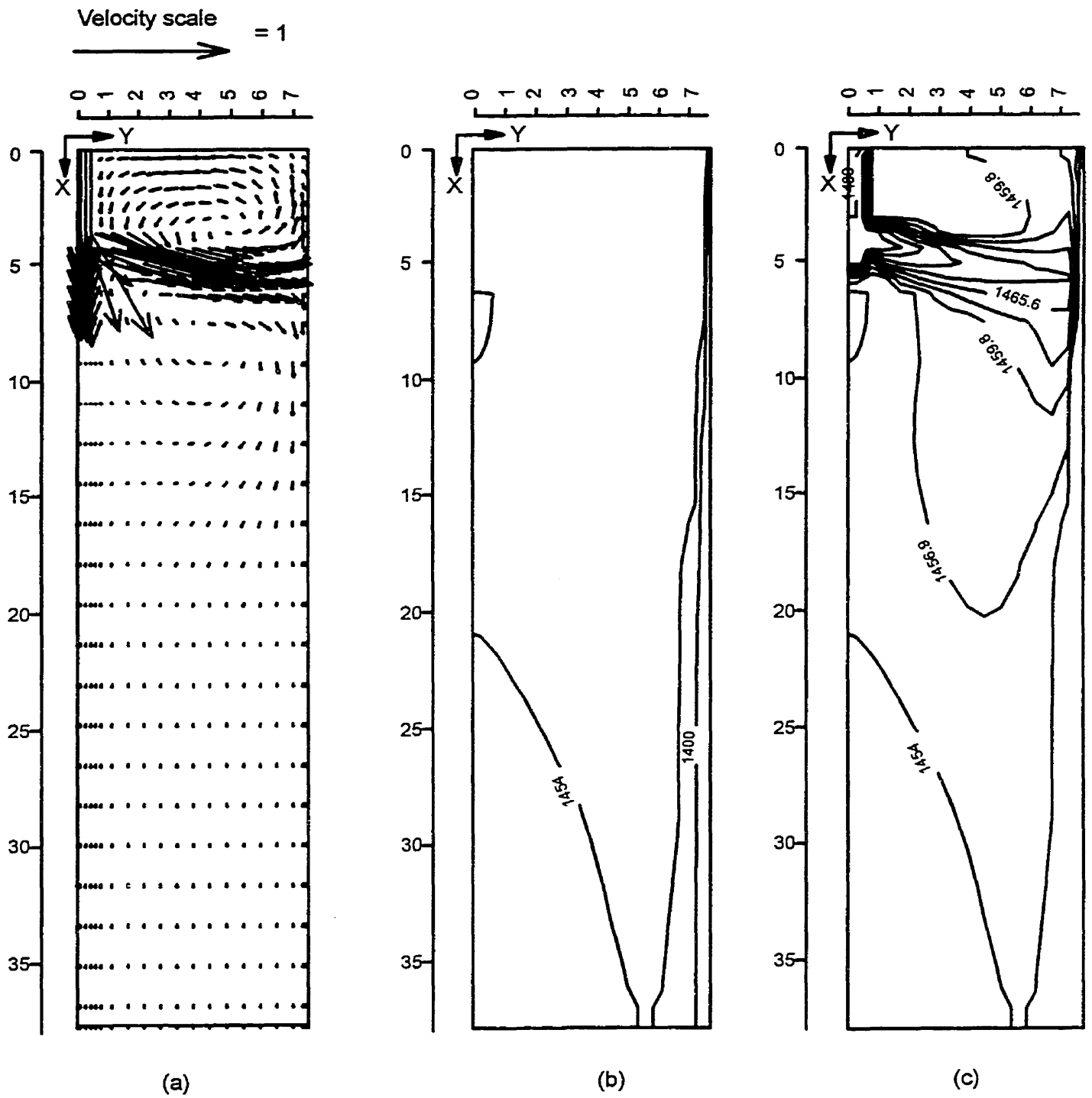


Fig. 2.5. Computed results at the vertical centrally symmetric plane paralleled to the wide face for a casting speed of 0.015 m/sec and 26°C superheat; (a) velocity vectors, (b) liquidus and solidus isotherms, (c) temperature contours.

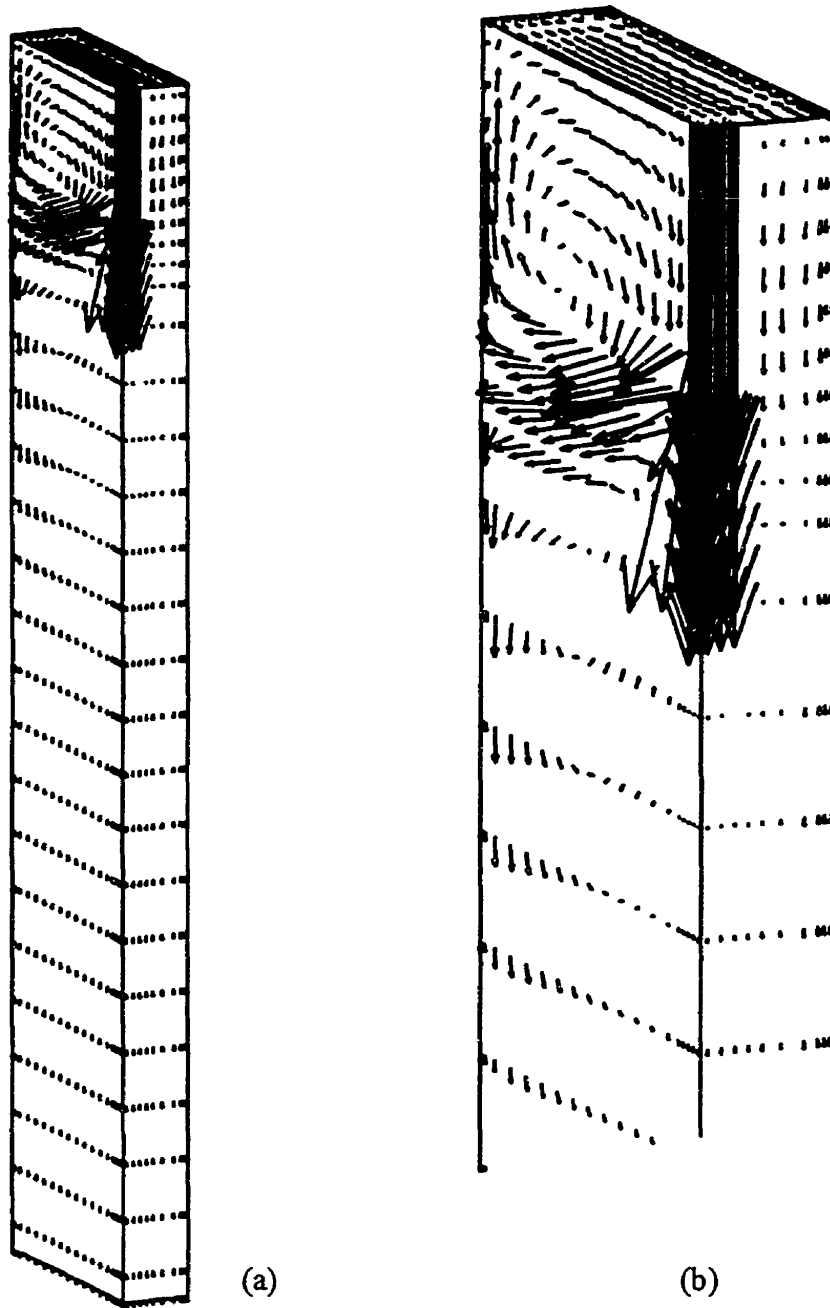


Fig. 2.6. 3-D surface plot of the velocity vectors for a casting speed of 0.015 m/sec and 26°C superheat; (a) the complete solution domain, (b) enlarged view of the top domain.

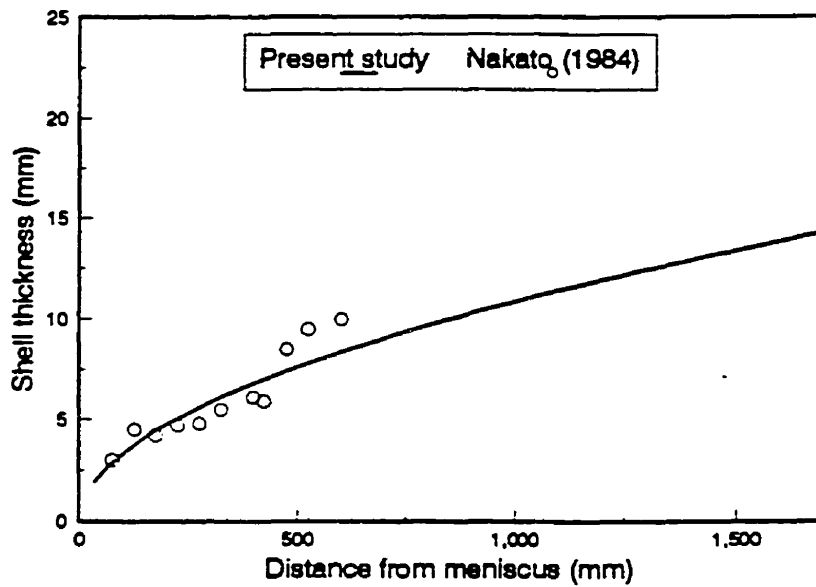


Fig. 2.7. Comparison of solidified shell thickness predicted in this study (for case B) with experimental data from Nakato et al. (1984).

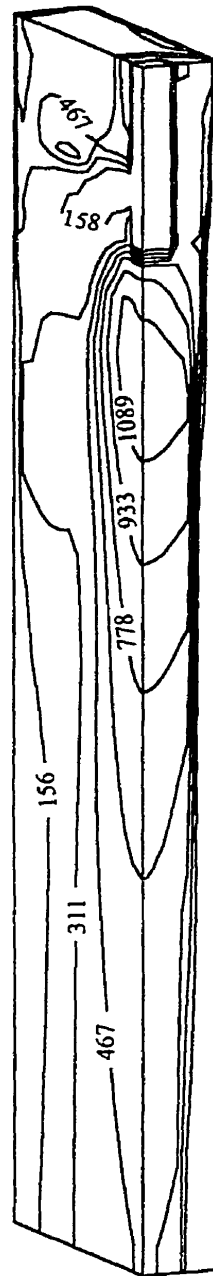


Fig. 2.8. 3-D surface contour plot of non-dimensional turbulent viscosity for a casting speed of 0.015 m/sec and 26°C superheat.

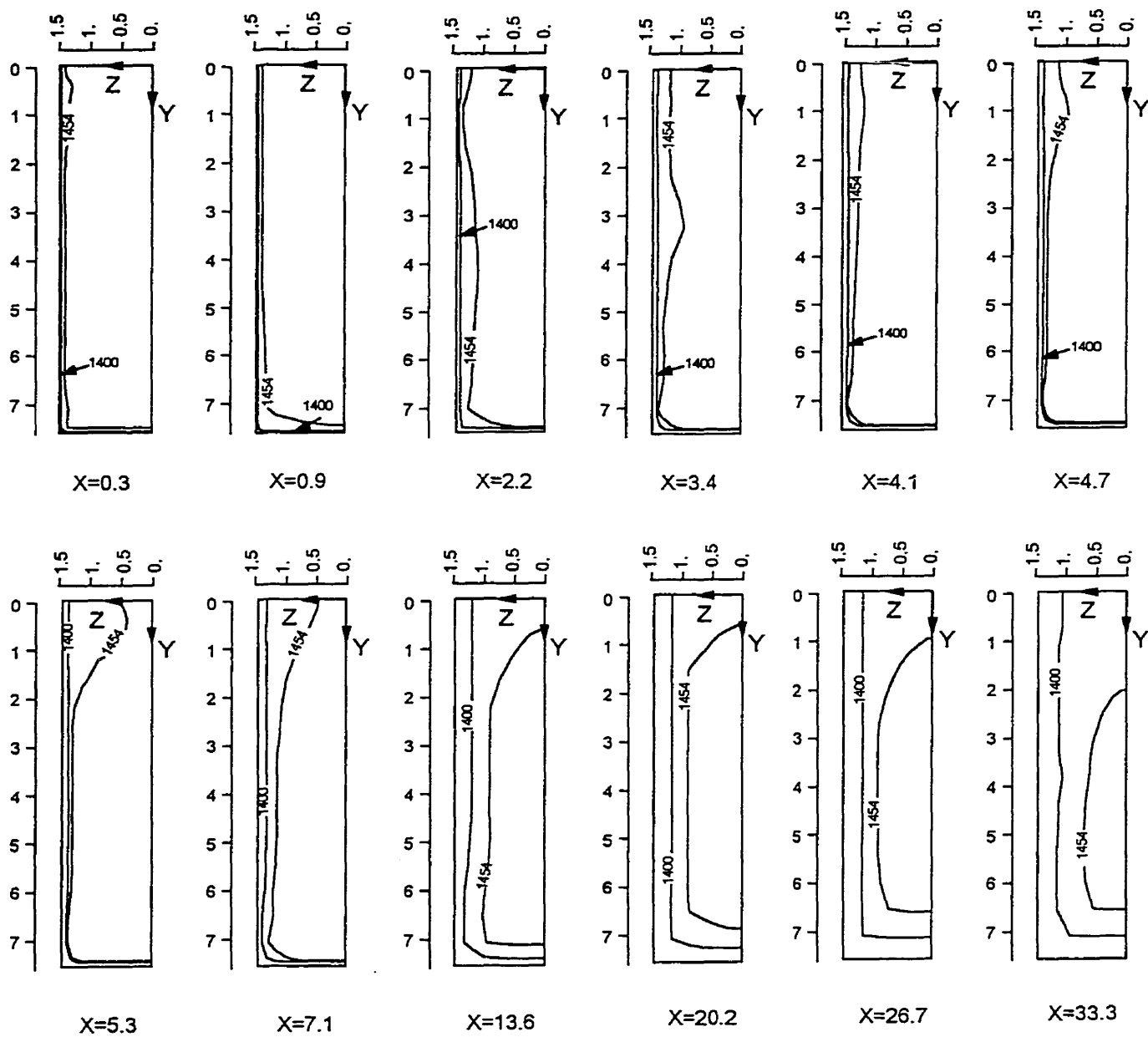


Fig. 2.9. Contours of solidus and liquidus temperatures at various transverse cross-sectional planes (Y-Z planes) for a casting speed of 0.02 m/sec and 26°C superheat.

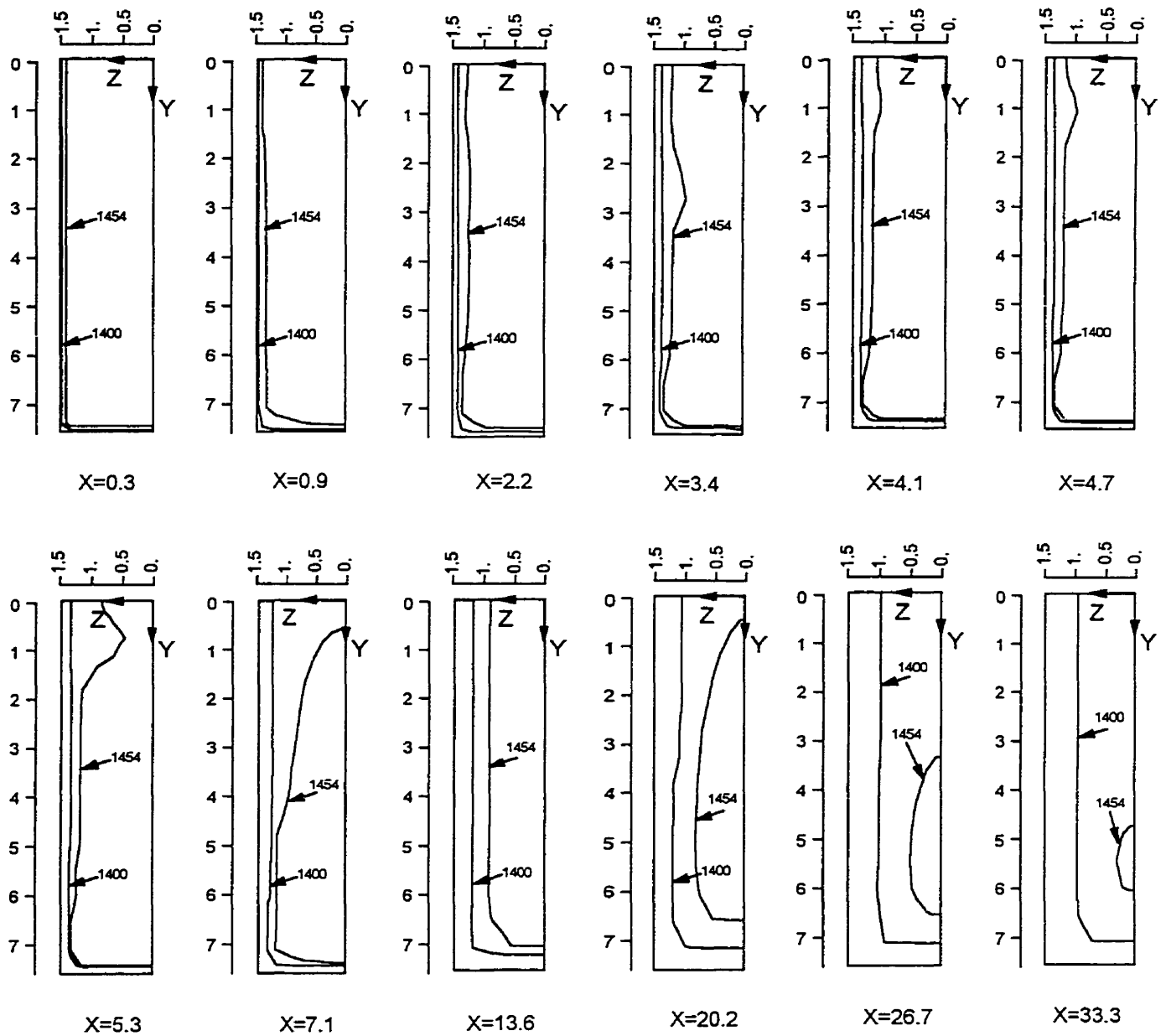


Fig. 2.10. Contours of solidus and liquidus temperatures at various transverse cross-sectional planes (Y-Z planes) for a casting speed of 0.015 m/sec and 26°C superheat.

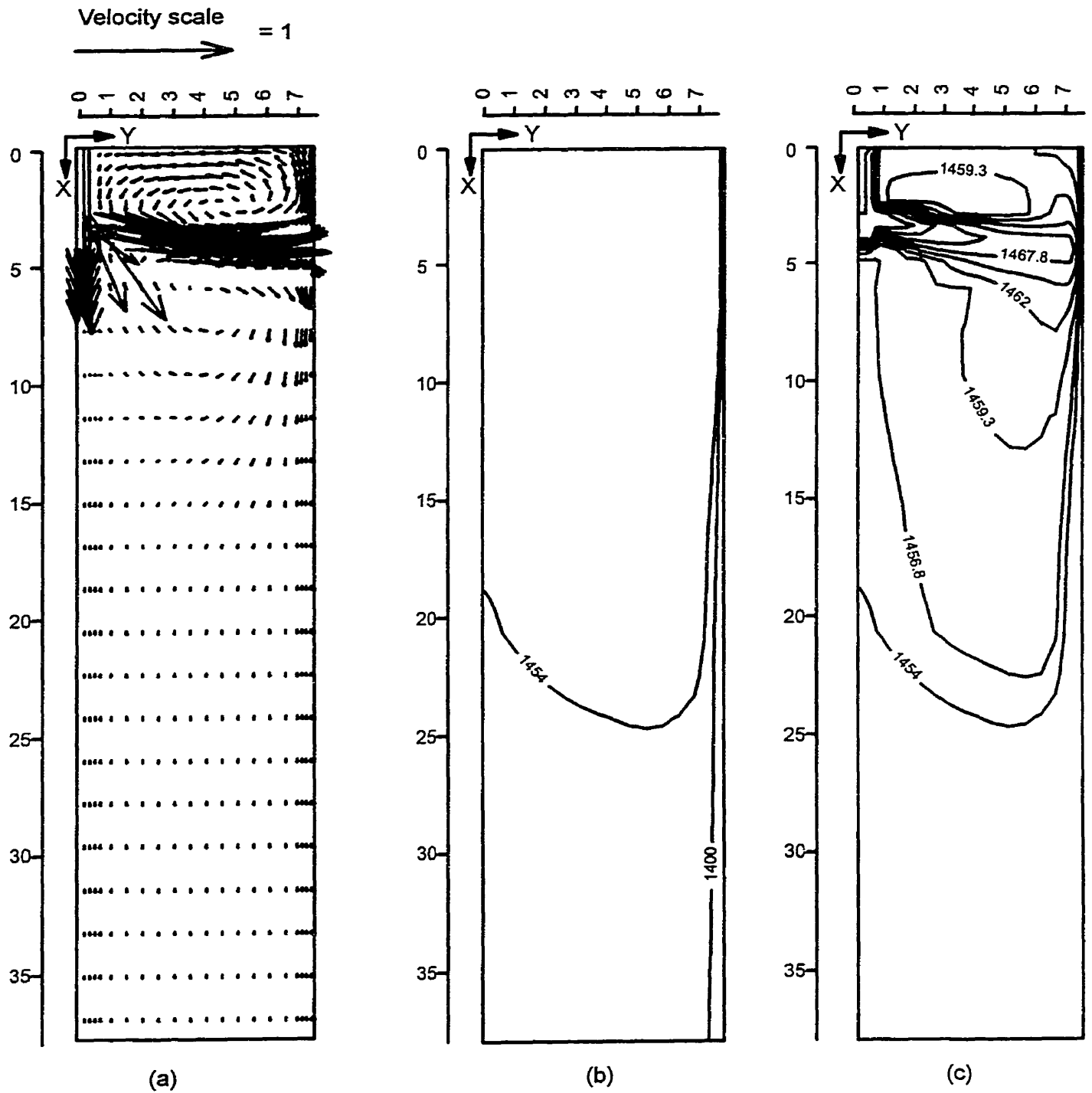


Fig. 2.12. Computed results at the vertical centrally symmetric plane paralleled to the wide face for a casting speed of 0.015 m/sec and 26°C superheat and $\text{SEN}=23\text{ cm}$; (a) velocity vectors, (b) liquidus and solidus isotherms, (c) temperature contours.

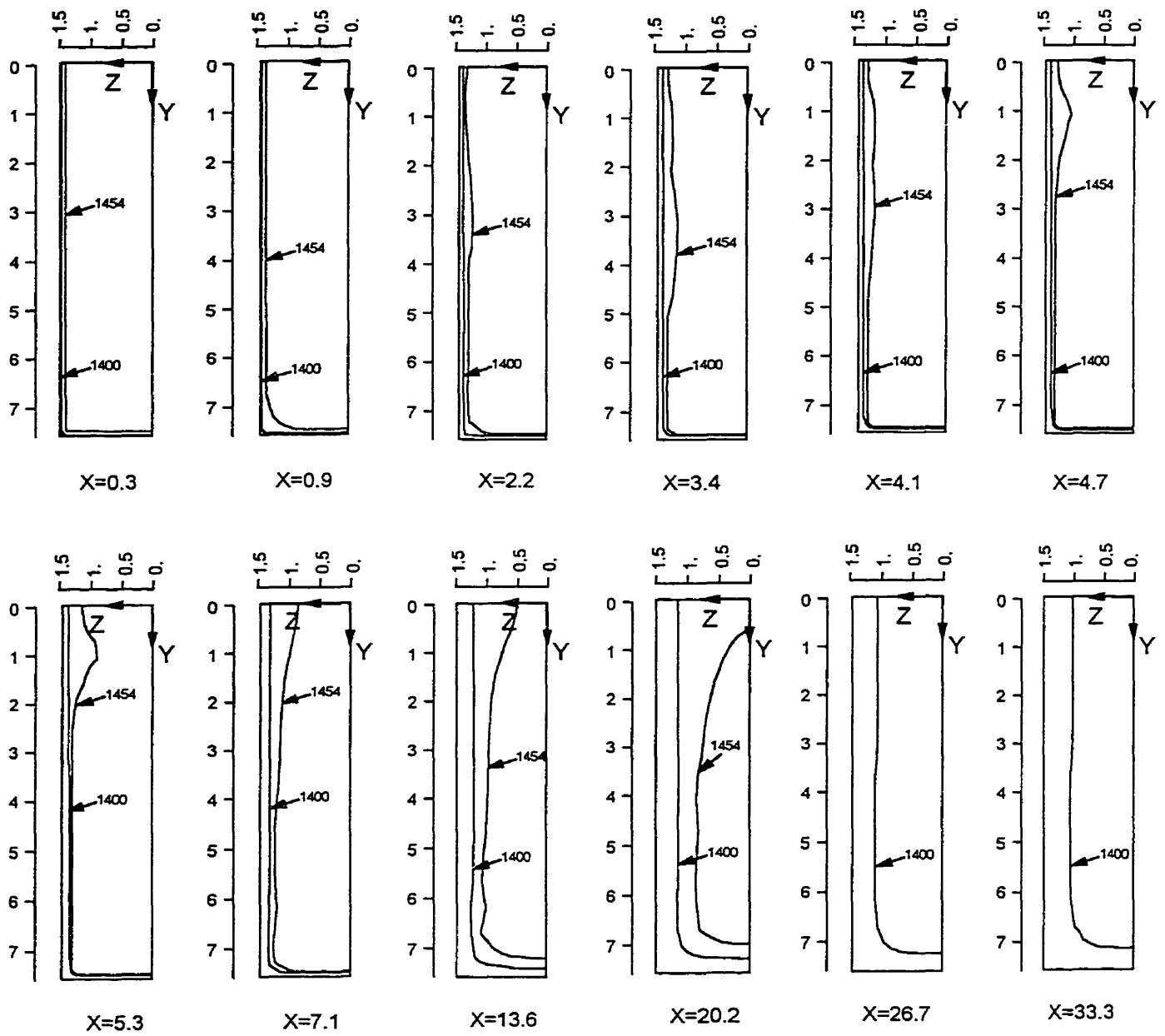


Fig. 2.13. Contours of solidus and liquidus temperatures at various transverse cross-sectional planes (Y-Z planes) for a casting speed of 0.015 m/sec and 26°C superheat and $\text{SEN}=23\text{ cm}$.

MOLD HEAT EXTRACTION RATE EFFECTS ON THE 3-D TURBULENT TRANSPORT PHENOMENA IN CONTINUOUS STEEL SLAB CASTERS

3.1 Introduction

In a continuous casting (CC) process the heat extraction begins in the mold and is followed by the spray and radiation cooling zones. In these three regions a sufficient heat is extracted to virtually complete the solidification of the slab to be cast. One of the important parameters controlling the operation of a CC machine is the heat extraction rate at the mold. The primary function of the mold in a CC operation is to extract sufficient heat from the liquid metal so that the solidified shell at the mold exit is thick and strong enough to hold the liquid steel without bulging or breaking. The design and the operation of the mold have an effect on the heat transfer mechanisms within the mold. This in turn determines the surface and interior quality of the cast.

The mold, which is usually made of pure copper or copper alloy, is a complex heat extraction device where all modes of heat transfer, namely conduction, convection, radiation and phase change take place. The mold is usually cooled from the outside by flowing water through fixed channels within the body of the mold. One of the major concerns of this type of heat extraction method is that locally, just below the meniscus, the mold suffers from the thermal cycling, which is due to nucleate boiling. This phenomenon often causes a drastic decrease in the local heat transfer rate and thus results in the unwanted increase in the mold wall temperatures. The heat transfer coefficient which has

been found to have the most significant affect on the mold wall temperature is affected by variables such as:

- 1) cooling water flow rate and velocity,
- 2) deposition of the mineral salts on the water mold interface,
- 3) mold wall thickness, and
- 4) liquid steel composition and flow characteristics adjacent to the mold walls.

On the hot surface of the mold, i.e. the internal surface of the mold, the heat transfer rate is primarily determined by the air gap formed due to shrinkage of the steel as it undergoes solidification. The air gap and its evolution provides the largest resistance to heat flow in the system. The air gap depends on several factors such as the grade of steel being cast, casting speed, initial superheat, inlet delivery, cooling water flow rate, etc. in a complex manner. The gap can change its width in both the longitudinal and transverse directions and renders it very difficult to characterize. Due to the nature of the mold geometry, the corners of the solidifying sections have heat extracted from two directions and as a result they are the first to shrink and lose contact with the mold. Even though the faces solidify, the ferro-static pressure from above is enough to bulge the faces so that contact with the mold is maintained for a longer period of time. This condition, referred to as reentrant corners causes a peripherally nonuniform heat transfer rate in the mold.

Air gap formation in the mold is the subject of much investigation and has proven to be extremely difficult to model mathematically. However, the consequent effect of the air gap on the mold operation, i.e. the heat extraction, has been obtained experimentally. The values of the heat transfer rate on the mold walls have been reported in the literature either in the form of empirical correlations or experimental observations.

On the other hand, in spite of intensive research activities related to the mathematical modeling of transport phenomena in the continuous casting (CC) processes, an advanced mathematical model, especially a 3-D model, which can enhance the quantitative and qualitative understanding of the industrial CC processes, is still not available. Mathematical models can play a major role in the optimization of the mold, and also spray cooling systems. Modeling of a CC process is concerned with the liquid-solid phase

change problems in which three-dimensional turbulent convective heat transfer in liquid side has an important effect on the growth of the solidified steel shell. Thus, a realistic model for a CC process should be capable of simulating coupled turbulent fluid flow, heat transfer and solidification.

3.2 Literature Survey

It appears that Asai and Szekely (1975) were the first authors who considered a two-dimensional model for a continuous billet casting system. In their study, the turbulent flow in the liquid zone was modeled using the one-equation turbulence model (Kolmogorov-Prandtl model), and the computations of the flow field within the mushy zone were carried out based on the variable viscosity model. They used two separate heat transfer coefficients of value 1.28 and $1.08 \text{ kW/m}^2 \text{ K}$ for the mold and spray zones, respectively. These numbers were the estimated values obtained from the Brimacombe and Weinberg's investigation (1973).

In a series of papers, Thomas and co-workers (1990a, 1990b, 1992) investigated the effect of superheat dissipation on the fluid flow and temperature fields in a continuous-slab casting system. They first solved both the 3-D and 2-D governing momentum and energy equations within the liquid pool in order to obtain heat flux at the solid-liquid interface. Then it was used in a separate one-dimensional solidification model to find the rate of growth of the solidifying shell. The heat flux extracted from the mold walls in their solidification modeling was according to a prescribed function of distance along the mold which varied from 4 MW/m^2 at the meniscus surface to about 1.2 MW/m^2 at the mold exit.

Flint (1990) reported the results of the heat transfer and fluid flow of the three-dimensional simulation of a continuous slab caster. He utilized a commercial code (PHOENICS) and said to have solved the momentum and enthalpy equations, and claimed to have implicitly accounted for the solidification process.

The expression used in this study for mold heat flux was the one determined empirically by Davies et al. (1988), in which the heat extraction rate was an exponential function of distance below the meniscus surface and casting speed.

Choudhary and Mazumdar (1994, 1995) have reported the two-dimensional modeling results of fluid flow, heat transfer and solidification for continuous steel billet casters. In terms of heat extraction rate from the mold wall and in the spray zone, they applied both an empirical correlation proposed by Savage and Pritchard (1954) and experimental observations reported by Lait and Brimacombe (1974).

Recently, Aboutalebi et al. (1995a, 1995b), carried out two-dimensional numerical studies to model coupled turbulent flow, heat transfer and macroscopic solidification in the mold and submold regions of a stainless steel slab caster. In these studies, the boundary conditions for the energy equation were identical to those of Lally et al. (1990) and Lait et al. (1974) studies.

Thus, according to the reported functions and experimental data in the literature for heat transfer rates from the mold walls of the stainless steel slab casters, three different energy boundary conditions are identified. These are :

- (1) the Savage and Pritchard (1954) correlation, which provides the values of heat flux as a function of distance below meniscus and casting speed, is presented by,

$$q_s = 2.67 - 0.33\sqrt{Z/U_c} \text{ MW/m}^2 \quad (3.1)$$

where Z and U_c are vertical distance from the meniscus along the mold and casting speed, respectively.

- (2) the averaged heat transfer coefficient along the mold which was obtained from the measured mold heat flux and proposed by Lait et al. (1974),

$$\gamma = 1.5 \text{ kW/m}^2 \text{K} \quad (3.2)$$

- (3) and the mold-averaged heat transfer coefficient suggested by Lally et al. (1990),

$$\gamma = 1.1 \text{ kW/m}^2 \text{K} \quad (3.3)$$

To the best of my knowledge, there exist no 3-D modeling studies of a continuous slab caster which have clarified the implications of using the above thermal boundary

conditions at the mold walls and the extent of solidification and growth of mushy layer development with the presence of turbulent convective recirculating flow in the mold. Thus, the objective of the study presented in this chapter is to first develop a comprehensive mathematical model for a continuous slab casting machine. The model should take into consideration the coupled turbulent fluid flow, heat transfer and solidification aspect of the process. The second objective of this study is to ascertain the effect of the above three popularly used heat transfer boundary conditions on the evolution of the solid and mushy layers in the mold.

3.3 Mathematical Formulation

In order to drive a mathematical model which is applicable to the continuous slab casting processes, the assumptions listed in Chapter 2 were applied here. The governing conservation equations presented in this chapter are based on the *continuum* model for binary alloys which was originally developed for laminar flow problems by Bennon and Incropera (1987). These equations were modified here in order to take into account the turbulent behavior of the liquid steel flow in the process. The final form of the equations derived in this chapter are compared with the corresponding equations presented in Chapter 2.

The development of the continuum model from mixture theory is based on the following principles:

- I) In alloy solidification, the system contains two phases; liquid and solid, and each phase behaves as an isolated subsystem in which the interaction with other mixture components should be properly treated.
- II) The two phase mixture forms a continuum in which any location in the domain can be occupied simultaneously by both phases considering the fact that all phases do not disappear simultaneously.
- III) The mixture properties can be obtained based on the mathematical mean of each phase properties.

IV) The two phase mixture behavior is governed by the equations similar to those governing the individual phases and are obtained from the summation of the individual component equations.

Considering the aforementioned assumptions and beginning from equations derived by Bennon and Incropera (1987) for laminar flow, the final form of the steady, time-averaged turbulent transport equations in Cartesian coordinate systems for turbulent condition can be written as:

conservation of mass:

$$\nabla \cdot (\rho \vec{V}) = 0 \quad (3.4)$$

conservation of momentum:

$$\text{div}(\rho \vec{V}u) = \text{div}\left(\mu_{\text{eff}} \frac{\rho}{\rho_l} \text{grad } u\right) - \frac{\partial P}{\partial x} - \frac{\mu_l}{K_p} \frac{\rho}{\rho_l} (u - u_s) + S_x \quad (3.5)$$

$$\text{div}(\rho \vec{V}v) = \text{div}\left(\mu_{\text{eff}} \frac{\rho}{\rho_l} \text{grad } v\right) - \frac{\partial P}{\partial y} - \frac{\mu_l}{K_p} \frac{\rho}{\rho_l} (v - v_s) + S_y \quad (3.6)$$

$$\text{div}(\rho \vec{V}w) = \text{div}\left(\mu_{\text{eff}} \frac{\rho}{\rho_l} \text{grad } w\right) - \frac{\partial P}{\partial z} - \frac{\mu_l}{K_p} \frac{\rho}{\rho_l} (w - w_s) + S_z \quad (3.7)$$

In momentum equations, the variable K_p represents the directionally independent permeability of the two phase mushy zone which was calculated using the Carman-Koseny equation for permeability of porous media as:

$$K_p = \frac{g_l^3}{D_1(1-g_l)^2} \quad (3.8)$$

The value of D_1 , at present, is a controversial issue, so far as the mushy solidification modeling is concerned, and for this the value proposed by Minakawa et al. (1987) was adopted in the present study.

conservation of energy:

$$\operatorname{div}(\rho \bar{V} h) = \operatorname{div}\left(\frac{k_m^{\text{eff}}}{c_s} \operatorname{grad} h\right) + \operatorname{div}\left[\frac{k_m^{\text{eff}}}{c_s} \operatorname{grad}(h_s - h)\right] - \operatorname{div}\left[\rho(\bar{V} - \bar{V}_s)(h_l - h)\right] \quad (3.9)$$

In the above equations, ρ , \bar{V} , k_m^{eff} and h are mixture density, velocity, effective thermal conductivity and enthalpy, respectively. These quantities can be obtained from mathematical mean expressions as follows:

$$\rho = \rho_l g_l + \rho_s g_s \quad (3.10)$$

$$\bar{V} = f_l \bar{V}_l + f_s \bar{V}_s \quad (3.11)$$

$$k_m^{\text{eff}} = k_l^{\text{eff}} g_l + k_s g_s \quad (3.12)$$

$$h = h_l g_l + h_s g_s \quad (3.13)$$

where, k_l^{eff} is effective liquid thermal conductivity, f_l and f_s are mass fraction and g_l and g_s are volume fraction of liquid and solid in the mushy region, respectively. k_l^{eff} is defined by the following expression:

$$k_l^{\text{eff}} = k_l + k_i = c_l \left(\frac{\mu_l}{\operatorname{Pr}_l} + \frac{\mu_i}{\operatorname{Pr}_i} \right) \quad (3.14)$$

and phase enthalpies are:

$$h_s = c_s T \quad (3.15)$$

$$h_l = c_s T + (c_l - c_s) T + L \quad (3.16)$$

In order to simplify the energy equation, the dependent variable of the energy equation, mixture enthalpy, has been changed to sensible energy, \bar{h} , which is identical to h_s . Thus, assuming $c_l = c_s$, the new form of the equation for the conservation of energy for the pseudo one-phase model becomes:

$$\operatorname{div}(\rho \bar{V} \bar{h}) = \operatorname{div}\left(\frac{k_m^{\text{eff}}}{c_s} \operatorname{grad} \bar{h}\right) - \operatorname{div}(\rho g_l \bar{V} L) - \operatorname{div}\left[\rho g_s (\bar{V} - \bar{V}_s) L\right] \quad (3.17)$$

A comparison between momentum and energy equations derived here based on the continuum model and their corresponding equations presented in Chapter 2. shows only an extra term appearing in continuum model energy equation, i.e. the last term in Eq. 3.17. The term physically represents the energy flux associated with relative phase motion. Assuming equiaxed solidification in the mold region, which implies no relative phase motion, and ignoring the relative velocity in the columnar dendritic solidification, the last term of the above equation can be dropped.

The effective viscosity, μ_{eff} , appearing in momentum equations is the sum of molecular and turbulent viscosity, $\mu_{eff} = \mu_l + \mu_t$, and turbulent viscosity can be estimated on the basis of the turbulent modeling formulation. In the present study, a modified version of the low-Re $k - \varepsilon$ turbulent model proposed by Launder and Sharma (1974) was adopted in which the turbulent viscosity is defined as a function of two turbulent quantities of k and ε .

$$\mu_t = \rho f_\mu c_\mu \frac{k^2}{\varepsilon} \quad (3.18)$$

Thus, to estimate the value of turbulent viscosity, two additional partial differential equations for k and ε should be solved as follows:

$$div(\rho \bar{V} k) = div \left[\left(\mu + \frac{\mu_t}{\sigma_k} \right) grad k \right] + G - \rho(\varepsilon + D_k) \quad (3.19)$$

$$div(\rho \bar{V} \varepsilon) = div \left[\left(\mu + \frac{\mu_t}{\sigma_\varepsilon} \right) grad \varepsilon \right] - c_1 f_1 \frac{\varepsilon}{k} G - c_2 f_2 \rho \frac{\varepsilon^2}{k} + E_\varepsilon \quad (3.20)$$

The values for E_ε , D_k , f_μ , c_1 , c_2 , c_μ , f_1 , f_2 , σ_k and σ_ε for the Launder-Sharma (1974) model are those listed in Table 2.1.

Boundary conditions:

Due to the two-fold symmetry condition, a quadrant of the slab caster was selected in this study to represent the computational domain, as shown in Fig. 2.1 (Chapter 2). The schematic grid layout used in the present computations is also similar to that provided in

this figure. The boundary conditions which are considered for the fluid flow, turbulent quantities and energy equations are listed in Table 3.1.

Table 3.1. Summary of the adopted boundary conditions.

positions	velocity	turbulent quantities	energy
inlet	$u = u_{in},$ $v = w = 0$	$k = 0.01 \times u_{in}^2,$ $\varepsilon = c_{\mu} k_{in}^{3/2} / 0.05D$	$h = h_{in}$
outlet	$\frac{\partial u}{\partial x} = \frac{\partial v}{\partial x} = \frac{\partial w}{\partial x} = 0$	$\frac{\partial k}{\partial x} = \frac{\partial \varepsilon}{\partial x} = 0$	$\frac{\partial h}{\partial x} = 0$
free surface	$u = \frac{\partial v}{\partial x} = \frac{\partial w}{\partial x} = 0$	$\frac{\partial k}{\partial x} = \frac{\partial \varepsilon}{\partial x} = 0$	$\frac{\partial h}{\partial x} = 0$
wide symmetry plane	$w = \frac{\partial u}{\partial z} = \frac{\partial v}{\partial z} = 0$	$\frac{\partial k}{\partial z} = \frac{\partial \varepsilon}{\partial z} = 0$	$\frac{\partial h}{\partial z} = 0$
narrow symmetry plane	$v = \frac{\partial u}{\partial y} = \frac{\partial w}{\partial y} = 0$	$\frac{\partial k}{\partial y} = \frac{\partial \varepsilon}{\partial y} = 0$	$\frac{\partial h}{\partial y} = 0$
wide face of slab	$u = u_s,$ $v = w = 0$	$k = \varepsilon = 0$	$q = 2.67 - 0.33\sqrt{x/u_c}$ or $\frac{\partial h}{\partial z} = -\frac{\gamma}{K}(h_s - h_a)$
narrow face of slab	$u = u_s,$ $v = w = 0$	$k = \varepsilon = 0$	$q = 2.67 - 0.33\sqrt{x/u_c}$ or $\frac{\partial h}{\partial y} = -\frac{\gamma}{K}(h_s - h_a)$

The governing equations along with the boundary conditions were nondimensionalized and then discretized via the control-volume-based finite-difference procedure proposed by Patankar (1980). A detailed information regarding the nondimensionalization of the governing equations can be found in Seyedein and Hasan (1997). A staggered grid system, in which the velocity components are stored midway

between the scalar storage locations, was used. In order to resolve the velocity and pressure fields in the momentum equations, the well known SIMPLE-algorithm suggested by Patankar (1980) was adopted. In order to obtain the practical grid-independent results both uniform and nonuniform grid distributions with different grid numbers were tested. To meet the reasonable accuracy and computational costs, $30 \times 25 \times 15$ grid numbers for x-, y- and z-direction respectively were selected for all of the numerical simulations reported here.

The discretized equations were solved iteratively using an implicit relaxation technique and employing the well-known line-by-line TDMA solver. The following convergence criterion was considered in the present computational study.

$$R_{\Phi} = \sum_{\text{all nodes}} \left| a_p \Phi_p - \sum_{nb} a_{nb} \Phi_{nb} - b \right| \leq 1 \times 10^{-3} \quad (3.21)$$

3.4 Results and Discussion

The information about heat extraction in the mold for stainless steel slab casters, obtained from the earlier studies, has been incorporated in the present three-dimensional numerical model for predicting the transport processes in continuous steel slab casters. This information has been classified under three different energy boundary conditions in the mold and is listed in Table 3.2.

Table 3.2. The various types of energy boundary conditions in the mold for stainless steel slab casters.

Various type	Type A	Type B	Type C
B.C.	$\gamma = 1.1$ $kW/m^2 K$	$\gamma = 1.5$ $kW/m^2 K$	$q = 2.67 - 0.33\sqrt{Z/U_c}$ kW/m^2

The flow pattern, as obtained from the implementation of the type-A energy boundary condition in the mold, with the operating conditions presented in Table 3.3, is illustrated in Fig. 3.1. As seen from this figure, two melt recirculation zones develop within the caster; one in the upper and another in the lower region of the caster. The upper recirculation zone is limited to the entrance flow impinging onto the narrow face of the slab from the bottom, and meniscus surface from the top. It also extends horizontally towards narrow and wide symmetry faces of the slab. The development of the lower recirculation zone under the nozzle port is due to the downward mass and momentum entrainment of molten steel flow after impingement onto the narrow face of the slab. The size of the lower recirculation zone is known to be dependent on the casting speed, nozzle type and geometry of the mold. However, the development of the mushy layer in the caster, which represents a porous medium with higher resistance against liquid steel flow, was found to be an important parameter affecting the penetration depth of the lower recirculation loop. To demonstrate the effect of the solidification process on the flow pattern, a separate run was carried out for fluid flow of molten steel in the absence of solidification. Figure 3.2 displays the vector plot in the wide symmetry plane of the caster for two different cases; one with, and another without, solidification. From this figure, it is seen that the depth of the lower recirculation loop for the fluid flow simulation with no solidification is about 2.7 meter, while the corresponding depth for a real CC process with solidification is almost 1.15 meter. Such a decrease in the flow penetration can be attributed to the effect of the D'arcy source term in the momentum equations for mushy region modeling. It is to be noted that the value of the D'arcy coefficient does affect the flow field, and the selection of this value at present, as has been stated earlier, is a controversial issue in alloy solidification modeling research. However, in the present study, the value proposed by Minakawa et al. (1987), which is based on the physical concepts of the dendritic solidification, was used.

Table 3.3. Thermophysical properties of stainless steel and geometrical parameters used for the simulations.

Variable	present work	Atlas Steel
thermal conductivity (liquid or solid)	$31 \text{ Wm}^{-1}\text{K}^{-1}$	15.9
specific heat (liquid or solid)	$700 \text{ Jkg}^{-1}\text{K}^{-1}$	681
latent heat of fusion	264 kJkg^{-1}	272
viscosity	$0.007 \text{ kgm}^{-1}\text{s}^{-1}$	0.007
density	7000 kgm^{-3}	7400
liquidus & solidus temperatures	1454 & 1400° C	1460-1399
inlet temperature	1480° C	1480
casting speed	0.02 ms^{-1}	0.0165
slab size	$1.27 \times 0.254 \text{ m}$	1.09×0.127
mold length	0.75 m	0.51
caster length simulated	3.0 m	3.0
nozzle submergence length	0.34 m	0.21

The velocity vector field at the symmetry plane parallel to the wide face is shown in Fig. 3.3 for three types of thermal energy boundary conditions used in this study. The comparison of these flow patterns shows a minimal difference in the upper recirculation zone which may be attributed to the thin solid and mushy layers developing in the mold. As one would expect, the length of the lower recirculation zone for a higher heat transfer coefficient on the mold wall is smaller than that for a lower one. In fact, this change in the flow field in the wide symmetry plane is influenced by the effect of the shear stress induced by wide faces of the strand. It was also demonstrated in the 2-D and 3-D water modeling study, carried out by Aboutalebi et al. (1996), that a 3-D model predicts a smaller, lower recirculation zone compared to the 2-D one, due to the effect of shear stress induced by the side walls. The present study also confirms a similar behavior for different heat

extraction rates. In fact, the higher heat transfer coefficient in the mold leads to thicker solid and mushy layers on the wide face of the slab. These thick layers in turn bring the side wall effects nearer to the symmetry plane and, consequently, decrease the size of the downward recirculation zone.

In an industrial continuous slab casting machine, turbulence plays a significant role in governing the transport processes. In order to get a quantitative picture of the turbulence effect in the caster, the non-dimensional turbulent eddy viscosity contours for various heat extraction rates in the mold are drawn for the top free surface and for the wide and narrow symmetry planes in Fig. 3.4. In all of the cases studied here, two regions of high turbulent energy are observed; one region is associated with the upper recirculation zone and the other region lies under the submerged nozzle. Although the distribution pattern for these cases is similar in appearance, the level of turbulent eddy viscosity changes slightly from case to case. For example, an increase in the heat transfer coefficient from 1.1 to 1.5 kW/m^2K results in a decrease of the turbulence level by about 10%, while a change in the heat transfer boundary condition from type A to type C causes the turbulence level to increase by about 20%.

The solidus and liquidus contours in the wide symmetry plane, predicted for various cases under study, are shown in Fig. 3.5. As expected, the solid and mushy layers for the lower heat transfer coefficient (type A) are thinner than those for the higher heat transfer coefficient. For cases A and B, the heat extraction rate from the mold walls depends on the wall temperature, and generally decreases downstream with the simultaneous decrease of the wall temperature, while for case C (heat flux formulation) the heat extraction rate decreases along the mold in proportion to the square root of the distance from the meniscus, X , as expressed in Table 3.2. For all the three cases, it is seen that the mushy layer, which develops on the wide face of the strand, grows and approaches to the symmetry plane from the center of the wide face faster than the other sides. In fact, the evolution of the solid and mushy layers are dictated by the difference between the heat extraction rate from the wall and the convective heat transfer in the liquid and mushy zones. The latter quantities are inevitably affected by the flow pattern in the mold. In case

B, the mushy layer, which forms on the wide plane, reaches to the wide symmetry plane under the mold comparatively faster than the other two cases. In case A, the developing mushy layer reaches to the symmetry plane in a similar fashion as case B, however, it remelts further downstream due to its exposure to the hot incoming recirculating melt in the lower loop. Figures 3.6 and 3.7 represent the developed solid and mushy layers for various simulated cases at the exit of the mold and submold, respectively. As seen in Fig. 3.7, in case C the solid layer that developed on the wide face of the slab is much more uniform compared to the other cases. This discrepancy can be attributed to the differences in the heat fluxes on the mold wall in these cases. In fact, for cases A and B the rate of heat extraction is dependent on the surface temperature. As a result, a peripherally nonuniform heat flux on the mold wall prevails for these two cases, while in case C the expression for the thermal boundary condition is such that it imposes a peripherally uniform heat flux on the mold wall. The high uniformity in the solid and mushy layers in the mold for case C, shown in Fig. 3.7, decelerates the growth of the mushy layer on the center line of the wide symmetry plane, which is also confirmed in Fig. 3.5. It is further seen from Fig. 3.7 that the lowest solid and mushy layer thicknesses appear in the narrow face of the slab, which indicate the highest superheat dissipation on this face due to the impingement of the hot incoming liquid metal.

The superheat temperature contours in the wide symmetry plane for various simulated cases are shown in Fig. 3.8. As expected from this figure, the temperature level decreases with the increase of the heat transfer coefficient on the mold walls. The lowest temperature level was obtained for case C which shows that the heat flux boundary condition employed for this case and presented in Table 3.2, generates a higher overall heat extraction in the mold compared to the other cases, namely cases A and B.

The computed surface temperature for all three cases under study, and for the two locations, one for the middle of the mold and the other for the submold exit, are displayed in Figs. 3.9 through 3.11. All these figures report a similar distribution of the surface temperature. The value of temperature along the narrow face is higher than that along the wide face of the slab. This is a consequence of the impingement of the superheated molten

steel onto the narrow face. The minimum value of the surface temperature is found to be at the corner of the strand which is due to the enhanced heat extraction rate from the two sides of the slab. At the mold exit, the surface temperature along the wide face of the slab increases with the increase of the distance from the corner temperature of about 600°C to a maximum value of approximately 1120°C . The surface temperature then decreases gradually to a value of about 950°C and remains almost constant at this value for most of the surface. The maximum value for the surface temperature along the wide face in the mold region reflects the effect of the impingement zone, and is seen to be cooled down quite rapidly at the submold exit where the flow pattern is almost uniform.

In order to compare the predicted results with experimental data, a separate run was carried out for the stainless steel slab caster in operation at Atlas Steel, Tracy, Quebec. In this case, a constant value of heat transfer coefficient of $1.5\text{ kW}/\text{m}^2\text{K}$ was used as the thermal boundary condition in the mold. This value of the heat transfer coefficient was also reported by Lait et al. (1974) who obtained this value from the measured heat flux data. The casting variables and the thermophysical properties which were used for this simulation correspond to the test case at Atlas Steel and are listed in Table 3.3. The predicted solidification profile at the narrow face of the slab has been compared with the experimental data in Fig. 3.12. The measured data in this figure were reported by Lait et al. (1974) and were obtained from autoradiographs using radioactive tracers. From this figure it is seen that the present 3-D model does predict the measured solidified shell thickness along the narrow face with a reasonable accuracy.

The surface temperature along the axial direction for the centerline of the wide and narrow faces of the slab are plotted in Fig. 3.13. This figure also represents the corresponding results obtained by Lait et al. (1974) using various simple one-dimensional conduction type simulation models. The open circle results represent the present predictions for heat transfer coefficient of $1.5\text{ kW}/\text{m}^2\text{K}$. Initially, there is a rapid fall of temperature from the top surface to about half of the mold length due to the increased thermal resistance of the growing solid shell. After this sharp decrease, the abrupt positive change in the slope of the temperature profile is due to the increased convective heat

transfer rate at the inner surface of the solidified shell imparted by the superheated inlet jet from the submerged nozzle. The upward shift and rebound of the slab surface temperature at the exit of the mold is the effect of the change of the thermal boundary condition from a higher heat extraction rate at the mold to a lower heat extraction rate in the secondary cooling zone. The gradual fall of the mid-face surface temperature further downstream is predominately the effect of purely conductive phase-change heat transfer. The solid line in this figure represents the fitting curve of the presently predicted results designated by open circles. The curves representing dotted and dashed results were obtained by Lait et al. using various one-dimensional conduction model equations with an effective thermal conductivity for the liquid phase equal to seven times the thermal conductivity of liquid steel. The dotted curve results are for the same constant heat transfer coefficient as the presently calculated open-circle results. The dashed results represent the temperature profile obtained by Lait et al. using the empirical mold heat flux correlation of Savage and Pritchard. Upon comparing the temperature profiles from the presently calculated 3-D and Lait et al. 1-D models, one can easily see that 1-D model grossly under-predicts the mid-face surface temperature along the whole length of the mold as well as for the secondary cooling zone. Also, it can be seen that with the Lait et al.s' 1-D conduction model it is not possible to capture the rebound of the surface temperature at the exit of the mold for a slab casting process. Generally, such one-D models for solidification are too elementary in nature for the modeling of the complex continuous slab casting processes since these models predict less than satisfactory results even for the solidification profiles. Another major weakness of 1-D models is that they are unable to predict the peripheral variations of the solidified shell thickness and the surface temperature.

3.5 CONCLUDING REMARKS

In order to examine the effects of mold heat extraction rates on a continuous stainless steel slab casting process a three-dimensional numerical study of coupled turbulent flow,

heat transfer and macroscopic solidification was carried out. Three different surface boundary conditions for the mold region involving two constant mold heat transfer coefficients and an empirical heat flow relationship were examined. The control volume based finite-difference model, along with the associated computer code, was developed to obtain the numerical solution of the coupled turbulent flow, heat transfer and macroscopic solidification in the mold and submold regions of an industrial size continuous caster for steel slabs. A modified low Reynolds number κ - ϵ model was used to account for the turbulence effects in the liquid and mushy regions. Numerical accuracy of the model was tested by comparing the predicted solidified shell thickness with the known published experimentally measured data obtained through a radioactive gold tracer technique for a stainless-steel slab caster. A very good agreement was obtained between the theoretically predicted and experimentally measured solid shell thickness.

The numerical results show that the effect of thermal boundary conditions in the mold region is quite dramatic in so far the thermal fields and solid shell profiles are concerned. The flow field and various turbulent quantities virtually showed no effect with the change of the thermal boundary condition in the mold. In the submold region, there was no significant effect of the change in the thermal conditions at the mold. The present study shows that the assignment of a correct (preferably experimental) mold heat flux distribution profile is important to study the initial development of the solid shell thickness in the mold. This study also shows that for an accurate and quantitative prediction of the solidified shell thickness, temperature profiles within and on the surface of the slab, velocity fields and various turbulent quantities, a three-dimensional coupled transport phenomena and solidification study is required. The temperature profiles obtained from the present study can be fed into a thermal stress model to calculate the stresses that develop in the casting slab. This study will aid in the future developments of new technologies dedicated to the improvement of the surface quality and to the increased productivity of the cast.

NOMENCLATURE

Symbol	Description
a_p, a_{nb}, b	coefficients in the discretized governing equations
c_1, c_2, c_μ	empirical constants for low Reynolds turbulent models
c_l	liquid specific heat
c_s	solid specific heat
D_1	Darcy coefficient
D_k	extra dissipation term in k -equation
E_ε	extra generation term in ε -equation
f_1, f_2, f_μ	empirical constants for low Reynolds turbulent models
g_l	liquid fraction
g_s	solid fraction
G	turbulent kinetic energy generation in k -equation
\bar{h}	sensible heat
h_l	liquid enthalpy
h_s	solid enthalpy
H	total heat (sensible heat and latent heat)
k	turbulent kinetic energy
k_l	liquid thermal conductivity
k_t	turbulent thermal conductivity
k_m^{eff}	mixture effective thermal conductivity
k_l^{eff}	effective thermal conductivity of liquid
k_s	solid thermal conductivity
K_p	permeability
P	Pressure
Pr	laminar Prandtl number

q_o	mold heat flux
Re_t	turbulent Reynolds number based on the turbulent quantities
S_Φ	source term associated with Φ
T	temperature
T'	fluctuation of temperature
T_{in}	inlet temperature
T_l	liquidus temperature
T_s	solidus temperature
u_i	velocity component in the i-th direction; corresponding to u , v and w
\bar{u}_i	time-average velocity component in i-th direction
u'_i	fluctuation of velocity in i-th direction
u_{in}	inlet velocity
u_s	casting speed

Greek Symbols

ε	turbulent kinetic energy dissipation rate
γ	convective heat transfer coefficient
Γ_Φ	diffusion coefficient associated with Φ value
μ	laminar viscosity
μ_e	effective viscosity equal to $\mu + \mu_t$
μ_t	turbulent viscosity
Φ	generalized dependent variable
ρ	mass density
σ_l	laminar Prandtl number
σ_t	turbulent Prandtl number
$\sigma_k, \sigma_\varepsilon$	empirical constants in turbulent model equations

References

- Aboutalebi M. R., Hasan M. and Guthrie R. I. L. Physical and numerical simulations of turbulent flow and inclusions distribution in the mold region of a slab caster, *Canadian Metallurgical Quarterly*, MS # M2439, Accepted for publication (Aug. 1996).
- Aboutalebi M. R., Hasan M. and Guthrie R. I. L., Numerical study of coupled turbulent flow and solidification for steel slab casters, *Numerical Heat Transfer: Part A*, Vol. 28, 279-297, (1995a).
- Aboutalebi M. R., Hasan M. and Guthrie R. I. L., Coupled turbulent flow, heat, and solute transport in continuous casting processes, *Metallurgical & Materials Trans.*, Vol. 26B, 731-744, (1995b).
- Asai S. and Szekely J., Turbulent flow and its effects in continuous casting, *Ironmaking and Steelmaking*, Vol. 3, pp. 205-213, (1975).
- Bennon W. D. and Incropera F. P., A continuum model for momentum, heat and species transport in binary solid-liquid phase change systems-I. model formulation, *Int. J. Heat Mass Transfer*, Vol. 30, No. 10, pp. 2161-2170, (1987).
- Brimacombe J. K. and Weinberg F., Continuous casting of steel - Part 2 Theoretical and measured liquid pool profiles in the mold region during the continuous casting of steel, *J. Iron Steel Inst.*, Vol. 211, No. 1, pp. 24-33, (1973).
- Choudhary S. K. and Mazumdar D., Mathematical modelling of transport phenomena in continuous casting of steel, *ISIJ International*, Vol. 34, No. 7, pp. 584-592, (1994).
- Choudhary S. K. and Mazumdar D., Mathematical modelling of fluid flow, heat transfer and solidification phenomena in continuous casting of steel, *Steel Research*, Vol. 66, No. 5, pp. 199-205, (1995).
- Davies R., Blake N. and Campbell P., Solidification modelling - an aid to continuous casting, *Proc. Verlag Stahleisen*, pp. 645-654, (1988).
- Flint P. J., A three-dimensional finite difference model of heat transfer, fluid flow and solidification in the continuous slab caster, *Steelmaking Conference Proceedings*, pp. 481-490, (1990).

- Huang X., Thomas B. G. and Najjar F. M., Modelling superheat removal during continuous casting of steel slabs, *Metall. Trans.*, Vol. 23B, pp. 339-356, (1992).
- Lait J. E., Brimacombe J. K. and Weinberg P., Mathematical modelling of heat flow in the continuous casting of steel, *Ironmaking Steelmaking*, Vol. 2, pp. 90-97, (1974).
- Lally B., Biegler L. and Henein H., Finite difference heat transfer modelling for continuous casting, *Metall. Trans.*, Vol. 21B, pp. 761-770, (1990).
- Lauder B. E. and Sharma B. I., Application of the energy dissipation model of turbulence to the calculation of flow near a spinning disc, *Letters in Heat and Mass Transfer*, Vol. 1, pp. 131-138, (1974).
- Minakawa S., Samarasekera I. V. and Weinberg F., Centerline porosity in plate castings, *Metall. Trans.*, Vol. 16B, pp. 245-255, (1987).
- Patankar S.V., *Numerical Heat Transfer and Fluid Flow*, Hemisphere/McGraw-Hill, Washington, (1980).
- Savage J. and Pritchard W. H., The problem of rupture of the billet in the continuous casting of steel, *J. Iron Steel Inst*, Vol. 178, pp. 267-277, (1954).
- Seyedein S. H. and Hasan M., A three-dimensional simulation of coupled turbulent flow and macroscopic solidification heat transfer for continuous steel slab casters, *Int. J. Heat Mass Transfer*, MS #IJ96/6498 (in press, Feb. 1997).
- Thomas B. G., Mika L. J. and Najjar F. M., Simulation of fluid flow inside a continuous slab-casting machine, *Metall. Trans.*, Vol. 21B, pp. 387-400, (1990a).
- Thomas B. G., Najjar M. F. and Mika L. J., The removal of superheat from continuous casting moulds, *F. Weinberg Int. Symp. on Solidification Processing, 29th CIM Conference, Hamilton*, pp. 131-145, (1990b).

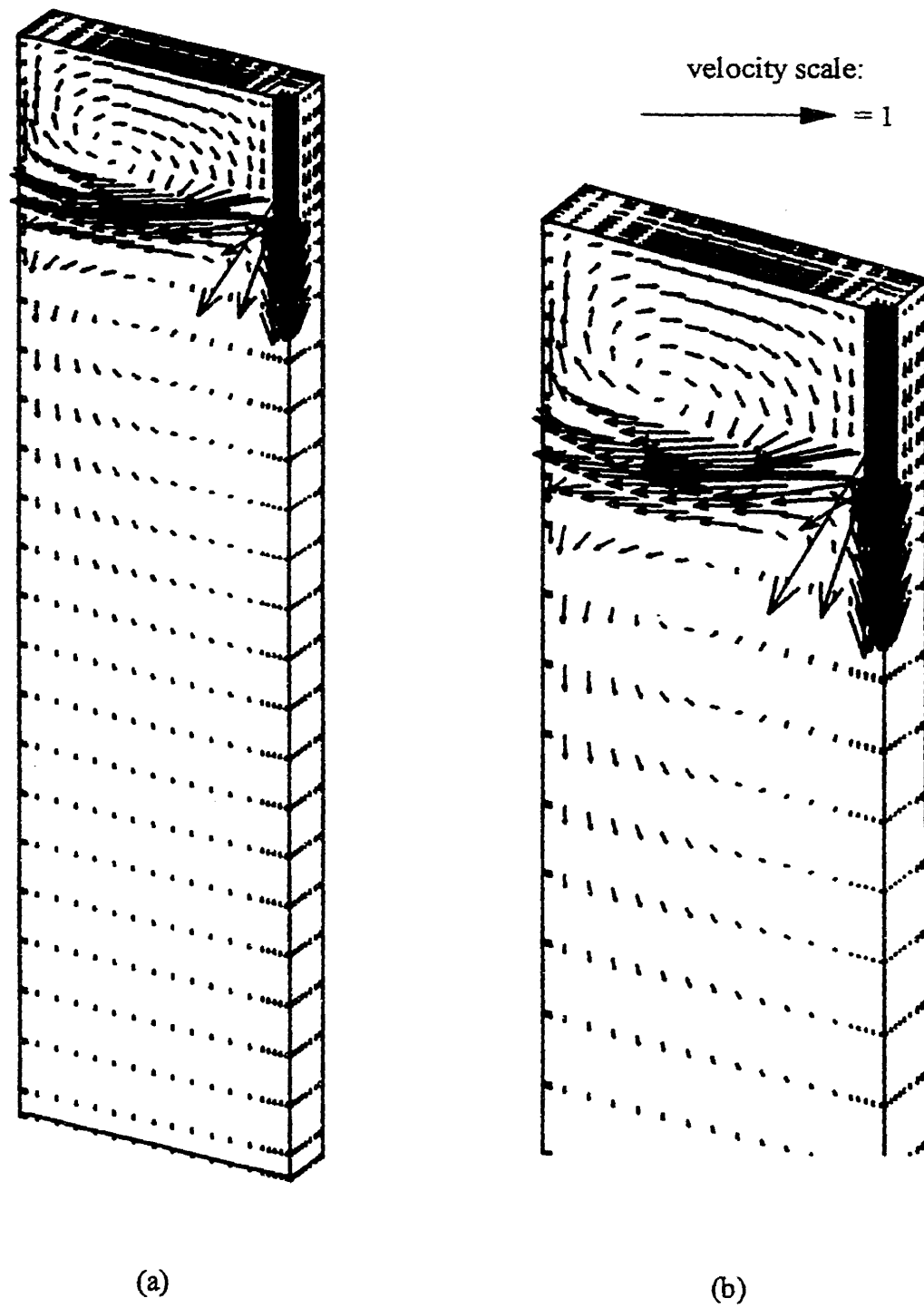


Fig. 3.1. 3-D surface plot of the velocity vectors for a casting speed of 0.015 m/sec , 26°C superheat and $\gamma = 1.1\text{ kW/m}^2\text{K}$ (type A B.C.); (a) the complete solution domain, (b) enlarged view of the top domain.

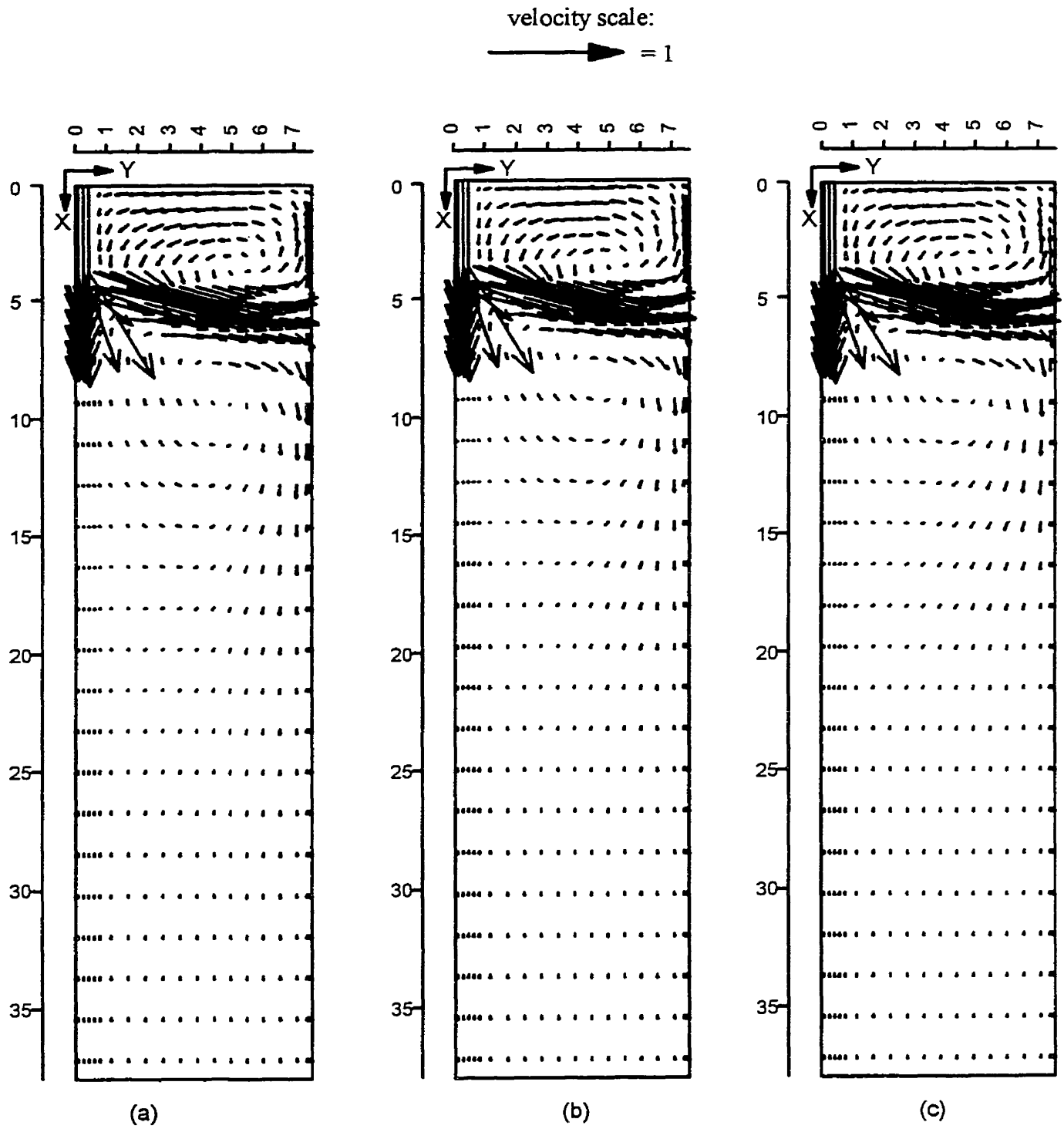


Fig. 3.3. Computed results of velocity vectors at the vertical centrally symmetric plane paralleled to the wide face for a casting speed of 0.015 m/sec , 26°C superheat and various thermal boundary conditions at the mold walls; (a) type A, (b) type B, and (c) type C.

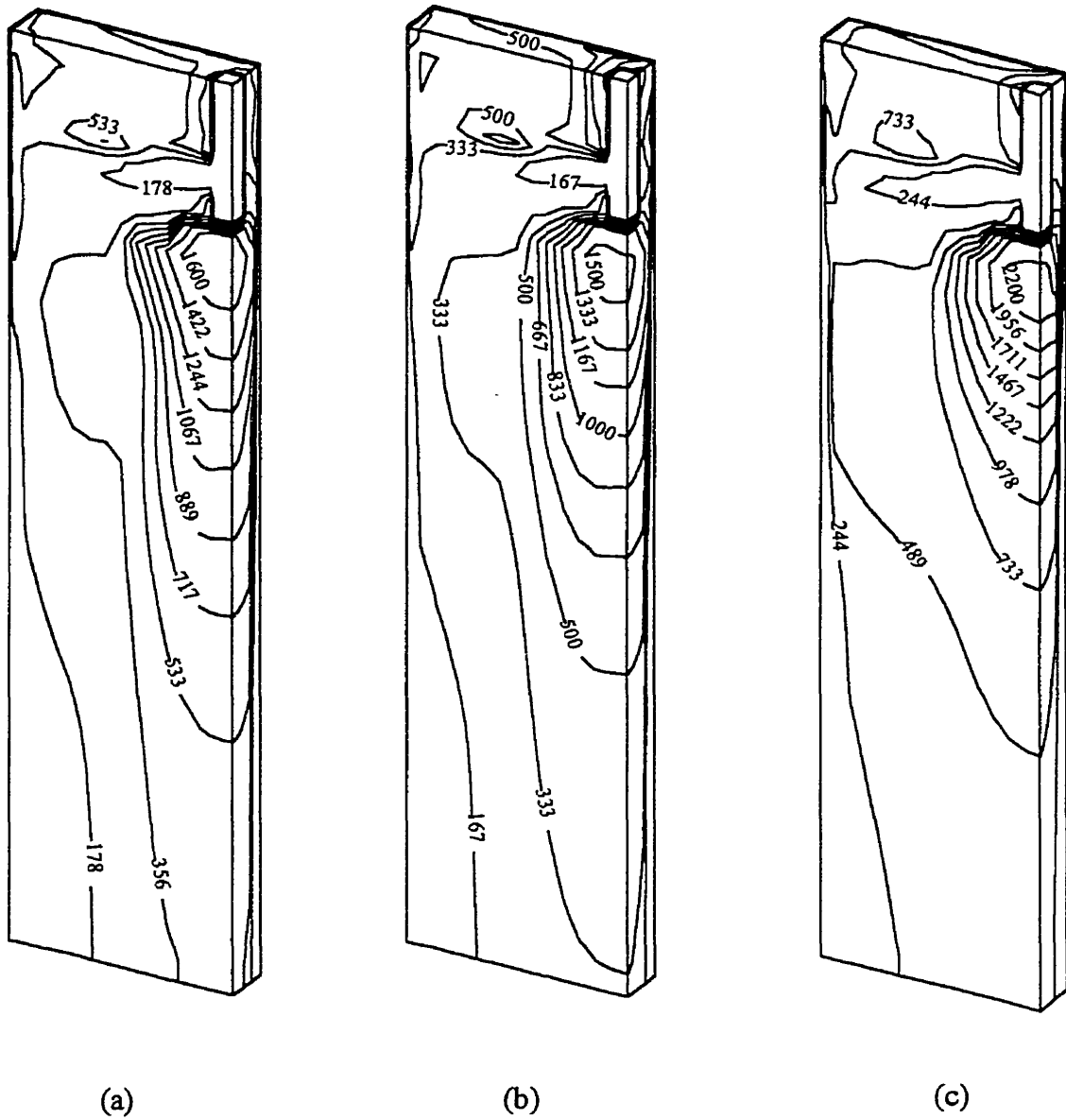


Fig. 3.4. 3-D surface contour plot of non-dimensional turbulent viscosity for a casting speed of 0.015 m/sec and 26°C superheat and various thermal boundary conditions at the mold walls; (a) type A, (b) type B, and (c) type C.

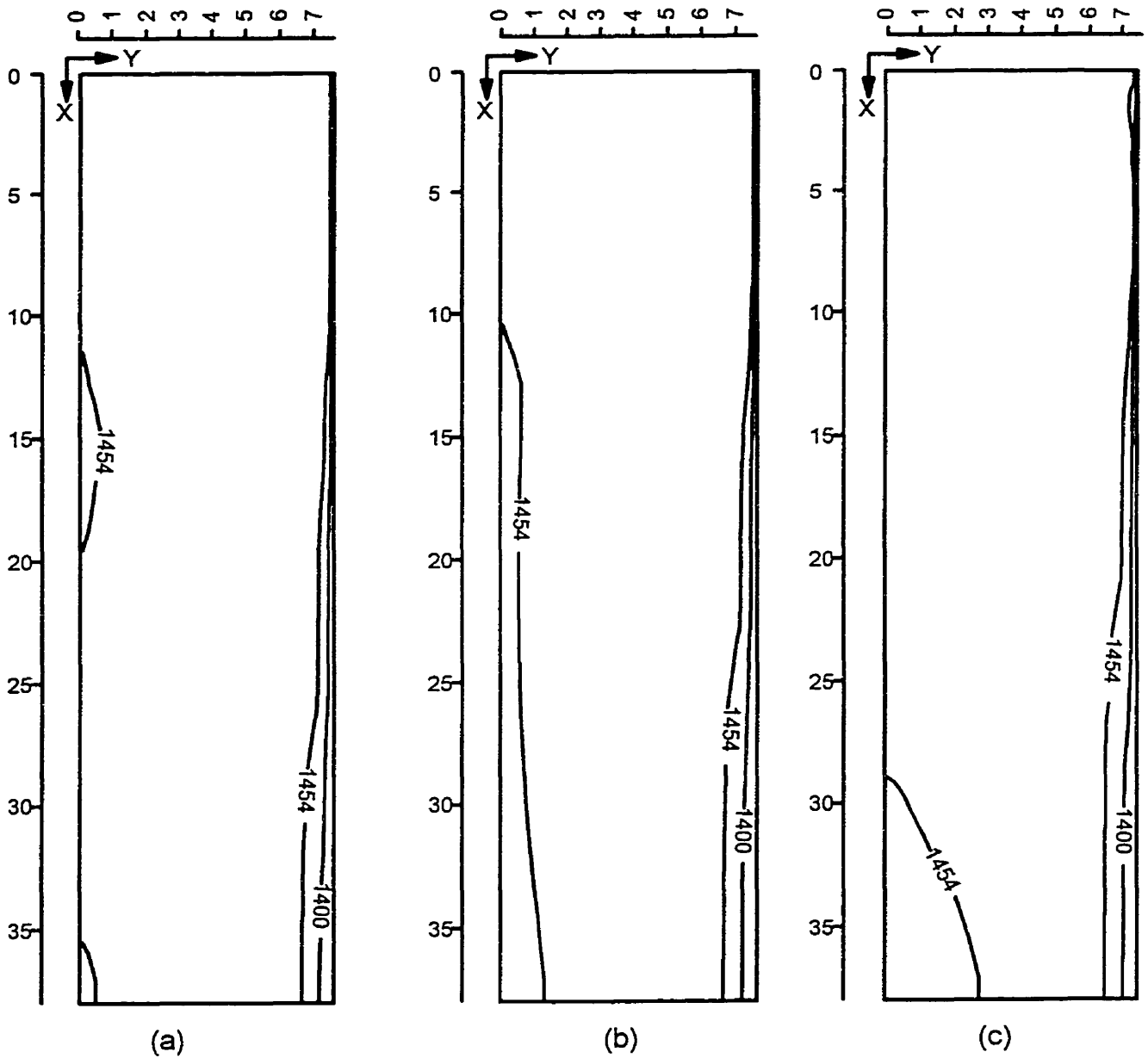


Fig. 3.5. Contours of solidus and liquidus temperatures at the vertical centrally symmetric plane paralleled to the wide face for a casting speed of 0.015 m/sec , 26°C superheat and various thermal boundary conditions at the mold walls; (a) type A, (b) type B, and (c) type C.

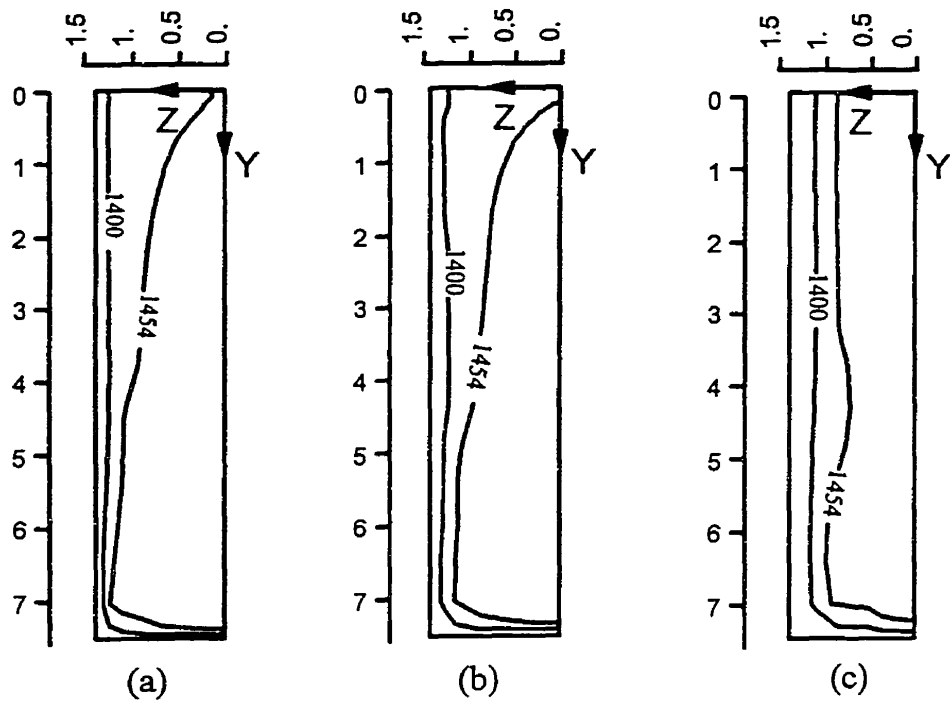


Fig. 3.6. Contours of solidus and liquidus temperatures for a transverse cross-sectional plane (Y-Z plane) at the exit of the mold for three types of thermal boundary conditions at the mold walls; (a) type A, (b) type B, and (c) type C.

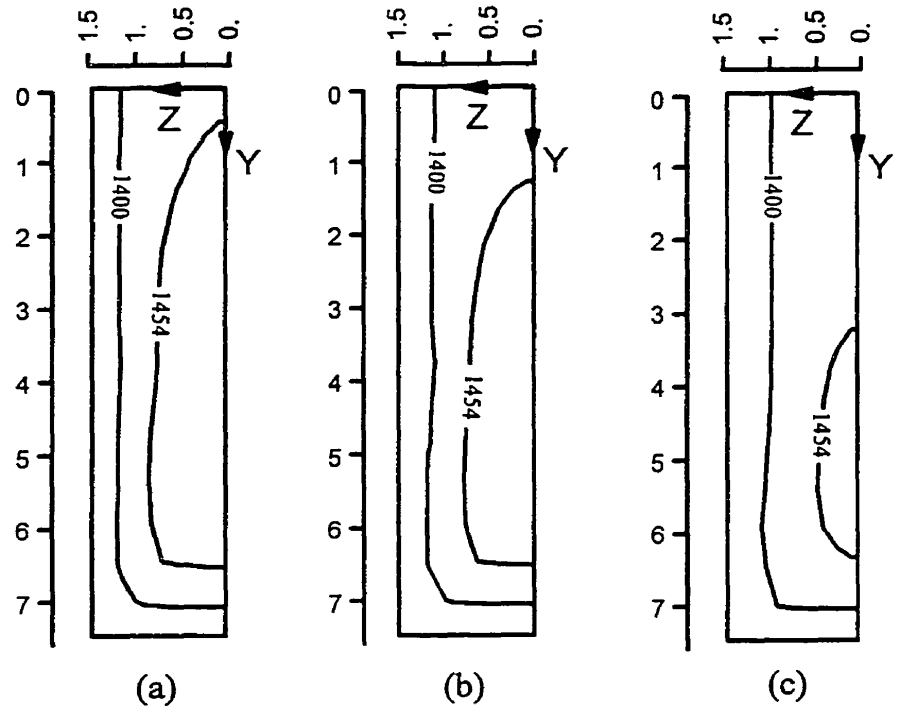


Fig. 3.7. Contours of solidus and liquidus temperatures for a transverse cross-sectional plane (Y-Z plane) at the exit of the submold region (3m below meniscus) for three types of thermal boundary conditions at the mold walls; (a) type A, (b) type B, and (c) type C.

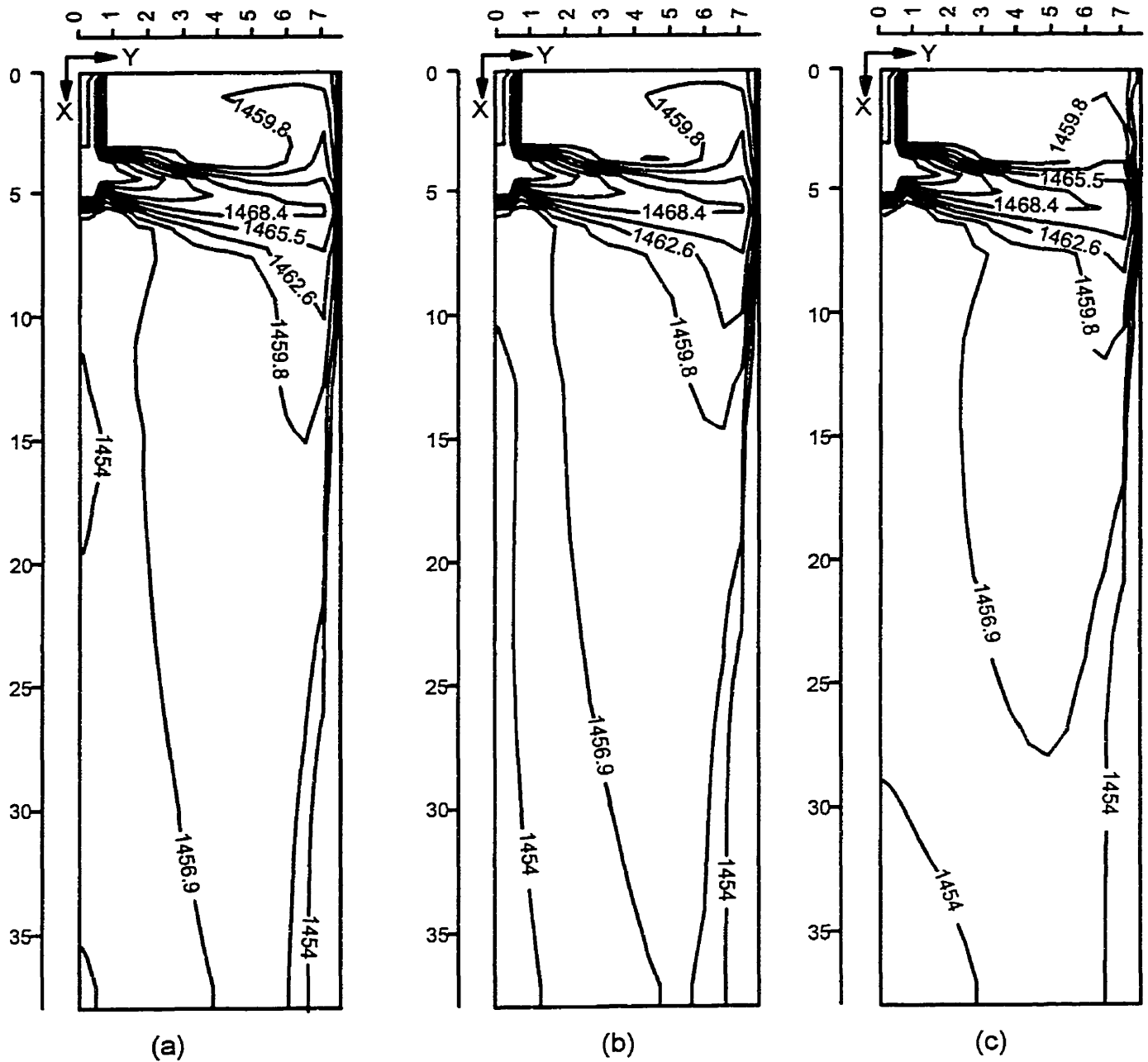


Fig. 3.8. Superheat temperature contours at the vertical centrally symmetric plane paralleled to the wide face for a casting speed of 0.015 m/sec , 26°C superheat and various thermal boundary conditions at the mold walls; (a) type A, (b) type B, and (c) type C.

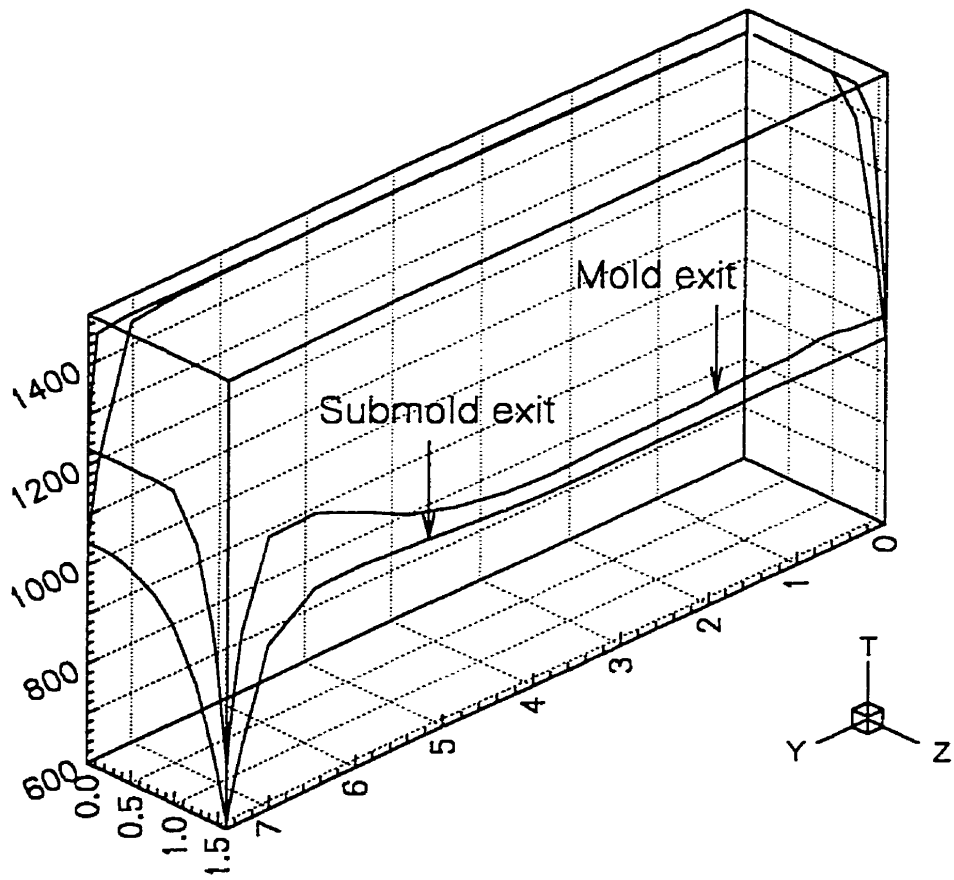


Fig. 3.9. Computed surface temperatures for the transverse planes at the exit of the mold and submold regions for type A thermal boundary condition.

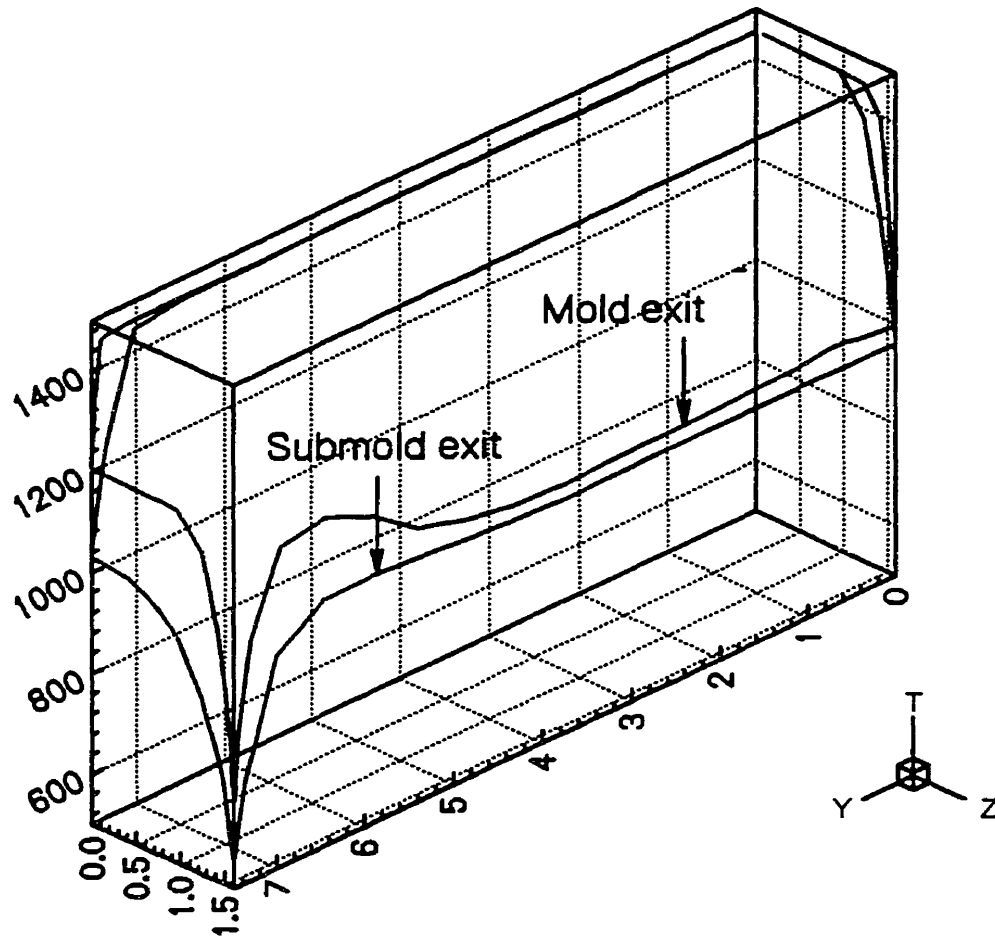


Fig. 3.10. Computed surface temperatures for the transverse planes at the exit of the mold and submold regions for type B thermal boundary condition.

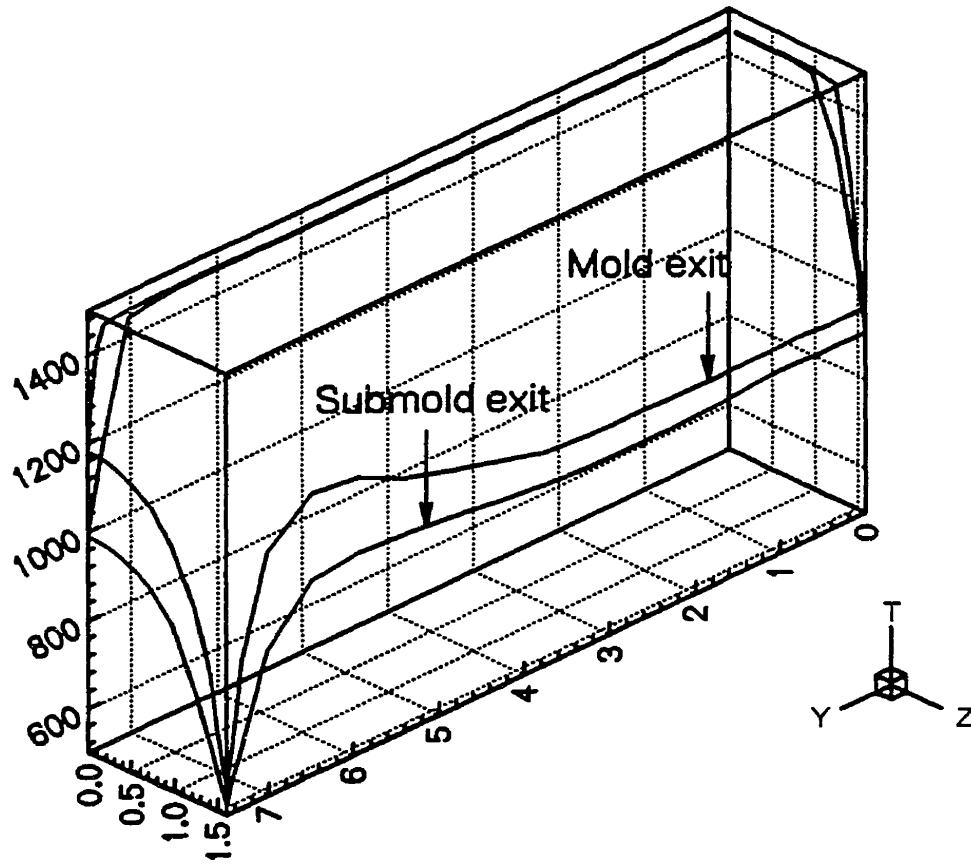


Fig. 3.11. Computed surface temperatures for the transverse planes at the exit of the mold and submold regions for type C thermal boundary condition.

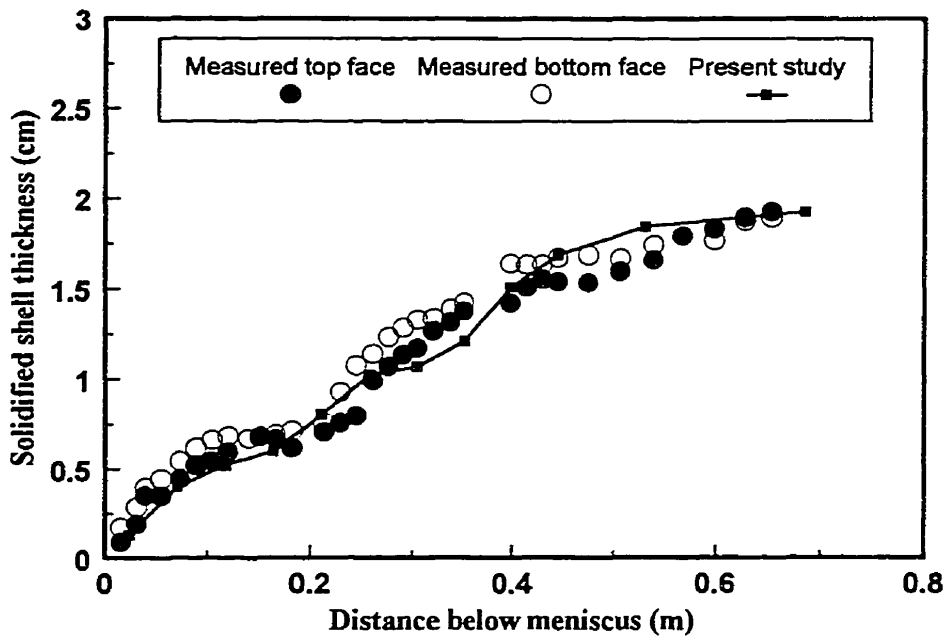


Fig. 3.12. Comparison of solidified shell thickness predicted in this study (type B thermal boundary condition used) with experimental data from Lait et al. (1974).

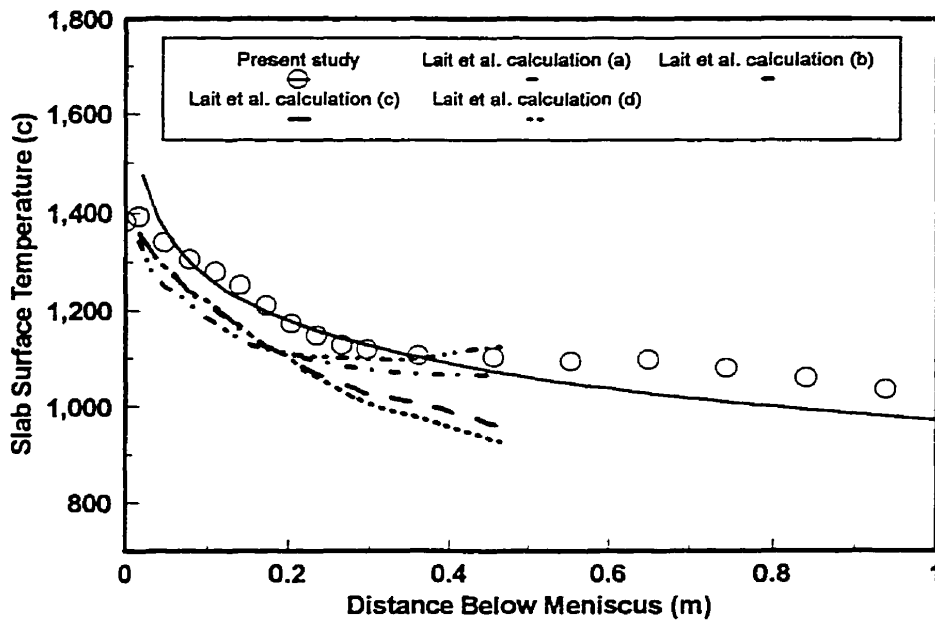


Fig. 3.13. Comparison of the predicted surface temperature profile with Lait et als' various one-dimensional models' predictions.

THE EFFECT OF DC MAGNETIC FIELD ON THE 3-D FLOW, HEAT TRANSFER AND SOLIDIFICATION IN THE CONTINUOUS CASTING MOLD

4.1 Introduction

Improvement of the performance of continuous casting processes has been a subject of extensive research in the metallurgical industry. The high-speed casting of the continuous casting operation is an essential objective of many of these studies, where the goal is toward improving the productivity without sacrificing the quality of the casts. However, increasing the casting speed generally results in a stronger jet flow impingement onto the narrow face of a slab and causes a thinner solid layer to develop there which may lead to a higher risk of break-out operation. In addition, it also faces disturbances of mold meniscus which give rise to the surface quality problems due to the entrapment of mold powder at the subsurface of slab. The other problem in high-speed casting is deep traveling of the inclusions in the caster which leads to the surface or internal defects caused by the entrapment of inclusions into the solidifying shell. In order to protect the solidifying shell on the narrow face of slab, prevent entrapment of undesirable substances in the solid layer and also achieve a stable meniscus level with minimum fluctuation, the fluid flow of the molten steel in the mold must be properly controlled. The progressive advances in the MHD technology and its application in metallurgy in the last decade has provided an effective way to suitably control the liquid steel flow field in the mold.

4.1.1 History of MHD

The sign of MHD comes from magnetohydrodynamics which is the name of the new branch of science born from the merging of magnetic, or electromagnetic, and hydrodynamic sciences. Such a merge in the science can be seen in other fields of sciences like astrophysics, physical chemistry, biochemistry and biomechanics. MHD usually is defined as the science which deals with the motion of electrically conducting fluids through the magnetic fields, or more generally, continuum mechanics of electrically conducting fluids in the presence of magnetic fields.

Typically the phenomena involving the MHD science can be classified into two parts. The first part deals with the generation of induced magnetic field and its interaction with imposed magnetic field and the second part discusses the motion of electric charge and electrically conduction fluid in the combined magnetic field.

The studies related to MHD were initiated with experiments that were carried out during the second and third decades of the 19th century. The report presented by Faraday (1832) may be considered among the first attempts in this field of science. The idea behind his experiment has been advanced to the modern MHD velocity meter or flow meter. His idea was also used as a basis for development of the MHD pump. An MHD pump is a device which converts the electrical energy of the current supplier into the mechanical energy of the pumped liquid. The basis of the MHD pump is to apply an electric field to a conducting fluid which is located in a magnetic field. If the electric field is perpendicular to the magnetic field it pumps the fluid in a direction perpendicular to both fields. Since the principle of the MHD generator is similar to that of the MHD pump, the idea of power generation using MHD was pursued.

The first attempt related to the theoretical study of MHD processes, particularly MHD flows in ducts, was made by Williams (1930). Even though the importance of MHD was demonstrated long ago, the serious theoretical studies related to MHD started in the 1950's, e.g. Alfven (1950). Thereafter, the application of MHD was gradually extended to the thermonuclear fusion reaction, plasma physics and activities related to the space travel. Metallurgy and casting have also benefited the results obtained from MHD research.

Nowadays, there are many metal processing operations where the overall process kinetics are considerably influenced by an electromagnetically driven flow field.

The metallurgical systems with electromagnetically driven recirculating flow field may be divided broadly into two categories: one where the electromagnetic force is generated by the passing a current between two electrodes immersed into a metallic melt, and the other where the field is produced by induction. The systems which can be considered in the first category have many industrial applications, such as smelting, electroslag refining, welding, arc furnace operation, etc. The development of the new electrodes with high melting points and electrical conductivities have enabled the materials processing industries to impose electric current directly on metals having high melting points. The second category in which the electric current induced by magnetic field produces electromagnetic force field has been mainly adopted in metal industries for electromagnetic pump, electromagnetic stirring in steel making, electromagnetic brake and stirring in the continuous casting systems, etc. Now, it has been recognized that the MHD phenomena can be effectively used to control the flow of molten metal without any direct contact with them and also to change the flow-velocity distributions for better mixing control and heat transfer. It has also been found that the application of MHD in continuous casting systems improves the surface quality of cast steel by homogenizing the meniscus temperature, stabilizing initial solidification and cleaning the surface layer. In addition, it also improves the internal quality of cast steel by preventing inclusions from penetrating deep into the pool and promoting the flotation of argon gas bubbles.

Among the various usage of magnetohydrodynamics relevant to the continuous casting processes, one can find in the commercial literature two types of applications. They are: (a) in-mold electromagnetic stirring, and (b) in-mold electromagnetic braking.

4.1.2 In-mold Electromagnetic Stirring

A typical continuous casting system with an in-mold electromagnetic stirrer is equipped with a linear motor installed in the wide face of the upper part of the water-cooled mold. The function of the linear motor is to horizontally recirculate molten steel

near the meniscus surface. This function can be achieved by imposing a traveling magnetic field in the range of 10 Hz which covers the full width of the mold. The efficiency of the electromagnetic stirring is critically dependent on the frequency of the traveling magnetic field and the distance between the linear motor and the meniscus.

4.1.3 In-mold Electromagnetic Braking

A typical in-mold electromagnetic braking technique uses a localized or level DC magnetic field to directly brake the flow of the molten steel discharging from the submerged entry nozzle. Various configurations of local or level DC magnetic fields have been proposed for braking or controlling of flow in the continuous casting molds. While reviewing the applications of the MHD technology to the continuous casting of steel slabs, Takeuchi (1995) reported that the technique of localized magnetic field faces problems related to the stability of the braking effect.

4.1.4 Principle of MHD Phenomena

For a better understanding of the general principle of the MHD brake, assume that we have an electrically conducting fluid which is moving in a channel having an imposed DC magnetic field as shown in Fig. 4.1. The interaction of fluid motion and magnetic field generates an induced electrical current in the direction perpendicular to the plane of velocity and magnetic field, i.e. y-direction. If no current is imposed in the other directions, i.e. x or z-direction and if the induced current in the fluid are taken to form closed loops lying in x-y planes with the axis in z-direction, then an induced magnetic field is produced acting in z-direction due to these currents. It is noted that in complicated cases, the induced current and magnetic field may contain components in all three directions. Now, the induced currents that cross the imposed and induced magnetic fields at right angles act as electromagnetic forces on the fluid. The force generated due to the imposed magnetic field is in the flow direction, i.e. z-direction, while the force created by the induced magnetic field acts in the x-direction and for this especial case influences the

boundary layer. The total electromagnetic force is called Lorentz force and its magnitude and direction can be obtained from the cross product of the current density and the magnetic field density.

$$\text{Lorentz force} = \mathbf{J} \times \mathbf{B} \quad (4.1)$$

The Lorentz force may oppose the fluid stream and can act as a braking force.

4.2 Literature Review

Although, there are numerous experimental and numerical studies related to general MHD flows, in this section a brief overview of the literature concerning modeling of MHD flows in metallurgical processes involving either turbulent or phase-change phenomena is given.

Murthy et al. (1988) experimentally and numerically studied the effect of the passage of a DC current between two electrodes immersed into a heated liquid metal on the velocity field and turbulent parameters. They obtained the electromagnetic force and flow fields through the solution of Maxwell's equations along with the turbulent Navier-Stokes equations. The authors then examined three different turbulent models; two variants of the $k - \varepsilon$ model as well as a mixing-length type model. They showed that the velocity fields predicted by all of these turbulent models were in good agreement with the measured data. Due to the large discrepancy in the prediction of turbulent parameters by these models, the authors stated that the selection of an appropriate model for heated liquid metal systems is difficult.

Saluja et al. (1990) carried out numerical simulations of fluid flow phenomena due to the electromagnetic stirring in a cylindrically shaped laboratory scale continuous casting system. One of the parameters which was extensively investigated in this work was the effect of alternating stirring frequency in the molten metal stream. They designed three different cases of stirring based on the switching frequency of the electromagnetic stirring and the direction of stirring. In this study, the free surface deformation of the melt was also predicted for a case with continuous electromagnetic stirring. In terms of the

mathematical modeling, the turbulent motion of the melt was characterized using the $k - \epsilon$ standard high-Re turbulent model. The turbulent kinetic energy was modified to take into account turbulence enhancement due to electromagnetic effects. The source term, which was added to the turbulent kinetic energy equation due to the electromagnetic effect, was estimated from the spectral theory of turbulence and is said to be applicable for magnetohydrodynamic processes with traveling magnetic field. However, its benefit is doubtful and has not yet been proven in the literature.

In 1993, Prescott and Incropera performed a 2-D numerical study on the magnetically damping fluid convection during the solidification of a binary metal alloy. The material used in their solidification study was Pb-19 pct Sn alloy. The liquid alloy stream was damped by the application of various constant external magnetic fields providing a Lorentz damping force on the fluid. They considered only the radial damping force, which was expressed as $F = -\sigma_e B^2 v$, having a constant magnetic field. The macrosegregation phenomena was also investigated in this study by incorporating solute transport equation into the mathematical formulation. Later, they (1995) advanced their modeling formulation by taking into account turbulent behavior of the liquid metal flow and electromagnetic stirring. The electromagnetic stirring was achieved by applying a time-varying magnetic field into the process and the Lorentz force was obtained through magnetic stirring. This force was characterized based on the magnetic field density frequency and the axial phase variation, i.e. wave number. The turbulent motion was modeled using a low-Re $k - \epsilon$ turbulent model. In this study, it seems that the low-Re $k - \epsilon$ proposed by Jones and Launder (1973) has been applied, however it is not clear why the associated source terms in the turbulent kinetic energy and energy dissipation rate equations have been eliminated. Very recently, Prescott et al. (1996) performed a set of experiments to investigate the effect of strength and direction of a traveling magnetic field on convection and macrosegregation during solidification. They found that electromagnetic stirring significantly affects the temperature distribution in favor of well mixed melt. Their experiments also revealed that the location of the initial solidification

and the degree of macrosegregation in the solidified ingot can be modified by changing the stirring direction.

Fireteanu and Gheysens (1994) modeled a new device, called the electromagnetic valve, for controlling the molten metal stream from the tundish to the mold. They studied the effect of the supply frequency and inductor pole pitch on the imposed limits of flow rate and the liquid jet characteristics, however they assumed that the fluid velocity has only one component in the longitudinal direction. Since the idea of electromagnetic valve for flow control in the shroud is a new concept and is presently at the trial stage, this study can be considered as the first step in the modeling of this subject which is required to be advanced by taking into account the other involving aspects such as 2D or 3D nature of the fluid flow and turbulent effects.

The numerical study carried out by Dutta et al. (1995) combined three-dimensional fluid flow modeling and phase-change phenomena for the thermal modeling of Gas Tungsten Arc Welding (GTAW) process. The liquid melt in the weld-pool was assumed to be driven by both buoyancy and Lorentz forces and the phase-change phenomenon including melting and solidification was treated based on the well-known enthalpy-porosity approach. The numerical procedure developed in their study is capable of simulating the moving arc over a rectangular plate. However, it can be only extended to the other similar processes having a laminar flow behavior.

Zhang et al. (1996) simulated the 2D steady-state flow of an Al-melt in a centrifugal casting process having an electromagnetic stirring system. They used stream-function and vorticity as the dependent variables for fluid flow calculations and solved numerically the momentum equations using a finite difference approach. They tested different values of the controlling parameters such as rotation rate and magnetic flux density. All computations were carried out for an Al-melt for temperatures higher than the melting point. Their study does not reflect the effect of solidification on the fluid flow patterns. A similar study was carried out by Li (1995) for modeling the production of aluminum in a tubular form. He used a commercial software, FIDAP, which is based on finite element method, for 2D simulations of turbulent flow in the pool, and used volume integral method for obtaining electromagnetic field distributions. He employed the high-Re

$k - \varepsilon$ turbulent model for prescribing turbulent properties. This study was performed for a single liquid phase and the shape of the liquid pool and the liquid-solid interface were arbitrarily fixed in advance, thereby eliminating inflow and outflow conditions. This modeling approach over simplified the actual process and yielded unrealistic results.

It seems that the studies reported by Washio et al. (1993) and Idogawa et al. (1993) are among earlier numerical reports for controlling molten flow in the continuous slab casting mold. Both of these studies were carried out in Kawasaki Steel Corp. Research laboratories in Japan. The purpose of these studies was directed towards the controlling of molten steel flow into the mold for solution of the problems such as entrapment of mold powder and argon gas bubbles at the surface of the slab during the high speed continuous casting processes. In both of these works, the molten steel flow discharged through immersed nozzle was controlled using an electromagnetic brake (EMBR) technology based on imposed D.C. magnetic fields. In Kawasaki's flow control design two pairs of magnetic poles were considered; one close to the meniscus surface (upper poles) for stabilizing the mold level and preventing powder entrapment, and another under the nozzle port for decreasing the flow speed in the mold for better flotation of inclusions and argon gas bubbles. In the former study (Washio et al. 1993), the authors conducted a set of experiments which showed that the application of the flow control in the mold results in the reduction of both average meniscus velocity and its fluctuation. Moreover, an increase in the amount of argon gas percentage close to the submerged entry nozzle and also a reduction in the gas fraction near narrow face of the slab led to the improvement in the problem of gas entrapment at the slab surface. The latter work (Idogawa et al. 1993) predicted the fluid flow field obtained from the numerical simulation of the continuous slab caster model with a flow control system. This numerical simulation was associated with the previous experimental study. Although, in a real continuous casting process, the presence of the solidified shell and accompanying mushy layers does affect the fluid flow pattern, this aspect was altogether neglected in their simulation. While, in this work the authors mentioned that the turbulence can be considered using the $k - \varepsilon$ model, it is not clear how and which version of this model was

implemented, especially the given formulations which express the laminar flow phenomena.

Similar numerical and experimental studies were carried out by Kollberg et al. (1996). The flow control mold examined in their study was the one developed by ABB. The ABB flow control mold was implemented for slab and thin slab casters with minimum thickness of 0.05 m, 1.3-2.1 m width and 1.3 to 5 m/min casting speed. Their reported experimental data for the case with shallow depth of the submerged nozzle showed an increase in the temperature of hot steel just below meniscus in the range of 6 to 10 °C, which is due to the combined effects of the magnetic field and the argon gas injection. The numerical simulation part of this work was carried out using a commercial software "FLOW3D". From the computer simulation runs they presented only the results of inclusion trajectories and velocity variations with time at the meniscus surface, which supported the experimental observations with respect to the cast quality.

The numerical study presented by Gardin et al. (1995) considered a flow-control mold equipped with two pairs of induction poles centered at 0.415 m under the meniscus surface and located at either side of the feeding submerged nozzle. They applied both argon gas bubble and electromagnetic braking to the caster and solved the governing equations using the commercial CFD code, "PHOENICS". The equations governing the motion of the liquid steel were written for the laminar flow condition, however the effective diffusivities used for gas volume fraction and inclusion concentration were set equal to effective kinematic viscosity of liquid steel. The latter was calculated from the standard $k - \epsilon$ turbulent model. In their model, they did not take into account the solidification of steel and they solved the energy equation for superheat temperature distribution only. They found that the application of the electromagnetic brake leads to an increase in the meniscus temperature, except near the narrow face.

Lehman et al. (1996) also carried out a numerical study at ABB industrial systems (Germany) to provide insight into the influence of electromagnetic braking exerted on the behavior of the metal flow in the mold. Three different configurations of the electromagnetic brake were selected in their parametric study; one with two magnetic fields placed and acted locally across the strand width, the second one with one magnetic

field covering the entire strand width, and the third one with two parallel magnetic fields along the entire strand width; one above and one below the nozzle ports. Although they did not mention the method of modeling, they concluded that upon application of the magnetic field across the entire width of the strand one can prevent deeper penetration of the inclusions compared to the conventional caster with locally placed magnetic field. In addition, they reported that the electromagnetic brake with two parallel magnetic fields is advantageous since their arrangements can lead to the smaller reduction in the average velocity at the meniscus and hence facilitates and maintains the steel flow from the narrow face towards the center of the strand.

The use of the electromagnetic field has recently been advanced to the new and innovative continuous casting process for clad steel slabs. Zeze et al. (1996) proposed a new process in which the mixing of two different molten steels in the mold pool of the continuous caster was suppressed with a level D.C. magnetic field (LMF). In their practice, two compositionally different molten steels were simultaneously supplied at two positions one above and another below the LMF through two separate nozzles. They could successfully produce clad steels using their innovative application of the electromagnetic braking. In the numerical part of their study, they modeled molten steel flow in the pool of a continuous caster in the presence and absence of LMF. The predicted results in this study clearly showed the effect of LMF in separating two molten steel flows in the process.

Today, the electromagnetic flow control is under study to be used as a confinement device instead of the side dams for twin-roll casting processes (Furuhashi and Asai 1994).

As seen from the above literature review, mathematical modeling can play an important role in understanding the various phenomena involving the continuous casting processes. Although the phase-change phenomenon and development of the mushy layer in the continuous casting system can considerably change the flow pattern in the caster, most of the previous studies related to the application of EMBR in such systems did not consider this aspect in their modeling of the process. The objective of the present work is

to develop a 3-D numerical code for the simulation of various aspects of transport phenomena such as solidification heat transfer and turbulent fluid flow in the presence of in-mold electromagnetic flow control systems. This work also covers an extensive numerical study on the various configurations of imposed magnetic field applied in the continuous slab casting system. The results obtained in this study may be used to optimize the parameters affecting the flow control of molten steel in the mold.

4.3 Mathematical Formulation of MHD

The mathematical formulation of electromagnetic forces on an electrically conducting fluid has two aspects:

- 1) Electric and magnetic aspects.
- 2) Fluid-mechanics aspect.

4.3.1 Electric and Magnetic Aspects

Considering a charge particle in space, according to the electromagnetic theory, three different forces may act on it. These forces can be described as follows:

I. The force per unit of its charge due to the all other charges present, known as the electrostatic field per unit charge \mathbf{E}_s . From Coulomb's law, \mathbf{E}_s is irrotational, i.e.

$$\text{curl } \mathbf{E}_s = 0. \quad (4.2)$$

It also implies that in any region having charges

$$\text{div } \mathbf{E}_s = \frac{q}{\epsilon_0} \quad (4.3)$$

where q (coul/m^3) is net charge per unit volume and ϵ_0 is a constant value.

The other forces are due to the motion of the particle charge in the magnetic field or in its induced magnetic field as follows:

II. Magnetic force per unit of the particle charge is $\mathbf{V} \times \mathbf{B}$. This force is perpendicular to both velocity and magnetic fields.

III. The force due to the change of electromagnetic field with time being the induced electric field per unit charge \mathbf{E}_i , defined as:

$$\text{div } \mathbf{E}_i = 0 \quad (4.4)$$

and

$$\text{curl } \mathbf{E}_i = -\frac{\partial \mathbf{B}}{\partial t} \quad (\text{Faraday's law}). \quad (4.5)$$

There is another strong condition on \mathbf{B} which can be obtained from the divergence of the Faraday's law, namely:

$$\text{div } \mathbf{B} = 0. \quad (4.6)$$

Defining total electric field $\mathbf{E} = \mathbf{E}_s + \mathbf{E}_i$ leads to:

$$\text{curl } \mathbf{E} = -\frac{\partial \mathbf{B}}{\partial t} \quad \text{and} \quad \text{div } \mathbf{E} = \frac{q}{\epsilon_0} \quad (4.7)$$

and total force on a particle per unit of its charge is called Lorentz force as:

$$\mathbf{F} = \mathbf{E} + \mathbf{V} \times \mathbf{B} \quad (4.8)$$

The other important law in electromagnetic which states how the magnetic field is related to the moving charges and electric field is Ampere-Maxwell law describing:

$$\text{curl } \frac{\mathbf{B}}{\mu_0} = \mathbf{J} + \epsilon_0 \frac{\partial \mathbf{E}}{\partial t} \quad (4.9)$$

where \mathbf{J} is current density and μ_0 is permeability of free space and has a constant value equal to $4\pi \times 10^{-7}$. Taking divergence of above equation yields to:

$$\text{div } \mathbf{J} = -\frac{\partial}{\partial t} (\epsilon_0 \text{div } \mathbf{E}) = -\frac{\partial q}{\partial t} \quad (4.10)$$

So far the Lorentz force has been developed in terms of forces on particles. To find the magnetic force for electrically conducting fluid, we can consider a small element of conducting media with volume δv including positive or negative charges p with velocity \mathbf{V} and sum the particle charge over the element to get:

$$\sum p = \text{net charge in element} = q\delta v \quad (4.11)$$

and

$$\sum p\mathbf{V} = \mathbf{J}\delta v \quad (4.12)$$

Momentum equations:

In the momentum equation the accumulation and convection of momentum should be balanced by pressure gradient, viscous stress and body force including Lorentz force.

$$\frac{D(\rho \mathbf{V})}{Dt} = -\nabla P + \mu \nabla^2 \mathbf{V} + \rho \mathbf{g} + \mathbf{J} \times \mathbf{B} \quad (4.19)$$

Now, the equation required for incompressible laminar MHD flow are completed:

$$\text{curl } \mathbf{E} = -\frac{\partial \mathbf{B}}{\partial t} \quad (\text{Faraday's law}) \quad (4.20)$$

$$\text{curl } \mathbf{B} = \mu_0 \mathbf{J} \quad (\text{Ampere's law}) \quad (4.21)$$

$$\mathbf{J} = \sigma(\mathbf{E} + \mathbf{V} \times \mathbf{B}) \quad (\text{Ohm's law}) \quad (4.22)$$

$$\text{div}(\rho \mathbf{V}) = -\frac{\partial \rho}{\partial t} \quad (\text{Continuity equation}) \quad (4.23)$$

$$\frac{D(\rho \mathbf{V})}{Dt} = -\nabla P + \mu \nabla^2 \mathbf{V} + \rho \mathbf{g} + \mathbf{J} \times \mathbf{B} \quad (\text{Momentum equation}) \quad (4.24)$$

with additional conditions expressed in Eqs. (4.6) and (4.16).

Introducing scalar variable of electric potential, ϕ , with the property of $\mathbf{E} = -\text{grad } \phi$, and using divergence of Ohm's law the new equation can be found as follows:

$$\nabla^2 \phi = \text{div } \mathbf{V} \times \mathbf{B} \quad (4.25)$$

The above equation may be used for the situation in which Re_m (magnetic Reynolds number) is low and induced magnetic field is negligible compared to the imposed magnetic field. This condition implies that the magnetic field, \mathbf{B} , in the governing equation to be replaced by a known magnetic field, \mathbf{B}_0 , and to ignore the Ampere's law equation. Thus, for the constant imposed magnetic field condition the governing equations for electromagnetic field become:

$$\nabla^2 \phi = \text{div } \mathbf{V} \times \mathbf{B}_0 \quad (4.26)$$

$$\mathbf{E} = -\text{grad } \phi \quad (4.27)$$

$$\mathbf{J} = \sigma(\mathbf{E} + \mathbf{V} \times \mathbf{B}_0) \quad (4.28)$$

4.4 MHD Equations for Continuous Slab Casting

The mathematical formulation for the process of continuous slab casting (with no EMBR) based on the continuum model for binary alloy phase-change problems and the application of low-Re $k-\varepsilon$ turbulent model proposed by Launder and Sharma (1974) was presented in Chapter 3. It is worthy to mention that the dependent variable of the energy equation, mixture enthalpy, was changed to sensible energy, \bar{h} , which is identical to solid enthalpy, h_s . As a result, assuming $c_l = c_s$, the new form of the equation for the conservation of energy for the pseudo one-phase model becomes:

$$\text{div}(\rho \mathbf{V} \bar{h}) = \text{div}\left(\frac{k_m^{\text{eff}}}{c_s} \text{grad} \bar{h}\right) - \text{div}(\rho g_l \mathbf{V} L) - \text{div}[\rho g_s (\mathbf{V} - \mathbf{V}_s) L] \quad (4.29)$$

The last term appearing in Eq. (4.29) represents the energy flux associated with relative phase motion. Assuming equiaxed solidification in the mold region, which implies no relative phase motion, and ignoring the relative velocity in the columnar dendritic solidification in the submold region, the last term of the above equation can be dropped. To take into account the electromagnetic effects, the momentum and energy equations are improved by adding Lorentz force into the former one and Joule heating source term into the latter one.

$$S_{\mathbf{V},MHD} = \mathbf{J} \times \mathbf{B} \quad (4.30)$$

$$S_{h,MHD} = \frac{\mathbf{J}^2}{\sigma} \quad (4.31)$$

4.4.1 Non-dimensionalization of the MHD Parameters

The dimensionless form of the equations governing the continuous slab casting processes without EMBR were given in Chapter 2. Here, the electromagnetic equations are also nondimensionalized using the following dimensionless parameters:

$$\mathbf{B}^* = \frac{\mathbf{B}}{\mathbf{B}_0}, \quad \mathbf{J}^* = \frac{\mathbf{J}}{\sigma u_{in} \mathbf{B}_0}, \quad \varphi^* = \frac{\varphi}{u_{in} \mathbf{B}_0 D} \quad (4.32)$$

Finally, the general form of the governing equation becomes as follows:

$$\frac{\partial(U_i \Phi^*)}{\partial X_i} = \frac{\partial}{\partial X_i} (\Gamma_{\Phi}^* \frac{\partial \Phi^*}{\partial X_i}) + S_{\Phi}^* \quad i = 1, 2, 3 \quad (4.33)$$

The value of Φ^* and associated value of Γ_{Φ}^* are given in Table 4.1.

4.4.2 Boundary Conditions

The boundary conditions used for fluid flow and heat transfer in the present study are identical to those given in Chapter 3. However, the values of the average heat transfer coefficients for mold and submold walls were fixed at 1.1 and $0.6 \text{ kW/m}^2 \text{ K}$, respectively, and the associated boundary conditions for electric potential are presented below:

External faces:

The normal gradient of electric potential for all external boundaries including meniscus, inlet, mold and submold walls, and outlet were set to zero in order to ensure no electric current passing through these surfaces.

$$\frac{\partial \Phi^*}{\partial n} = 0 \quad (4.34)$$

Symmetry planes:

The symmetry boundary condition for electric potential, in contrary to the fluid flow and heat transfer boundary condition, implies that its value to be equal to zero.

$$\Phi^* = 0 \quad (4.35)$$

4.5 Solution Method

The numerical code developed for the simulation of turbulent fluid flow and macroscopic solidification heat transfer in the continuous slab casting was further extended to incorporate the solution of electric potential equation, calculation of current density and Lorentz force and coupling of electromagnetic and fluid dynamic equations. It is noted that this code was successfully checked for the prediction of turbulent fluid flow, heat transfer and solidification in the continuous slab caster without the implementation of electromagnetic field.

Table 4.1. Summary of the non-dimensional governing equations.

Equation	Φ^*	Γ_Φ^*	S_Φ^*
Continuity	1	0	0
U-momentum	U	$\frac{1}{Re}(1+\mu_t^*)$	$-\frac{\partial P^*}{\partial X} + \frac{\partial}{\partial X_i} \left(\Gamma_\Phi^* \frac{\partial U_i}{\partial X} \right) - \frac{A^*}{Re}(U-U_s) + N(J_y^* B_z^* - J_z^* B_y^*)$
V-momentum	V	$\frac{1}{Re}(1+\mu_t^*)$	$-\frac{\partial P^*}{\partial Y} + \frac{\partial}{\partial X_i} \left(\Gamma_\Phi^* \frac{\partial U_i}{\partial Y} \right) - \frac{A^*}{Re}(V-V_s) + N(J_z^* B_x^* - J_x^* B_z^*)$
W-momentum	W	$\frac{1}{Re}(1+\mu_t^*)$	$-\frac{\partial P^*}{\partial Z} + \frac{\partial}{\partial X_i} \left(\Gamma_\Phi^* \frac{\partial U_i}{\partial Z} \right) - \frac{A^*}{Re}(W-W_s) + N(J_x^* B_y^* - J_y^* B_x^*)$
Kinetic energy	k^*	$\frac{1}{Re} \left(1 + \frac{\mu_t^*}{\sigma_k} \right)$	$\frac{G^*}{Re} - \varepsilon^* + \frac{D_k^*}{Re}$
Rate of energy dissipation	ε^*	$\frac{1}{Re} \left(1 + \frac{\mu_t^*}{\sigma_\varepsilon} \right)$	$\frac{1}{Re} f_1 C_1 G^* \frac{\varepsilon^*}{k^*} - C_2 f_2 \frac{\varepsilon^{*2}}{k^*} + \frac{E_\varepsilon^*}{Re^2}$
Energy	h^*	$\frac{1}{Re} \left(\frac{1}{Pr} + \frac{\mu_t^*}{\sigma_t} \right)$	$-\left(\frac{\partial U \Delta H^*}{\partial X} + \frac{\partial V \Delta H^*}{\partial Y} + \frac{\partial W \Delta H^*}{\partial Z} \right) + N \frac{u_{in}}{\Delta H_f} \mathbf{J}^2$
Electrical potential	ϕ^*	1	$div(\mathbf{V} \times \mathbf{B})$

where:

$$G^* = \mu_t^* \left(\frac{\partial U_i}{\partial X_j} + \frac{\partial U_j}{\partial X_i} \right) \frac{\partial U_i}{\partial X_j}, \quad D_k^* = 2 \frac{\partial \sqrt{k^*}}{\partial X_i} \frac{\partial \sqrt{k^*}}{\partial X_i}, \quad Re_t = Re \frac{k^{*2}}{\varepsilon^*},$$

$$E_\varepsilon^* = 2\mu_t^* \left(\frac{\partial^2 U_i}{\partial X_j \partial X_k} \right) \left(\frac{\partial^2 U_i}{\partial X_j \partial X_k} \right), \quad f_\mu^* = e^{\frac{-3.4}{(1+Re_t^*/50)^2}}, \quad \mu_t^* = Re C_\mu f_\mu^* \frac{k^{*2}}{\varepsilon^*},$$

$$N = \frac{\sigma B_0^2 D}{\rho u_{in}}, \quad A^* = \frac{C^*(1-g_i)^2}{g_i^3 + q}, \quad \mathbf{J}^* = -\nabla^* \phi^* + \mathbf{U} \times \mathbf{B}^*, \quad f_2 = 1 - 0.3 e^{-Re_t^2},$$

$$f_1 = 1, \quad C_\mu = 0.09, \quad C_1 = 1.44, \quad C_2 = 1.92, \quad \sigma_k = 1.0, \quad \sigma_\varepsilon = 1.3, \quad \sigma_t = 0.9$$

The method of solution adopted in this code is based on the control-volume based finite difference scheme. The solution domain, which is the first 3 meters of the caster, was first discretized into the control volumes as illustrated in Fig. 2.1 (Chapter 2). A staggered grid and variable arrangement was used (Fig. 2.2, Chapter 2)) in which all scalar variables such as pressure, density, turbulent quantities and electric potential were located at the center of the control volumes, while velocity components u , v and w were displaced in the x -, y - and z -direction respectively, to lie in the middle of the main control volume faces. The control volumes for solving the momentum equations were also displaced with the displacement of the velocity components. In order to resolve the velocity-pressure coupling in the momentum equations, a SIMPLE algorithm proposed by Patankar (1980) was adopted. The discretized equation as well as criterion used for converged solution are identical to those explained in Chapter 2.

4.6 Results and Discussion

For ascertaining the effectiveness of electromagnetic braking effect, calculations were conducted for a slab caster with various types of electromagnetic braking. Five different commercially used magnetic field configurations were selected and their effects on the flow field in the mold were investigated. The schematic illustration of these devices have been provided in Figs. 4.2-4.5. The type A-EMBR, which is named as localized electromagnetic braking, contains two magnetic fields located at the center of the slab; one close to the meniscus and the other one under the nozzle port (Fig. 4.2). In the second type (Fig. 4.3) which is also known as level magnetic field (LMF), one magnetic field covers the entire strand width. The position of LMF can totally change the flow distribution especially in the upper part of the mold. In type B-EMBR, the LMF is located close to the meniscus, while in type C-EMBR, the LMF is positioned under the nozzle port. The next configuration, type D-EMBR, is designed in such a way that two magnetic fields are placed close to the meniscus at either sides of the nozzle, (Fig. 4.4). This device

is usually used for stabilizing the meniscus surface. Type E-EMBR or so-called electromagnetic flow control device which is shown in Fig. 4.5, has two parallel magnetic fields covering the entire width of strand; one at the top and another at the bottom sides of the nozzle port. In the present study, the flow distributions for the above five configurations of the magnetic fields have been simulated numerically and the usefulness of each of the EMBR devices has been discussed. In order to ascertain the effects of the magnetic field density on the fluid flow pattern, additional simulation runs were carried out for type E-EMBR system for two magnetic flux densities. The contribution of the electric potential to the current density (Ohm's law) was also checked by analyzing the results obtained from a separate simulation run performed for type E-EMBR after neglecting the electric potential term in the Ohm's law equation.

The casting and electromagnetic conditions as well as the thermophysical properties of stainless steel 304 used in this simulation are given in Table 4.2.

4.6.1 Effect of Magnetic Field Configurations

Figure 4.6 shows the calculated results of the flow patterns at the wide symmetry plane as well as the paralleled planes, one at half thickness and the other near the broad face of slab caster in which no magnetic field is applied. This figure is presented as the reference for comparison of the various magnetic field designs. As seen, two recirculation loops appear in the mold which are separated by jet flow discharging from the nozzle port. However, while approaching the broad face of the slab the magnitude of velocity decreases, the upper recirculation flow is still considerable in the plane near the broad face (Fig. 4.6-c). The length of lower recirculation flow, which can affect the entrapment of inclusions in the solidifying shell, depends on the slab geometry, casting speed, nozzle design and magnetic field application. Similar results for various configurations of EMBR for analyzing the effect of magnetic field application in the mold are plotted in Figs. 4.7 through 4.11. The minimum effect of the magnetic effect was observed in type A-EMBR with two localized magnetic fields located in the nozzle area below and above the nozzle port. In type A-EMBR, the flow in the region between the nozzle and wide face of the slab reduces with the applied magnetic field, it slightly lowers the strength of the upper

recirculation loop. As a result, the magnitude of the average tangential velocity close to the meniscus surface decreases by about 35%. Also, the lower magnetic field located underneath the nozzle reduces the upward flow under the nozzle. This causes the downward velocity in the impingement area to be spread over a wider area and results in a more uniform velocity profile. Generally, due to the development of high-strength, opposite direction Lorentz force in the nozzle zone for the EMBR design such as type (A), where magnetic field crosses the submerged nozzle, a higher ferrostatic pressure would be required for maintaining the production level of the caster to a level equal to that without an EMBR.

Table 4.2. Thermophysical properties of steel, electromagnetic condition and geometrical parameters used for the simulation.

Variable	Quantities	Variable	Quantities
thermal conductivity (liquid or solid)	$31 \text{ Wm}^{-1} \text{ K}^{-1}$	electrical conductivity	7.19×10^5 $\text{kg}^{-1} \text{ m}^{-3} \text{ q}^2 \text{ s}$
specific heat (liquid or solid)	$700 \text{ Jkg}^{-1} \text{ K}^{-1}$	inlet temperature	1480° C
latent heat of fusion	264 kJkg^{-1}	solidus temperature	1400° C
magnetic flux density	$0.1\text{-}0.3 \text{ tesla}$	liquidus temperature	1454° C
nozzle port width	0.058 m	casting speed	0.02 ms^{-1}
nozzle port height	0.1 m	viscosity	$0.007 \text{ kgm}^{-1} \text{ s}^{-1}$
caster length simulated	3.0 m	density	7000 kgm^{-3}
nozzle submergence length	0.34 m	slab width	1.27 m
mold wall heat transfer coefficient	$1.1 \text{ kWm}^{-2} \text{ K}$	mold length	0.75 m
submold wall heat transfer coefficient	$0.6 \text{ kWm}^{-2} \text{ K}$	slab thickness	0.254 m

In type B-EMBR, which is equipped with a magnetic field over the entire width of the strand at the meniscus surface, the upper recirculation zone is mainly affected by the presence of the magnetic field (Fig. 4.8). Due to the suppression of the upper recirculation flow, most of the inflow is deflected downward, which may cause more inclusions entrapment into the submold of the caster. However, the increase in the upward velocity under the nozzle may help the flotation of the penetrated inclusions. In this case, the flow pattern in the near broad plane is uniform and is close to the casting speed, except at the meniscus where the flow is much weaker due to the direct effect of the imposed magnetic field.

For type C-EMBR, the flow pattern presented in Fig. 4.9 shows that the lower recirculation loop vanishes with the application of high electromagnetic field just under the nozzle port. It is also seen that the type C-EMBR causes a strong reduction in the jet velocity of liquid steel discharging from the nozzle port and consequently results in a more uniform flow in the entire cross section of the slab downstream. Although the upper recirculation loop is also affected by the magnetic fields, it is still strong and is extended to the meniscus surface as well as near the broad face of the slab.

The predicted flow pattern obtained from the application of the type D-EMBR in the caster shows almost the same flow characteristics to that of type B-EMBR (Fig. 4.10). These two types of the EMBR designs are identical except at the nozzle area where the magnetic field is excluded in type (D) design. A comparison between velocity vectors near the broad face for types (D) and (B) shows that the downward velocity close to the center of the meniscus is much higher and is closer to the casting speed in type D-EMBR than that in type B-EMBR. In general, type (D) design of flow control is preferable compared to type (B) design due to the development of only a weak Lorentz force inside the nozzle which acts against the inlet flow.

The type E-EMBR design, which is a combination of types (B) and (C), benefits from the advantages of both of the later designs. In this design, the lower recirculation zone as well as the upper recirculation zone are greatly weakened and jet flow is prevented from impinging on the narrow face of the slab (Fig. 4.11). The high reduction in

the average velocity of the liquid steel at the meniscus may also prevent the returning of the floated inclusions from the meniscus into the mold.

For a detailed study on the flow control function of various EMBR configurations, the velocity pattern for four cross-sections of the slab at different depths are plotted in Figs. 4.12 through 4.16. It is to be noted that the velocity-scale used for representing the flow at the cross-section corresponding to the impingement area is one fourth of the velocity-scale used for the other cross-sections. In all these cases, a liquid stream is found at the meniscus which flows from the narrow face of the slab towards caster. Compared to a casting process without an EMBR, it was found that the average velocity of the molten steel at the meniscus reduces for all the EMBR systems used in the present study. For a constant magnetic field density, the amount of the meniscus flow velocity reduction depends on the EMBR configuration. The highest meniscus flow reduction was found to be about 91% for type B-EMBR in which the magnetic field covers the entire width of the strand. When the nozzle area is excluded from the magnetic field, type D-EMBR, this reduction is about 85%. The comparison between the velocity fields presented in Figs. 4.15 and 4.13 shows that in type D-EMBR the molten steel flow can easily penetrate the center of slab in which there is no magnetic field imposed.

The cross-sectional flow field for type C-EMBR, presented in Fig. 4.14 indicates that the magnitude of the tangential velocity close to the narrow face of the slab reduces greatly. Thus type C-EMBR would provide a successful prevention of the impingement of jet flow to the narrow face of the slab, however the reduction of the average velocity at the meniscus is not strong and stands at around 45% of no EMBR case. The results indicating both prevention of the jet flow impingement as well as meniscus flow reduction of about 89% for type E-EMBR are presented in Fig. 4.16. It is to be noted that for both cases of (C) and (E) with magnetic field under the nozzle port, the transverse cross-sectional flow decreases significantly under the nozzle and gradually vanishes further downstream.

Figure 4.12, which shows the transverse cross-sectional flow of slab caster with type A-EMBR, reveals that when the magnetic field is located at the center of the mold, a relatively good improvement in the flow of the steel in the entire depth of the mold can be

obtained. However, when it is compared with the other types of EMBR it shows inferior effect on the overall flow pattern.

4.6.2 Effect of Magnetic Field Density

Figures 4.17 through 4.20 provide 3-D surface plots of the flow field on the meniscus, wide and narrow symmetry planes for various magnetic field densities tested in type E-EMBR. As seen from these figures, the length of the lower recirculation zone decreases with the increase of the magnetic field density, B_0 . The depth of the lower recirculation loop decreases from 1.7 m for no magnetic field to 1.1, 0.85 and 0.7 m for the imposed magnetic flux densities, of 0.1, 0.2 and 0.3 tesla, respectively. Similarly, the corresponding reduction of the average velocity of the liquid steel at meniscus for the above magnetic densities are around 62%, 83% and 89%, respectively. The impinging of the jet flow from the nozzle port on the narrow face of the slab is also weakened by increasing B_0 .

4.6.3 Effect of Electric Field Consideration

As mentioned earlier, the current density can be obtained from the Ohm's law (Eq. 4.22). In cases in which the electric current is not imposed directly to the electrically conducting fluid, the current due to the induced electric field may, in some cases, be neglected. One example in which the electric field effect was neglected is the study carried out by Prescott and Incropera (1993) on the effect of electromagnetic force on damping of the convective flow during solidification of a binary metal alloy. When the conductive current part in the Ohm's law equation is neglected, the equation for current density can be replaced by the following equation:

$$\mathbf{J} = \sigma \mathbf{V} \times \mathbf{B} \quad (4.35)$$

and electric potential equation is eliminated from the governing equations.

In the present study, a couple of extra runs were performed for analyzing the effect of the electric field intensity on the flow pattern of the slab with type E-EMBR in which the induction of electric field intensity was neglected.

Figure 4.21 shows the 3-D velocity vector at the meniscus, wide and narrow symmetry planes of the slab without effect of electric field intensity. A comparison between this figure and the corresponding results of the case with electric field intensity presented in Fig. 4.20 indicates that the liquid steel flow is almost unchanged at the meniscus. However, due to the diffusion of electric potential, according to its Poisson equation, the electric field may spread over a wider volume and affects the jet flow and impingement area. Thus, the contribution of E in J is that it increases the Lorentz force in the middle of the mold and results in a higher reduction of the magnitude of jet flow and weakening of the upper recirculation loop as well as the strength of the impingement flow.

4.6.4 Effect of Magnetic Field on Mushy Region Solidification

Figures 4.22 and 4.23 represent the developments of the solidifying shell and mushy layer along the wide and narrow faces of the slab caster at various transverse cross-sectional planes without and with type E-EMBR system, respectively. In these runs, all other casting parameters such as the casting speed, liquid steel superheat, heat transfer coefficients at the mold and submold walls were kept constant as listed in Table 4.2. A comparison between these two cases shows that for the case with EMBR, the mushy layer in the region close to the meniscus is thicker than that with no EMBR. This difference can be attributed to the effect of an upper magnetic field which causes a strong reduction in the liquid velocity at the top of the mold. The upper magnetic field also behaves like an obstacle and acts against the penetration of the liquid into the top part of the mold and consequently reduces the temperature at the meniscus surface. The reduction of the average temperature at the meniscus directly depends on the magnitude of the imposed magnetic field density. Computational results show the reduction of about 2.1, 2.7 and 3.1°C in the average meniscus temperature for 0.1, 0.2 and 0.3 *tesla* magnetic field densities, respectively. It is noted that for type C-EMBR systems in which no magnetic pole is located near the meniscus, the hot liquid steel easily recirculates at the meniscus and, contrary to the type E-EMBR, increases the meniscus temperature except near the region close to the narrow face.

In the case with no magnetic brake, a very thin layer of solidified shell as well as the mushy zone that develop on the mold walls, below the meniscus, are progressively thickened with the downward distance as more heat is extracted through the mold walls. The remelting of a part of the mushy region, especially at the narrow face of the slab further downstream, is due to the impingement of the superheated liquid steel from the inlet nozzle on to the mold wall. The side streams from this inlet flow are responsible for shifting the mushy layer in the direction of the flow. Upon the application of EMBR, the jet impingement on the narrow face of the slab is prevented and the hot liquid steel discharged from the nozzle port expands horizontally towards the wide face of the slab, (see Fig. 4.15b-c). As seen in Fig. 4.23, the horizontally expanding jet remelts the developed mushy layer on the middle half of the wide face instead of the narrow face as seen in the case with no magnetic field. Behind the nozzle port and lower magnetic poles where the effect of strongly discharged convective flow is damped, the liquid steel gradually loses its superheat and the growth of the mushy layer on the wide face resumes.

As mentioned before, one of the advantages of the EMF's application in a continuous slab casting system is the improvement in the minimum thickness of the solidifying shell at the mold exit. Figure 4.24 shows the minimum thickness of the solid shell at the mold exit at the narrow and wide faces of the slab respectively, for the caster with type E-EMBR and for the conventional caster without an EMBR. A comparison between these results shows that the minimum thickness of the solid layer at the exit of the mold, which normally locates at the narrow face of the slab, increases by increasing the magnetic flux density. However, for a higher magnetic flux density such as 0.3 tesla the location of the minimum solid shell thickness changes to the wide face of the slab. The reason for this can be attributed to the flow of the hot liquid steel close to the broad face of the slab due to the wider expansion of the inlet jet flow caused by the strong braking force.

4.6.5 Effect of Magnetic Field on Inclusion Distributions

As mentioned in Section 4.1 the application of a magnetic field in a continuous slab casting process may improve the internal quality of the cast through reduction of the

inclusion depth penetration. In order to predict the distribution of the nonmetallic inclusions in the slab caster, more sophisticated calculations have been carried out here. In this regard, a separate equation has been derived for the mass conservation of the inclusions in which the inclusions are assumed to have an identical size and spherical shape with a constant diameter. The inclusions are also considered to diffuse in the caster with the effective diffusivity equal to turbulent kinematic viscosity of the liquid metal. In addition, the slip velocity of the inclusions is presumed to be constant and has been calculated from the Stokes' law. Upon invoking the above assumptions, the continuity equation for the inclusions can be written as:

$$(u + u_{inc}) \frac{\partial C}{\partial x} + v \frac{\partial C}{\partial y} + w \frac{\partial C}{\partial z} = \frac{\partial}{\partial x} \left(D_e^c \frac{\partial C}{\partial x} \right) + \frac{\partial}{\partial y} \left(D_e^c \frac{\partial C}{\partial y} \right) + \frac{\partial}{\partial z} \left(D_e^c \frac{\partial C}{\partial z} \right) \quad (4.36)$$

where C , D_e^c and u_{inc} are normalized concentration, effective diffusivity and terminal velocity of the inclusions, respectively. The inclusion concentration is normalized based on the inlet concentration to represent C at the inlet equal to 1 and the terminal velocity of the inclusions can be obtained from the following Stokes' law relationship:

$$u_{inc} = \frac{gd^2(\rho_{inc} - \rho_f)}{18\mu_f} \quad (4.37)$$

The inclusion continuity equation, Eq. 4.36, can be solved separately with the known velocity field obtained from the fluid flow and solidification modeling simulation. To clarify the effect of magnetic field in the improvement of the inclusion distributions in the continuous casting processes, a set of runs was conducted for a typical caster with type E-EMBR and various magnetic field densities. Figure 4.25 represents the distributions of the inclusions having $280 \mu m$ diameter along the wide symmetry plane for a conventional caster without a magnetic field and the one where three different magnetic field densities are examined. In Fig. 4.25a, due to the high downward velocity along the narrow face of the slab, the inclusions travel much deeper into the caster, while braking of the fluid velocity due to the imposition of a magnetic field in the mold in effect decreases the penetration depth of the inclusions. The shape of the inclusion concentration contours in the lower part of the mold for the latter cases also show that the inclusion concentration has a higher value near the narrow face and a lower value at the center of the mold.

Basically, the upward fluid velocity developed at the middle of the mold and under the nozzle favors the inclusion flotation there and thereby decreases the concentration level. From these results, it was found that the concentration contour of 0.062 reaches to the depth of about 2.2 *m* for the conventional caster without a magnetic field and decreases to 1.25, 0.85 and 0.65 *m* for imposed magnetic field densities of 0.1, 0.2 and 0.3 tesla, respectively. Figure 4.26 displays the effect of inclusion size on their penetrations for a caster with 0.3 tesla imposed magnetic field density. A comparison between these cases shows that decreasing the inclusion size from 280 μm to 250 and 235 μm increases the penetration depth of 0.062 concentration contour to 1.6 and 2.15 *m*, respectively. The reason for this is that the reduction of the inclusion size decreases the Stokes' law velocity of the particles and reduces the inclusion removal rate through flotation. It is worthy to note that, when the Stokes' law velocity of the particle reaches to the casting speed, the present study shows an uniform concentration field equal to the inlet concentration in the entire caster. The reason for this is the fact that the upward flotation velocities of inclusions of diameter 225 μm or less are lower than that of the casting speed and hence cannot overcome the predominantly downward flow of the molten steel in the caster mold.

4.6.6 Induced Current Density and Lorentz Force

For a caster with type E-EMBR system, the induced current density and Lorentz force vectors in various surfaces parallel to the wide face of the slab are presented in Figs. 4.27 and 4.28, respectively. It is noted that both figures show dimensionless vectors, namely non-dimensional induced current density computed as $\mathbf{J}^* = \mathbf{J} / \sigma u_{in} \bar{\mathbf{B}}_0$ and non-dimensional Lorentz force calculated as $(\mathbf{LF})^* = N \mathbf{J}^* \times \mathbf{B}^*$. Two regions of high induced currents correspond to the upper and lower magnetic fields, however the magnitude of \mathbf{J}^* close to the meniscus is smaller due to the lower fluid velocity at that region. The relatively high current induced at the surface near broad plane can be attributed to the

contribution of the electrical intensity on the calculated current density through Ohm's law.

The distribution of the Lorentz force at the upper part of the mold (Fig. 4.28), which is in the opposite direction of the upper recirculating flow, clearly shows the breaking effect of the flow. Similar breaking patterns can also be seen under the nozzle port which result in a relatively uniform axial velocity field under the jet flow. This figure also shows that in type E-EMBR, which contains the top magnetic field passing through the nozzle, a very strong Lorentz force also is generated inside the nozzle which opposes the inlet steel flow. In order to avoid such undesired forces in the nozzle zone, it is better to modify type E-EMBR by excluding the nozzle area from the top magnetic field. This new system of flow control can be designed by combining type D-EMBR and type C-EMBR as shown in Fig. 4.29. It is interesting to mention that this modification does not change the velocity field significantly and only causes the high opposing force in the submerged nozzle to be eliminated. The other advantages of this modification is the possibility of using different magnetic field densities in the upper and lower poles. Therefore, by imposing a smaller magnetic field density at the upper pole, the reduction of the meniscus average temperature can be appropriately controlled.

4.7 Concluding Remarks

The three-dimensional control volume based finite-difference computer code tested and presented in the studies reported in Chapters 2 and 3 have been further developed to take into account the effect of magnetohydrodynamics phenomena in the slab casting process. This task was tackled by introducing the Maxwell's equations and their appropriate boundary conditions into the model. The phase-change phenomena modeling capabilities of the program made it possible to simulate the reciprocal effects of the MHD and solidification in the process operation. In this study, the usefulness of five different configurations of the in-mold electromagnetic braking systems for a continuous slab casting process is investigated and their effects, specifically on the flow pattern in the mold, are documented. The numerical results reveal that the effect of induced electrical

field in the electric current density is quite significant in the continuous casting operation and can not be ignored in the formulation. The predicted results also show that the length and strength of the upper and lower recirculation loops may be changed by the application of DC electromagnetic fields. In general, it is proved that the EMBR systems can be successfully used to control the molten steel flow in the mold and prevent the so-called impingement flow on the narrow face of the slab. The magnetic field located at the meniscus suppresses the upper recirculation loop and leads to the reduction of the meniscus-averaged temperature. However, the magnetic field located under the nozzle reduces the downward flow close to the narrow face and directs most of the flow to circulate in the upper part of the mold and thereby increases the average temperature at the meniscus. The quality of the cast improves due to the enhancement of the inclusion removal rate in the casters with EMBR compared to the conventional slab caster without an EMBR. This can be attributed to the reduction of the downward velocity of the liquid steel due to braking effect. The model predicts that the minimum thickness of the slab at the exit of the mold increases upon imposition of the electromagnetic field on the caster mold. This should enable the steel industries to increase the casting speed and hence the production level. In terms of the fluid flow in the mold, the caster system with EMBR design having two magnetic fields covering the entire width of the strand, one located at the meniscus and the other under the nozzle, appears to be more controllable. However, the overall performance further increases in the newly proposed EMBR system in which two magnetic fields, one acting at the top and another acting at the bottom, can be set independently with unequal magnetic flux densities.

NOMENCLATURE

Symbol	Description
A	Darcy coefficient
\mathbf{B}	magnetic flux density vector
\mathbf{B}_0	imposed magnetic flux density
a_p, a_{nb}, b	coefficients in the discretized governing equations
C_1, C_2, C_μ	empirical constants for low Reynolds turbulent models
c_s	solid specific heat
C	morphology constant
D	nozzle hydraulic diameter
D_k	extra dissipation term in k -equation
\mathbf{E}	electric field vector
\mathbf{E}_s	electrostatic part of \mathbf{E}
\mathbf{E}_i	induced part of \mathbf{E}
E_ϵ	extra generation term in ϵ -equation
\mathbf{F}	Lorentz force
f_1, f_2, f_μ	empirical constants for low Reynolds turbulent models
G	turbulent kinetic energy generation in k -equation
g_l	liquid fraction
\mathbf{g}	gravitational acceleration vector
\bar{h}	sensible heat
\mathbf{J}	current density vector
k	turbulent kinetic energy
k_m^{eff}	mixture effective thermal conductivity
$L, \Delta H_f$	latent heat of fusion
N	interaction parameter
n	normal direction to the surface

P	Pressure
p	particle charge
Pr	laminar Prandtl number
q	net charge density
Re	Reynolds number
Re_t	turbulent Reynolds number based on the turbulent quantities
S_ϕ	source term associated with Φ
u_i	velocity component in the i-th direction; corresponding to u , v and w
U_i	non-dimensional velocity
u_{in}	inlet velocity
\mathbf{V}	velocity field
\mathbf{V}_s	solid velocity

Greek Symbols

ΔH	nodal latent heat
δv	element volume
ε	turbulent kinetic energy dissipation rate
ε_0	permittivity of free space, 8.854×10^{-12} in MKS unit
Γ_ϕ	diffusion coefficient associated with Φ value
μ	laminar viscosity
μ_0	permeability of free space, $4\pi \times 10^{-7}$ in MKS unit
μ_t	turbulent viscosity
Φ	generalized dependent variable
ϕ	electric potential
ρ	mass density
σ	electrical conductivity
σ_t	turbulent Prandtl number
$\sigma_k, \sigma_\varepsilon$	empirical constants in turbulent model equations

References

- Alfven H., *Cosmical electromagnetics*, Clarendon press, Oxford, (1950).
- Dutta P., Joshi Y., and Janaswamy R., Thermal modeling of gas tungsten arc welding process with nonaxisymmetric boundary conditions, *Numerical Heat Transfer Part A-Applications*, Vol. 27, No. 5, pp. 499-518, (1995).
- Fireteanu V. S. and Gheysens R., Numerical modeling of the electromagnetic flow rate control of molten metals, *IEEE Transactions on Magnetics.*, Vol. 30, No. 5, pt. 2, p 3343-3346, (1994).
- Furuhashi S., and Asai S., Stability analysis for confining molten metal puddle by electromagnetic force in twin roll process, *Journal of the Iron and Steel Institute of Japan - Tetsu to Hagane*, Vol. 80, No. 5, pp. 371-376, (1994).
- Gardin P., Galpin J. M., Regnier M. C., and Radot J. P., Liquid steel flow control inside continuous casting mould using a static magnetic field, *IEEE Transactions on Magnetics*, Vol. 31, No. 3, pt. 1, pp. 2088-2091, (1995).
- Idogawa A., Sugizawa M., Takeuchi S., Sorimachi K., and Fujii T., Control of molten steel flow in continuous casting mold by two static magnetic fields imposed on whole width, *Materials Science and Engineering - A - Structural Materials*, Vol. 173, No. 1, pp. 293-297, (1993).
- Kollberg S. G., Hackl H. R., and Hanley P. J., Improving quality of flat rolled products using electromagnetic brake (EMBR) in continuous casting, *Iron and Steel Engineer*, Vol. 73, No. 7, pp. 24-28, (1996).
- Lauder B. E., and Sharma B. I., Application of the energy dissipation model of turbulence to the calculation of flow near a spinning disc, *Letters In Heat and Mass Transfer*, Vol. 1, pp. 131-138, (1974).
- Lehman A., Tallback G., and Rullgard A., Electromagnetic braking improves steel quality in continuous casting, *ASEA Brown Boveri Review*, No. 1, pp. 4-10, (1996).

- Li B. Q., A finite-element analysis of magnetically driven recirculating flow in electromagnetic near net shape casting, *Journal of Materials Processing Technology*, Vol. 55, No. 3, pp. 351-359, (1995).
- Murthy A., Szekely J., and El-Kaddah N., Experimental measurement and numerical computation of velocity and turbulence parameters in a heated liquid metal system, *Met. Trans. B*, Vol. 19B, pp. 765-775, (1988).
- Patankar S. V., *Numerical Heat Transfer and Fluid Flow*, Hemisphere, Washington, D.C., (1980).
- Prescott P. J., and Incropera F. P., Magnetically damped convection during solidification of a binary metal alloy, *Journal of Heat Transfer-Trans. of the ASME*, Vol. 115, No. 2, pp. 302-310, (1993).
- Prescott P. J., and Incropera F. P., The effect of turbulence on solidification of a binary Metal alloy with electromagnetic stirring, *Journal of Heat Transfer-Trans. of the ASME*, Vol. 117, No. 3, pp. 716-724, (1995).
- Prescott P. J., Incropera F. P., and Gaskell D. R., Influence of electromagnetic stirring on the solidification of a binary metal alloy, *Experimental Heat Transfer*, Vol. 9, No. 2, pp. 105-131, (1996).
- Saluja N. S., Ilegbusi O. J., and Szekely J., Fluid flow phenomena in the electromagnetic stirring of continuous casting system, Part 1: The behavior of a cylindrically shaped laboratory scale installation, *Steel Research*, Vol. 61, No. 10, pp. 455-466, (1990).
- Takeuchi E., Applying MHD technology to the continuous casting of steel slab, *JOM*, Vol. 47, No. 5, pp. 42-45, (1995).
- Washio M., Sugizawa M., Moriwaki S., Kariya K., Idogawa S., and Takeuchi S., Development of flow controlled mold for high speed continuous casting using electromagnetic brake, *Revue de Metallurgie - Cahiers d'Information Techniques*, Vol. 90, No. 4, pp. 507-512, (1993).
- Williams E. J., The induction of EMF's in a moving fluid by a magnetic field and its application to an investigation of the flow of liquids, *Proc. Phys. Soc.*, Vol. 44, p. 466, (1930).

Zeze M., Tanaka H., Takeuchi E., and Mizoguchi S., Continuous casting of clad steel slab with level magnetic field brake, *Proceedings of the 79th Steelmaking Conf., ISS-AIME, Pittsburgh*, March 24-27, pp. 225-230, (1996).

Zhang W., Yang Y., Liu Q., Zhu Y., and Hu Z., Numerical simulation of fluid flow in electromagnetic centrifugal casting, *Modelling and Simulation in Materials Science and Engineering*, Vol. 4, No. 4, pp. 421-432, (1996).

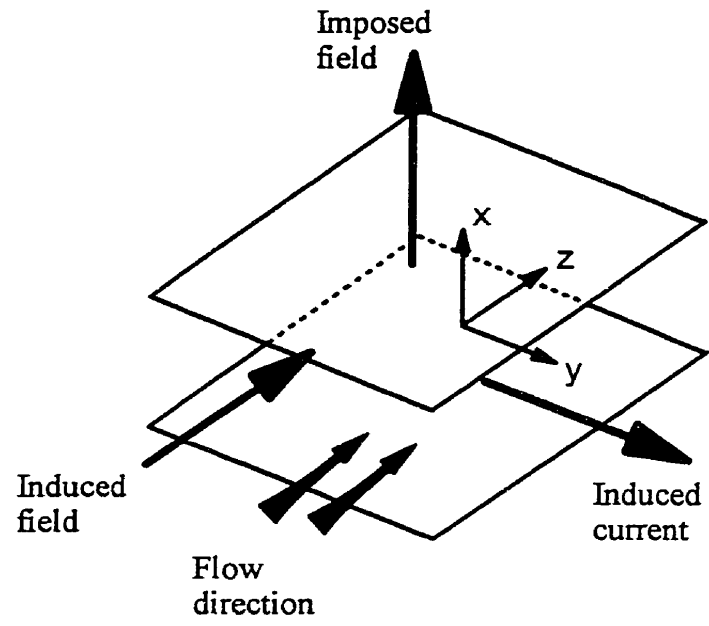


Fig. 4.1. Magnetohydrodynamic flow in a duct (Hartmann flow).

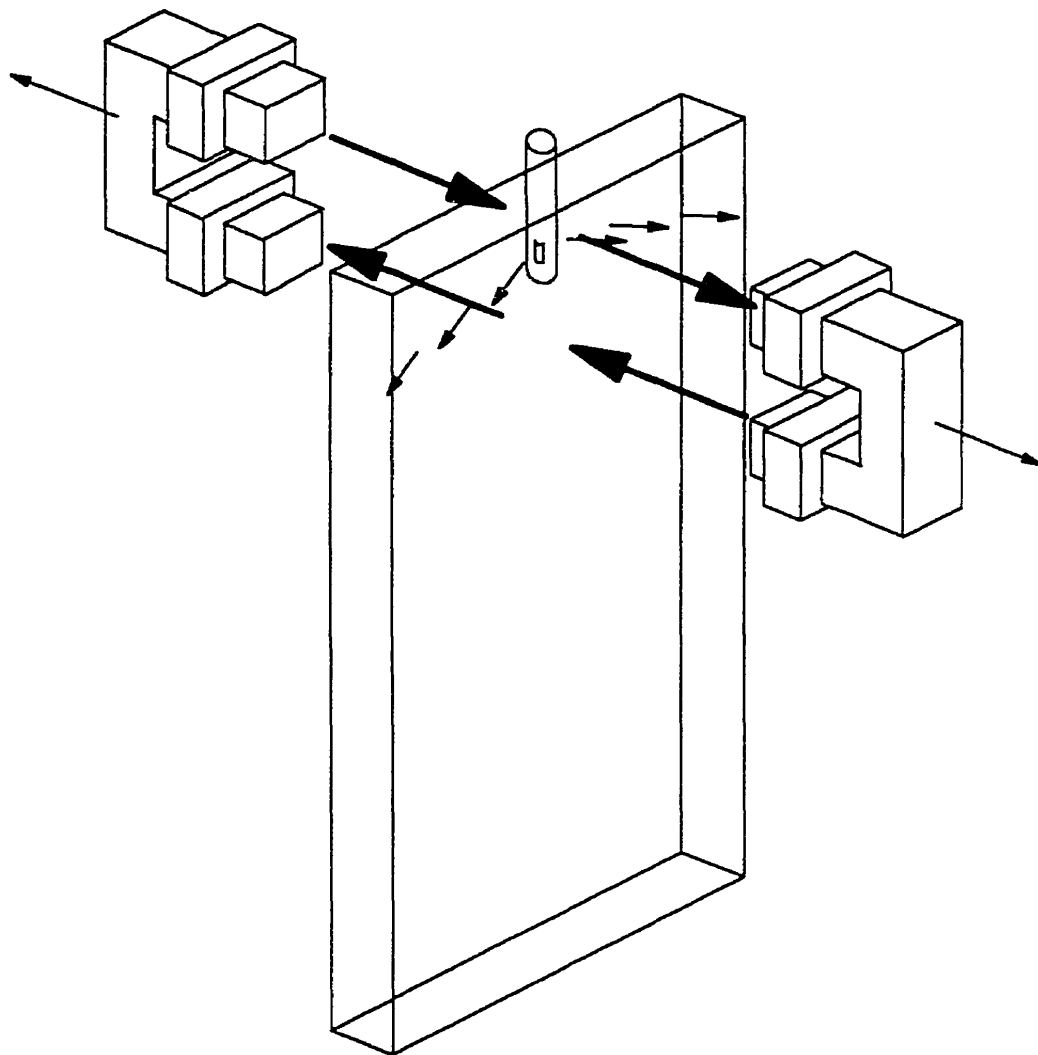


Fig. 4.2. A schematic diagram of type A-EMBR design for continuous slab casters.

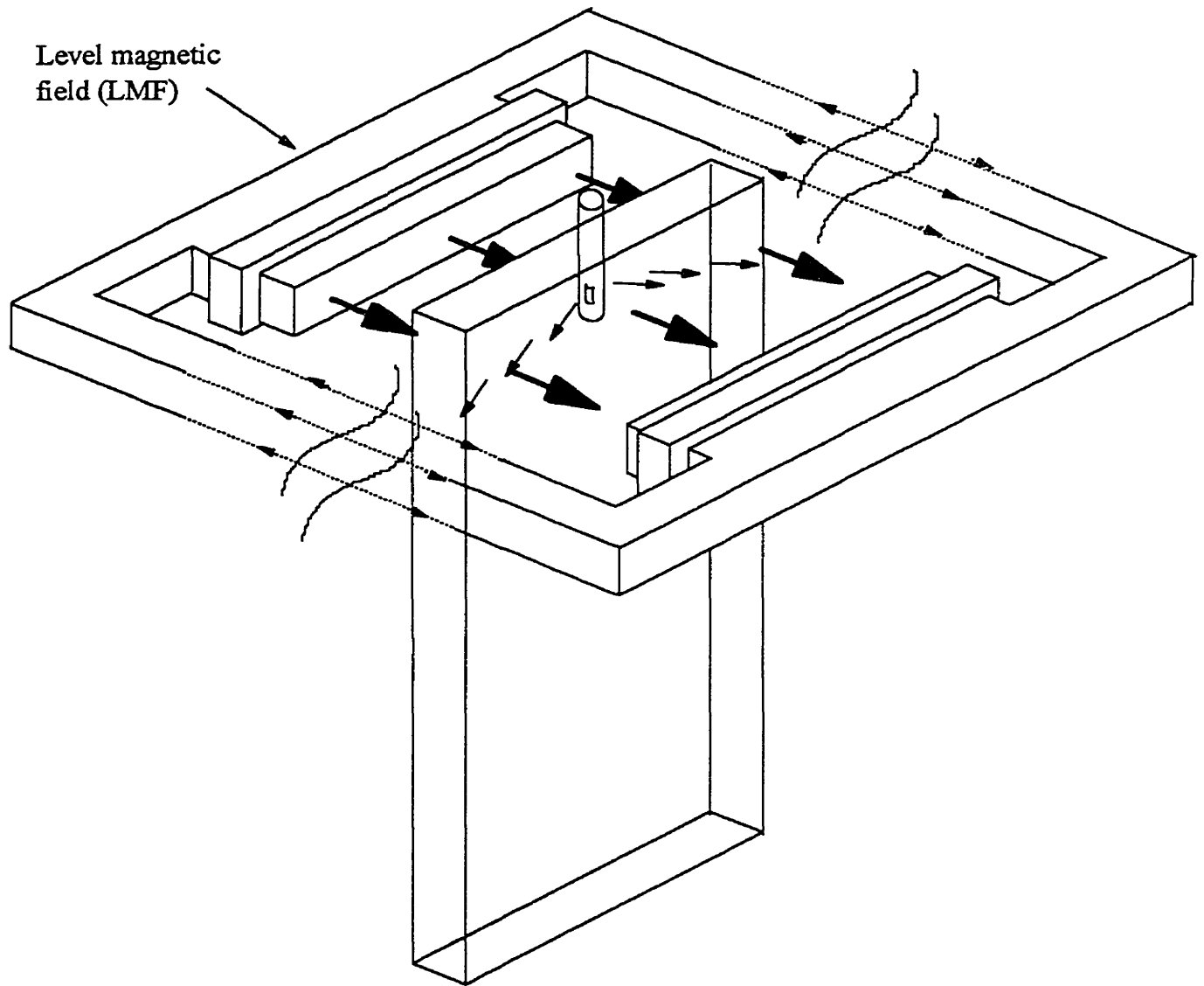


Fig. 4.3. Application of level magnetic field (LMF) in the continuous slab casters; type C-EMBR with LMF located under the nozzle, type B-EMBR with LMF located at the meniscus (although not shown here).

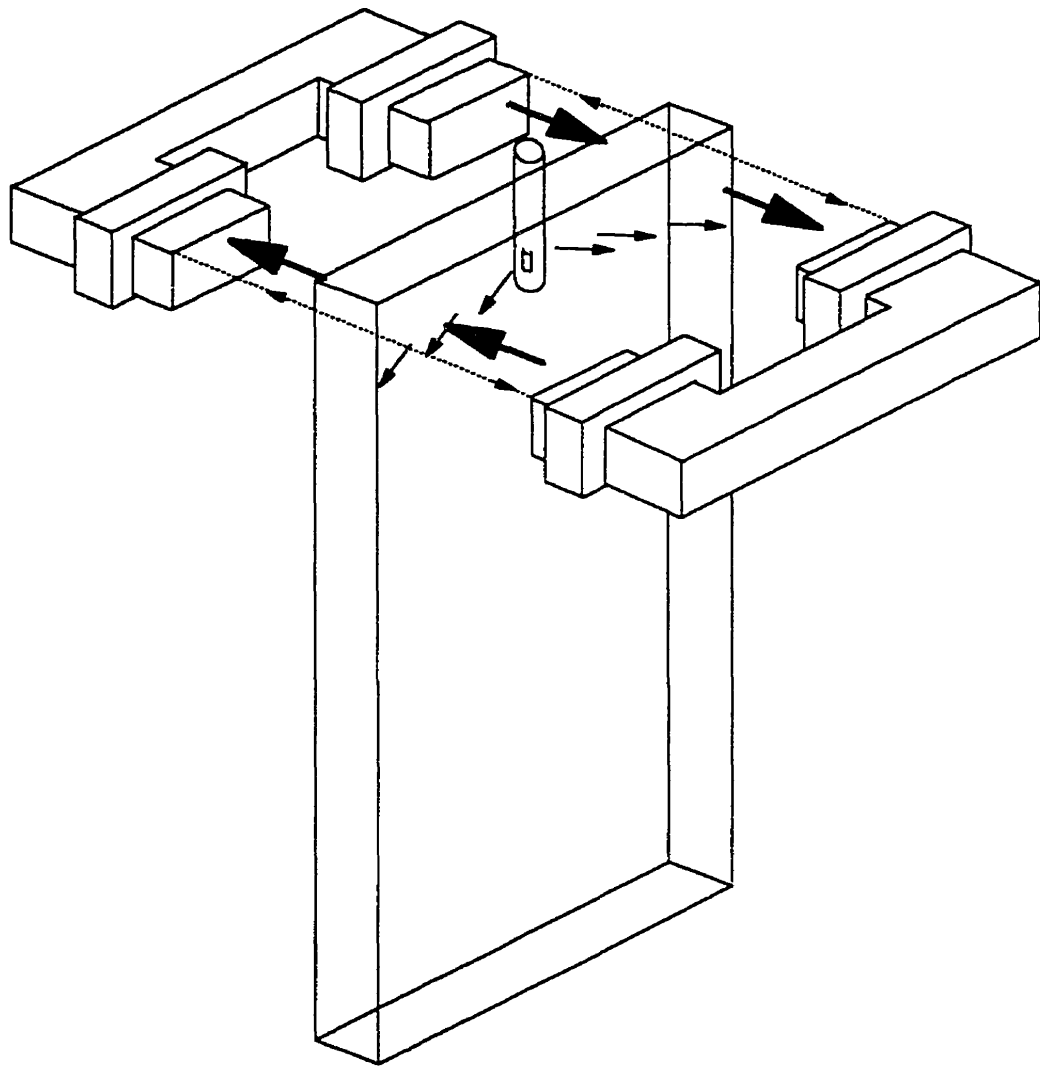


Fig. 4.4. A schematic diagram of type D-EMBR design for continuous slab casters.

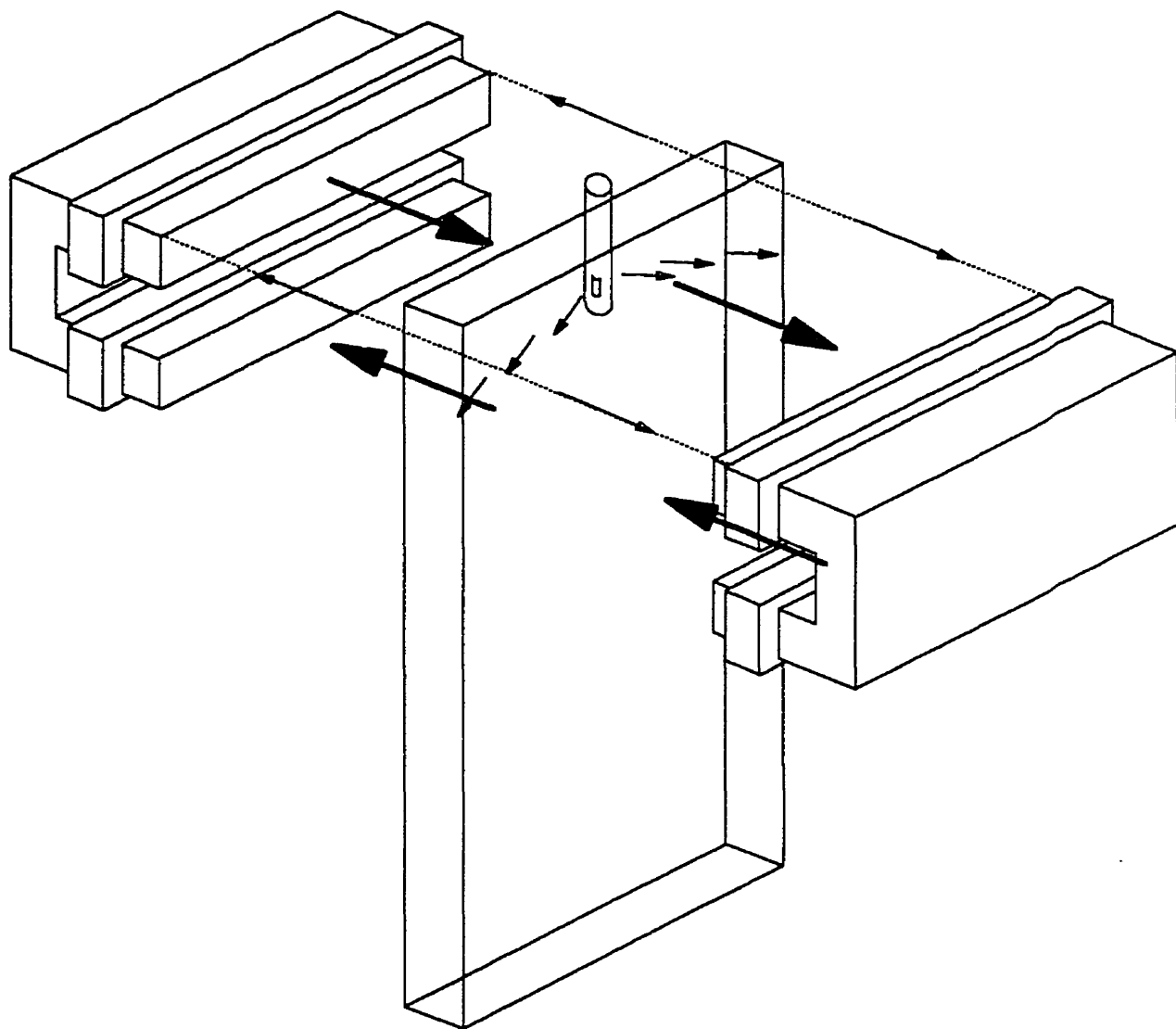


Fig. 4.5. A schematic diagram of type E-EMBR design for continuous slab casters.

velocity scale: $\longrightarrow = 0.45$

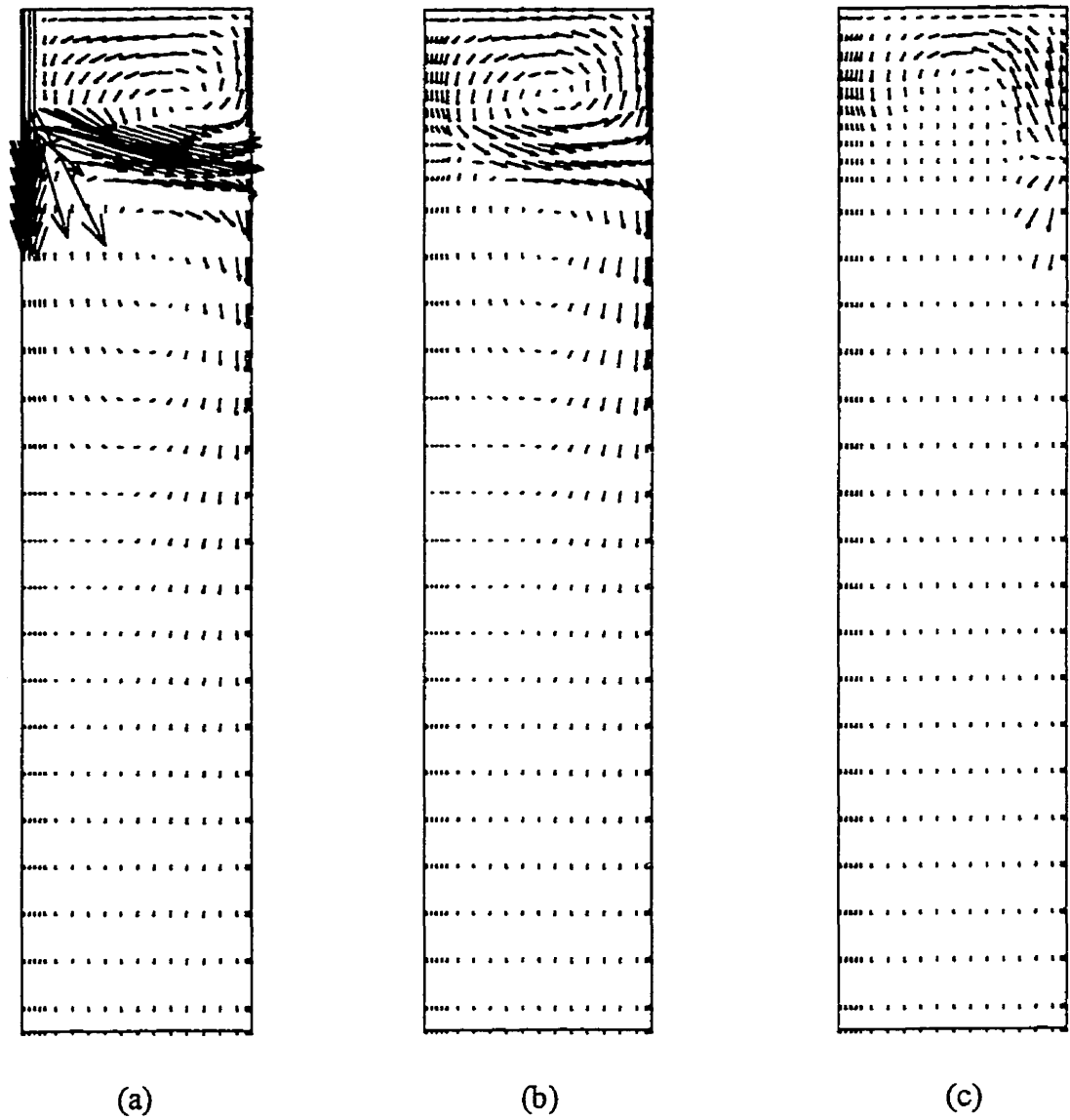


Fig. 4.6. 2-D velocity field for a conventional continuous slab caster without magnetic field; (a) wide symmetry plane, (b) parallel wide plane at half thickness, (c) wide plane near the broad face.

velocity scale: $\longrightarrow = 0.45$

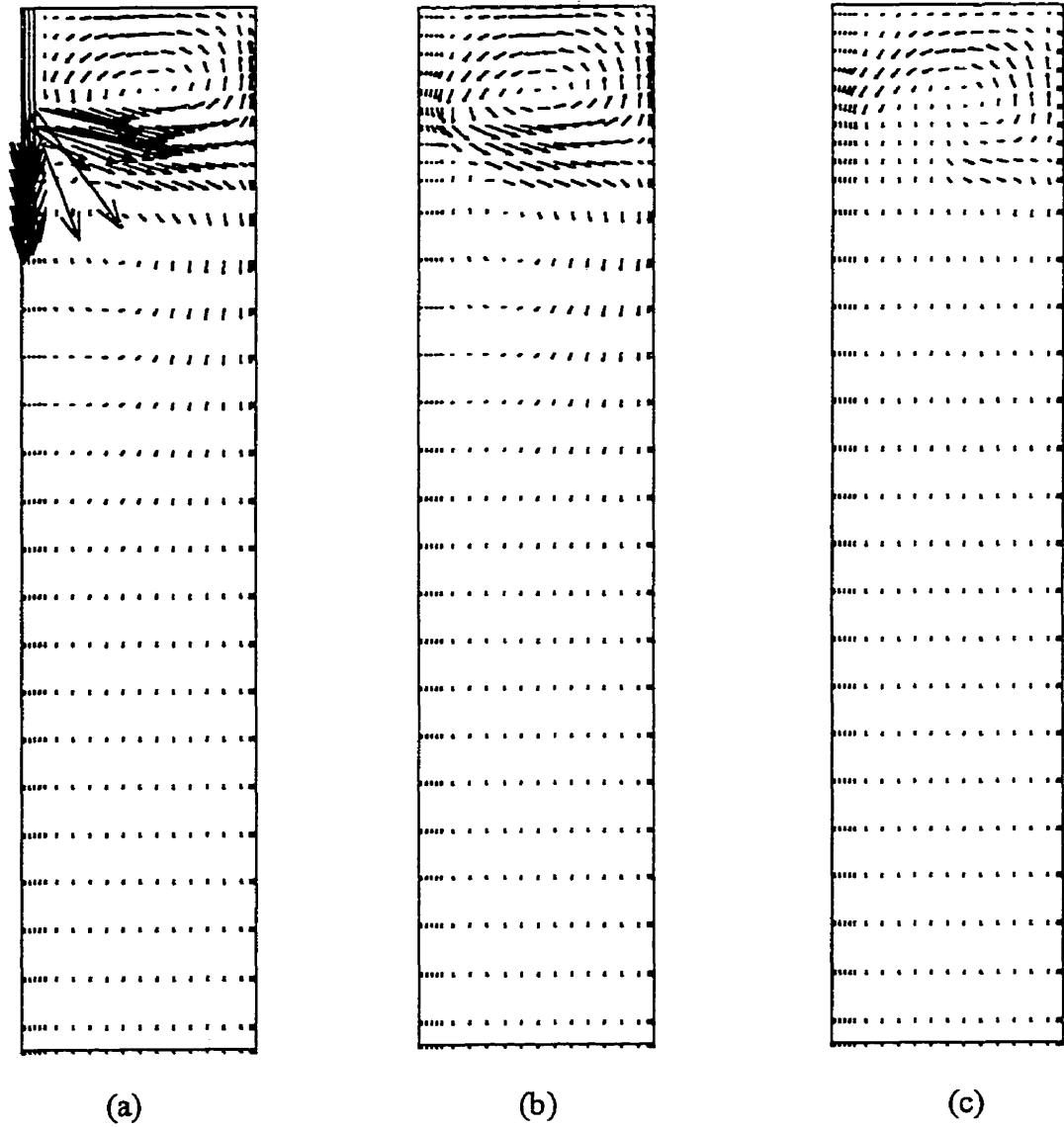


Fig. 4.7. 2-D velocity field for a typical continuous slab caster with type A-EMBR; (a) wide symmetry plane, (b) parallel wide plane at half thickness, (c) wide plane near the broad face.

velocity scale: $\longrightarrow = 0.45$

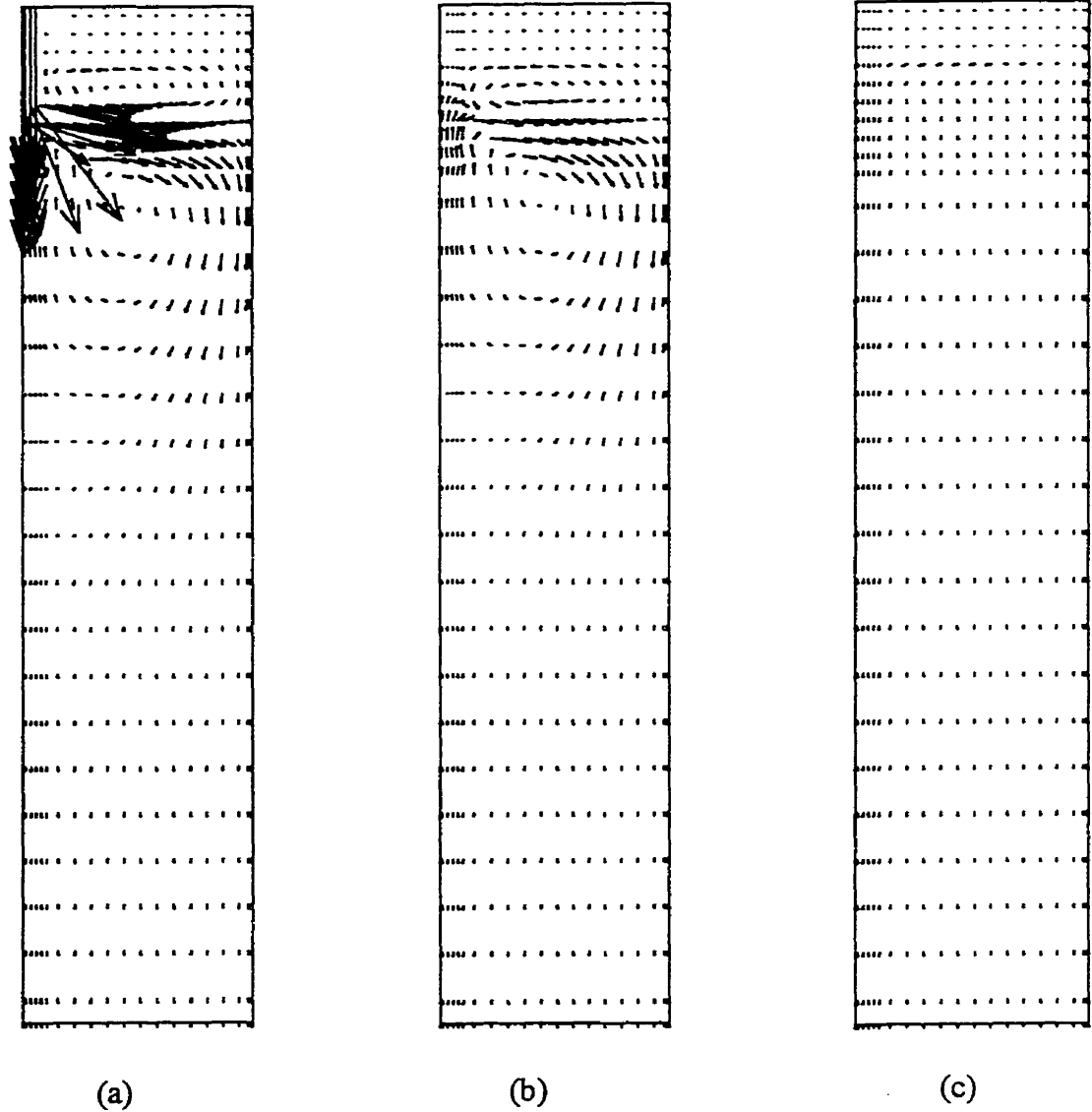


Fig. 4.8. 2-D velocity field for a typical continuous slab caster with type B-EMBR; (a) wide symmetry plane, (b) parallel wide plane at half thickness, (c) wide plane near the broad face.

velocity scale: \longrightarrow = 0.45

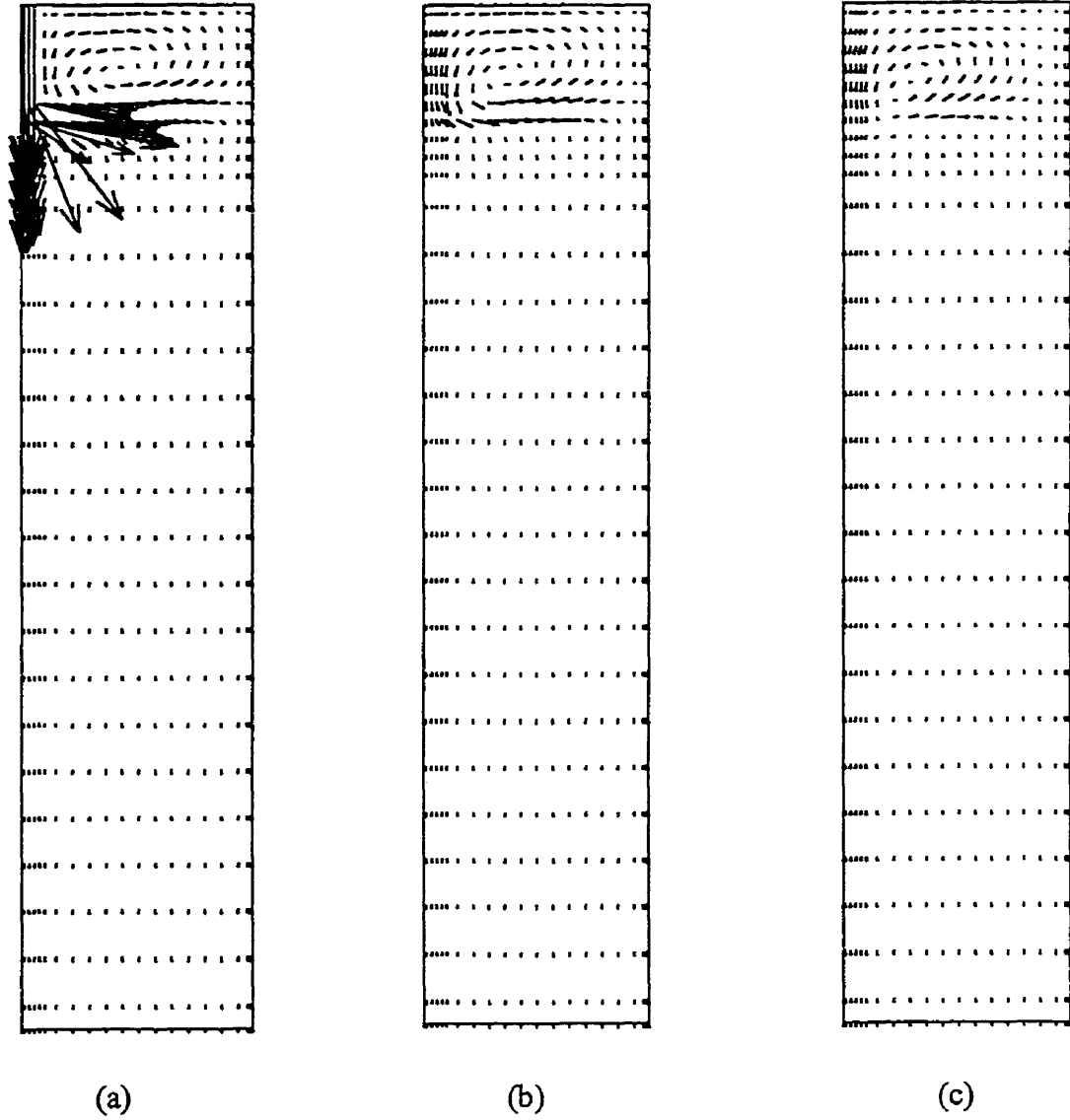


Fig. 4.9. 2-D velocity field for a typical continuous slab caster with type C-EMBR; (a) wide symmetry plane, (b) parallel wide plane at half thickness, (c) wide plane near the broad face.

velocity scale: $\longrightarrow = 0.45$

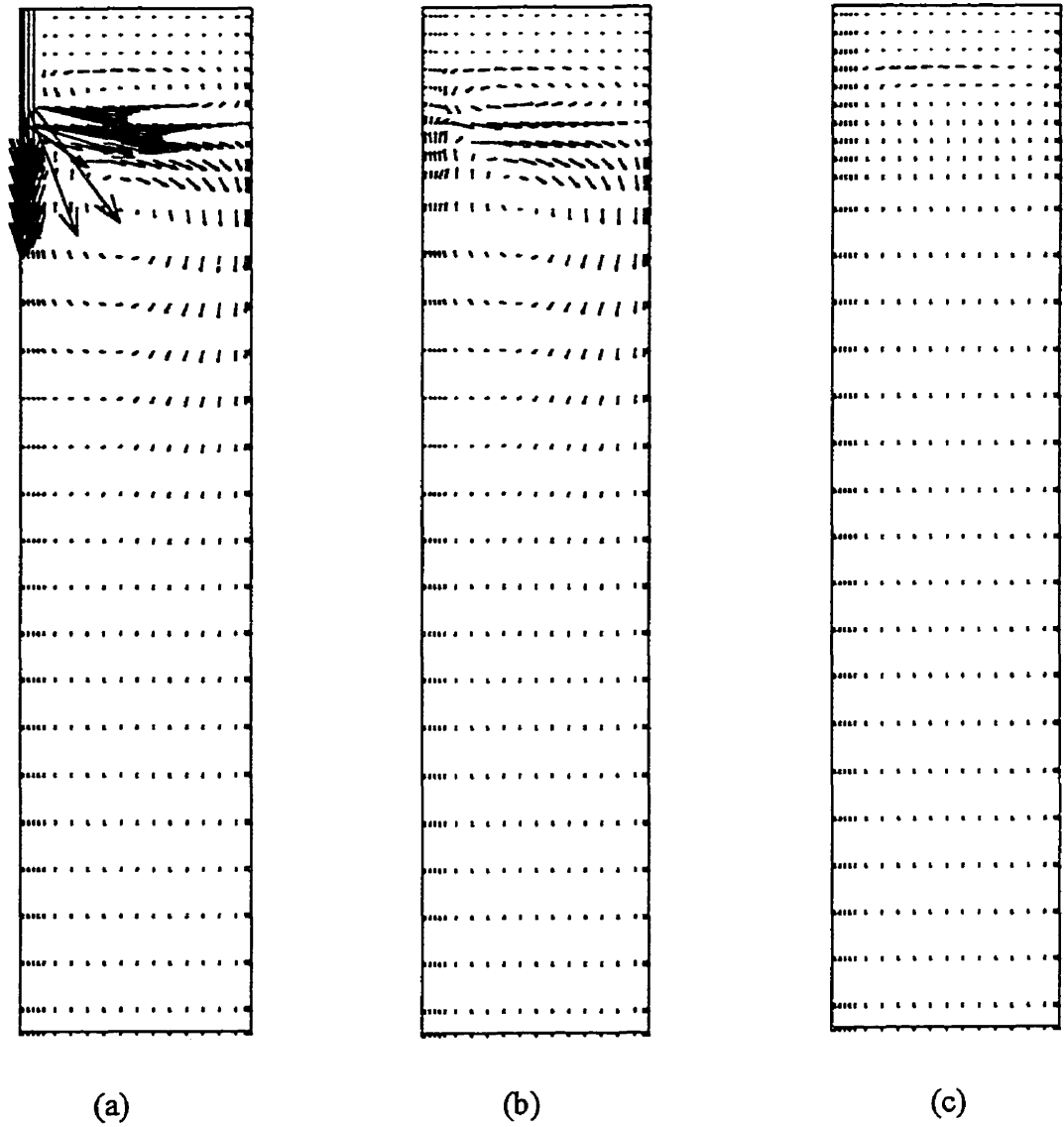


Fig. 4.10. 2-D velocity field for a typical continuous slab caster with type D-EMBR; (a) wide symmetry plane, (b) parallel wide plane at half thickness, (c) wide plane near the broad face.

velocity scale: $\longrightarrow = 0.45$

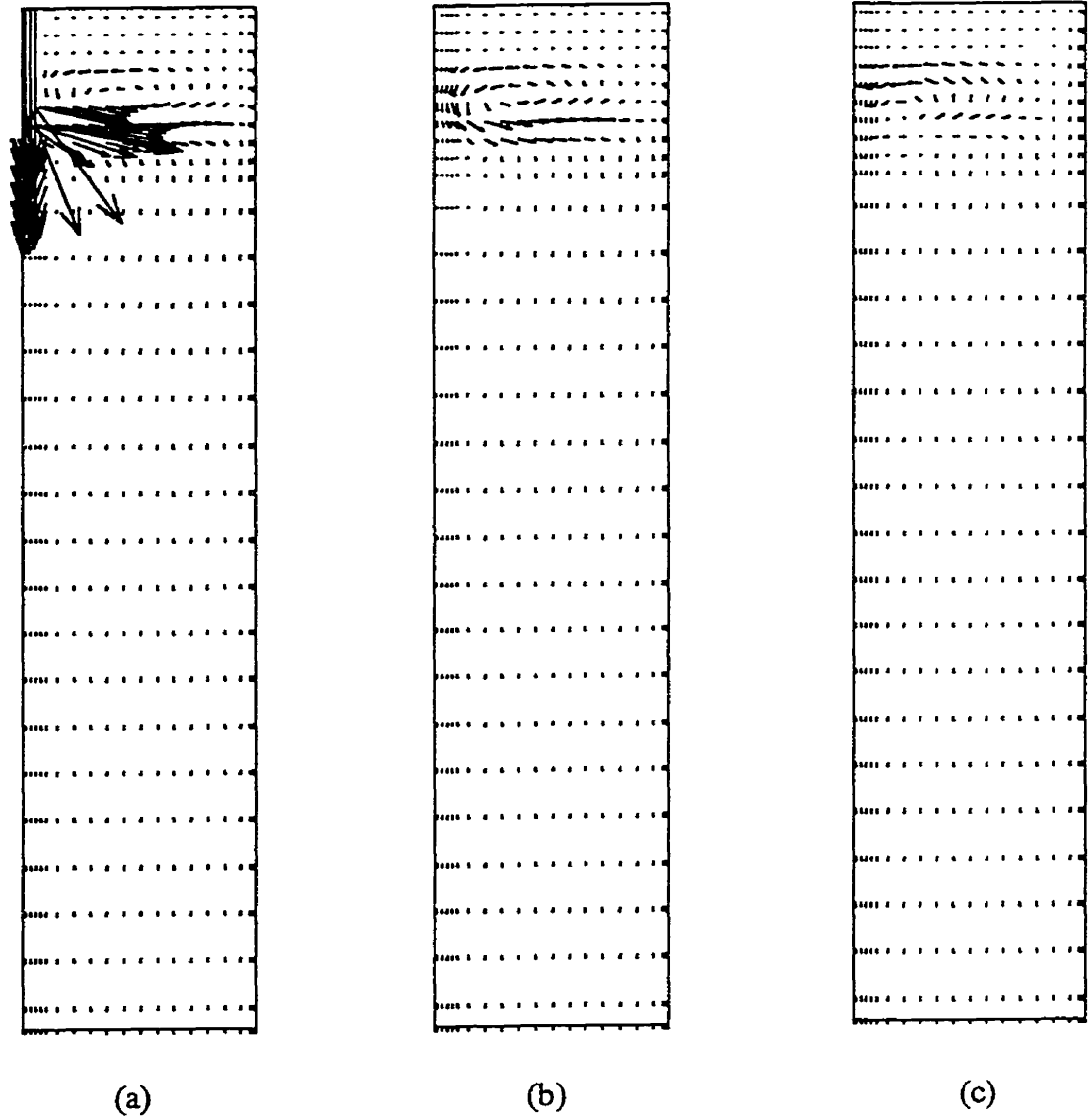


Fig. 4.11. 2-D velocity field for a typical continuous slab caster with type E-EMBR; (a) wide symmetry plane, (b) parallel wide plane at half thickness, (c) wide plane near the broad face.

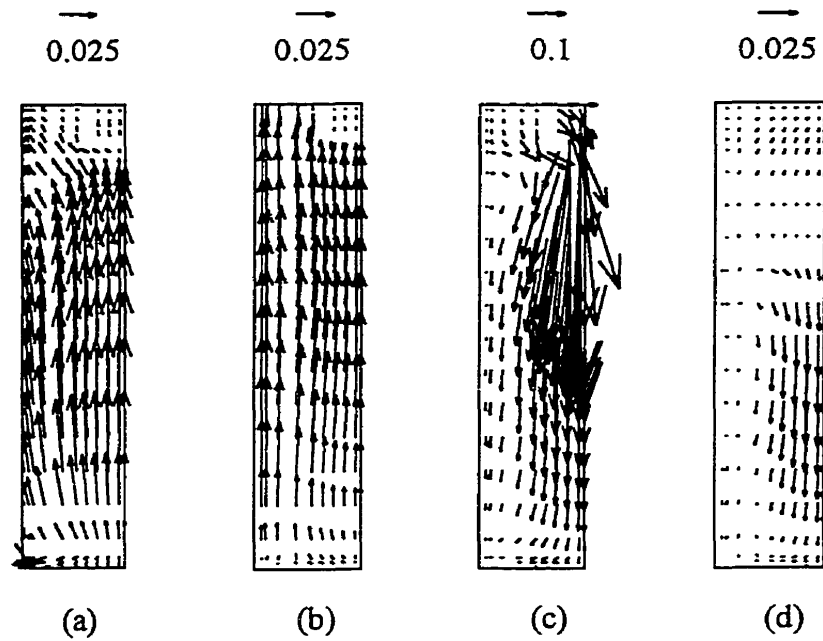


Fig. 4.12. 2-D velocity vectors at various transverse cross-sectional planes for a continuous slab caster with type A-EMBR; (a) 2.6 cm depth, (b) 18.4 cm depth, (c) 34.1 cm depth, (d) 55 cm depth.

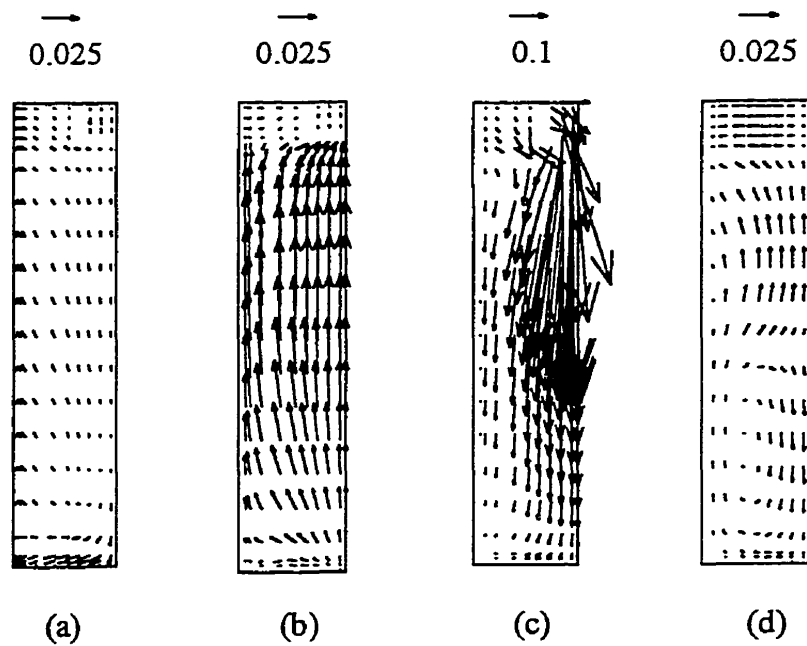


Fig. 4.13. 2-D velocity vectors at various transverse cross-sectional planes for a continuous slab caster with type B-EMBR; (a) 2.6 cm depth, (b) 18.4 cm depth, (c) 34.1 cm depth, (d) 55 cm depth.

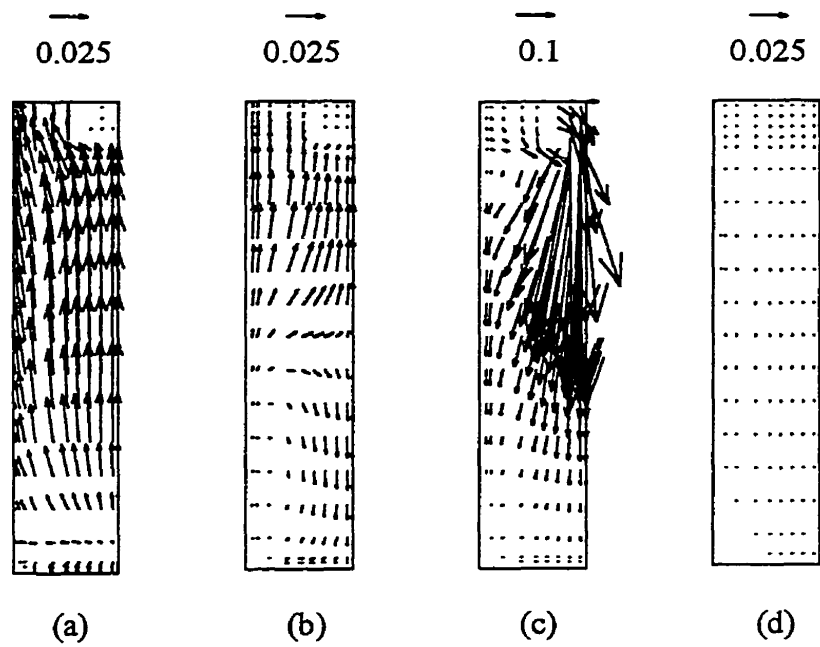


Fig. 4.14. 2-D velocity vectors at various transverse cross-sectional planes for a continuous slab caster with type C-EMBR; (a) 2.6 cm depth, (b) 18.4 cm depth, (c) 34.1 cm depth, (d) 55 cm depth.

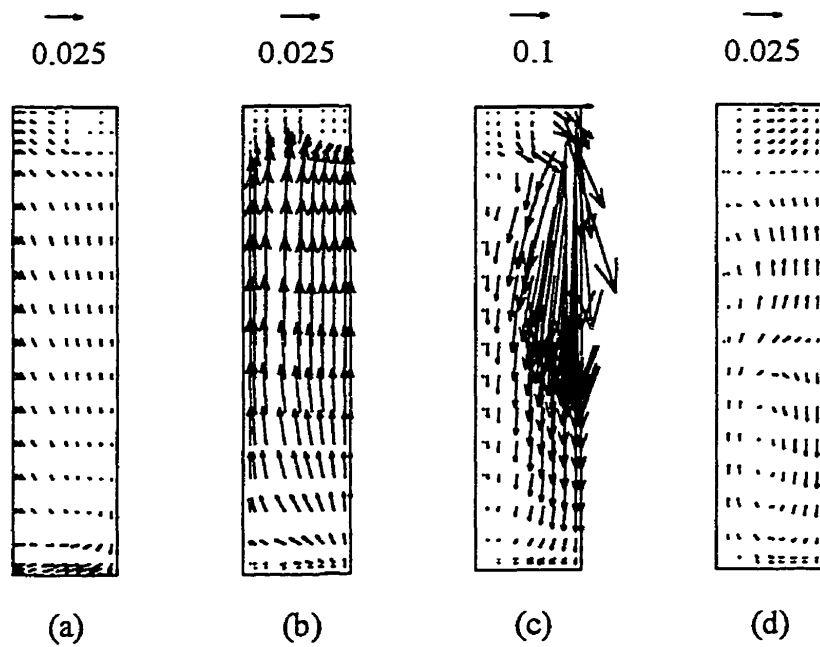


Fig. 4.15. 2-D velocity vectors at various transverse cross-sectional planes for a continuous slab caster with type D-EMBR; (a) 2.6 cm depth, (b) 18.4 cm depth, (c) 34.1 cm depth, (d) 55 cm depth.

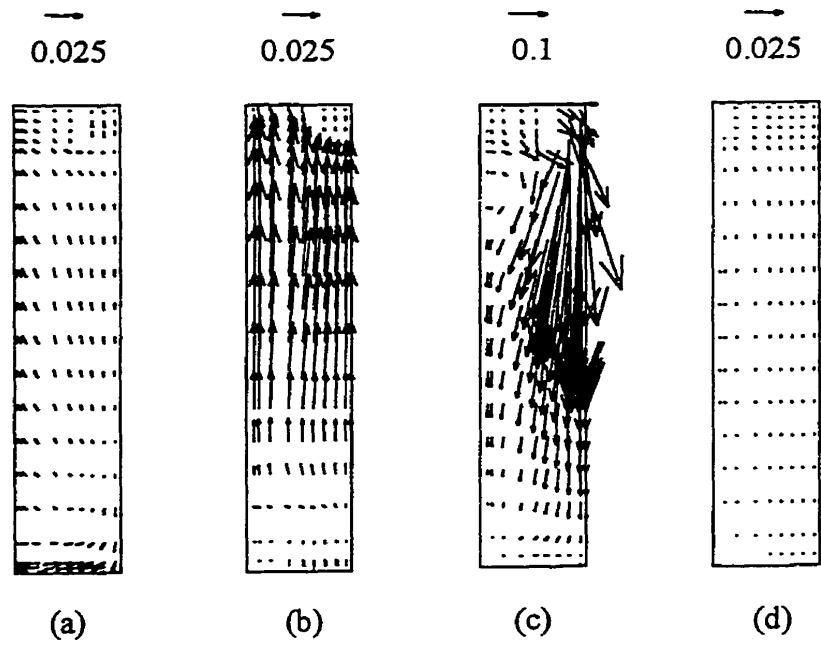


Fig. 4.16. 2-D velocity vectors at various transverse cross-sectional planes for a continuous slab caster with type E-EMBR; (a) 2.6 cm depth, (b) 18.4 cm depth, (c) 34.1 cm depth, (d) 55 cm depth.

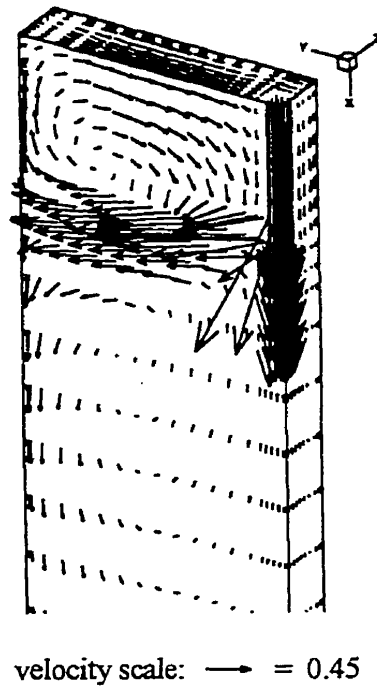
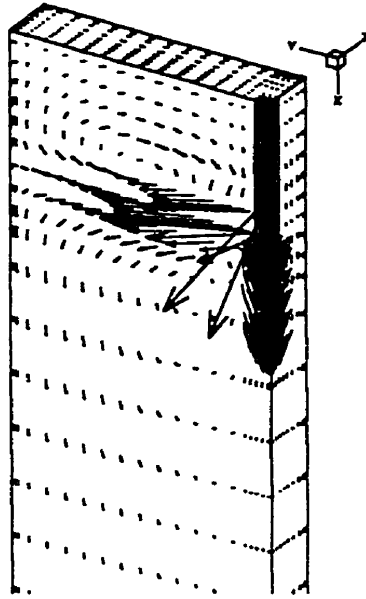
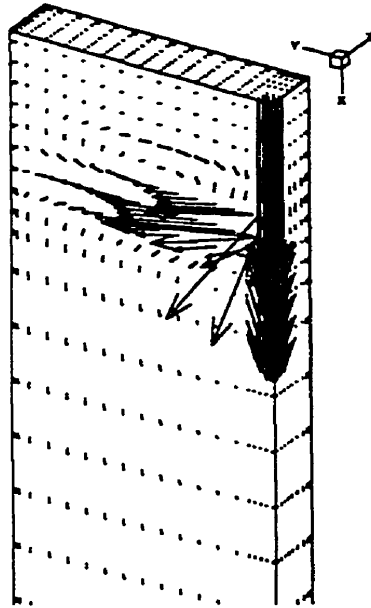


Fig. 4.17. 3-D surface plot of the velocity vectors for a conventional continuous slab caster without EMBR.



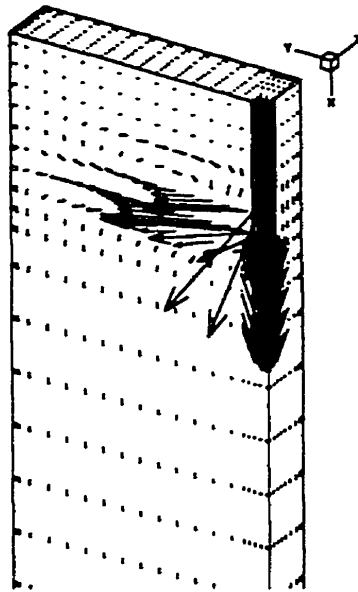
velocity scale: $\rightarrow = 0.45$

Fig. 4.18. 3-D surface plot of the velocity vectors for a typical continuous slab caster with type E-EMBR and 0.1 tesla magnetic flux density.



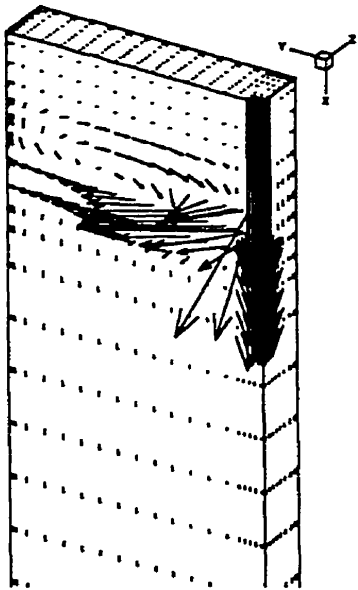
velocity scale: $\rightarrow = 0.45$

Fig. 4.19. 3-D surface plot of the velocity vectors for a typical continuous slab caster with type E-EMBR and 0.2 tesla magnetic flux density.



velocity scale: $\rightarrow = 0.45$

Fig. 4.20. 3-D surface plot of the velocity vectors for a typical continuous slab caster with type E-EMBR and 0.3 tesla magnetic flux density.



velocity scale: $\rightarrow = 0.45$

Fig. 4.21. 3-D surface plot of the velocity vectors for a typical continuous slab caster with type E-EMBR, 0.3 tesla magnetic flux density and without electric field consideration.

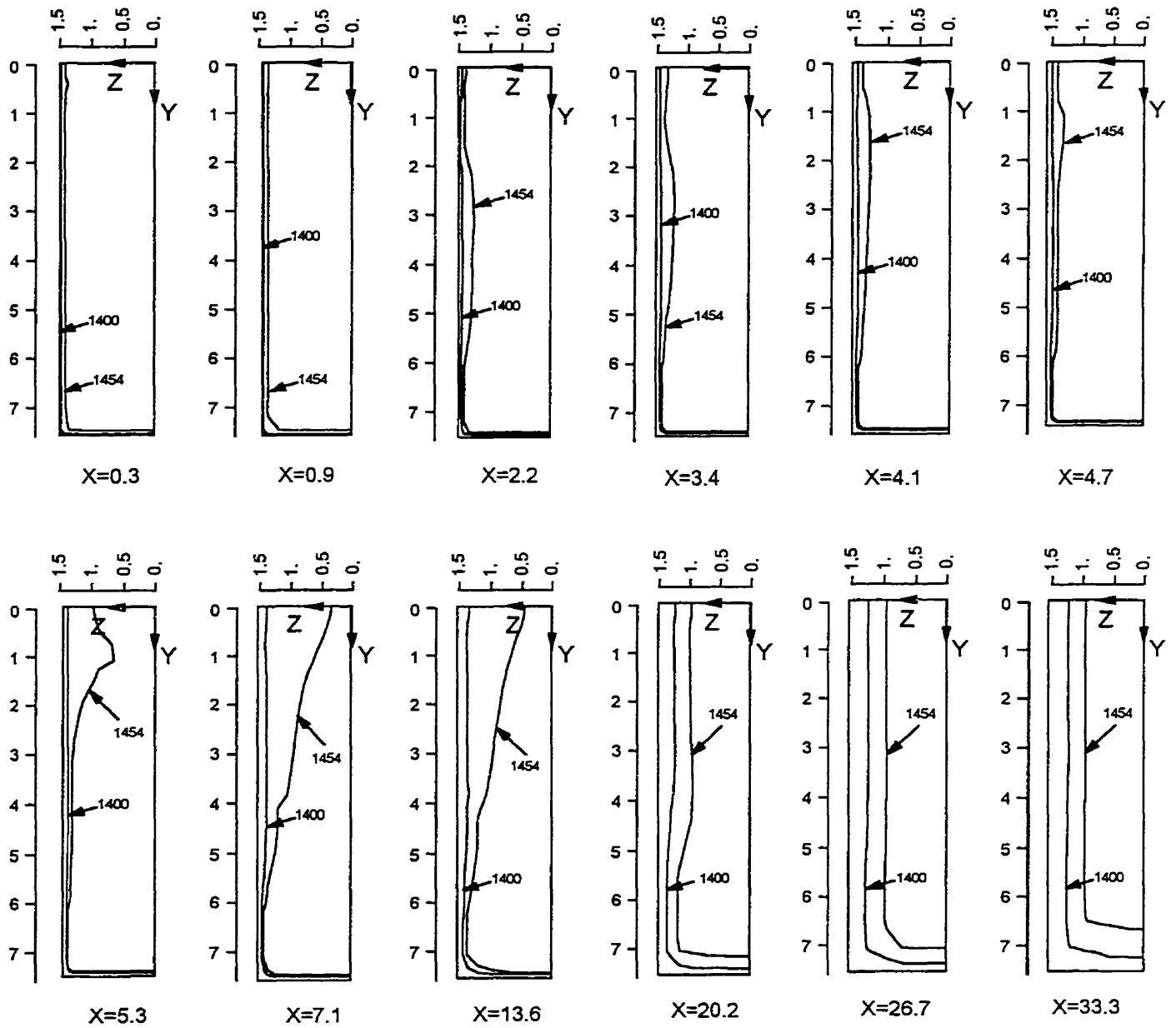


Fig. 4.22. Contours of solidus and liquidus temperatures at various transverse cross-sectional planes (Y-Z planes) for a conventional continuous slab caster without an EMBR device.

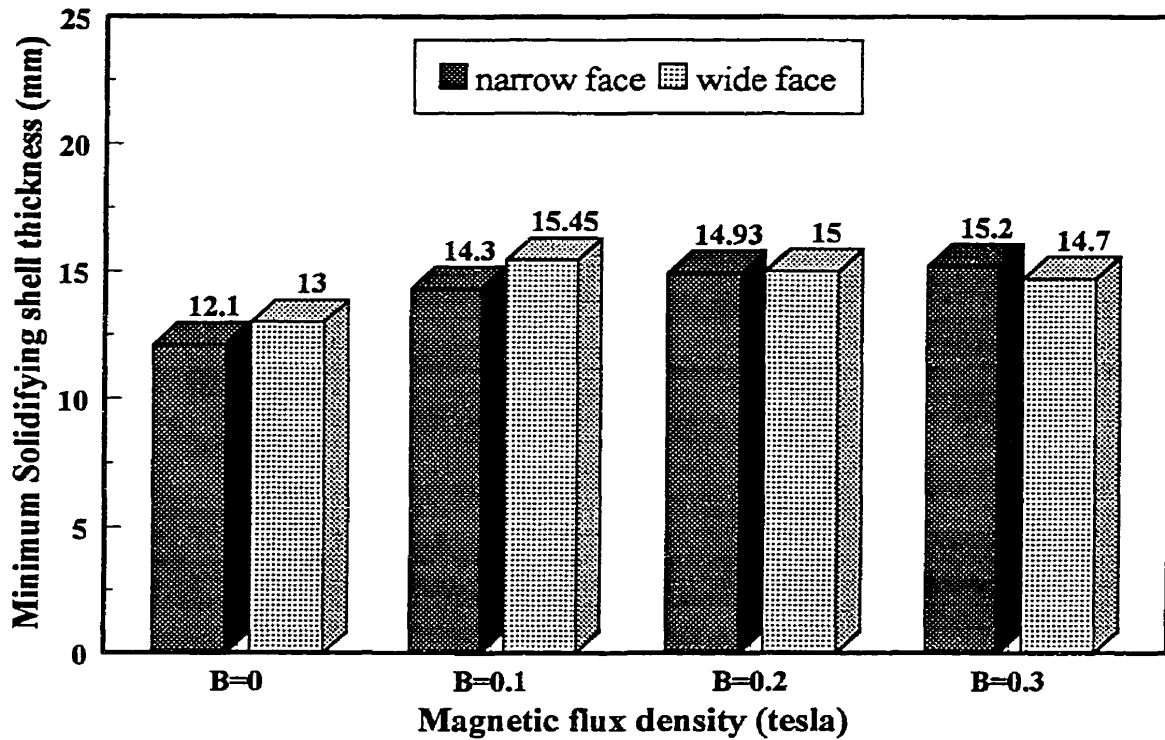


Fig. 4.24. Effect of magnetic flux density on the minimum thickness of the solidified shell at the mold exit of a continuous slab caster with type E-EMBR device.

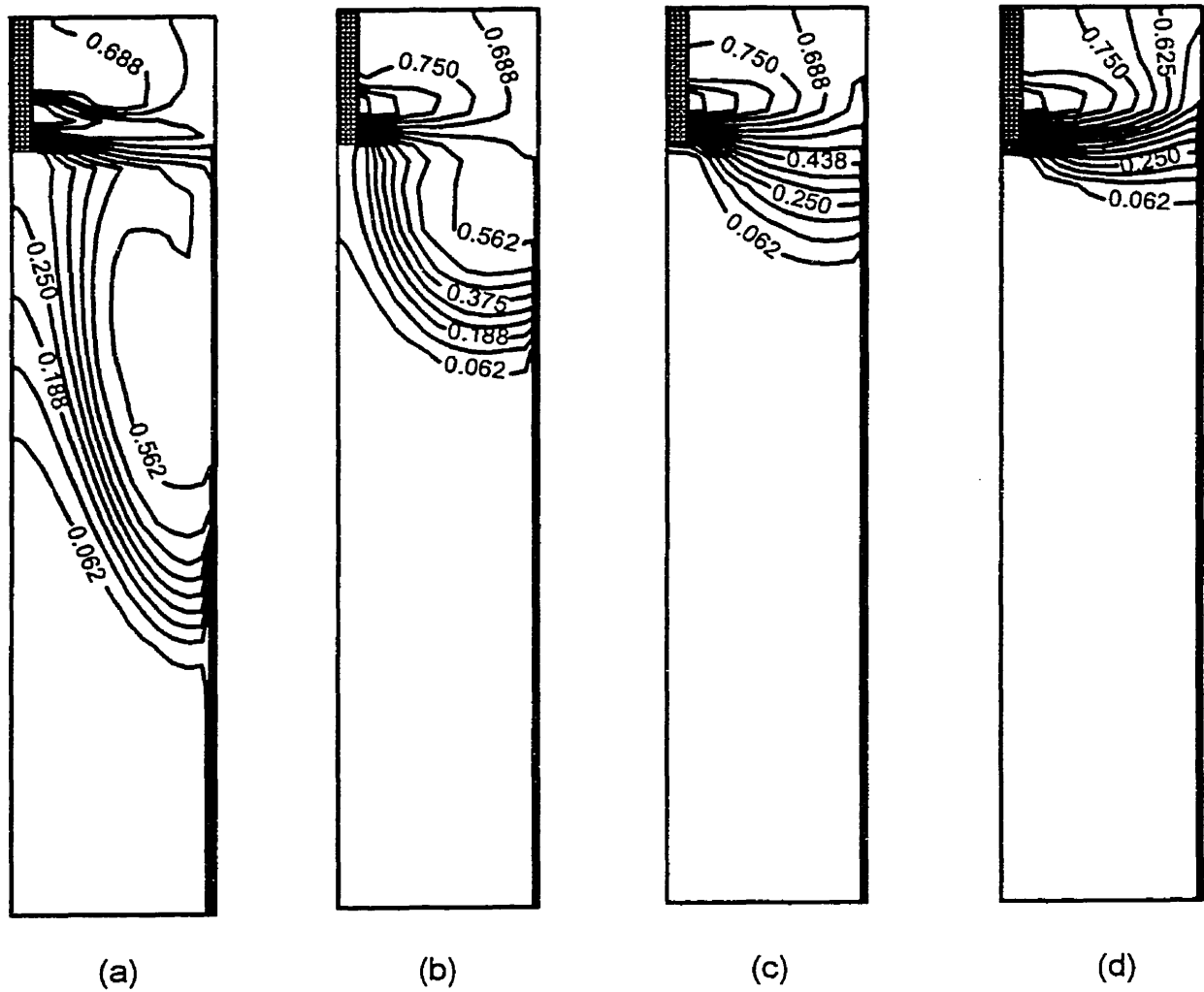


Fig. 4.25. Effect of magnetic flux density on distribution of the inclusions with 0.28 mm diameter in the wide symmetry plane of a continuous slab caster with type E-EMBR device; (a) 0 tesla, (b) 0.1 tesla, (c) 0.2 tesla, (d) 0.3 tesla.

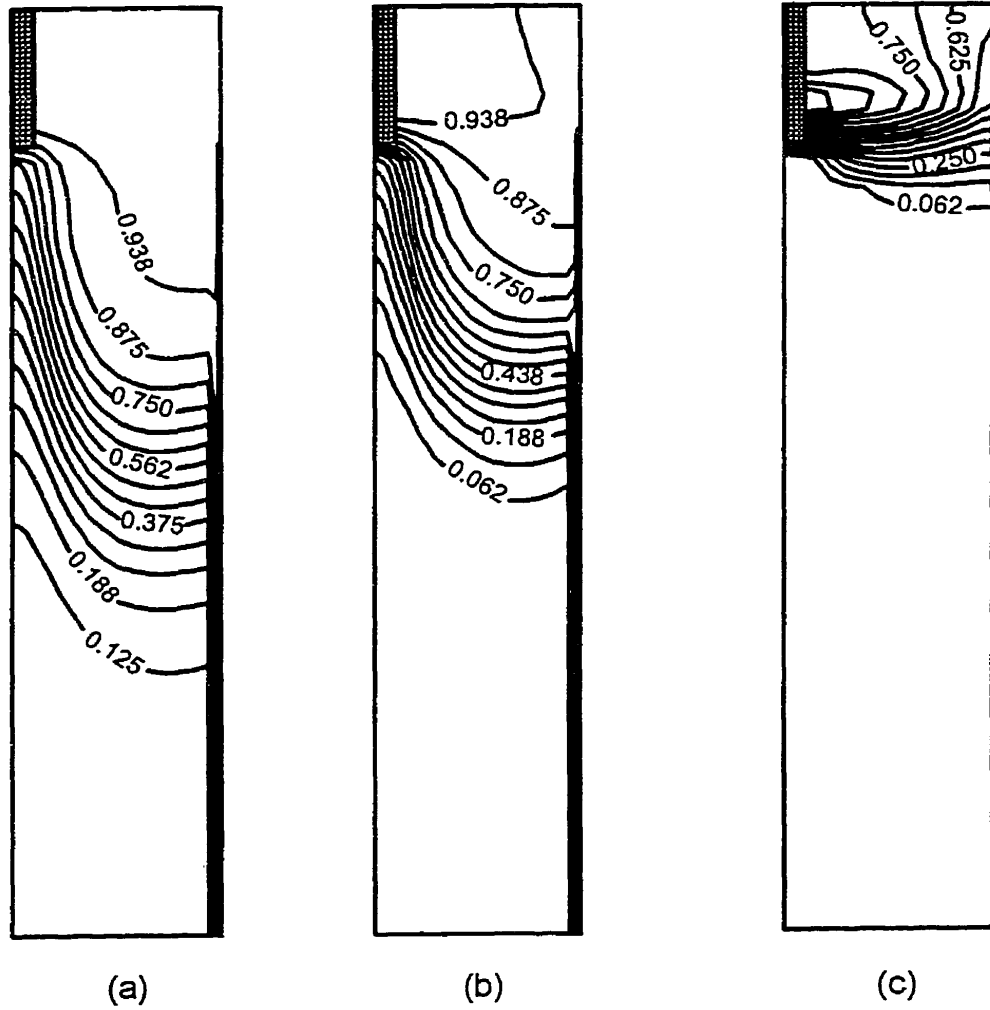


Fig. 4.26. Effect of inclusion size on distribution of the inclusions in the wide symmetry plane of a continuous slab caster with type E-EMBR device, 0.3 tesla magnetic flux density and various inclusion diameters; (a) 0.235 mm, (b) 0.255 mm, (c) 0.285 mm.

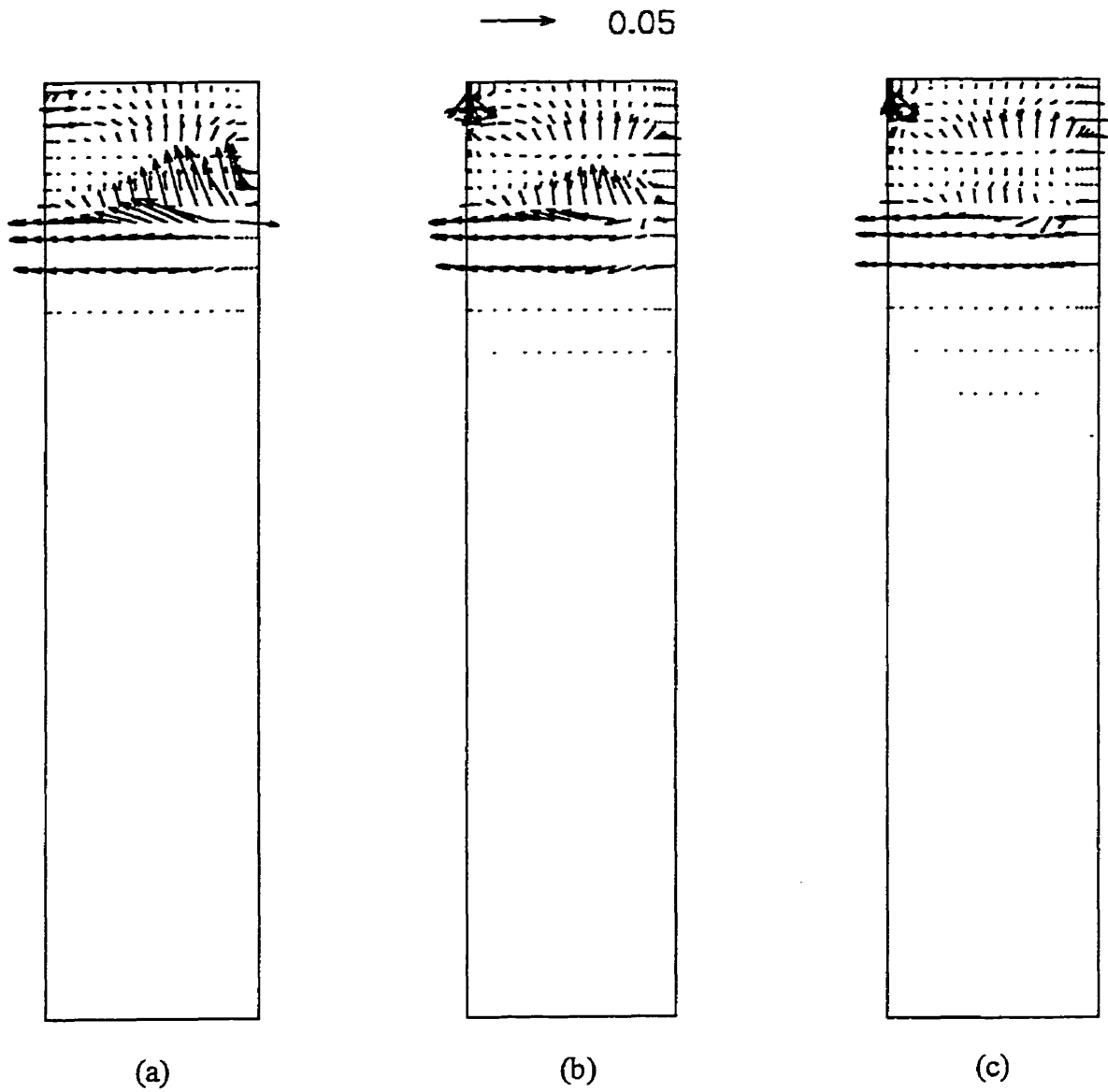


Fig. 4.27. Predicted induced current density vectors for various faces paralleled to the wide symmetry plane of a caster with type E-EMBR and 0.3 tesla magnetic flux density; (a) wide symmetry plane, (b) the surface at the half-thickness, (c) the surface close to the broad face.

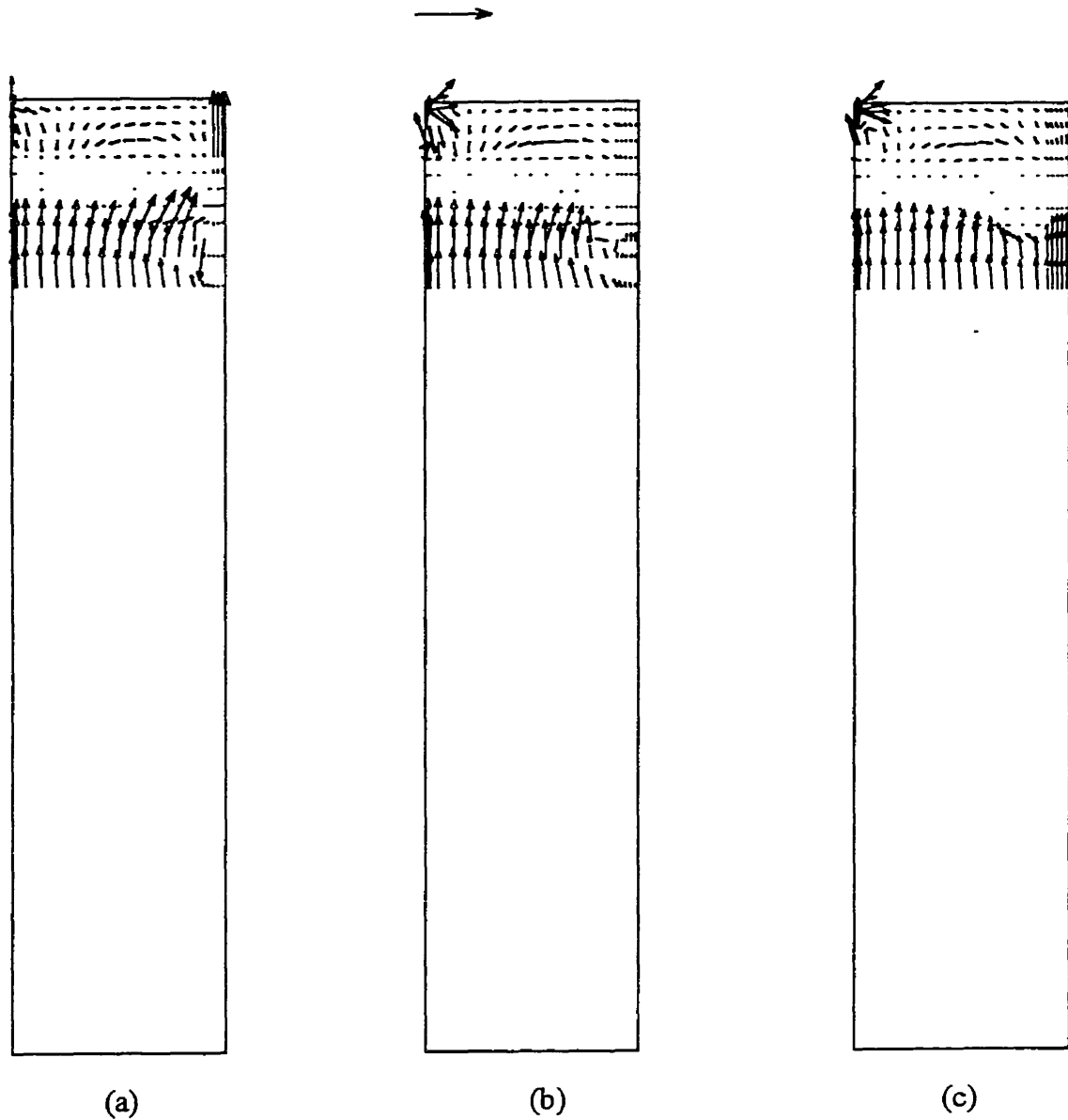


Fig. 4.28. Predicted Lorentz force vectors for various faces paralleled to the wide symmetry plane of a caster with type E-EMBR and 0.3 tesla magnetic flux density; (a) wide symmetry plane, (b) the surface at the half-thickness, (c) the surface close to the broad face.

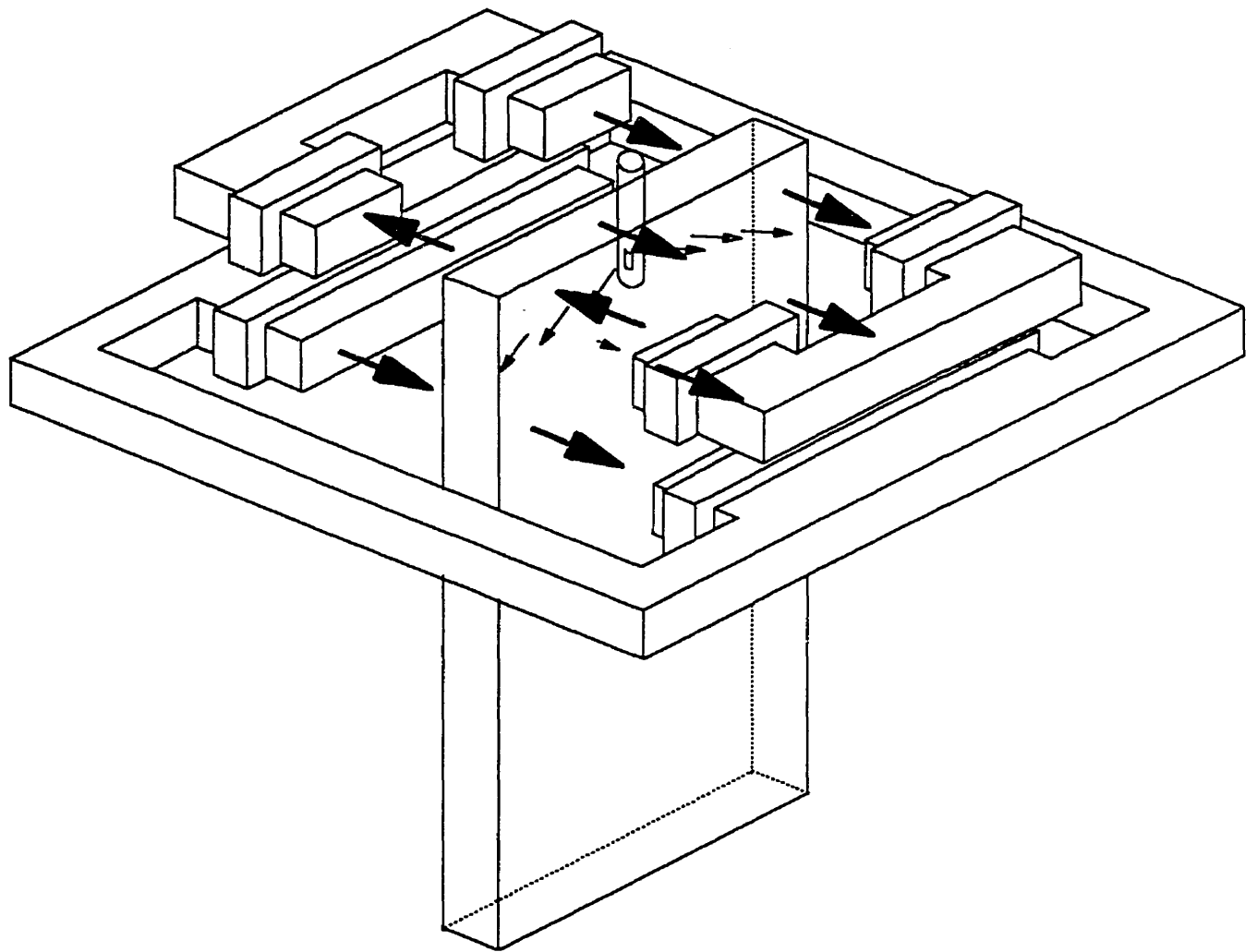


Fig. 4.29. A schematic diagram of the proposed design of EMBR (type E-EMBR) for continuous slab casters.

THE EFFECT OF ARGON GAS INJECTION ON THE 3-D FLOW, HEAT TRANSFER AND SOLIDIFICATION STUDIES IN THE CONTINUOUS SLAB CASTING OPERATION

5.1 Introduction

When liquid steel is solidified by the continuous casting method, blockage of the casting ducts of the nozzle system, or so-called nozzle clogging can take place and seriously hamper the productivity of the casting process. One of the main reasons of nozzle clogging is attributed to the reactions that occur in the nozzle due to the natural sucking of air through cracks, pores or joints in the nozzle walls. The reoxidation products such as alumina associated with this reaction may either deposit on the nozzle walls and cause clogging, or enter into the mold in the form of inclusions. The inclusions which penetrate deeply into the mold can be trapped by the solidifying shell and create surface or internal defects of the product. To eliminate the problem of air aspiration into the nozzle, the nozzle duct is pressurized through the injection of an inert gas such as argon into the submerged entry nozzle (SEN). The positive pressure thus created inside the nozzle can reverse the direction of the suction through any probable crack or junctions on the nozzle wall. Argon gas injection also intensifies the turbulence in the nozzle and alleviates sticking of the inclusions onto the nozzle walls. The argon gas injection also has a secondary benefit in the mold, in that the inclusions removal rate in the mold is enhanced through their attachment on the bubbles and traveling to the meniscus surface. It is also believed that the injection of argon can help degassing of the steel in the mold by favoring the diffusion of the other dissolved gases into the ascending argon bubbles.

On the other hand, the argon gas bubbles blown into the SEN, get trapped in the solidifying shell and form blowholes in the cast and become a source of the internal or surface defects and give rise to the quality problems in the cast products. In order to prevent such defects, the motion and distribution of the argon gas bubbles in the mold must be controlled. The motion of the gas bubbles depends on the fluid flow pattern of the molten steel in the mold. Moreover, the buoyancy force generated in the liquid steel due to the argon gas blown into the mold also influences the liquid steel flow pattern and consequently all related transport phenomena such as heat transfer, phase-change, mixing, solute segregation, turbulence and inclusion trajectories are affected in variable degrees.

In addition to the injection of argon gas through SEN for the prevention of nozzle clogging in continuous casting processes, argon gas has numerous applications in metallurgical processes. Specifically, it is being used considerably in the ladle and tundish stations of the secondary steel making processes for the purpose of steel stirring. Gas-stirring in these vessels plays an effective role in steel refining, homogenization of the temperature and chemical composition of the steel, speeding up the melt/slag reaction and also removal of nonmetallic inclusions.

5.2 Literature Review

The metallurgical processes involving the phenomena of gas-stirring and bubble dispersion have received considerably attention among researchers during last two decades. The studies related to the argon-steel flow, especially in ladles and tundishes, have been classified in different ways by Thomas et al. (1994) and Zhu et al. (1995) and are not repeated here. In this section, only those studies which are related to the argon gas injection into the mold of continuous casting systems are reviewed.

To the best of the author's knowledge only a very limited number of works have been reported on the problem of gas dispersion in the continuous casters. Bessho et al.(1991) appear to have been the first to consider argon gas injection in their continuous casting study. They performed both experimental and numerical investigations on the

continuous casting processes for a slab. They used a four-port immersion nozzle for the flow feeding to their water model set up and tested a wide range of water and gas volumetric flow rate combinations. The authors also succeeded in simulating the three-dimensional distribution of bubbles and liquid flow by solving the time-averaged, turbulent Navier-Stokes equations as well as a gas-dispersion model equation. In terms of turbulent modeling, they applied the high-Re $k-\epsilon$ turbulent model, however it is not clear from their paper why the extra second derivative source terms, which naturally arise in the momentum equations, were not considered. Nevertheless, the upward deflected fluid flow and gas concentration distribution obtained in their study showed a reasonable agreement with experimental data and made it possible to evaluate the effect of buoyant force of the gas bubbles on the fluid flow in subsequent parametric studies. They further extended their mathematical model to find the non-metallic inclusions distribution by incorporating a new equation into the model for inclusion concentration. This equation is identical to the gas continuity equation but with a different terminal velocity for the inclusion.

Later, Thomas et al. (1994) carried out a study similar to that of Bessho et al. (1991) and investigated a wide range of parameters affecting the simulation of the two-phase (gas-liquid) flow in the continuous slab casting systems. They developed a 3-D, pseudo single-phase numerical model based on the finite-volume method and was used for the simulation of liquid steel flow as well as for the argon gas bubble dispersion. The turbulent behavior of the motion was modeled using the high-Re $k-\epsilon$ turbulent model with the associated near wall formulation. The velocity fields obtained in their study were later used in the separate models for heat transfer and mass transfer studies for the prediction of superheat dissipation and grade intermixing of a slab caster, respectively. The authors successfully applied their model to extensively investigate the effect of argon gas injection rate and bubble size on the various transport phenomena prevailing in a typical continuous casting operation. They found that through the injection of argon gas a significant change in the position of the impingement point on the narrow face of slab and upper recirculation loop can be realized. Although, they did not model the inclusion and gas bubble entrapment in the solidifying shell, their results for gas fraction distribution at

meniscus revealed that the region close to the center of the wide face of a slab is exposed to a higher gas fraction and propensity of defects associated with pinholes.

According to the above few existing studies related to bubble injection in a slab caster, it is clear that on one hand the fluid flow in the mold plays a significant role in the distribution of the gas and on the other hand it is influenced by the gas-buoyant forces. However, the casting process is a phase-change problem and to study the entrapment of the gas bubbles in the solidifying shell and ascertain the effect of gas injection on solidification, a simulation model (which must include the fluid flow and solid-liquid phase-change phenomena) is required. Unfortunately, none of the previous studies incorporated the phase-change aspect of the casting process in their modeling. Therefore, the main objective of the present investigation is to develop a general 3-D numerical code for analyzing the effect of injected argon gas on the fluid flow in the continuous casting mold by simultaneously taking into account the turbulent and solidification heat transfer phenomena into the simulation model. This work also presents the results of an extensive parametric study on the various bubble size and gas injection rate applied in the continuous slab casting system which may be used to optimize the operation of the caster.

5.3 Mathematical formulation

The equations governing the transport phenomena in the continuous slab casting without gas injection were already derived on the basis of a continuum model for binary alloy solidification and presented in Chapter 3. The formulation of the continuum model was originally developed for laminar flow conditions by Bennon and Incropera (1987). In order to take into account the effect of turbulence on the transport equations, the continuum model of Bennon and Incropera was modified here using the Launder and Sharma (1974) version of low-Re $k-\epsilon$ turbulent model. To drive the mathematical formulation and simplify numerical calculations, the assumptions listed in Chapter 3 were also applied here.

5.3.1 Gas Dispersion Model

To take into account the buoyant force acting on the steel motion due to the gas injection, an extra source term in the form of momentum per unit volume was added to the momentum equation in the axial direction, x . This extra source term can be prescribed as a function of gas bubble concentration, g_g , as follows:

$$S_{g,x} = -\rho_s g_g g \quad S_{g,y} = 0 \quad S_{g,z} = 0 \quad (5.1)$$

To derive the above source terms one can begin from the general form of the momentum equation in continuum model (Bennon and Incropera 1987) as follows:

$$\nabla \cdot (\rho \vec{V} u_i) = \nabla \cdot \left(\sum_k \mu_k \nabla (g_k u_{i_k}) \right) - \nabla \cdot \left(\sum_k g_k \rho_k (\vec{V}_k - \vec{V}) (u_{i_k} - u_i) \right) - \frac{\partial P}{\partial x_i} + \rho B_i + F_i \quad (5.2)$$

where ρB_i is body force and can be extended as:

$$\begin{aligned} \rho \vec{B} &= (\rho_s g_s + \rho_l g_l + \rho_g g_g) \vec{g} \\ &= (\rho_s g_s + \rho_l g_l + \rho_g g_g + \rho_l g_g - \rho_l g_g) \vec{g} \\ &= (\rho_s g_s + \rho_l g_l + \rho_l g_g) \vec{g} - (\rho_l g_g - \rho_g g_g) \vec{g} \end{aligned} \quad (5.3)$$

and assuming $\rho_l = \rho_s = \rho_{st}$ and neglecting gas density in comparison with steel density, the body force simplifies to:

$$\rho \vec{B} = \rho_{st} \vec{g} - \rho_{st} g_g \vec{g} \quad (5.4)$$

In the numerical formulation, the second term of the above equation is treated as an extra source term in the x-momentum equation due to the gas buoyant force.

5.3.1.1 Assumptions

The distribution of argon-gas bubble concentration, g_g , can be obtained through the solution of the gas-continuity equation. To drive the mass conservation equation for the gas phase, the following assumptions were made:

- 1) The system is in a steady state condition.
- 2) The bubbles are assumed to behave as a rigid body having a spherical shape.
- 3) The gas bubbles have been thermally expanded before feeding to the caster and there is no change of the bubble diameter in the mold due to the temperature or pressure variations.
- 4) Instead of calculation of low-density gas-phase velocity through a separate momentum equation, the bubbles in the liquid steel are assumed to have a constant slip velocity which in axial direction is equal to their terminal velocity and in other directions equal to zero. The terminal velocity of the bubbles in the liquid phase itself was calculated using an empirical correlation developed by Soo (1967) and tested in continuous casting processes by Thomas et al. (1994).

$$u_t = \exp\left[-8.373 - 2.6306(\ln d_g) - 0.25(\ln d_g)^2\right] \quad (5.5)$$

- 5) Since the vertical slip velocity of the gas bubbles, if trapped in the solidifying shell, reaches to zero, the actual terminal velocity of the bubbles penetrated into the mushy layer (if happen), needs to be modified. In fact, the terminal velocity should vary within the mushy zone from its calculated value at the liquid phase (Eq. 5.5) to zero at the solid phase. In the absence of any model or theoretical information for terminal velocity in the mushy region, in the present study, it is assumed that the terminal velocity of a bubble varies linearly as a function of liquid fraction in the mushy zone.

$$u_t^e = g_l u_t \quad (5.6)$$

- 6) The turbulent Schmidt number is assumed to be one and the effective mass-diffusivity of gas bubbles in the mixture is prescribed as equal to the turbulent viscosity of the mixture.

Applying the above assumptions, the continuity equation for bubbles becomes:

$$(u - u_t^e) \frac{\partial g_g}{\partial x} + v \frac{\partial g_g}{\partial y} + w \frac{\partial g_g}{\partial z} = \frac{\partial}{\partial x} \left(D_e^g \frac{\partial g_g}{\partial x} \right) + \frac{\partial}{\partial y} \left(D_e^g \frac{\partial g_g}{\partial y} \right) + \frac{\partial}{\partial z} \left(D_e^g \frac{\partial g_g}{\partial z} \right) \quad (5.7)$$

where

$$D_e^g = \frac{\mu_t}{\rho S c_t} = \nu_t \quad (5.8)$$

5.3.1.2 Non-dimensionalization of governing equations

Considering the dimensionless parameters given in Chapter 3, the transport equations governing a continuous slab casting process with gas injection can be cast into a general non-dimensionalized form as follows:

$$\frac{\partial(U_i \Phi^*)}{\partial X_i} = \frac{\partial}{\partial X_i} (\Gamma_\phi^* \frac{\partial \Phi^*}{\partial X_i}) + S_\phi^* \quad i = 1, 2, 3 \quad (5.9)$$

where the value of Φ^* and associated value of Γ_ϕ^* are given in Table 5.1.

It is to be noted that the source term related to the phase motion has been dropped from the energy equation. This can be justified according to the assumption of equiaxed solidification in the mold region and negligible relative phase velocity in the dendritic solidification believed to be occurring in the submold region.

5.3.2 Boundary Conditions

The boundary conditions used for fluid flow and heat transfer in the present study are identical to those given in Chapter 3, however, the value of average heat transfer coefficient for mold and submold walls were fixed at 1.1 and $0.6 \text{ kW/m}^2 \text{ K}$, respectively. For gas distribution, the normal gradient of gas volume fraction, g_g , was set to zero at all boundaries except at the inlet. It is clear that the above boundary conditions with zero normal velocity on the wall and symmetry planes satisfy no gas flow through these boundaries. However, the gas bubbles can leave the caster from the meniscus surface at a rate proportional to their terminal velocities. The boundary conditions also take into account the fact that any bubble trapped in the solidifying shell can also exit the caster with the casting speed.

Table 5.1. Summary of the non-dimensional governing equations.

Equation	Φ^*	Γ_ϕ^*	S_ϕ^*
Continuity	1	0	0
U-momentum	U	$\frac{1}{Re}(1+\mu_i^*)$	$-\frac{\partial P^*}{\partial X} + \frac{\partial}{\partial X_i} \left(\Gamma_\phi^* \frac{\partial U_i}{\partial X} \right) - \frac{A^*}{Re}(U-U_s) - \frac{1}{Fr} g_g$
V-momentum	V	$\frac{1}{Re}(1+\mu_i^*)$	$-\frac{\partial P^*}{\partial Y} + \frac{\partial}{\partial X_i} \left(\Gamma_\phi^* \frac{\partial U_i}{\partial Y} \right) - \frac{A^*}{Re}(V-V_s)$
W-momentum	W	$\frac{1}{Re}(1+\mu_i^*)$	$-\frac{\partial P^*}{\partial Z} + \frac{\partial}{\partial X_i} \left(\Gamma_\phi^* \frac{\partial U_i}{\partial Z} \right) - \frac{A^*}{Re}(W-W_s)$
Kinetic energy	k^*	$\frac{1}{Re} \left(1 + \frac{\mu_i^*}{\sigma_k} \right)$	$\frac{G^*}{Re} - \varepsilon^* + \frac{D_k^*}{Re}$
Rate of energy dissipation	ε^*	$\frac{1}{Re} \left(1 + \frac{\mu_i^*}{\sigma_\varepsilon} \right)$	$\frac{1}{Re} f_1 C_1 G^* \frac{\varepsilon^*}{k^*} - C_2 f_2 \frac{\varepsilon^{*2}}{k^*} + \frac{E_\varepsilon^*}{Re^2}$
Energy	h^*	$\frac{1}{Re} \left(\frac{1}{Pr} + \frac{\mu_i^*}{\sigma_t} \right)$	$-\left(\frac{\partial U \Delta H^*}{\partial X} + \frac{\partial V \Delta H^*}{\partial Y} + \frac{\partial W \Delta H^*}{\partial Z} \right)$
Gas concentration	g_g	$\frac{\mu_i^*}{Re}$	$U_i^e \frac{\partial g_g}{\partial X}$

where:

$$G^* = \mu_i^* \left(\frac{\partial U_i}{\partial X_j} + \frac{\partial U_j}{\partial X_i} \right) \frac{\partial U_i}{\partial X_j}, \quad D_k^* = 2 \frac{\partial \sqrt{k^*}}{\partial X_i} \frac{\partial \sqrt{k^*}}{\partial X_i}, \quad \mu_i^* = Re C_\mu f_\mu^* \frac{k^{*2}}{\varepsilon^*},$$

$$E_\varepsilon^* = 2 \mu_i^* \left(\frac{\partial^2 U_i}{\partial X_j \partial X_k} \right) \left(\frac{\partial^2 U_i}{\partial X_j \partial X_k} \right), \quad f_\mu^* = e^{\frac{-3.4}{(1+Re_i^*/50)^2}}, \quad Re_i = Re \frac{k^{*2}}{\varepsilon^*},$$

$$Fr = \frac{u_{in}^2}{gD}, \quad Re = \frac{\rho u_{in} D}{\mu}, \quad f_2 = 1 - 0.3 e^{-Re^2}, \quad A^* = \frac{C^*(1-g_l)^2}{g_l^3 + q}, \quad f_1 = 1,$$

$$C_\mu = 0.09, \quad C_1 = 1.44, \quad C_2 = 1.92, \quad \sigma_k = 1.0, \quad \sigma_\varepsilon = 1.3, \quad \sigma_t = 0.9$$

5.4 Solution Method

To solve the fully coupled partial differential equations listed in Table 5.1, along with their boundary conditions, a 3-D numerical code was developed based on the control-volume finite-difference method. Due to the symmetry conditions only a quarter of the slab was selected for modeling and it was first divided into the control volumes as illustrated schematically in Fig. 2.1 (Chapter 2). Then the governing equations were discretized into algebraic form as follows:

$$\alpha_p \phi_p = \sum_{\substack{nb \\ \text{all neighbouring points}}} \alpha_{nb} \phi_{nb} + b \quad (5.10)$$

In the method of discretization, the convective terms were evaluated using a power-law scheme and the source terms were considered to vary stepwise at the face of the control volumes. The well-known SIMPLE algorithm originally proposed by Patankar (1980) was employed in order to resolve the velocity-pressure coupling in the momentum equations. The algebraic equations obtained from the discretization of the governing equations were solved sequentially in an iterative manner using a TDMA solver and the iteration loop was terminated when the maximum of absolute residual calculated for each of the variables was less than a small number chosen here as 0.001.

5.5 Results and Discussion

A 3-D numerical code was developed to simulate turbulent fluid flow, solidification heat transfer and argon gas bubble dispersion in a typical industrial continuous stainless steel slab casting system. In this caster, the liquid steel is fed into the mold with dimensions of 1.27 m x 0.254 m x 0.75 m (width x thick x height), through a submerged entry nozzle (SEN) located at the center of the mold. For computational simplicity, the nozzle is assumed to have a square cross-section with inner length of 85 mm. The submergence depth, defined as the distance from meniscus and nozzle port

center, was kept constant at 0.34 *m*. The nozzle ports were also assumed to be in a rectangular shape. The thermo-physical properties of 304 stainless steel, casting conditions and information on gas bubble injection used in the present simulations are listed in Table 5.2. The validity of the code was already tested, as explained in Chapters 2 and 3, through the prediction of fluid flow and solidification phenomena in continuous slab casting processes. The gas dispersion model adopted in the present code was also verified by conducting an additional numerical simulation with the conditions listed in Table 5.2 which were taken from the experimental and numerical studies carried out by Bessho et al. (1991).

Figure 5.1 shows 3-D surface velocity vectors and gas volume fraction distributions at the meniscus, and upper part of the wide and symmetry planes for the condition used by Bessho et al. (1991). From this figure, one can see that the region in which the high gas volume fraction exists is expanded more vertically due to the four-port nozzle used in this case. The latter causes a reduction in the liquid steel velocity at the nozzle port compared to the traditional two-port nozzles. The bi-modal shape of the gas fraction contours close to the nozzle ports are also associated with the special nozzle port shape used by Bessho et al. The gas bubbles are gradually mixed with distance from the nozzle ports and produce smoother gas bubble contours. To compare the obtained results with those predicted by Bessho et al. the flow field and gas distribution are presented for the wide symmetry plane in Figs. 5.2 and 5.3, respectively. As seen in these figures, a similar trend of the water velocity field and gas penetration was found in these two studies. A quantitative comparison between the measured data and calculated results at two different depths of the mold is presented in Fig. 5.4. The present model predicts a similar trend for gas volume fraction variation, however the underprediction of gas concentration in the region far from the nozzle ports can be attributed to the assumption of spherical shape for bubbles, which is not necessarily true in the high turbulent process of continuous casting. The non-spherical shape of the bubbles may cause an increase in the drag force acting from the jet onto the bubbles and consequently forces the bubbles to travel deeper towards the narrow face. On the other hand, it may also decrease the actual

terminal velocity of the bubbles, which can yield again to higher residence times for bubbles in the mold and their deeper penetration towards the impingement region.

Table 5.2. Thermophysical properties of steel, casting conditions and geometrical parameters used for the simulation.

Variable	Present study	Bessho et al. (1991)
slab width	1.27 m	1.5
slab thickness	0.254 m	0.22
nozzle port width	0.058 m	0.08 at top 0.06 at bottom
nozzle port height	0.1 m	0.056 for top port 0.072 for bottom port
nozzle submergence length	0.34 m	0.19 to top port center
caster length simulated	3.0 m	3.0
casting speed	0.02 ms ⁻¹	0.02
viscosity	0.007 kgm ⁻¹ s ⁻¹	0.001
density	7000 kgm ⁻³	1000
thermal conductivity (liquid or solid)	31 Wm ⁻¹ K ⁻¹	
specific heat (liquid or solid)	700 Jkg ⁻¹ K ⁻¹	
latent heat of fusion	264 kJkg ⁻¹	
liquidus temperature	1454° C	
solidus temperature	1400° C	
inlet temperature	1480° C	
mold length	0.75 m	
mold wall heat transfer coefficient	1.1 kWm ⁻² K	
submold wall heat transfer coefficient	0.6 kWm ⁻² K	

Figure 5.5 represents the effect of solidification and gas bubble injection on the predicted 3-D velocity field at the meniscus, wide and narrow symmetry planes with and without gas injection for the conditions listed in Table 5.2 and under the column of present study. The 3 mm diameter argon gas bubbles were assumed to enter into the caster having 11% gas volume fraction with the temperature identical to the inlet superheated steel temperature. Generally, the liquid steel discharging into the mold impinges on the narrow face of the slab and is then divided into upward and downward flows which create an upper and a lower recirculating loop, respectively. The length of the lower recirculation loop was found to be dependent on the development of the solid and mushy layers, which are directly related to the casting speed and mold and submold heat extraction rates. As explained in Chapter 3 the lower recirculation loop extends much deeper into the mold in the case of water as fluid in which no solidification takes place. The injection of gas bubbles into the caster significantly changes the molten steel flow pattern in the mold. The change in the flow field is more visible above the nozzle port where a very strong buoyant force is acting upward on the steel motion. In fact, most of the gas entering the caster through immersion nozzle is seen to float upward after releasing from nozzle ports. Parts of the gas are also carried horizontally with convective jet which is weakening by traveling towards the narrow face of the slab.

Figure 5.6 represents gas volume fraction distribution for two cases, one with and another without solidification, in which the gas blown conditions are similar to those mentioned for Fig. 5.5. As seen in this figure, only a very small portion of gas bubbles may penetrate the narrow face of the slab and most of these are accumulated around the nozzle ports. A comparison between the results shown in these two figures indicates that there is only a small change in gas bubble distributions for these cases. When the solidification phenomena takes place in the mold, the existence of the solid and mushy layers may increase the resistance against which the gas must flow to arrive at the narrow face. This limits the horizontal penetration of the gas bubbles and causes the gas bubbles to be more crowded around the nozzle. On the other hand, the accumulation of the gas bubbles at the

center of the mold leads to a higher gas concentration close to the solidifying shell growing on the broad face of the slab.

5.5.1 Effect of Bubble Size

Figures 5.7 and 5.8 show the effect of gas bubble size injected into the mold on the flow pattern and gas dispersion, respectively, for three different diameter of bubbles, i.e. 1, 2 and 3 *mm* and for the case of no gas injection. In the case of no gas injection, the counterclockwise rotation of the molten steel flow in the upper recirculation loop causes a liquid motion at the meniscus towards the center of slab. However, the injection of gas leads the main steel stream discharging from nozzle port to be deflected upward and after reaching the stagnation point at the meniscus, is divided into two flows; one directed to the narrow face and the other one towards the slab center. The location of the stagnation point at the meniscus shifts towards the center of the slab by increasing the bubble size due to the more concentrated gas bubbles close to the nozzle zone. The increase of the bubble diameter causes an increase in the terminal velocity of the bubbles and consequently an enhancement on the floatation of the bubbles. The latter fact is the principal reason that the gas bubbles have been more concentrated around the nozzle port at the center of the mold for the 3 *mm* diameter bubble, while they are penetrated more horizontally across the mold for the 1 *mm* diameter bubble. The gas bubble concentration contours at the meniscus for these three cases also show that, when bubble size is small, i.e. 1 *mm*, much more area of the slab wide face is affected by the presence of the gas.

For a better appreciation of the gas dispersion and gas entrapment in the solidifying shell, the gas volume fraction contours in the transverse cross-sectional planes of the slab at various depths for 3 and 1 *mm* bubble sizes have been plotted in Figs. 5.9 and 5.10, respectively. A comparison of these contour plots shows that the gas fraction at the slab surface for 1 *mm* bubble size is almost 5 to 8 times greater than that for 3 *mm* bubble size. Some of the bubbles which were close to the wide face of the slab were trapped in the mushy and solid layers, whereas the bubbles close to the narrow face could easily escape and leave the caster through meniscus. This observation can be addressed by

the fact that the mushy layer developing on the narrow face at the top part of the mold is very thin due to the impingement of the hot liquid steel jet there. The difference between the gas volume fractions along the narrow and wide faces at the meniscus can be viewed as one other factor for the above remark on the bubble entrapments. For both cases, the bubble concentration contours in the cross-sectional plane at a non-dimensional depth of 4.7, which is located under the nozzle port, remained unchanged further downstream and represent the solid region in which the argon gas bubbles were trapped. As seen in these figures, for 1 mm gas bubble the entire width of the slab is affected by the entrapped gas in the solidifying shell, and for 3 mm bubble only a small area close to the center displays the gas entrapment. The maximum and average values of gas bubble fraction entrapped in the first 6 mm layer of solidifying shell for 3 mm bubble were found to be 0.13×10^{-2} and 0.47×10^{-3} , respectively. These values for 1 mm bubble injection were found to increase to 0.7×10^{-2} and 0.3×10^{-2} , respectively. While the location of the maximum bubble entrapment for 3 mm bubble corresponds to the maximum gas fraction at the meniscus, for the 1 mm bubble injection two maximums were obtained both of which are located at the wide face of the slab; one close to the center and the other close to the corner.

5.5.2 Effect of Gas Injection Rate

To study the effect of gas injection rate on the flow field in the mold, three different inlet gas volume fractions were selected and tested numerically for the injection of a constant diameter bubble of 3 mm. Figures 5.11 and 5.12 provide the 3-D surface velocity vector plot and gas concentration distributions, respectively, at the meniscus, narrow and wide symmetry planes of the slab for various gas injection rates. Although the location of the stagnation point at the meniscus did not change with the variation of the gas injection rate, the strength of the two liquid streams at the meniscus, which are directed towards the narrow face and center of the slab, increased considerably with the increase in the inlet gas volume fraction. The higher value of the velocity at the meniscus, which is associated with a higher level of turbulence, may drag the mold powder and collected inclusions at the meniscus towards the narrow face and increase the possibility of

a greater inclusion entrapment in the solidifying shell. Similarly, the downward velocity along the narrow face becomes greater for higher gas blown rate, which increases the depth of the lower recirculation loop as well as the penetration depth of the inclusions.

5.5.3 Effect of Gas Injection on Mushy Region Solidification

Although the argon gas injection was proved to have a significant effect on the fluid flow in the actual operation of a continuous slab casting system, a minimal change was seen in the development of the solid and mushy layers. Figures 5.13 and 5.14 represent the solidus and liquidus contours for the various transverse cross-sectional planes of the slab without and with gas injection, respectively. A comparison of these results indicates that most of the differences between these two figures are related to the development of the mushy regions. In the case of no gas injection, the wavy shape of the mushy-liquid interface and remelting of a part of the mushy region, especially at the wide face of the slab and around the nozzle port ($X=3.5-5$), is due to the horizontal expansion of the hot liquid steel jet discharging from the nozzle port. When gas is blown into the caster, the inflow steel is deflected upward after leaving the nozzle port and upon approaching to the meniscus it produces a region with higher sensible heat content and prevents the thickening of the mushy layer developed on the wide face of slab for a depth up to about 3.4. A relatively thin mushy layer formed at the center of the wide face for higher depths in the case of gas injection is due to the quick returning of the hot liquid steel from the center of the meniscus. In fact, when gas is blown into the mold, the upper recirculation loop becomes smaller and the liquid steel stays for a shorter time in the upper part of the mold and returns downward with a relatively higher temperature. The meniscus temperature is moderately influenced by the gas injection. The average temperature close to the meniscus was found to increase due to gas blown into the caster. This increase in temperature was dependent on both gas injection rate and bubble size. The average temperature rise at the meniscus for 11% gas injection rate was predicted to be about 1.7, 3.2 and 5.1° C for 3, 2 and 1 mm bubble size, respectively. Similarly, for a constant bubble

diameter of 3 mm the above average temperature increased by about 1.7, 2.5 and 3° C for the injection of 11, 16 and 22% gas volume fraction at the inlet, respectively.

5.6 Concluding Remarks

In the continuous slab casting processes the nozzle clogging is prevented by pressurizing the nozzle through the injection of an inert gas such as argon into the nozzle. To protect the quality of the cast, the motion and distribution of the gas in the mold as well as their effect on the fluid flow in the mold should be appropriately controlled. In this part, the three-dimensional mathematical model developed in the previous parts is further advanced by incorporating the gas dispersion model into the program. The coupling of the solidification with the other transport phenomena in this numerical simulation makes it possible to study the entrapment of the gas bubbles in the solidifying shell. After validation of the code by comparison of the predicted results of the gas distribution and fluid flow in the mold with those available in the literature, the productive runs are carried out to investigate the effect of the important parameters such as bubble size and gas injection rate on the process operation. The obtained results show that the flow discharging from the nozzle port immediately deflects upward and changes the size of the upper recirculation loop. The injection of the gas in the studied conditions reverses the flow at the meniscus close to the narrow face and generates a stagnation region at the free surface. The results also show that the stagnation region at the meniscus shifts towards the center of slab for higher bubble sizes. Increasing of the gas injection rate intensifies the changes in the flow pattern and increases the average meniscus velocity which may drag the inclusions or powder from meniscus into the caster. The gas bubbles with smaller sizes can travel deeper towards the narrow face of the slab and spread wider in the mold. The simulation results also indicate that the entrapment of the bubbles increases by decreasing of the bubble size. For 11% gas injection rate at the inlet and 1 *mm* bubble size almost the entire width of the slab shows gas entrapment with the level 0.1% and greater, while for 3 *mm* bubble size only a small area of wide face close to the center of the slab shows similar entrapment.

NOMENCLATURE

Symbol	Description
a_p, a_{nb}, b	coefficients in the discretized governing equations
\bar{B}	buoyant force per unit mass
c_1, c_2, c_μ	empirical constants for low Reynolds turbulent models
D	hydraulic diameter of SEN
c_s	solid specific heat
d_g	bubble gas diameter
D_e^g	effective diffusivity of gas bubbles
D_k	extra dissipation term in k -equation
E_ε	extra generation term in ε -equation
f_1, f_2, f_μ	empirical constants for low Reynolds turbulent models
Fr	Froude number
g_g	gas fraction
g_l	liquid fraction
g_s	solid fraction
G	turbulent kinetic energy generation in k -equation
k	turbulent kinetic energy
P	Pressure
Pr	laminar Prandtl number
Re	laminar Reynolds number
Re_t	turbulent Reynolds number based on the turbulent quantities
$S_{g,x}$	buoyant force per unit volume in x-direction due to gas injection
S_Φ	source term associated with Φ
Sc_t	turbulent Schmidt number
u_i	time-average velocity component in the i-th direction

u_s	casting speed
u_t	terminal velocity of bubble gas
u_t^e	effective terminal velocity of bubble gas

Greek Symbols

ε	turbulent kinetic energy dissipation rate
Γ_Φ	diffusion coefficient associated with Φ value
μ	laminar viscosity
μ_t	turbulent viscosity
Φ	generalized dependent variable
ρ	mass density
ρ_g, ρ_l, ρ_s	gas, liquid and solid densities, respectively
σ_l	laminar Prandtl number
σ_t	turbulent Prandtl number
$\sigma_k, \sigma_\varepsilon$	empirical constants in turbulent model equations

Superscripts

*	nondimensional variables
capital letters	nondimensional variables

References

- Bennon W. D. and Incropera F. P., A continuum model for momentum, heat and species transport in binary solid-liquid phase change systems-I. model formulation. *Int. J. Heat Mass Transfer*, Vol. 30, No. 10, pp. 2161-2170, (1987).
- Bessho N., Yoda R., Yamasaki H., Fujii T., Nozaki T. and Takatori S., Numerical analysis of fluid flow in continuous casting mold by bubble dispersion model, *ISIJ International*, Vol. 31, No. 1, pp. 40-45, (1991).
- Launder B. E., and Sharma B. I., Application of The Energy Dissipation Model of Turbulence to The Calculation of Flow Near a Spinning Disc, *Letters In Heat and Mass Transfer*, Vol. 1, pp. 131-138, (1974).
- Patankar S. V., *Numerical Heat Transfer and Fluid Flow*, Hemisphere, Washington, D.C., (1980).
- Soo S. L., *Fluid dynamics of multiphase system*, Blaisdell Publishing Co., Waltham, MA, (1967).
- Thomas B. G., Huang X., and Sussman R. C., Simulation of argon gas flow effects in a continuous slab caster, *Met. Trans.*, Vol. 25B, pp. 527-547, (1994).
- Zhu M.-Y., Sawada I., Yamasaki N., and Hsiao T.-C., Numerical simulation of three-dimensional fluid flow and mixing process in gas-stirred ladles, *ISIJ International*, Vol. 36, No. 5, pp. 503-551, (1996).

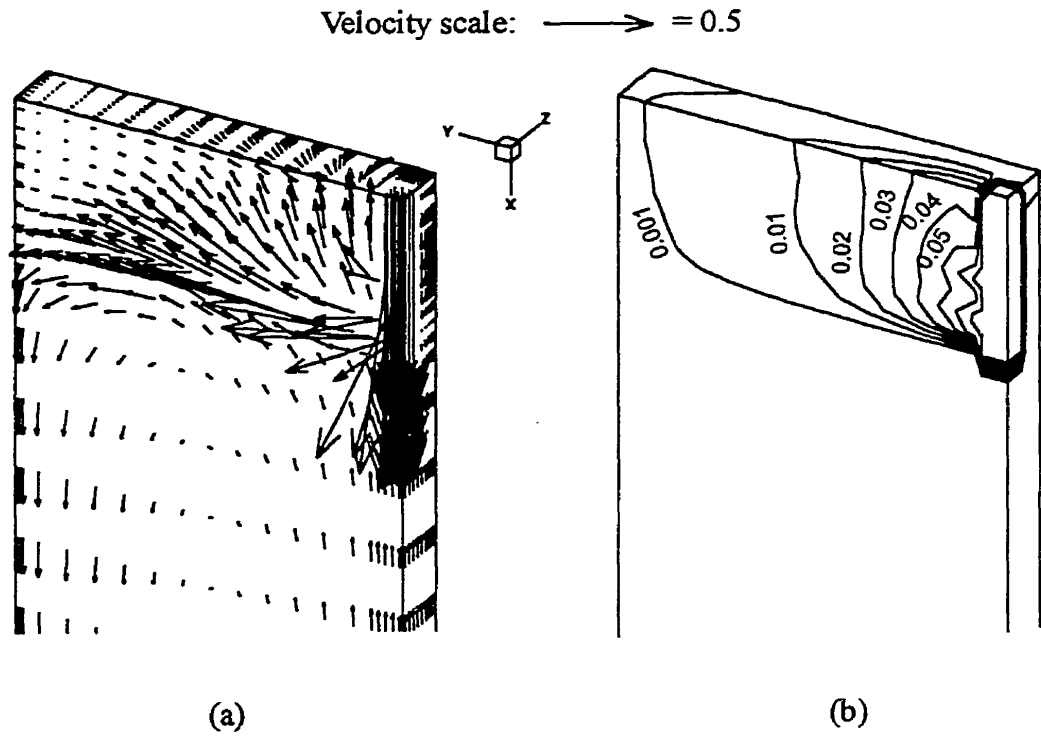


Fig. 5.1. 3-D surface plot of the velocity vectors and gas volume fraction for a continuous slab caster operating with the condition used by Bessho et al. (1991); (a) velocity field, (b) gas volume fraction distribution.

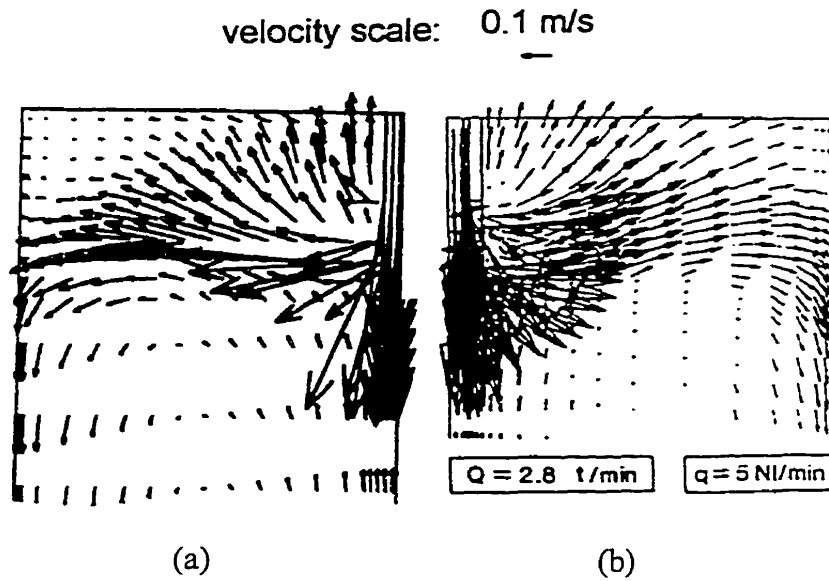


Fig. 5.2. Predicted liquid velocity profiles in the water modeling operating with the condition used by Bessho et al. (1991); (a) present study, (b) Bessho's prediction.

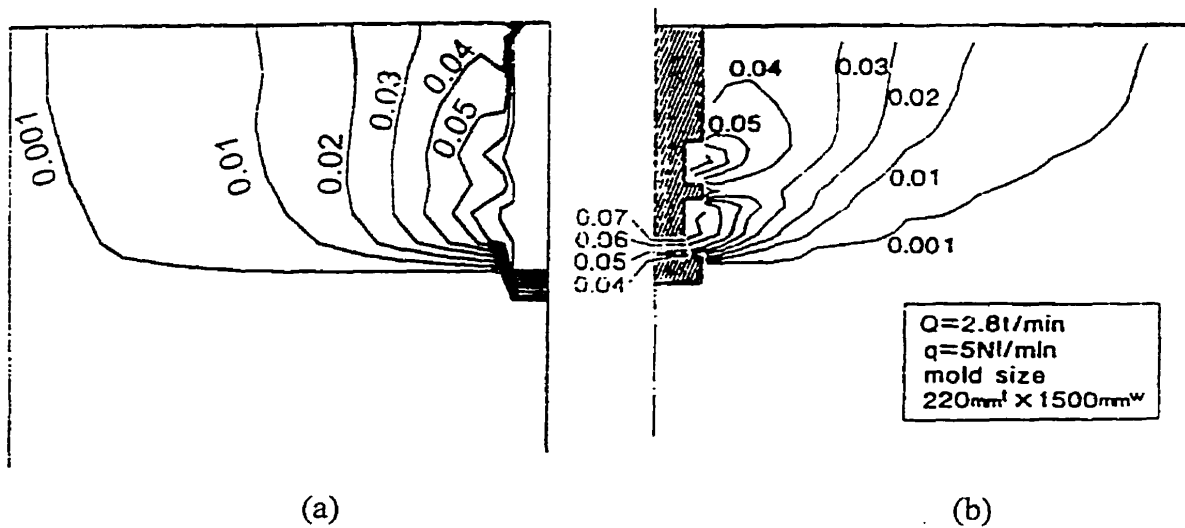


Fig. 5.3. Predicted gas volume fraction distributions in the water modeling operating with the condition used by Bessho et al. (1991); (a) present study, (b) Bessho's prediction.

Bessho et al's

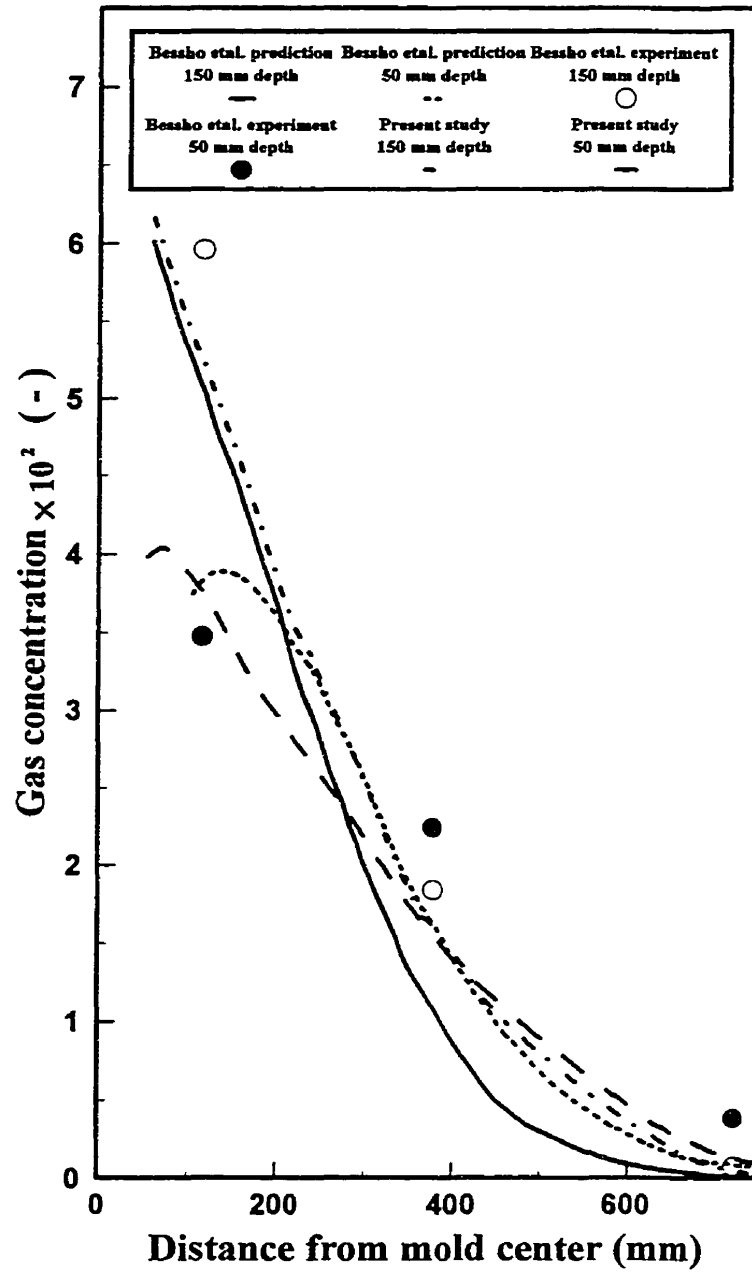


Fig. 5.4. A comparison between predicted gas volume fraction distributions in the present study and those obtained numerically and experimentally by Bessho et al. (1991) for water modeling.

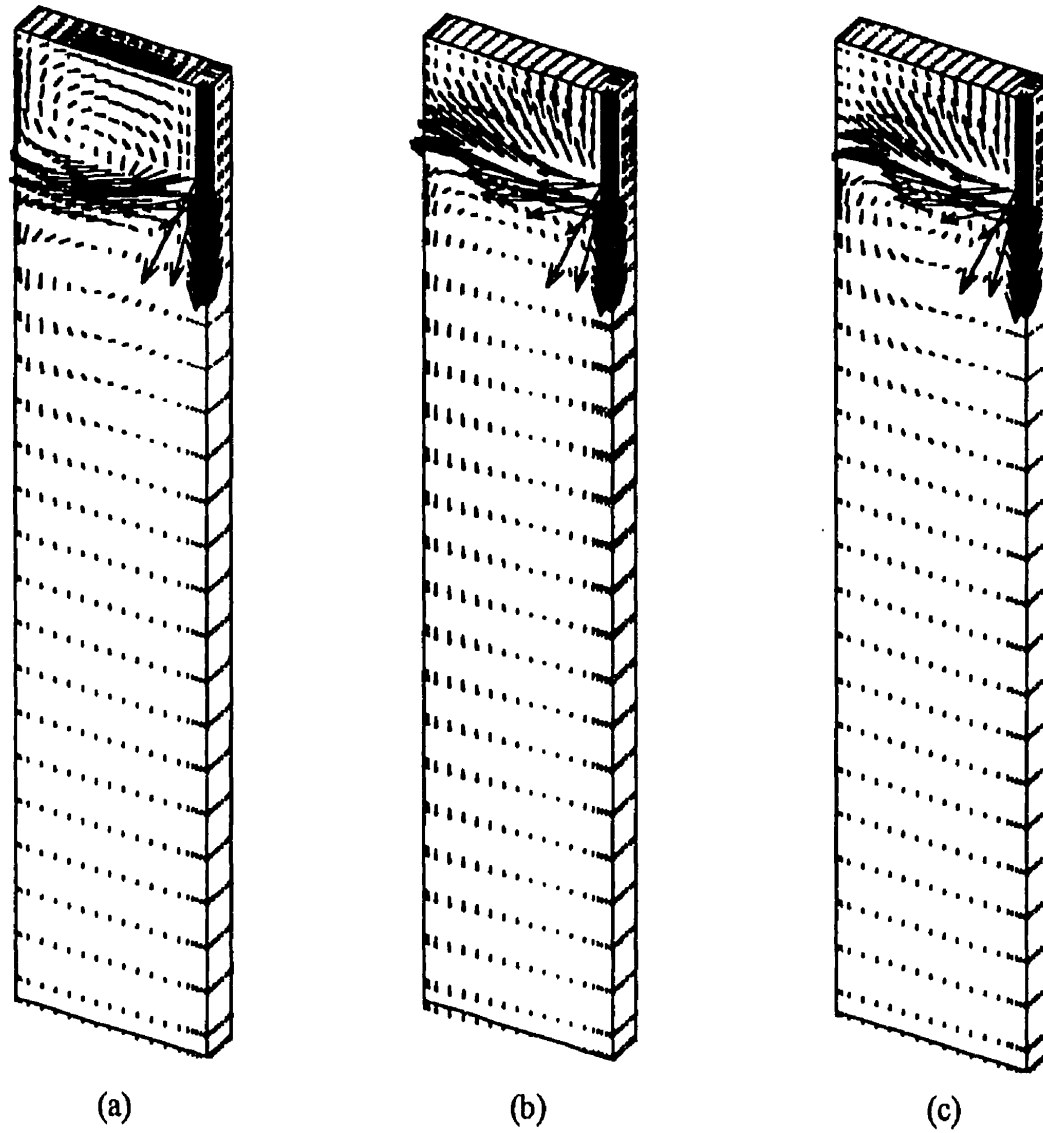


Fig. 5.5. 3-D surface plot of the velocity vectors for a continuous slab caster at various conditions; (a) with solidification and without gas injection, (b) with gas injection and without solidification, (c) with both solidification and gas injection.

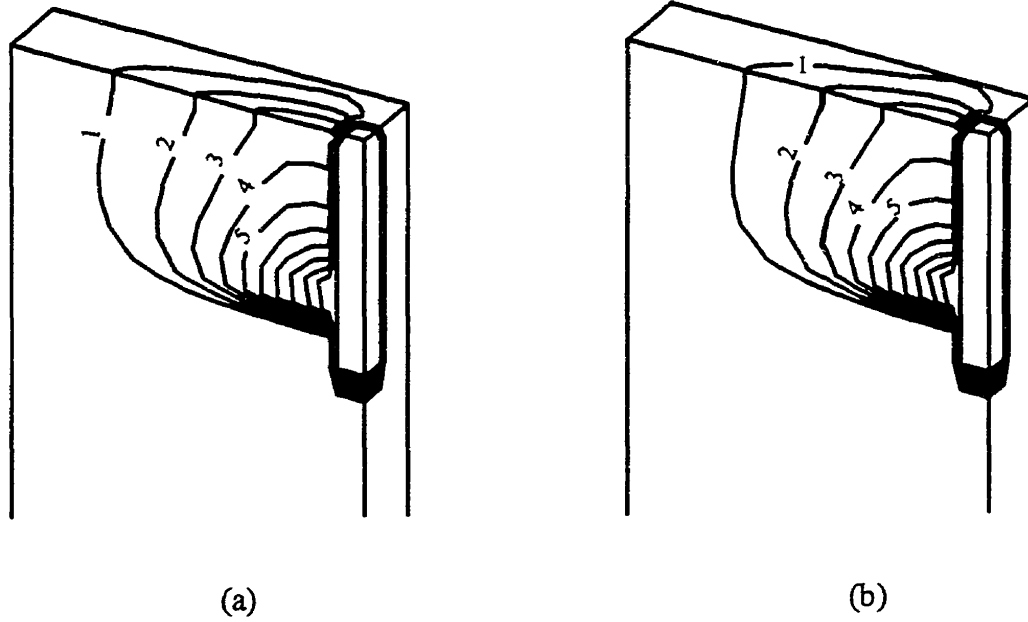


Fig. 5.6. 3-D surface plot of gas volume fraction contours for a continuous slab caster; (a) without solidification, (b) with solidification.

Velocity scale: $\longrightarrow = 0.5$

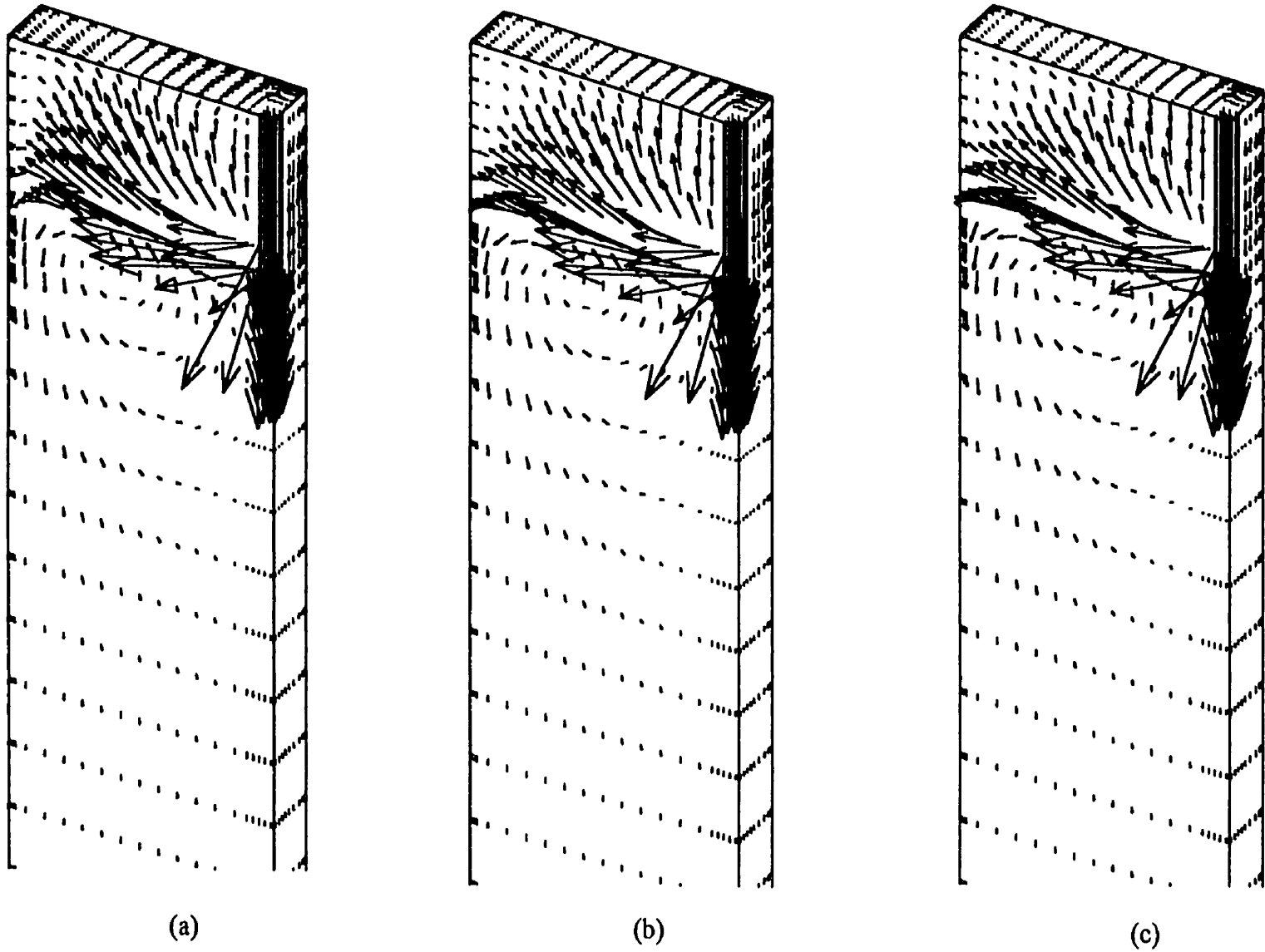


Fig. 5.7. Effect of argon gas bubble size on 3-D surface plot of velocity vectors for a continuous slab caster with inlet injection rate of 11% and various bubble size; (a) 1 mm, (b) 2 mm, (c) 3 mm.

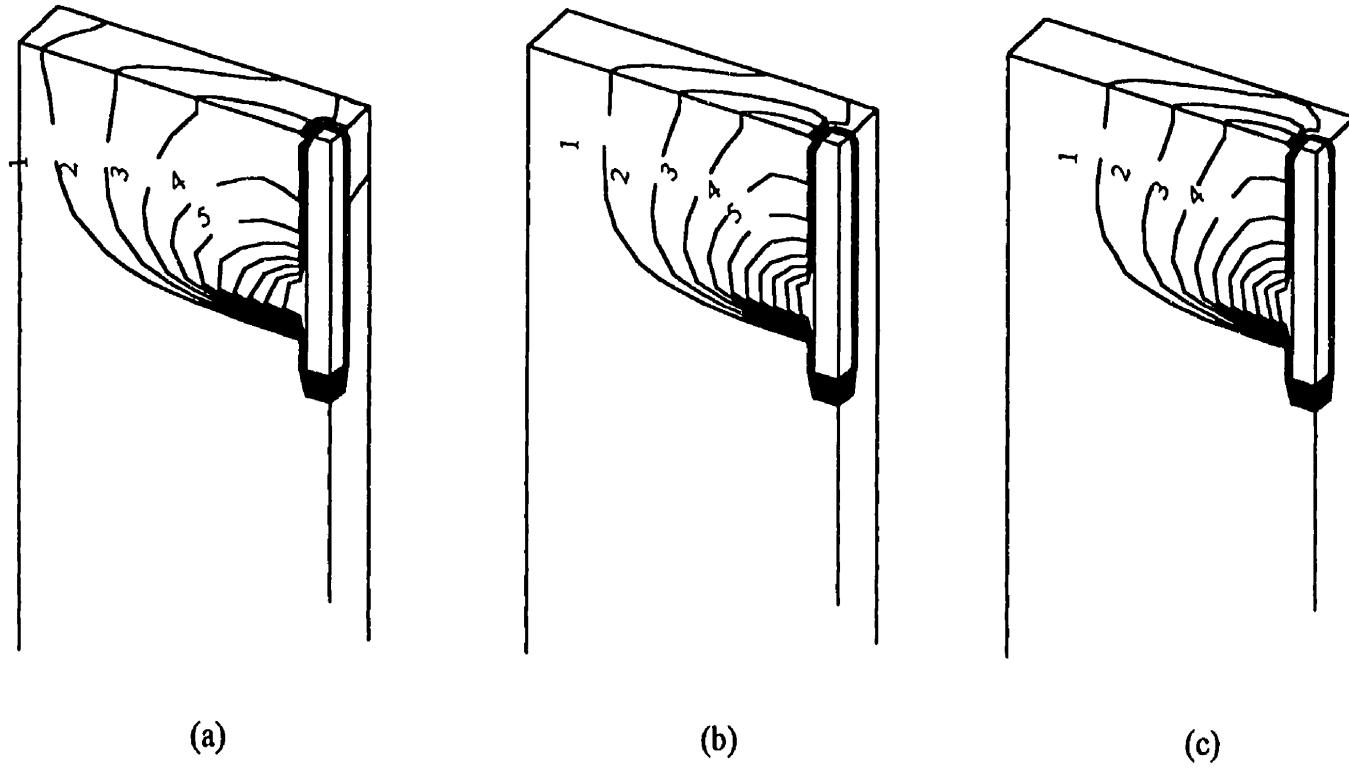


Fig. 5.8. Effect of argon gas bubble size on 3-D surface plot of gas volume fraction contours for a continuous slab caster with inlet injection rate of 11% and various bubble size; (a) 1 mm, (b) 2 mm, (c) 3 mm.

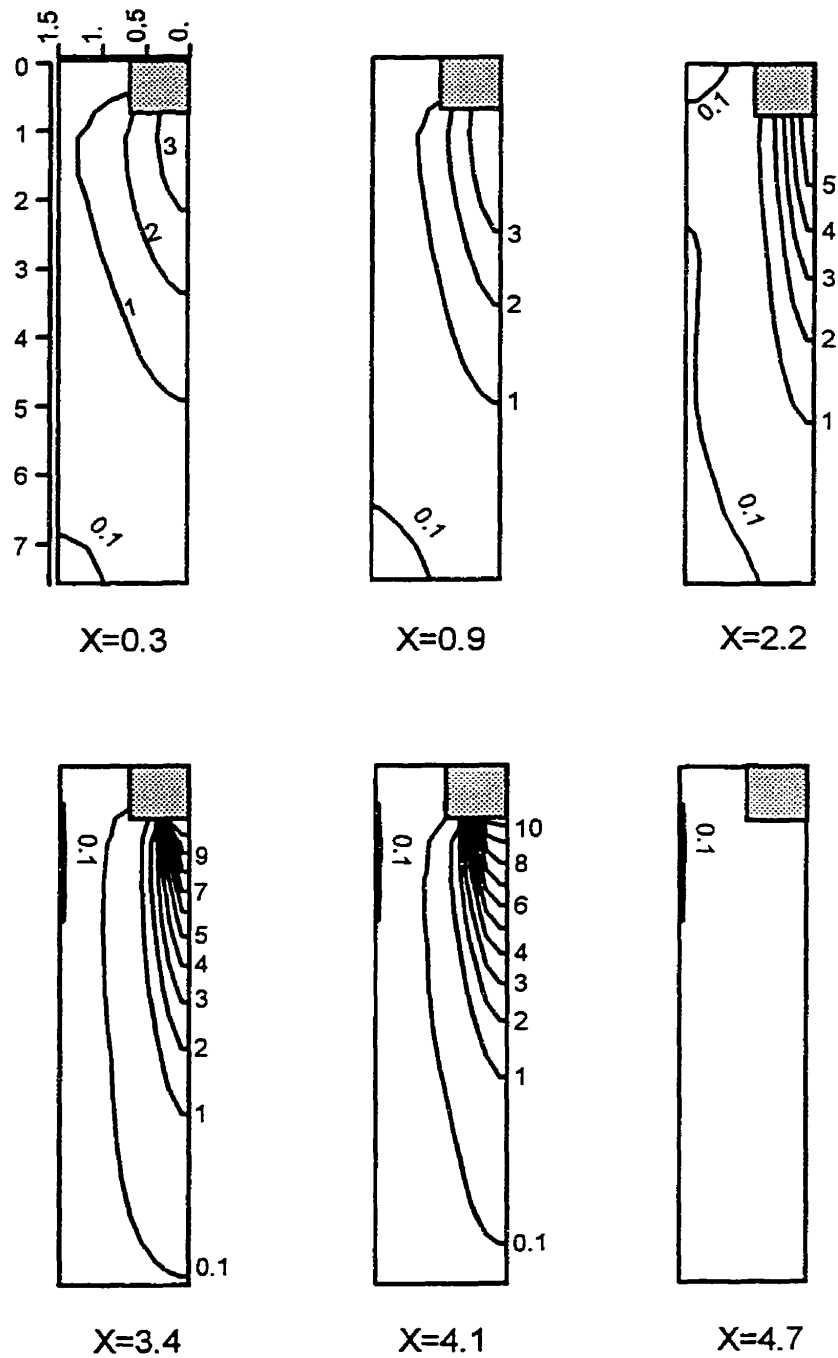


Fig. 5.9. Gas volume fraction contours in the various cross-sectional planes of a continuous slab caster with 11% gas injection rate and 3 mm bubble size.

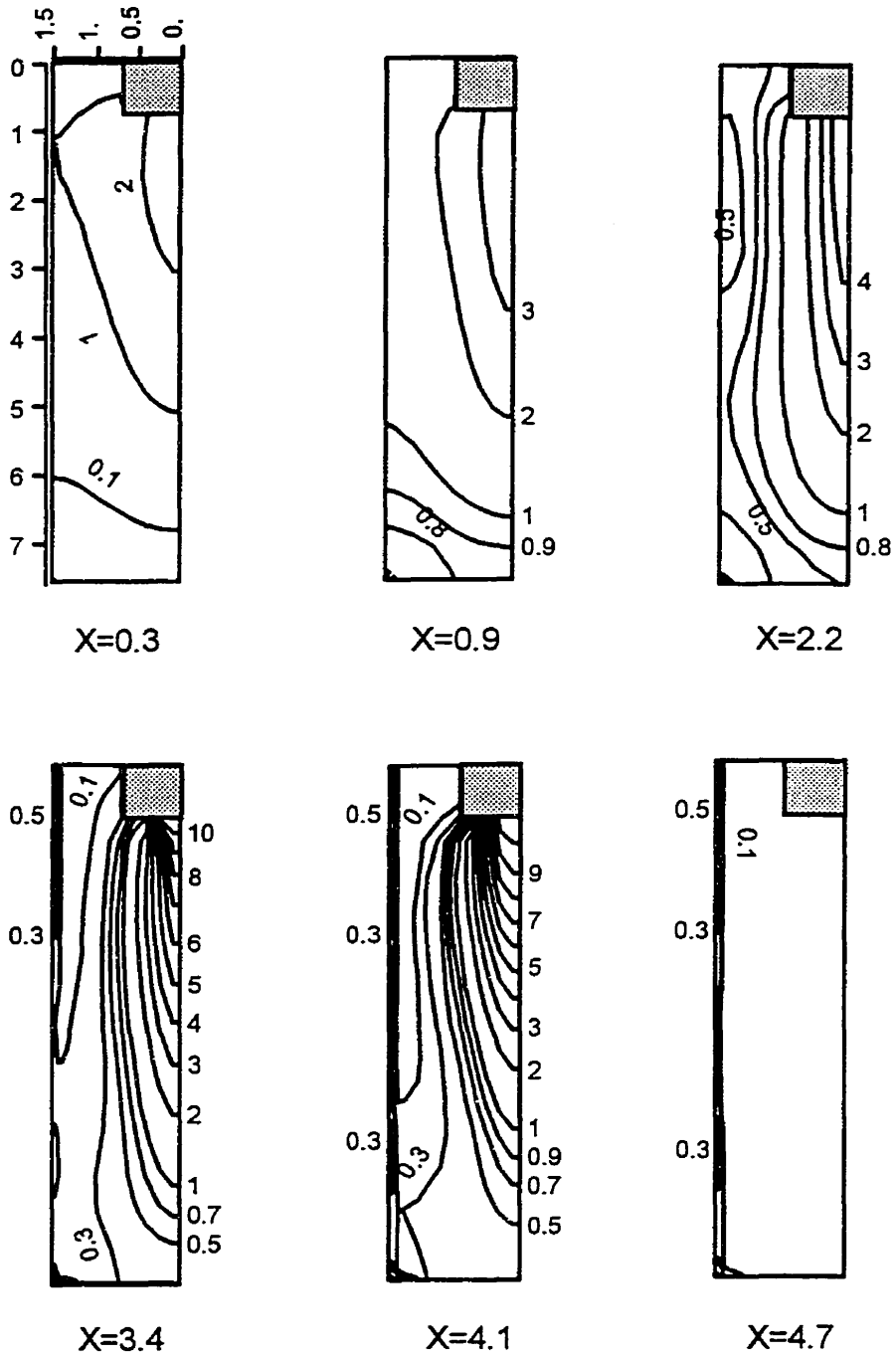


Fig. 5.10. Gas volume fraction contours in the various cross-sectional planes of a continuous slab caster with 11% gas injection rate and 1 mm bubble size.

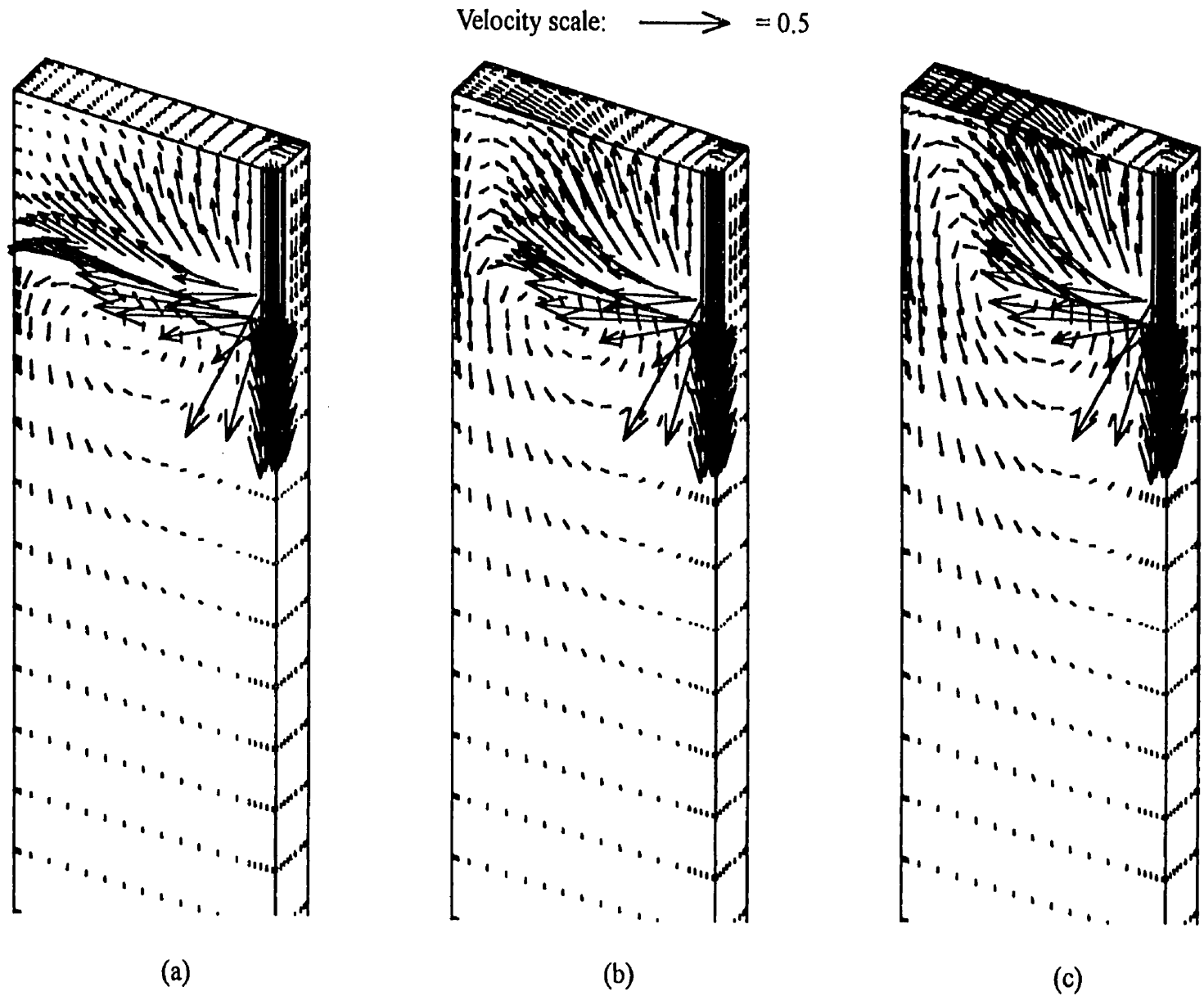


Fig. 5.11. Effect of argon gas injection rate on 3-D surface plot of velocity vectors for a continuous slab caster with bubble size of 3 mm and various inlet gas injection rate; (a) 11%, (b) 16%, (c) 22%.

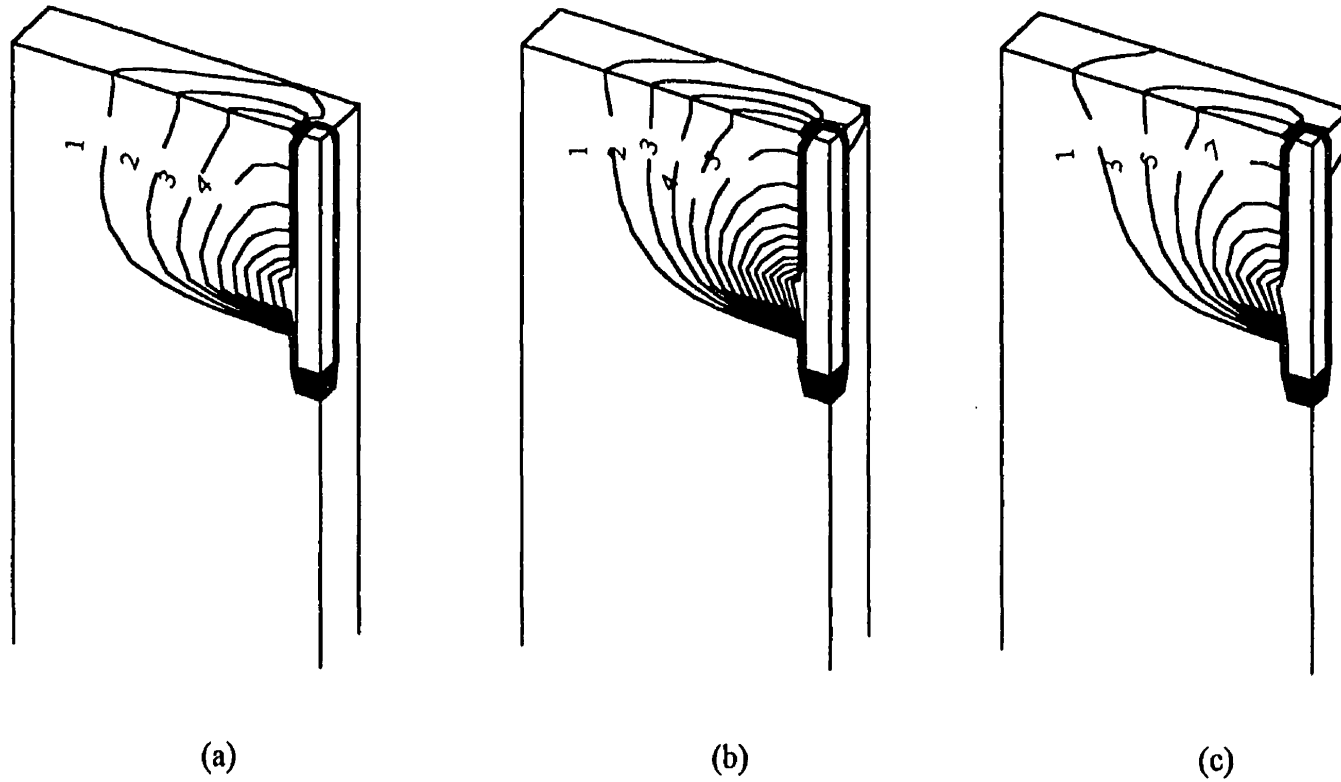


Fig. 5.12. Effect of argon gas injection rate on 3-D surface plot of gas volume fraction contours for a continuous slab caster with 3 mm bubble size and various gas injection rate; (a) 11%, (b) 16%, (c) 22%.

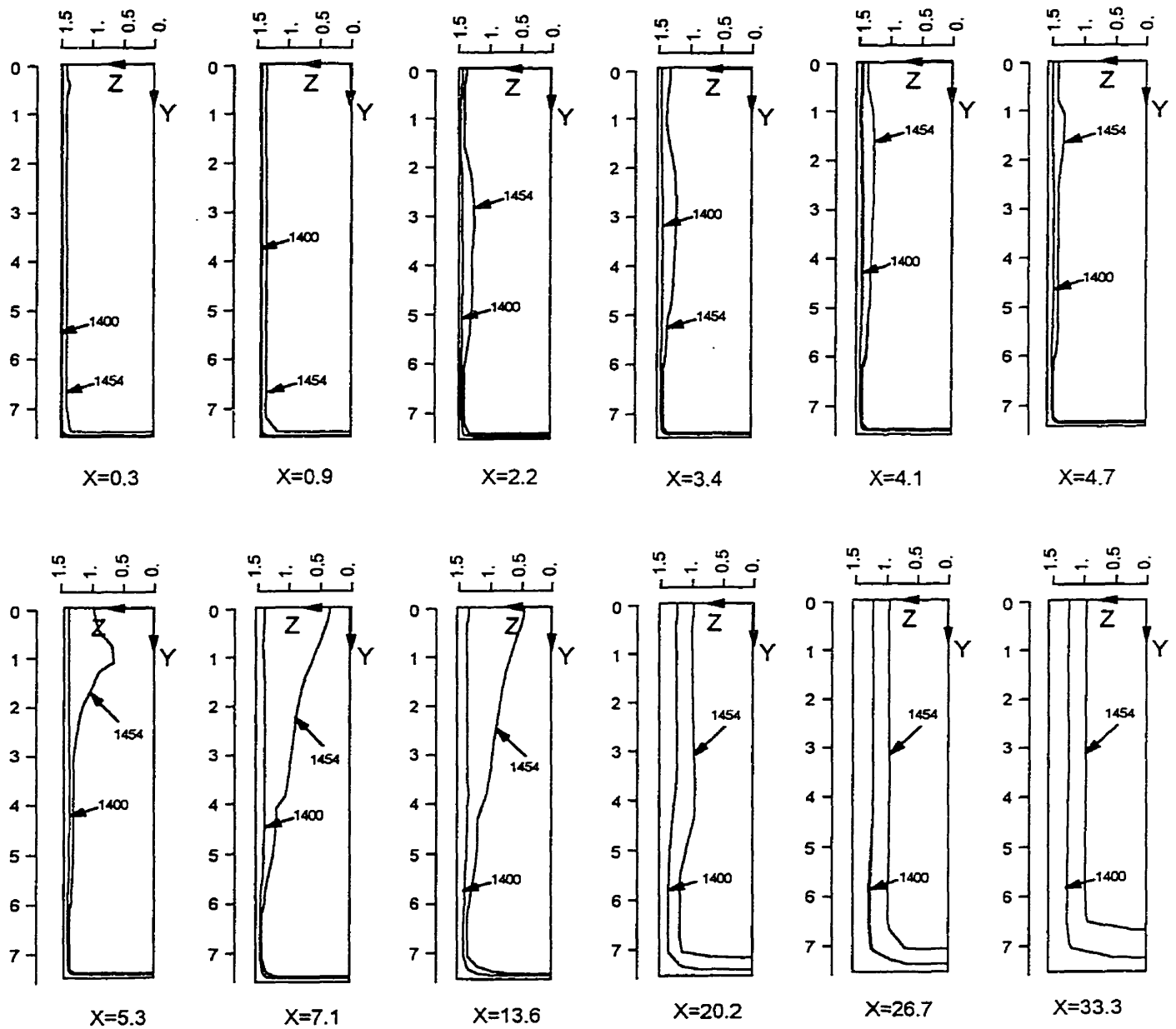


Fig. 5.13. Contours of solidus and liquidus temperatures at various transverse cross-sectional planes (Y-Z planes) for a conventional continuous slab caster without gas injection.

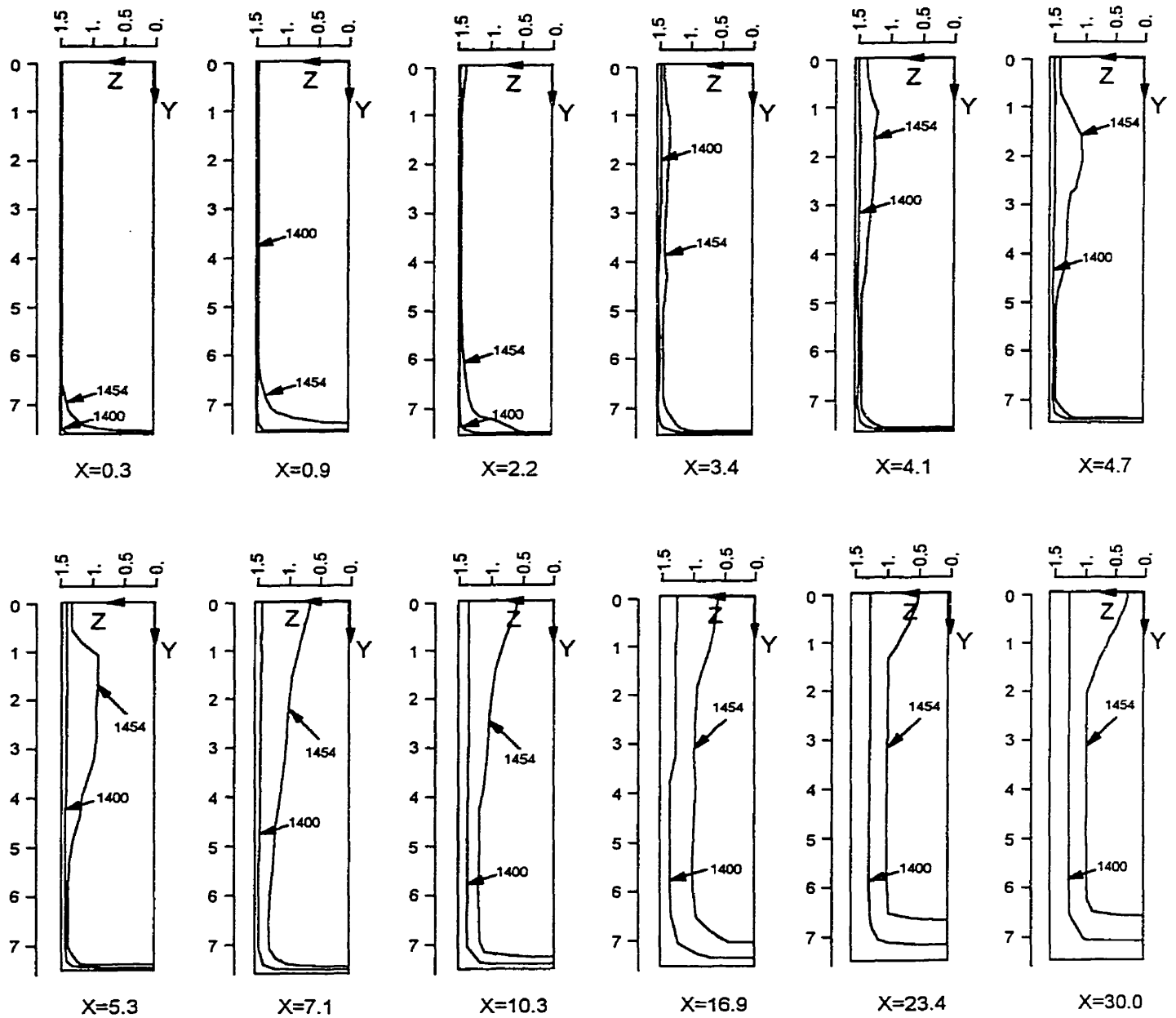


Fig. 5.14. Contours of solidus and liquidus temperatures at various transverse cross-sectional planes (Y-Z planes) for a continuous slab caster with gas injection rate of 11% at inlet and bubble size of 3 mm.

A NUMERICAL STUDY OF TURBULENT TRANSPORT PHENOMENA AND SUPERHEAT DISSIPATION IN A TWIN-ROLL CASTER

6.1 Introduction

Presently, in the western world and in Japan, slabs, billets and blooms of steel are commercially manufactured predominantly through the process of continuous casting. In the past ten years increased efforts have been put by the steel industries worldwide to produce casts near to the final shape and dimension, a process often called *near-net shape casting*. The near-net shape casting facility can have a number of advantages including reduced investment and production costs, increased production yield, energy saving, the possibility of producing new and improved casts.

Among the various efforts undertaken to produce near-net shape casts, the one which has received the most attention from the steelmakers and equipment manufacturers is the vertical twin-roll casting process. The twin-roll casting process has gone through many stages of developments. Recently, a major manufacturer of steel (Nippon Steel Corp., Japan) has announced the construction of the world's first commercial twin-roll caster. The plant is expected to produce thin strips at the end of 1997.

In a vertical twin-roll process, the molten steel is supplied through a nozzle into the wedge-shaped cavity formed by the two-counter rotating water-cooled rolls and two side dams. When the superheated melt comes in contact with the cooled rolls, a thin solidified shell is formed on the surface of each roll. With the continuous extraction of heat through

the moving rolls, the shells gradually grow in thickness, and if right conditions prevail, the two shells finally contact with each other and weld together at the nip of the rolls (minimum clearance between the rolls) and the material exits the system in the form of a solidified sheet.

Considering the complexities involving the operation of a twin-roll casting system, a comprehensive mathematical model can play a significant role to achieve a successful development of such processes.

6.2 Prior Studies

In general, mathematical models developed for twin-roll casting processes can be classified into four main categories, namely, heat flow, isotherm fluid flow, thermal-fluid flow and thermomechanical modelings. In the following section an overview of the previous studies regarding these aspects of the process is presented:

6.2.1 Heat Flow Modeling

Since in the process of twin-roll casting, heat transfer plays a significant role in the operation of phase transformation, the development of the simplest models was based on the pure heat flow modeling. The mathematical modeling in this type was initiated with a simple one-dimensional transient and advanced two-dimensional steady state or transient. The basic idea in one-dimensional heat conduction modeling is that the convection heat transfer at the solid liquid interface as well as heat conduction along the casting direction are neglected. This idea was applied to the mathematical formulation for heat flow in twin-roll casting by O'Malley and Karabin (1988), Caron et al. (1990) and Hirt et al. (1988) for aluminum, and Ozawa et al. (1988) and Kraus (1986) for steel. Perhaps Kraus (1986) and Ozawa et al. (1988) can be specified among the more comprehensive ones of one-dimensional heat flow modeling. The former one developed a 1-D transient conduction heat transfer model for an inclined twin-roll process. He used a finite element method to solve the modeled equation and investigated a modeling parameter sensitivity in carbon

steel systems. The latter one used the finite difference scheme for the solution of the 1-D transient heat transfer equations for both roll and strip. They applied their model for predicting casting of steel strips ranging from 0.2 to 0.5 mm thick and presented extensive parametric studies affecting the casting performance such as: strip thickness, casting speed, cooling water rate and roll material. Bagshaw et al. in a series of studies (1986a, 1986b, 1987, 1988) developed a steady state, two-dimensional finite difference model to describe heat flow in the rolls and strip for a horizontal twin-roll caster. Assuming a very large roll curvature and neglecting the reverse flow, they fixed a uniform flow in the domain. The domain was approximated to be a rectangular surface. They also carried out experimental studies in an Al-Cu alloy system using a horizontal twin-roll caster, and determined the heat transfer coefficients by fitting the predicted strip temperatures at the exit to the ones obtained experimentally. Later, they investigated the effect of strip thickness and roll material on the strip temperature using the mathematical model developed earlier. Caron et al. (1990) and Romanowski et al. (1992), in two separate studies, took into account the effect of roll curvature by including a slice of one-half strip thickness along with the roll surface in their 2-D conduction models. They assumed that the slice of metal moves at the same speed as the roll and neglected the heat transfer at the hotter surface of the strip. Masounave et al. (1988) also developed a 2-D heat conduction model in which the solidification was modeled using the equivalent heat capacity method. They calculated liquid and solid fractions under the assumption of linear relationship between temperature and phase fraction.

6.2.2 Isothermal Fluid Flow Modeling

Modeling of this type can be used to control the liquid metal pool and optimize the design and configuration of the twin-roll casting machines. Bayer-Steinhauer (1992) developed both 2-D and 3-D numerical models to study the fluid flow phenomena between the casting rolls. In their studies, they obtained two recirculation zones which developed due to the interactions of the convective inflow and the roll shear flow. They also showed that a slot nozzle can provide a more uniform velocity distribution compared to the round

caster is easier compared to that of a vertical caster, since the variations of the aspect ratio of the control volumes in a horizontal twin-roll caster are much smaller than that in the vertical one. In order to treat the flow behavior of the liquid, mushy and solid aluminum phases, they assumed that aluminum behaved as the non-Newtonian fluid with a temperature and strain rate dependent viscosity. In order to estimate the solid strip viscosity they used a correlation, which was obtained after fitting the tensile test results. By patching the data of viscosity at T_{liq} and T_{sol} they obtained an exponential function for continuous viscosity function said to be valid for the liquid, mushy and solid regions. One of the weaknesses of this modeling approach is the lack of physical interpretation of viscosity variation in the mushy region.

Ha et al. (1994) developed a program for analyzing the two-dimensional, unsteady transport phenomena in the molten region of a twin-roll continuous casting process. They used their program to predict the velocity and temperature fields along with the solidification profiles for molten steel. Although their computer program seems to be capable of predicting the solidification process in the wedge-shaped thermal cavity, they did not take into account the turbulent effect in their modeling, which must be considered in order to model an industrial size twin-roll casting process. They used the laminar flow equations even for cases when the flow is in fact turbulent. Thus, their obtained results are not realistic for the high production rates used in their study.

Hwang et. al. (1995) considered the start-up problem of the twin-roll casting operation and obtained a numerical simulation of the flow and heat transfer process. They employed a commercial software, PROCAST, which is based on the finite element method. Their study consists of tracking the free surface and the temporal variations of the flow and temperature fields during the filling process of the wedge-shaped pool. In this study molten metal was introduced to the system and progressively developed the metal pool between the rolls. The transient pool level was tracked to reach an optimum level for the withdrawal of the strip. The shape of the free surface was found numerically using a volume of fluid (VOF) approach. Although this study showed how to model the transient

filling process of a twin-roll caster, unfortunately it too was limited for flow situations in which the fluid motion is in laminar condition.

Later, Hwang et al. (1996) carried out numerical and experimental investigations to obtain the relationship between the flow characteristics and the surface quality for an inclined twin-roll strip caster. In this study, three feeding positions with 60° inflow angle, two inclined angles of the rolls' assembly and two melt pool levels were tested both experimentally and numerically. They found that the wrinkles on the surface of the thin strip can be improved by increasing the depth of the melt pool. They postulated that the recirculation flow located at the triple intersection point of melt/air/roll is mainly responsible for the slag and/or dross trapping. In order to decrease the strength of this vortex and allow a stable flow near the meniscus, they recommended a higher roll angle (30°) along with an inclined feeding position closer to the lower roll for the successful operation of the caster.

Very recently, Kang et al. (1996), in a numerical study of a twin-roll casting process, considered both cooling rolls and molten steel as the solution domain and applied a finite difference method for fluid flow, heat transfer and phase transformation in a molten steel pool. Subsequently, they obtained the temperature distributions in the cooling rolls by using a finite element method and coupling the heat transfer results obtained from the finite-difference model of the molten metal region. Then, they applied the calculated results into a thermo-elasto-plastic model in order to analyze the deformation of the rolls and for the prediction of rolls' life. While the physical properties of molten steel and casting conditions used in this study show that the motion of liquid steel is turbulent, unfortunately these authors committed the same error as Ha et al. (1994) by using the laminar transport equations for turbulent flow conditions.

In general, all the above modeling studies in this category were developed for laminar flow conditions except for the one carried out by Murakami et al. (1993) which considered the turbulent motion of the liquid steel in the melt pool. Unfortunately, the latter study faced with serious convergence difficulties and failed to model thin-strip twin-

roll casters. Accordingly, there can be seen a lack in the literature related to the turbulent heat and flow modeling of twin-roll casting of the thin strips.

6.2.4 Thermomechanical Modeling

The models presented by Miyazawa and Szekely (1981), Roadman et al. (1984), Karabin and Smelser (1985) and Ju and Inoue (1991) fall under this category. The underlying principle of this type of modeling is to combine the thermomechanical deformation model for the simulation of the hot rolling process which takes place in a twin-roll casting system with the modeling of solidification happening at the same time. Perhaps the model introduced by Miyazawa and Szekely (1981) was the first model in this category. They used a power function formulation for the stress-strain rate relationship in the modeling of hot rolling deformation of a twin-roll caster. Although, they considered the fluid flow in their solidification modeling, their model is incomplete and unreliable due to the implementation of some unrealistic fluid flow assumptions. The model developed by Karabin and Smelser (1985) consists of two uncoupled submodels: one for the 1-D transient conduction heat transfer and the other for the hot rolling process. An earlier model developed by Roadman et al. (1984) is more comprehensive since it is based on the coupling of the above two submodels. The latter authors examined their model for the casting of aluminum at high temperatures considering its viscoelastic behavior. The more comprehensive model developed by Ju and Inoue (1990) took into account the elastic-plastic behavior of the metal with solidification due to heat conduction.

6.2.5 Closure

The present investigation can be considered as a study under the thermal-fluid flow modeling category. The main objective of the study presented in this chapter is to develop a computer code for the modeling of thin-strip twin-roll casters considering the turbulence behavior of the melt flow in the mold. Due to the numerical convergence difficulties associated with the modeling of the wedge-shaped cavity having a very high aspect ratio, the mathematical model presented in this chapter is focused only on the coupled turbulent

fluid flow and heat transfer for the melt between the rolls. The second objective of this study is to investigate the way the superheat is removed in a twin-roll caster machine operating under various casting speeds and roll gaps. The idea is to quantify the local heat transfer coefficients on the liquid side of the solidifying shell which may be used in a separate modeling for solidification.

6.3 Mathematical Modeling

Figure. 6.1. shows a two-dimensional schematic diagram of a vertical twin-roll casting system. It is assumed that the molten steel is steadily fed through a non-submerged nozzle at the free surface of the wedge-shaped pool formed by two counter-rotating rolls and the supplied liquid steel. Due to the long width of the strip and considering the negligible side dam effect the mathematical modeling of the caster can be simplified to two-dimensional formulation. The tangential velocity of the rolls is kept constant at the casting speed. In order to study the superheat removal during the process, the temperatures at both roll surfaces are assumed to be equal to the liquidus temperature. Because of the formation of thin solid and mushy layers in a real twin-roll process, this assumption is valid for the superheat dissipation in the liquid phase only.

6.3.1 Turbulent Modeling

As mentioned in Chapter 2, in modeling turbulent flows, the instantaneous quantities in the Navier-Stokes equations are replaced with the time average values and fluctuating terms. In the eddy viscosity approach, the Reynolds stress terms, $\overline{\rho u'_i u'_j}$, and the turbulent heat fluxes, $\overline{\rho u'_j T'}$, appearing in the averaged equations are specifically modeled. The only model which has been widely used in non-aeronautical fields is the $k - \varepsilon$ model. A detail description of this model was presented in Chapter 2. Among various versions of $k - \varepsilon$ turbulent models, the model proposed by Launder and Sharma (1974) was chosen for this

study. This model does not require the explicit value of the distance from a wall and can be applied directly for the modeling of solidification problems.

Considering steady state, two-dimensional incompressible fluid flow and using Launder and Sharma low-Reynolds $k - \epsilon$ turbulent model, the governing equations can be written as:

Continuity equation:

$$\frac{\partial(\rho u)}{\partial x} + \frac{\partial(\rho v)}{\partial y} = 0 \quad (6.1)$$

u-momentum equation:

$$\begin{aligned} \frac{\partial(\rho uu)}{\partial x} + \frac{\partial(\rho vu)}{\partial y} = & \frac{\partial}{\partial x} \left(\mu_e \frac{\partial u}{\partial x} \right) + \frac{\partial}{\partial y} \left(\mu_e \frac{\partial u}{\partial y} \right) - \frac{\partial P}{\partial x} \\ & + \frac{\partial}{\partial x} \left(\mu_e \frac{\partial u}{\partial x} \right) + \frac{\partial}{\partial y} \left(\mu_e \frac{\partial v}{\partial x} \right) \end{aligned} \quad (6.2)$$

v-momentum equation:

$$\begin{aligned} \frac{\partial(\rho uv)}{\partial x} + \frac{\partial(\rho vv)}{\partial y} = & \frac{\partial}{\partial x} \left(\mu_e \frac{\partial v}{\partial x} \right) + \frac{\partial}{\partial y} \left(\mu_e \frac{\partial v}{\partial y} \right) - \frac{\partial P}{\partial y} \\ & + \frac{\partial}{\partial y} \left(\mu_e \frac{\partial v}{\partial y} \right) + \frac{\partial}{\partial x} \left(\mu_e \frac{\partial u}{\partial y} \right) \end{aligned} \quad (6.3)$$

Energy equation:

$$\frac{\partial(\rho u T)}{\partial x} + \frac{\partial(\rho v T)}{\partial y} = \frac{\partial}{\partial x} \left(\Gamma_T \frac{\partial T}{\partial x} \right) + \frac{\partial}{\partial y} \left(\Gamma_T \frac{\partial T}{\partial y} \right) \quad (6.4)$$

Turbulent kinetic energy equation:

$$\frac{\partial(\rho uk)}{\partial x} + \frac{\partial(\rho vk)}{\partial y} = \frac{\partial}{\partial x} \left(\Gamma_e \frac{\partial k}{\partial x} \right) + \frac{\partial}{\partial y} \left(\Gamma_e \frac{\partial k}{\partial y} \right) + G - \rho \epsilon - D_k \quad (6.5)$$

Turbulent kinetic energy dissipation equation:

$$\frac{\partial(\rho u \varepsilon)}{\partial x} + \frac{\partial(\rho v \varepsilon)}{\partial y} = \frac{\partial}{\partial x} \left(\Gamma_\varepsilon \frac{\partial \varepsilon}{\partial x} \right) + \frac{\partial}{\partial y} \left(\Gamma_\varepsilon \frac{\partial \varepsilon}{\partial y} \right) + C_1 f_1 \frac{\varepsilon}{k} G - C_2 f_2 \rho \frac{\varepsilon^2}{k} + E_\varepsilon \quad (6.6)$$

where:

$$E_\varepsilon = \frac{2\mu\mu_t}{\rho} \left[\left(\frac{\partial^2 u}{\partial x^2} \right)^2 + \left(\frac{\partial^2 v}{\partial x^2} \right)^2 + \left(\frac{\partial^2 u}{\partial y^2} \right)^2 + \left(\frac{\partial^2 v}{\partial y^2} \right)^2 \right] \quad (6.7)$$

$$G = \mu_t \left\{ \left[\frac{\partial u}{\partial y} + \frac{\partial v}{\partial x} \right]^2 + 2 \left[\left(\frac{\partial u}{\partial x} \right)^2 + \left(\frac{\partial v}{\partial y} \right)^2 \right] \right\} \quad (6.8)$$

$$D_k = 2\mu \left[\left(\frac{\partial \sqrt{k}}{\partial x} \right)^2 + \left(\frac{\partial \sqrt{k}}{\partial y} \right)^2 \right] \quad (6.9)$$

$$\Gamma_T = \frac{\mu_t}{\sigma_t} + \frac{\mu_t}{\sigma_t}, \quad \Gamma_k = \mu + \frac{\mu_t}{\sigma_k}, \quad \Gamma_\varepsilon = \mu + \frac{\mu_t}{\sigma_\varepsilon}, \quad \mu_\varepsilon = \mu_t + \mu_t, \quad (6.10)$$

$$\mu_t = \rho C_\mu f_\mu \frac{k^2}{\varepsilon}, \quad f_\mu = e^{\left(-3.4 / \left(1 + \frac{Re_t}{50} \right)^2 \right)}, \quad Re_t = \frac{\rho k^2}{\mu \varepsilon}, \quad (6.11)$$

and the values for coefficients used in this model are listed in Table 6.1.

Table 6.1. The empirical constants for low-Re $k - \varepsilon$ turbulent model of Launder and Sharma.

coefficient	c_μ	c_1	c_2	σ_k	σ_ε	σ_t
value	0.09	1.44	1.92	1.0	1.3	0.9

6.3.2 Body Fitted Coordinate Implementation

One method for applying the finite volume method to flow and heat transfer problems in an arbitrary shaped domain would be to overlay a rectangular grid on to the domain boundaries and use the so called 'block-off' technique to those volumes which lie outside the flow domain boundaries as shown in Fig. 6.2. This technique has several disadvantages, among which are: (a) questionable representation of fluxes at the boundary, (b) the requirement of laborious preprocessing or manual interpolation of the boundary

conditions to the adjacent rectangular grid nodes, and (c) inefficient usage of computer resources require performing for calculations for the nodes that lie outside the domain boundaries.

On the other hand, the boundary fitted coordinate technique can be adopted to the control volume finite difference method to eliminate above problems in the solution of transport equations for irregular shaped domain. Grid generation is an efficient means by which the boundary fitted coordinate systems can be used.

Several investigators have focused on the grid generation techniques for the optimal control of the grid lines for regions having large transport gradients and for the greatest possible degree of orthogonality. In spite of extensive research in this field, the generation of orthogonal grids is computationally expensive and is sometime impossible for some special geometries with acute angles in the boundary. In these cases, non-orthogonal grids can be accurately and efficiently produced with ease for all shapes. Two major advantages of this coordinate system are:

- a). Since the boundaries are located on the coordinate lines, then the boundary condition in this system can be satisfied more accurately than in Cartesian coordinates.
- b). The ability to create a curvilinear coordinate system for any shape of geometry regardless of its complexity and to transfer the governing equations to its uniform rectangular grid domain. For this reason there is no necessity to change the procedure of control volume finite difference solution of the partial differential equations.

The grid generated should have the following properties:

1. The mapping of the physical domain onto the computational domain should guarantee one-to-one correspondence of grid-lines such that the same families do not cross each other.
2. Smoothness of grid distribution.
3. The possibility for orthogonality.
4. Option for grid clustering.

It should be mentioned that all of the above advantages can not be simultaneously achieved using any grid generation technique known to date. The various types of grid generation techniques which have been used in the CFD literature are listed below:

I. Algebraic Grid Generation Techniques.

II. Numerical Grid Generation or Partial Differential Equation Techniques.

II-1. Elliptic grid generators

II-2. Hyperbolic grid generators

II-3. Parabolic grid generators

III. Mixed Grid Generation Techniques.

Among the various types of grid generation techniques listed above, the algebraic grid generator was used in the present work because of its simplicity in the application. A short explanation of the basic formulation common in various techniques is provided in this section. Detailed explanations of each grid generation techniques are available in the literature, such as Hoffmann (1988) and Hoffman (1992).

Generally, the grid points in the computational domain are related to the corresponding points in the physical domain by any type of equations such as:

$$\begin{aligned}\xi &= \xi(x, y), \\ \eta &= \eta(x, y)\end{aligned}\tag{6.12}$$

where ξ and η represent the coordinates in the computational domain. To transform the above equations, the role of dependent and independent variables are interchanged and become:

$$\begin{aligned}x &= x(\xi, \eta), \\ y &= y(\xi, \eta)\end{aligned}\tag{6.13}$$

Figure 6.3 shows the grid layout in the physical domain provided by a power law form of algebraic grid generation scheme and its corresponding lay out in the computational domain. As seen in this figure, the grid refinement is located close to the roll surface where high gradients of the transport variables are expected.

The next step after grid generation in BFC technique is to transfer the equations from the physical space into a computational space. In the computational space the coordinates ξ and η are perpendicular to each other. The intersection of ξ -constant and η -constant lines makes the grid points of the computational domain.

The general form of the governing equations in the physical coordinate system can be written as follows:

$$\frac{\partial(\rho u \Phi)}{\partial x} + \frac{\partial(\rho v \Phi)}{\partial y} = \frac{\partial}{\partial x} \left(\Gamma_{\phi} \frac{\partial \Phi}{\partial x} \right) + \frac{\partial}{\partial y} \left(\Gamma_{\phi} \frac{\partial \Phi}{\partial y} \right) + S_{\phi}(x, y) \quad (6.14)$$

Once the governing equations are transformed to the computational domain, the scalar quantities such as temperature, turbulent kinetic energy and its dissipation rate, remain unchanged regardless of the system of coordinates being used, but those variables representing vector quantities, change continuously depending on the orientation of the curvilinear coordinates at any given point in the geometric domain. In transforming the equations to the new coordinate system (ξ, η) it is possible to maintain physical velocities u and v as the dependent variables or use the velocity components normal to ξ -constant and η -constant instead of the physical velocities. Figure 6.4 shows the velocity components at the surfaces of a typical control volume in the Cartesian and nonorthogonal planes.

Applying the chain rule for $d\xi$, $d\eta$, dx and dy in the general transformation, the following relations for derivatives can be obtained:

$$\begin{bmatrix} x_{\xi} & x_{\eta} \\ y_{\xi} & y_{\eta} \end{bmatrix}^{-1} = \begin{bmatrix} \xi_x & \xi_y \\ \eta_x & \eta_y \end{bmatrix} \quad (6.15)$$

or:

$$\begin{bmatrix} y_{\eta} & -x_{\eta} \\ -y_{\xi} & x_{\xi} \end{bmatrix} = J \cdot \begin{bmatrix} \xi_x & \xi_y \\ \eta_x & \eta_y \end{bmatrix} \quad (6.16)$$

where:

$$J = x_{\xi} y_{\eta} - y_{\xi} x_{\eta} \quad (6.17)$$

Using above metric expressions, the chain rule of partial differentiation provides:

$$\frac{\partial \Phi}{\partial x} = \frac{\partial \Phi}{\partial \xi} \frac{\partial \xi}{\partial x} + \frac{\partial \Phi}{\partial \eta} \frac{\partial \eta}{\partial x} \quad (6.18)$$

or:

$$\begin{aligned} \Phi_x &= \Phi_\xi \frac{y_\eta}{J} - \Phi_\eta \frac{y_\xi}{J} \\ &= \frac{\Phi_\xi y_\eta - \Phi_\eta y_\xi}{J} \end{aligned} \quad (6.19)$$

and for y-direction derivative it becomes:

$$\frac{\partial \Phi}{\partial y} = \frac{\partial \Phi}{\partial \xi} \frac{\partial \xi}{\partial y} + \frac{\partial \Phi}{\partial \eta} \frac{\partial \eta}{\partial y} \quad (6.20)$$

or:

$$\begin{aligned} \Phi_y &= \Phi_\xi \frac{-x_\eta}{J} + \Phi_\eta \frac{x_\xi}{J} \\ &= \frac{\Phi_\eta x_\xi - \Phi_\xi x_\eta}{J} \end{aligned} \quad (6.21)$$

Applying the above derivative expressions into the governing equations yields to the general form of the transformed governing equations in (ξ, η) coordinate system as follows:

$$\begin{aligned} \frac{\partial(\rho U \Phi)}{\partial \xi} + \frac{\partial(\rho V \Phi)}{\partial \eta} &= \frac{\partial}{\partial \zeta} \left[\Gamma_\Phi \left(\frac{\alpha}{J} \frac{\partial \Phi}{\partial \xi} - \frac{\beta}{J} \frac{\partial \Phi}{\partial \eta} \right) \right] \\ &+ \frac{\partial}{\partial \eta} \left[\Gamma_\Phi \left(\frac{\gamma}{J} \frac{\partial \Phi}{\partial \eta} - \frac{\beta}{J} \frac{\partial \Phi}{\partial \xi} \right) \right] + JS_\Phi(\xi, \eta) \end{aligned} \quad (6.22)$$

where the metric coefficients α , β , and γ , and also contravariant velocity components U and V are:

$$\begin{aligned} J &= x_\xi y_\eta - y_\xi x_\eta, & \alpha &= x_\xi^2 + y_\eta^2, \\ \beta &= x_\xi x_\eta + y_\xi y_\eta, & \gamma &= x_\xi^2 + y_\xi^2, \\ U &= uy_\eta - vx_\eta, & V &= vx_\xi - uy_\xi \end{aligned} \quad (6.23)$$

where Φ represents the general dependent variable and Γ_Φ and $S_\Phi(\xi, \eta)$ are associated diffusion coefficient and source term for variable Φ , respectively. The source term in the transferred equations, $S_\Phi(\xi, \eta)$, taking on different values for different Φ 's as follows:

Continuity:

$$S(\xi, \eta) = 0 \quad (6.24)$$

X-momentum:

$$S_u(\xi, \eta) = -\frac{1}{J} \left(y_\eta \frac{\partial P}{\partial \xi} - y_\xi \frac{\partial P}{\partial \eta} \right) + \frac{1}{J} \frac{\partial}{\partial \xi} \left[\frac{\mu_e y_\eta}{J} \left(\frac{\partial U}{\partial \xi} + \frac{\partial V}{\partial \eta} \right) - \mu_e \frac{\partial v}{\partial \eta} \right] + \frac{1}{J} \frac{\partial}{\partial \eta} \left[\frac{\mu_e y_\xi}{J} \left(\frac{\partial U}{\partial \xi} + \frac{\partial V}{\partial \eta} \right) + \mu_e \frac{\partial v}{\partial \xi} \right] \quad (6.25)$$

Y-momentum:

$$S_v(\xi, \eta) = -\frac{1}{J} \left(x_\xi \frac{\partial P}{\partial \eta} - x_\eta \frac{\partial P}{\partial \xi} \right) + \frac{1}{J} \frac{\partial}{\partial \eta} \left[\frac{\mu_e x_\xi}{J} \left(\frac{\partial U}{\partial \xi} + \frac{\partial V}{\partial \eta} \right) - \mu_e \frac{\partial u}{\partial \xi} \right] + \frac{1}{J} \frac{\partial}{\partial \xi} \left[\frac{\mu_e x_\eta}{J} \left(\frac{\partial U}{\partial \xi} + \frac{\partial V}{\partial \eta} \right) + \mu_e \frac{\partial u}{\partial \eta} \right] \quad (6.26)$$

Energy:

$$S_T(\xi, \eta) = 0 \quad (6.27)$$

Turbulent kinetic energy:

$$G(\xi, \eta) = \frac{\mu_t}{J^2} \left[\alpha(u_\xi^2 + v_\xi^2) + \gamma(u_\eta^2 + v_\eta^2) - 2\beta(u_\xi u_\eta + v_\xi v_\eta) - J(u_\xi v_\eta - u_\eta v_\xi) \right] \quad (6.28)$$

$$D_k(\xi, \eta) = \frac{2\mu}{J^2} \left[\left(y_\eta \frac{\partial \sqrt{k}}{\partial \xi} - y_\xi \frac{\partial \sqrt{k}}{\partial \eta} \right) + \left(x_\xi \frac{\partial \sqrt{k}}{\partial \eta} - x_\eta \frac{\partial \sqrt{k}}{\partial \xi} \right) \right] \quad (6.29)$$

Similarly, for the turbulent energy dissipation rate equation, source terms can be transferred to the new coordinate system.

6.3.3 Boundary conditions

Along the roll surface, the no-slip boundary condition for velocities, zero value for k and ε and a fixed liquidus temperature for the thermal energy balance equation were used, i.e.

$$u = u_{roll} \cos\theta, \quad v = -u_{roll} \sin\theta, \quad k = \varepsilon = 0, \quad T_{roll} = T_{liq}.$$

At the symmetry plane, the normal velocity v was taken to be zero, while the gradient of tangential velocity u as well as all other transport variables were all set to be zero:

$$v = 0, \quad \alpha \frac{\partial \Phi}{\partial \xi} - \beta \frac{\partial \Phi}{\partial \eta} = 0, \quad \text{where } \Phi \text{ represents } u, k, \varepsilon \text{ and } T.$$

Similarly, for the top free surface: $u = 0, \beta \frac{\partial \Phi}{\partial \xi} - \gamma \frac{\partial \Phi}{\partial \eta} = 0$. (Φ is v, k, ε and T).

The flow and temperature at the outlet surface in the physical domain were assumed to be fully developed: $\beta \frac{\partial \Phi}{\partial \xi} - \gamma \frac{\partial \Phi}{\partial \eta} = 0$. (Φ is u, v, k, ε and T).

Finally, at the nozzle exit plane the uniform profiles for all the variables were used as follows:

$$u = u_{in}, \quad v = 0, \quad k = 0.01u_{in}^2, \quad \varepsilon = \frac{c_{\mu} k^{1.5}}{0.05w}, \quad T = T_{in} = T_{superheat}.$$

6.4 Numerical Solution

The primitive form of the governing transport equations along with the boundary conditions were made discrete by the staggered-grid control-volume finite difference

method. The discretized form of the momentum equations in the non-orthogonal body-fitted coordinate system include pressure gradients in both ξ and η directions. These pressure gradients at the boundaries were found either by a backward or a forward difference scheme as appropriate. The well known SIMPLE algorithm of Patankar (1980) was employed to resolved the pressure-velocity couplings in the momentum equations. The convective terms, which appeared in the discretized set of equations, were calculated using a hybrid formulation.

The discretization of the turbulent equations were carried out similar to their laminar counter-parts. For a detailed description of the discretization of the governing transport equations for laminar flow, the reader is referred to Seyedein et al. (1994). The line-by-line method was used to obtain a converged solution iteratively, and the iteration loop for the solution of the non-linear discretized equations was terminated if their maximum absolute residuals (normalized by the corresponding fluxes at the inlet) were less than 0.001.

The sequence of operations followed in the code is given in the form of a flow chart in Fig. 6.5. The variable u denotes the velocity in the x -direction at the 'e' and 'w' locations of the east and west faces while the variable \hat{u} denotes the same velocity at the 'n' and 's' locations of the north and south faces of a control volume. Similarly, the variable v denotes the velocity in the y -direction at the 'n' and 's' locations of the north and south faces while the variable \hat{v} denotes the same velocity at the 'e' and 'w' locations of the east and west faces of a control volume. The location of these velocity components are shown in Fig. 6.6.

To verify the algorithm, numerical tests were performed to ensure that the solutions were grid-independent. In all of the cases, the total number of grids in the y -direction ensured that the first node adjacent to the roll surface is in the laminar sublayer, which is a required condition for the low-Re $k-\epsilon$ turbulence model employed in this work. Three different grid numbers, i.e. 32×32 , 42×42 and 52×52 , were tested for a sample case with the roll gap thickness equal to 10 mm and roll velocity equal to 1m/s. The variation of the velocity component in the x -direction and the turbulent kinetic energy at $x = 0.12m$ for three different grid distributions are shown in Figs. 6.7 and 6.8, respectively. Because

of the insignificant difference in the results of the velocity and the turbulent kinetic energy obtained in 42×42 and 52×52 grid distributions, and for the sake of computational economy, most of the runs were performed with the 42×42 grid layout. The parameter ranges studied in the present work are roll speed $1-3\text{ m/s}$, roll gap thickness $4-20\text{ mm}$, and inlet temperature $1464-1484^\circ\text{C}$ (superheat, $SH = 10-30^\circ\text{C}$).

6.5 Results and Discussion

The geometrical parameters of the physical domain and the transport properties of the molten stainless steel used are listed in Table 6.2.

Table 6.2. Physical properties of stainless steel and the geometrical parameters used for the calculations.

variable	value	variable	value
viscosity	$0.007\text{ kgm}^{-1}\text{ s}^{-1}$	roll diameter	1200 mm
density	7000 kgm^{-3}	pool depth	385 mm
specific heat	$700\text{ Jkg}^{-1}\text{ K}^{-1}$	gap thickness	$0.004-0.02\text{ m}$
thermal conductivity	$31\text{ Wm}^{-1}\text{ K}^{-1}$	nozzle width	0.018 m
liquidus temperature	1454°C	roll speed	$1-3\text{ m/s}$
inlet temperature	$1464-1484^\circ\text{C}$		

6.5.1 Flow Patterns

The calculated velocity vectors for a roll speed equal to 1 m/s and for three different gap thicknesses are shown in Fig. 6.9. The interaction between the shear flow induced by the roll and the convective flow supplied through the inlet nozzle is responsible for

creating two strong counter-rotating vortices especially for higher roll gap thickness. It is to be noted that the inlet velocity, which is calculated from mass balance between inlet and outlet, differs for various gap thicknesses. For roll gap thickness of 4 mm the inlet flow region is confined close to the nozzle zone and the upper part of the pool, the reason is that in this case the convective inflow is too weak and shear flow is more dominant. For roll gap thicknesses of more than 4 mm which were used, the axial location, where inverse velocity vanishes, shows the length of the recirculation zone. The recirculation length increases with the increase in roll gap thickness. This effect is due to the fact that for a fixed inlet nozzle, a higher gap thickness requires a higher mass flow rate and consequently stronger convective flows at the inlet zone. The thickness of the fluid layer moving with the roll also increases slightly along the roll. This momentum boundary-layer thickness decreases to a minimum value at the location of the vanishing reverse flow and increases further downstream. The change of the momentum boundary layer thickness along the roll can be attributed to the variation of the transport phenomena on the roll.

For a fixed roll gap of 10 mm , the effect of the roll speed on the velocity field is shown in Fig. 6.10. Although, the length of the recirculation zones does not change appreciably due to the roll speed variation between 1 and 3 m/s , the increase in roll velocity is responsible for the generation of stronger turbulence in the entire cavity. In order to show quantitatively the level of turbulence, the ratio of turbulent viscosity to molecular viscosity is presented in the form of contour plots. Figure. 6.11 shows the non-dimensional turbulent viscosity for roll speed equal to 1 m/s and for three gap thicknesses. Similarly, a comparison between turbulent viscosity for a constant gap thickness but for three different roll speeds is presented in Fig. 6.12. In each of these two figures, the high level of turbulent viscosity is located at the center of the pool and also at the middle of the free surface. From these two figures, one can see that the predicted value of turbulent viscosity for the thinner gap is smaller than that for the thicker one which is due to the change in the overall magnitude of the mass flow rate passing through the pool. For a fixed roll gap, the turbulent viscosity for the higher roll speed increases drastically, and the high turbulence region that develops at the free surface may be responsible for the

formation of a wavy free surface, leading to a defective product from the twin-roll caster machine.

Figure 6.13 gives turbulent kinetic energy contours for a roll speed of 1 m/s but for three different roll gap thicknesses, ($4, 10$ and 20 mm). The inlet flow causes strong turbulence, and the high region of turbulent kinetic energy appears adjacent to the nozzle entrance. The high energy zone expands vertically and reaches to the center of the left recirculation zone, where the highest value of k exists. Since the value of k is zero at the solid wall, a large k -gradient develops near the roll surface, particularly in the middle of the pool, where a fraction of inlet flow impinges on the roll. Although the value of k varies for different gap thickness, a comparison of the k values in these cases shows a similar trend in the relative variations in the entire pool. (Fig. 6.13)

6.5.2 Heat Transfer

The calculated energy field in this study is presented in the form of temperature contours in the pool and the local Nusselt number distributions along the roll surface. Figure 6.14 represents the temperature profiles for roll gap thickness equal to 10 mm , $u_{roll} = 1\text{ m/s}$ and $SH = 10 - 30^\circ\text{C}$. The bulk temperature in the pool depends upon the inlet superheat of the melt, particularly, the increase in inlet superheat temperature increases the temperature of the free surface. A high temperature gradient exists close to the roll surface, which increases due to the decrease of the pool cross-section downstream. The effects of the roll speed and gap thickness on the temperature contours are illustrated in Figs. 6.15 and 6.16, respectively. These figures show that the isotherms start from the free surface and extend downstream. Figure 6.15 shows that, about 27% of the delivered superheat is removed within about 75% of the vertical distance from the meniscus surface. For higher roll speed of 2 and 3 m/sec this value drops to about 20% and 13% respectively. The comparison of the three cases with different roll speeds shown in Fig. 6.15 reveals that the higher roll speed shifts the temperature contours towards the roll

surface, resulting in higher temperature gradient and higher heat flux. From Fig. 6.16 it is seen that for 20°C delivered superheat and casting speed of 2 m/sec , only about 10% of the superheat is removed when the roll gap is 20 mm . This value goes up and reaches to about 60% for roll gap thickness of 4 mm (Fig. 6.16-a). The reason for the latter case is the fact that the inlet superheated jet penetrates only a small vertical distance and most of the melt in the cavity is under the influence of the moving cooled rolls. It is to be noted that the input energy delivered to the twin-roll caster is different for the three cases shown in Fig. 6.16 (a-c). Therefore, one should be cautious while interpreting the temperature contours shown in this figure in terms of the fraction of the total superheat removed. The isotherms in all of these figures show that the temperature gradient along the free surface boundary is so small that the variation of the surface tension with temperature, which can lead to the Marangony effect at this boundary, can be safely neglected.

For an isothermal roll surface, the heat transfer coefficient over the roll surface can be represented in the form of a local Nusselt number:

$$Nu_l = \frac{h_l w}{K} = \frac{w}{(T_{in} - T_r)} \left. \frac{\partial T}{\partial n} \right|_{roll} \quad (6.30)$$

Note that the above definition of the local Nusselt number is based on the temperature difference of the inlet melt and the liquidus temperature at the roll surface and not the more traditional temperature difference $(T_{in} - \bar{T})$, where \bar{T} is the bulk temperature of the melt in the cavity.

Figure 6.17 shows the variation of the Nu_l along the roll surface for a roll gap thickness of 10 mm , $SH = 10^\circ\text{C}$ and three different roll speeds. This figure shows that with the increase of the roll speed, the heat flux along the roll surface increases quite dramatically for the most part of the roll. A less dramatic change near the top free surface is due to the relatively strong influence of the roll motion. The effect of the gap thickness on the Nu_l distribution for three different roll speeds is shown in Figs. 6.18 through 6.20. For a roll speed equal to 1 m/s (Fig. 6.18), the change in the Nu_l in all of these cases indicates that up to the middle of the roll surface, Nu_l remains almost unchanged,

representing the region dominated by the shear flow boundary-layer. For a higher roll gap thickness ($t = 20 \text{ mm}$), the first jump of the Nu_t around the middle of the roll surface can be attributed to the weak impingement of the inlet mass flow on the roll surface. The second jump in the Nu_t profile further downstream shows the region which is governed by the strong turbulent convective flow. At the location of the second jump of the Nu_t , the thermal boundary-layer at the roll is thinner due to the reduction of the cross-sectional area of the flow which results in an increase in the Nu_t . For lower gap thicknesses, e.g. $t = 4 \text{ mm}$ and 10 mm , Nu_t near the middle region gradually decreases and becomes almost constant further downstream for $t = 4 \text{ mm}$; while for 10 mm , Nu_t after decreasing again rises near the nip of the rolls.

6.6 Concluding Remarks

A finite volume discretization of the turbulent Navier-Stokes and energy equations has been used in conjunction with a low-Reynolds number $k - \epsilon$ turbulence model to predict mean flow, turbulent characteristics and heat transfer in the wedge-shaped liquid steel pool of a twin-roll continuous steel strip caster. A special feature of the present numerical scheme is the application of the non-orthogonal boundary-fitted coordinates in terms of physical variables on a staggered grid arrangement. The results show that, for the range of parameters typically expected from an industrially operating caster, two recirculation zones develop in the liquid pool. For a higher roll gap thickness, the two recirculation zones are almost of equal size but for a small roll gap, the recirculation zone develops near the inlet jet is much smaller compared to the one that develops due the motion of the roll. The former recirculation bubble is confined only to the top part of the caster's nozzle zone. For high casting speeds, a high level of turbulence develops at the free surface of the liquid pool, which may lead to the formation of surface waves and eventually yield poor quality products. The local heat transfer coefficients at the roller surface, which are plotted in the form of local Nusselt numbers, show that up to about one-half of the total contact length from the free surface down the roll, the local Nusselt numbers remain essentially unchanged for higher roll gap thicknesses. For a fixed casting

about one-half of the total contact length from the free surface down the roll, the local Nusselt numbers remain essentially unchanged for higher roll gap thicknesses. For a fixed casting speed, the local Nusselt number profile versus distance along the roll surface shows two distinct positive upward slope changes: one near the middle of the roll surface and the other near the roll nip. The first positive change in slope is due to the jet impingement from the return flow of the incoming inlet jet on the melt shear layer carried by the rotating roll. The second rapid change is due to the progressive thinning of the thermal boundary-layer at the roll, caused by the increased turbulent convective flow as a result of the reduction in cross-sectional area of the flow in the downstream section of the wedge-shaped cavity. For a lower roll gap ($t = 4$ mm), at the middle of the roll Nu_t decreases and then gradually increases further downstream. The importance of the present study is that it provides for the first time, in a quantitative manner, the local rates of heat transfer to be expected from the liquid to the solid-liquid interface, in the presence of a turbulent convective recirculating bulk liquid flow, in a twin-roll solidification casting process. This study will help to develop simple solidification heat transfer models for the solidifying shell on the roll for the complex twin-roll solidification-casting problems.

NOMENCLATURE

Symbol	Description
c_1, c_2, c_μ	empirical constants for low Reynolds turbulent models
E_ϵ	extra generation term in ϵ equation
f_1, f_2, f_μ	empirical constants for low Reynolds turbulent models
G	turbulent kinetic energy generation in k -equation
h	convective heat transfer coefficient
J	Jacobian of the transformation
k	turbulent kinetic energy
P	Pressure
\bar{P}	time-average pressure
R_t	turbulent Reynolds number based on the turbulent quantities
S	source term
S_Φ	source term associated with Φ
T	temperature
T'	fluctuation of temperature
\bar{T}	time-average temperature
T_i	liquidus temperature
T_{in}	inlet temperature
u_i	velocity component in the i-direction
\bar{u}_i	time-average velocity component in i-direction
u'_i	fluctuation of velocity in i-direction
u_{in}	inlet velocity
u_r	roll velocity
U	contravariant velocity component in ξ -direction

V	contravariant velocity component in η -direction
W	nozzle width
$x_\xi, x_\eta, y_\xi, y_\eta$	metric derivatives

Greek Symbols

α, β, γ	geometric relations between coordinate systems
ε	turbulent kinetic energy dissipation rate
Γ_Φ	diffusion coefficient associated with Φ value
μ	laminar viscosity
μ_e	effective viscosity equal to $\mu_l + \mu_t$
μ_t	turbulent viscosity
Φ	transported scalar
ρ	mass density
σ_l	Prandtl number
σ_t	turbulent Prandtl number
$\sigma_k, \sigma_\varepsilon$	empirical constants in turbulent model equations
ξ, η	axes of nonorthogonal curvilinear coordinate system

References

- Bagshaw M. J., Hunt J. D., and Jordan R. M., A steady state model for roll casting, *Modeling and control of Casting and Welding Processes*, (Warrendale, PA: TMS) pp. 135-147, (1986a).
- Bagshaw M. J., Hunt J. D., and Jordan R. M., Modeling and control of casting and welding processes, *Engineering Foundation Conf.*, Santa Barbara, Jan. 12-17, pp. 135-147, (1986b).
- Bagshaw M. J., Hunt J. D., and Jordan R. M., Heat line formation in a roll caster, *Applied Scientific Research*, Vol. 44, No. 1-2, pp. 161-174, 1987.
- Bagshaw M. J., Hunt J. D., and Jordan R. M., A theoretical and experimental study of heat line formation in a roll caster, *Cast Metals*, Vol. 1, pp. 16-22, (1988).
- Bayer-Steinhauer H. et al., "Umformtechnik", *Aachener Atahlkolloquium*, Eurogress, pp. 2-12, (1992).
- Caron, S. Essadigi E., Hamel F. G., and Masounave J., Numerical modeling of heat transfer in high productivity rate twin-roll casting process, *Light Metals 1990*, ed. C.M. Bickert (Warrendale, PA: TMS), pp. 967-973, (1990).
- Ha M. Y., Kim K., Kim K. C., and Lee S. W., Transient analysis of thermo-fluid phenomena in twin-roll continuous casting, *Int. J. Heat Mass Transfer*, Vol. 37, No. 14, pp. 2059-2068, (1994).
- Hirt G., Kopp R., and Bayer H., Analysis of the double-roller process for the production of thin steel strip, *Near Net Shape Manufacturing, ASM International*, pp. 131-138, (1988).
- Hoffman J. D., *Numerical Methods For Engineers And Scientists*, McGraw-Hill, U.S.A., (1992).
- Hoffmann K. A., Rutledge W. H. and Robi P. E., Hyperbolic grid generation techniques for blunt body, *Numerical Grid Generation in Computational Fluid Dynamics*, Pineridge press, (1988).

- Hwang J. D., Lin H. J., Hwang W. S., and Hu C. T., Numerical simulation of metal flow and heat transfer during twin roll casting, *ISIJ International*, Vol. 35, No. 2, pp. 170-177, (1995).
- Hwang J. D., Lin H. J., Jang J. S. C., Hwang W. S., and Hu C. T., Relationship between flow characteristics and surface quality in inclined twin roll strip casting, *ISIJ International*, Vol. 36, No. 6, pp. 690-699, (1996).
- Ju D.-Y. and Inoue T., Solidification behavior and viscoplastic deformation in the strip casting process by twin roll method, *Nippon Kikai Gakkai Ronbunshu*, Vol. 57, No. 537, pp. 1147-1154, (1991).
- Karabin M. E., and Smelser R. E., *ASME technical paper WAHT-32/ASME*, (1985).
- Kim Y.D., and Kang, C.G., Solidification behavior for liquid metal and mushy state pouring in strip continuous casting, *International Conference on New Smelting Reduction and Near Net Shape Casting Technologies for Steel*, (Seoul, South Korea), pp. 792-801, (1990).
- Kang C. G., Kim Y. D., and Lee S. W., A solidification and cooling roll deformation analysis considering thermal flow in twin roll strip continuous casting process, *Melt Spinning, Strip Casting and Slab Casting*, eds., E.F. Matthys and W.G. Truckner, (Warrendale, PA: TMS), pp. 65-87, (1996).
- Kraus H. G., Finite-element model and feasibility study of thin strip continuous Casting of steel, *Numerical Heat Transfer*, Vol. 10, pp. 63-77, (1986).
- Lauder B. E., and Sharma B. I., Application of the energy dissipation model of turbulence to the calculation of flow near a spinning disc, *Letters In Heat and Mass Transfer*, Vol. 1, pp. 131-138, (1974).
- Masounave J. et al., The design and implementation of the IMRI strip caster, *Proc. Int. Symp., Casting of Near Net Shape Products*, Eds. Sahai et al., pp. 473-492, (1988).
- Miyazawa K., and Szekely J., A mathematical model of the splat cooling process using the twin-roll technique, *Met. Trans.*, Vol. 12A, pp. 1047-1057, (1981).

- Miyazawa K., Mizoguchi T., Nakamura N., and Ohashi T., The formation of thin steel strip in a laboratory scale twin-roll casting, "Casting of Near Net Shape Products" Sahai et al. (Ed.) *Proc. Int. Symp. in Honolulu, Hawaii*, pp. 629-643, (1988).
- Mo A., and Hoydal S. H., Mathematical modeling of temperature, melt flow, deformation and stress in aluminum twin roll casting, "Modeling of Casting, Welding and Advanced Solidification Processes VI", T. S. Piwonka, V. Voller and L. Katgerman, (Eds.), *The Mineral, Metals & Materials Society*, pp. 671-677; (1993).
- Murakami H., Hasan M., and Guthrie R. I. L., Computational study of the transport processes in a twin-roll stainless steel caster, *Proceedings of the International Symposium on Strip Casting, Hot and Cold Working of Stainless Steels*, Eds. N. D. Ryan, A. J. Brown and H. J. McQueen, Quebec City, Quebec, August 1993, pp. 35-52, (1993).
- Murakami H., *Modeling of Turbulent Flow, Heat Transfer and Solidification in a Twin-Roll Caster*, Ph.D. Thesis, Mining and Metallurgical Eng. Dept., McGill University, (1993).
- O'Malley R. J., and Karabin M. E., A theoretical and experimental study of the roll casting process, *Modeling and control of Casting and Welding Processes*, Eds. A.F. Giamei and G.J. Abbaschian (Warrendale, PA: TMS), pp. 149-168, (1988).
- Ozawa M., Kogiku F., Yukumoto M., Miyake S., and Kan T., Heat transfer analysis of twin-roll casting, *Modeling of Casting and Welding Processes IV*, (Palm Coast, Florida, USA), 17-22 Apr. 1988, pp. 255-263, (1988).
- Patankar S. V., *Numerical Heat Transfer and Fluid Flow*, Hemisphere Publishing Co., Washington, D.C., (1980).
- Roadman R. E., Berman H. M., and Lalli L. A., Application of a viscoplastic finite element model to the roll casting process, *Aluminium*, Vol. 60, No. 12, pp. 911-914, (1984).
- Romanowski C. et al., *Melt Spinning and Strip Casting: Research and Implementation*, ed. E.F. Matthys, (Warrendale, PA: TMS), pp. 225-262, (1992).

- Saitoh T., Hojo H., Yaguchi H., and Kang C. G., Two-dimensional method for twin-roll continuous casting, *Met. Trans.*, Vol. 23B, pp. 381-390, (1989).
- Seyedein S. H., Hasan M., and Mujumdar A. S., Laminar flow and heat transfer from multiple impinging slot jets with an inclined confinement surface, *International Journal of Heat and Mass Transfer*, Vol. 37, No. 13, pp. 1867-1876, (1994).
- Takuda H., Hatt N., Teramura M., and Kokado J.-I., Simple model for thermal calculation in twin-roll strip casting process, *Steel Research*, Vol. 61, no. 7, pp. 312-317, (1990).

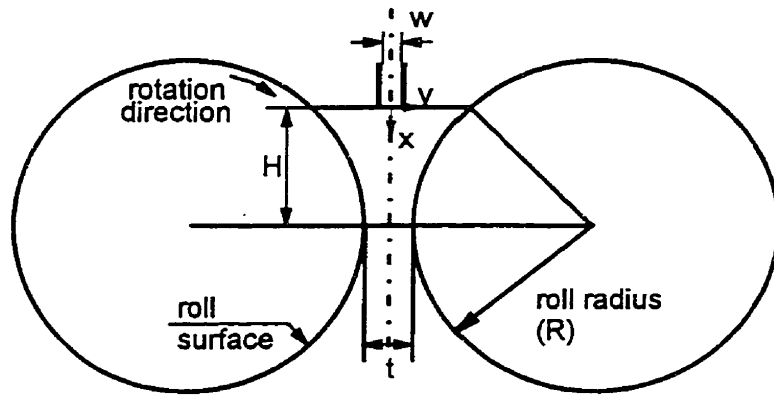


Fig. 6.1. A schematic configuration of a vertical twin-roll casting machine.

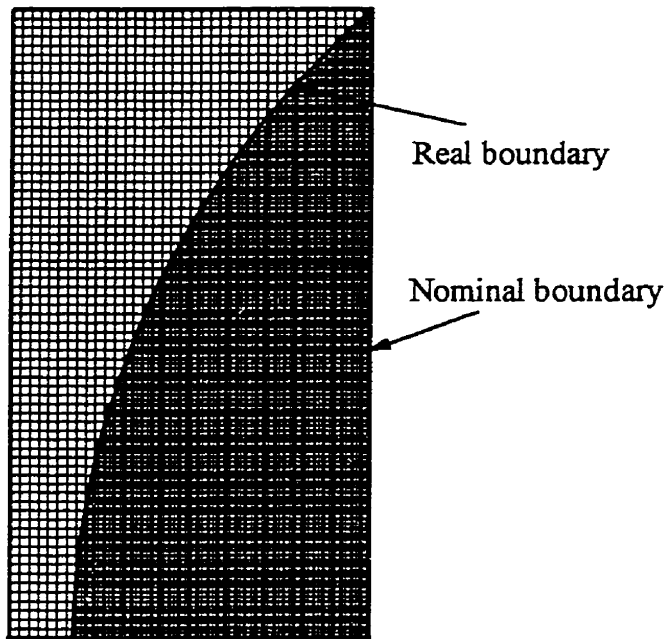


Fig. 6.2. Blocked-off region for complex geometry of twin-roll caster in Cartesian domain.

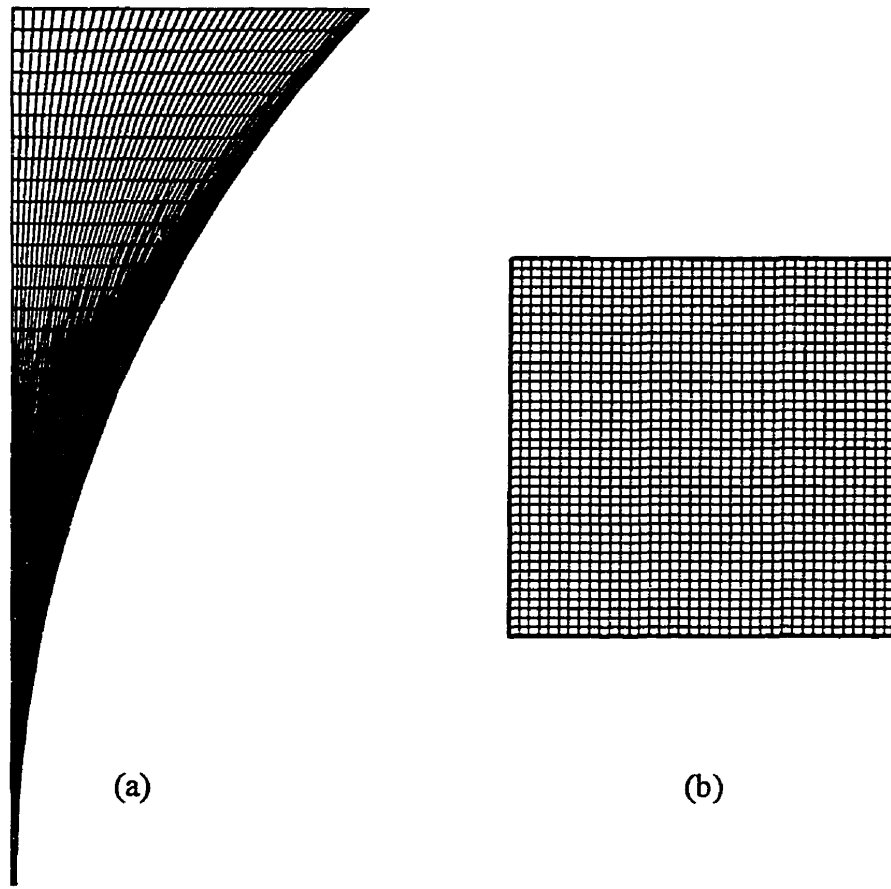


Fig. 6.3. Grid layout in the physical domain and its transformation into the rectangular coordinate system; (a) physical domain, (b) computational domain.

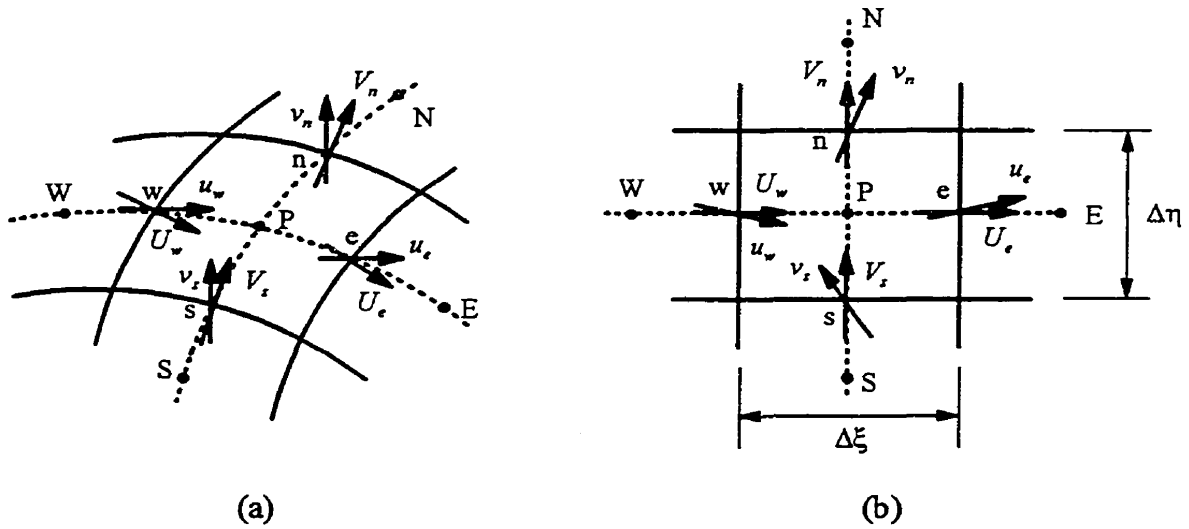


Fig. 6.4. Velocity components in physical and computational domains; (a) physical domain, (b) computational domain.

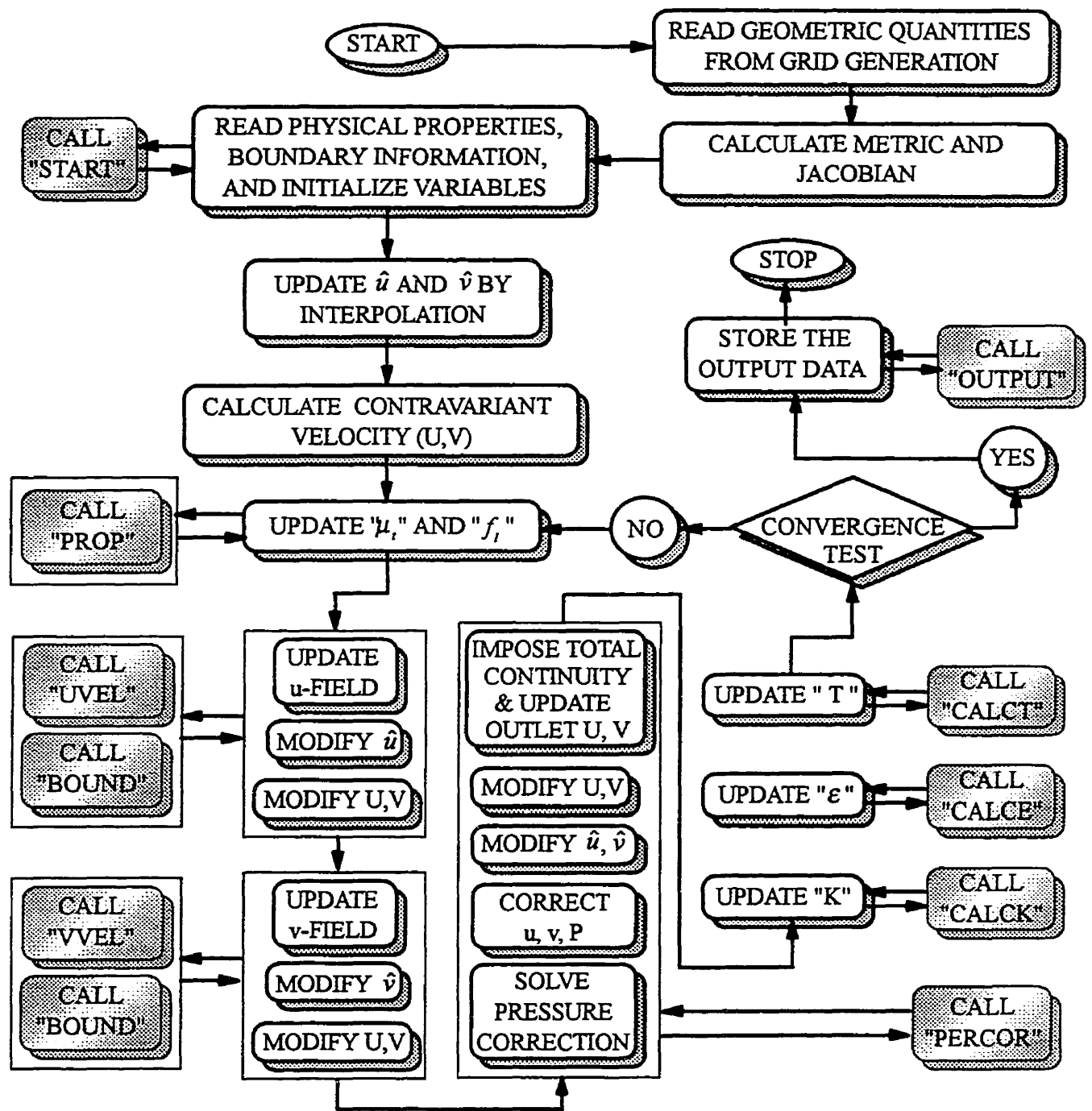


Fig. 6.5. Computational flow diagram for 2-D BFC code.

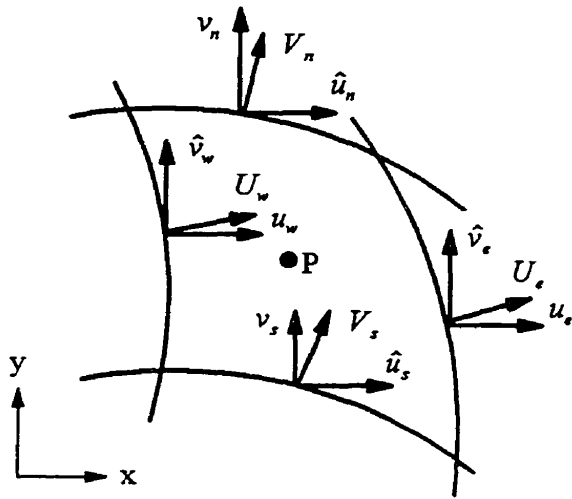


Fig. 6.6. Location of the velocity components for a typical control volume.

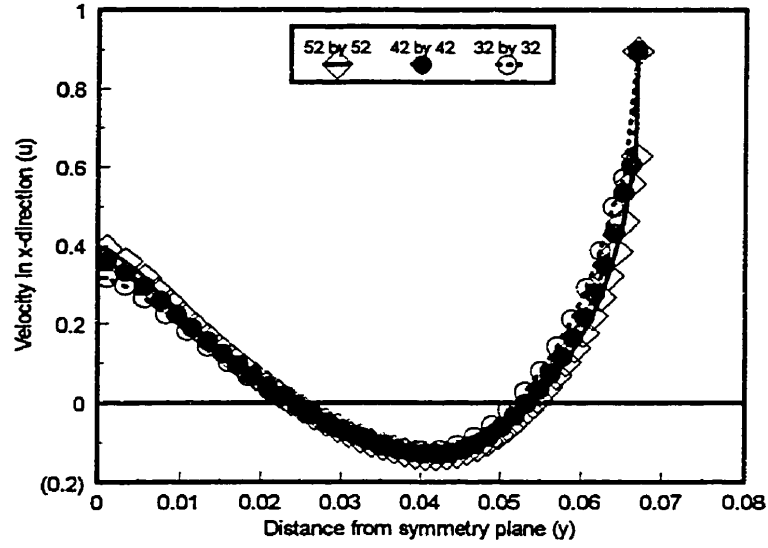


Fig. 6.7. Effect of grid number on u-component velocity profile at a depth of 0.12 m across the cross-section of the cavity for $t=10$ mm and $u_r = 1m/s$.

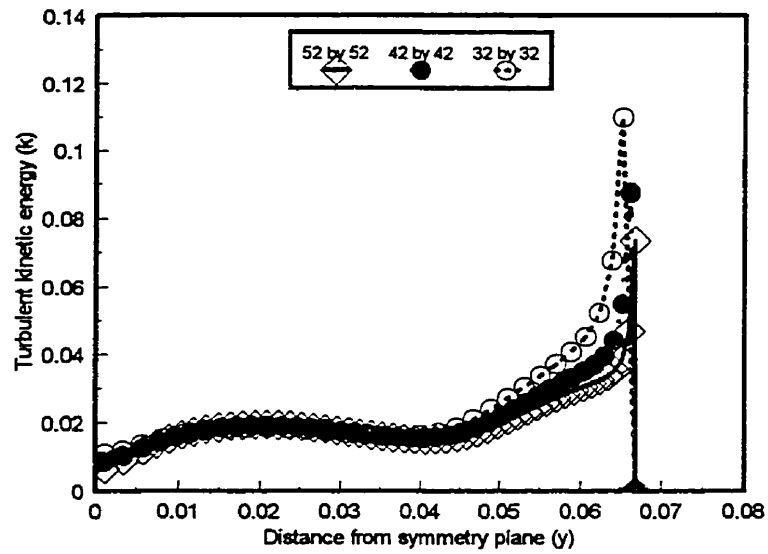
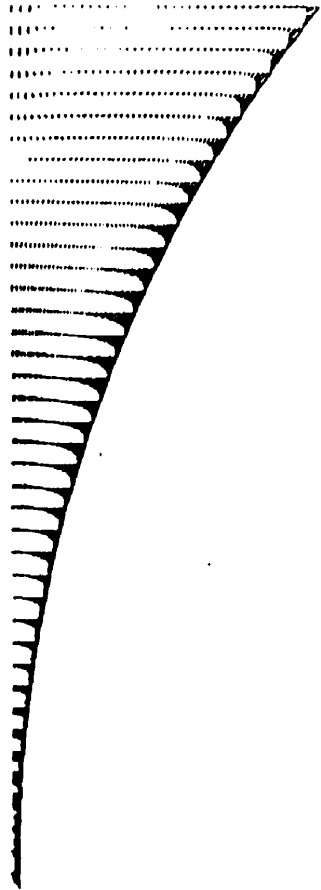


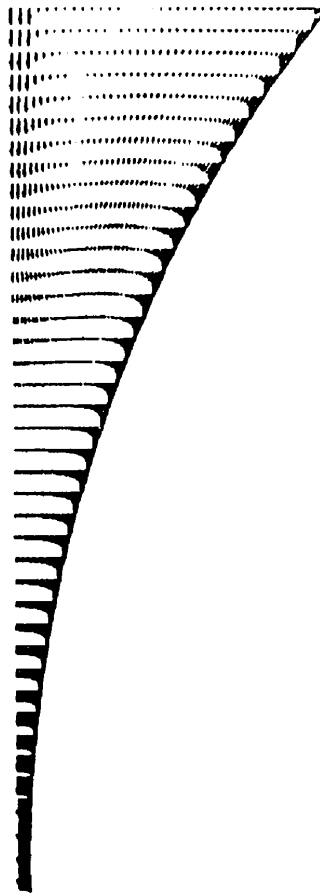
Fig. 6.8. Effect of grid number on turbulent kinetic energy profile at a depth of 0.12 m across the cross-section of the cavity for $t=10$ mm and $u_r = 1m/s$.

Largest Velocity
= 1.15



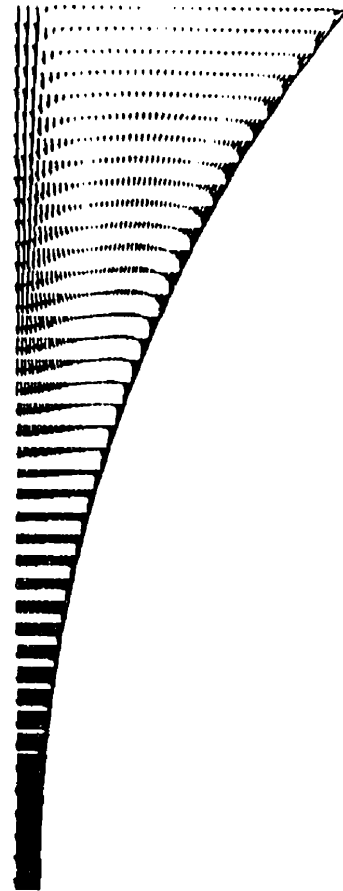
a)

Largest Velocity
= 1.07



b)

Largest Velocity
= 1.12



c)

Fig. 6.9 .Effect of the roll gap thickness on the velocity field for $u_r = 1m/s$; (a) $t=4$ mm, (b) $t=10$ mm, (c) $t=20$ mm.

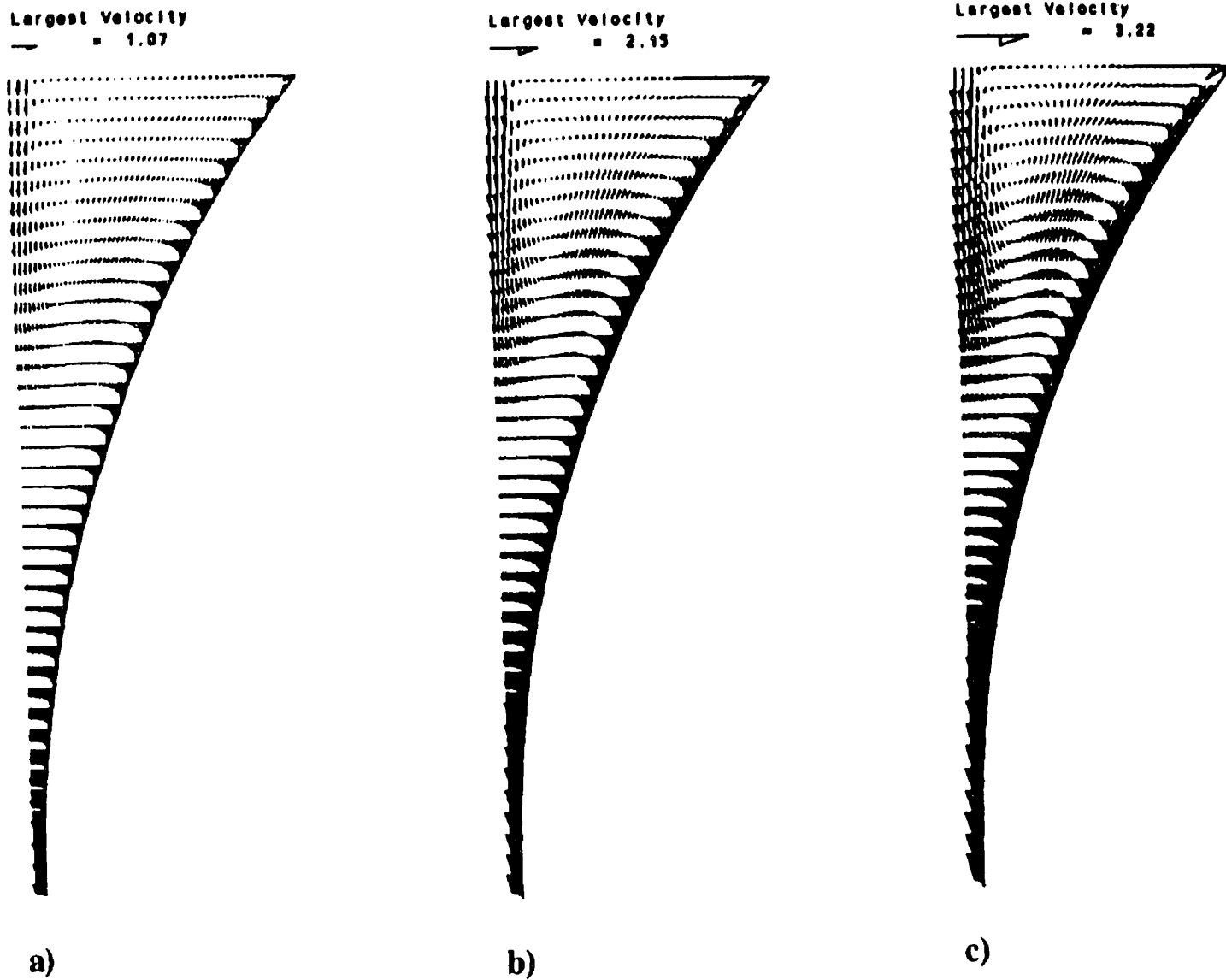
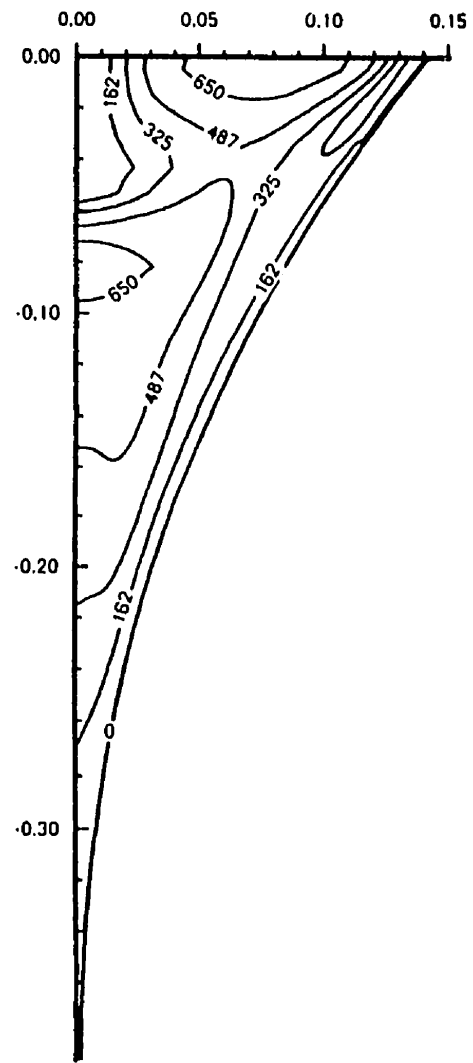
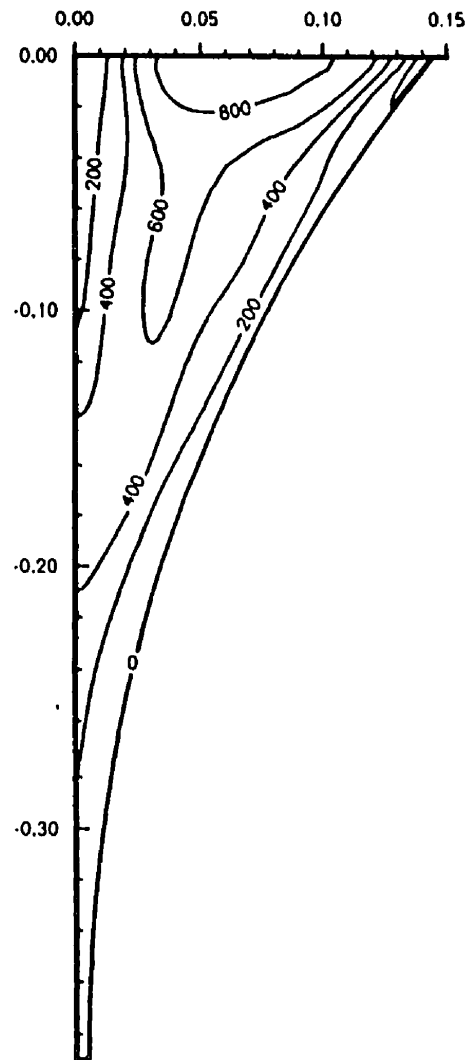


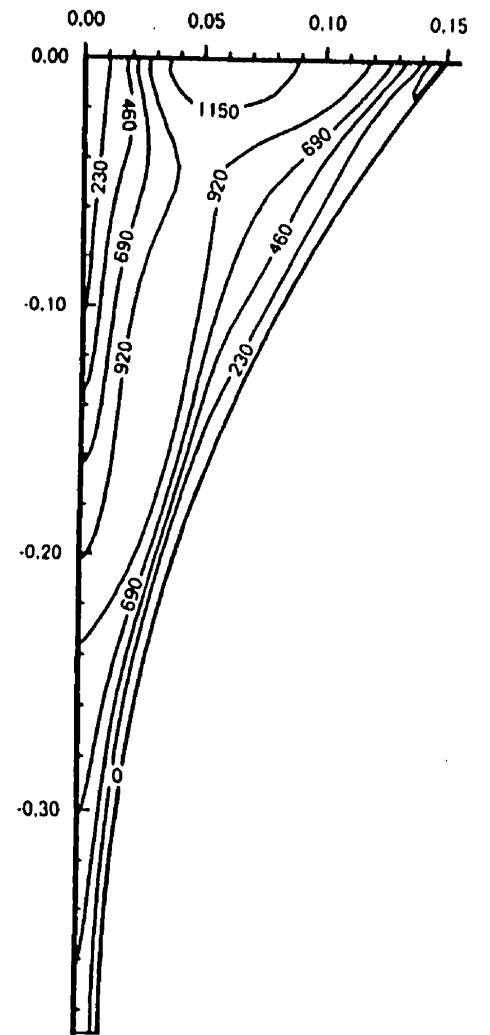
Fig. 6.10. Comparison of the velocity profile for a constant gap thickness ($t=10$ mm) and different roll speeds; (a) $u_r = 1\text{ m/s}$, (b) $u_r = 2\text{ m/s}$, (c) $u_r = 3\text{ m/s}$.



a)



b)



c)

Fig. 6.11. Comparison of the non-dimensional turbulent viscosity for $u_r = 1 \text{ m/s}$ and different gap thicknesses; (a) $t=4$ mm, (b) $t=10$ mm, (c) $t=20$ mm.

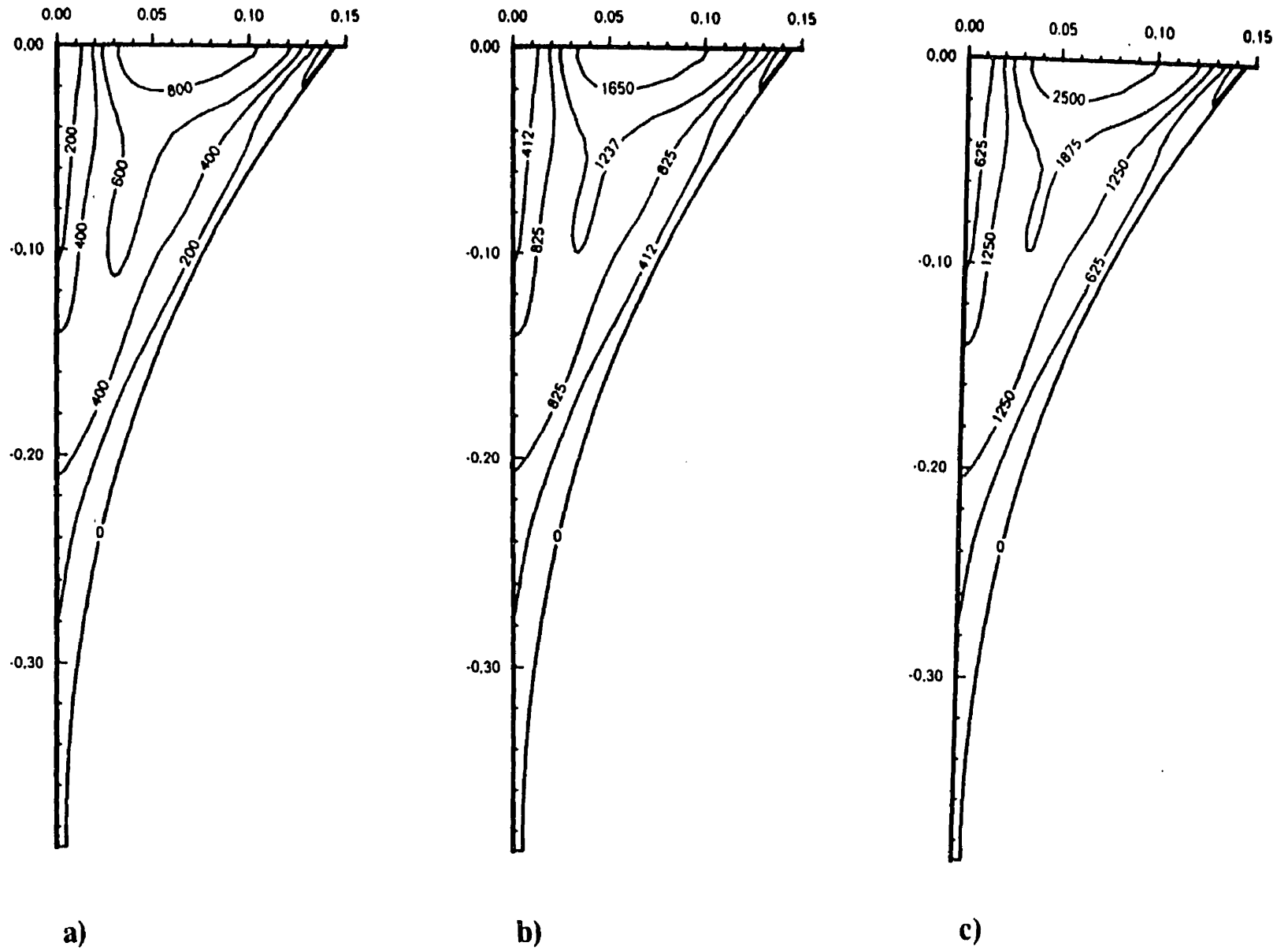
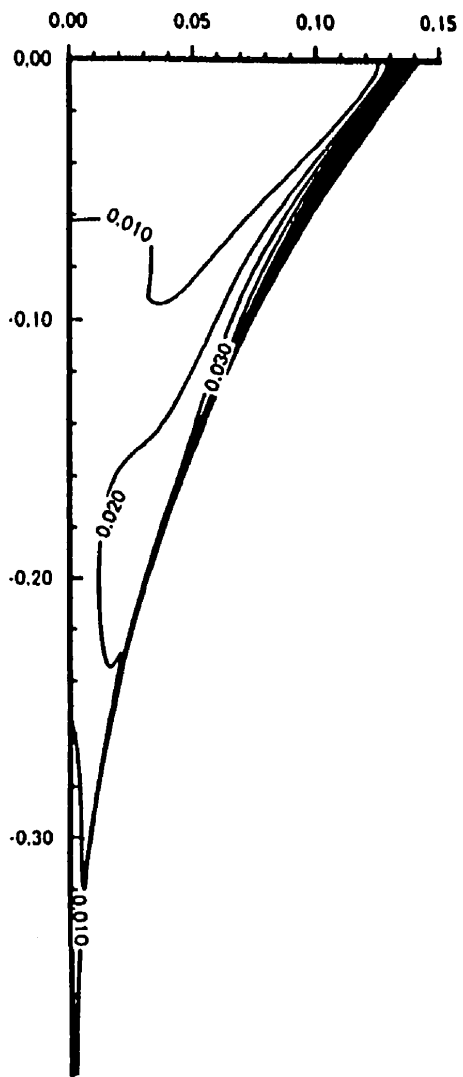
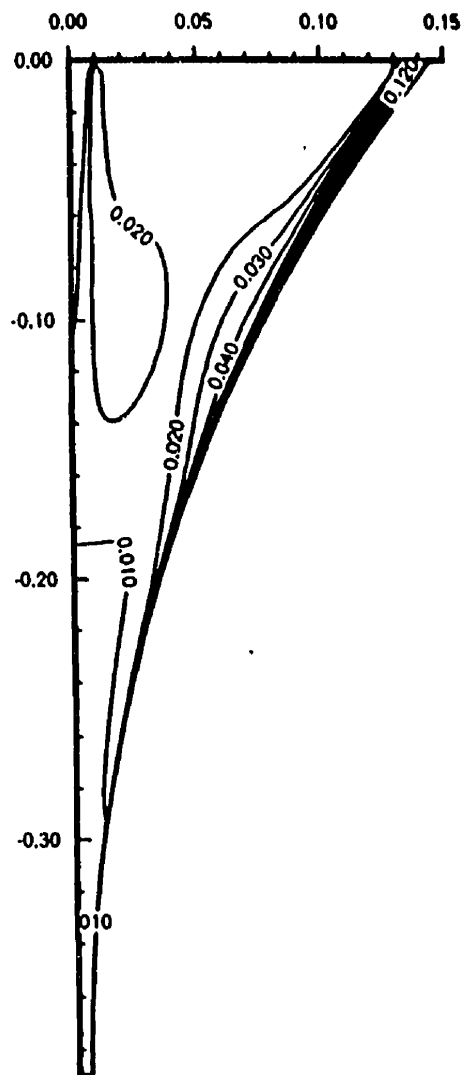


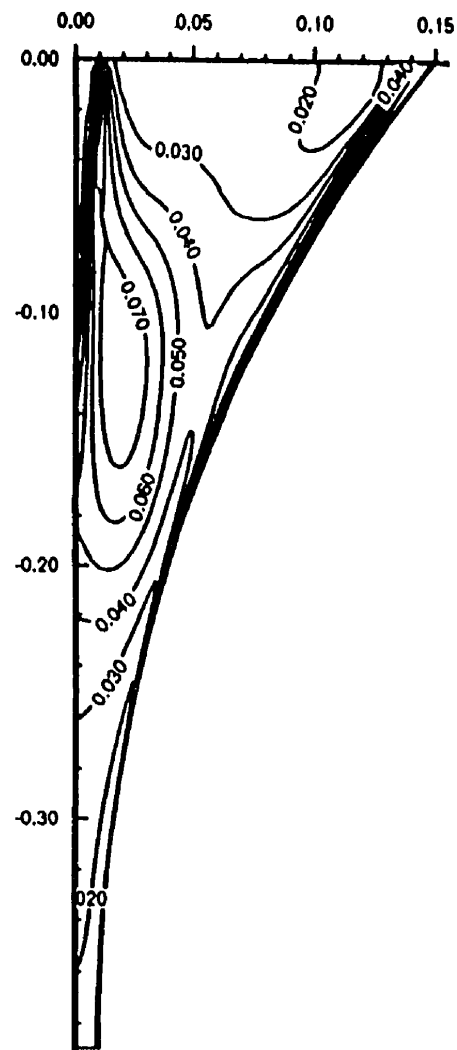
Fig. 6.12. Comparison of the non-dimensional turbulent viscosity for $t=10 \text{ mm}$ and different roll speeds; (a) $u_r = 1 \text{ m/s}$, (b) $u_r = 2 \text{ m/s}$, (c) $u_r = 3 \text{ m/s}$.



a)

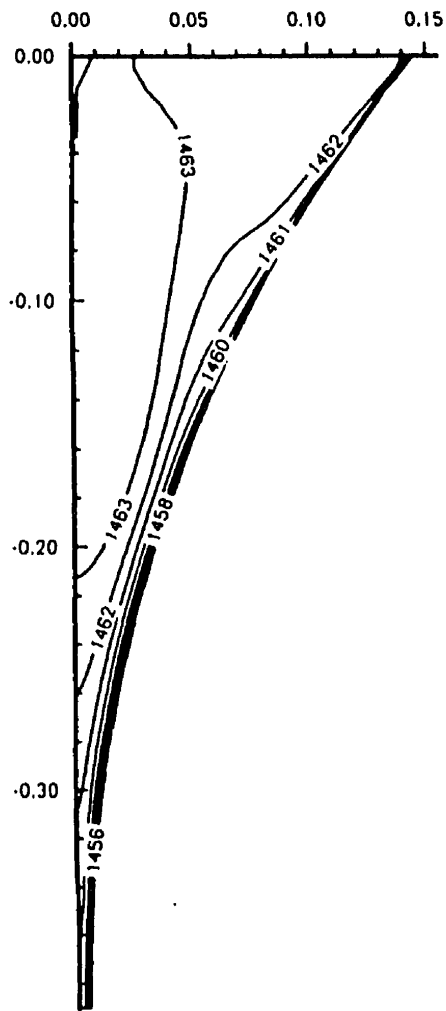


b)

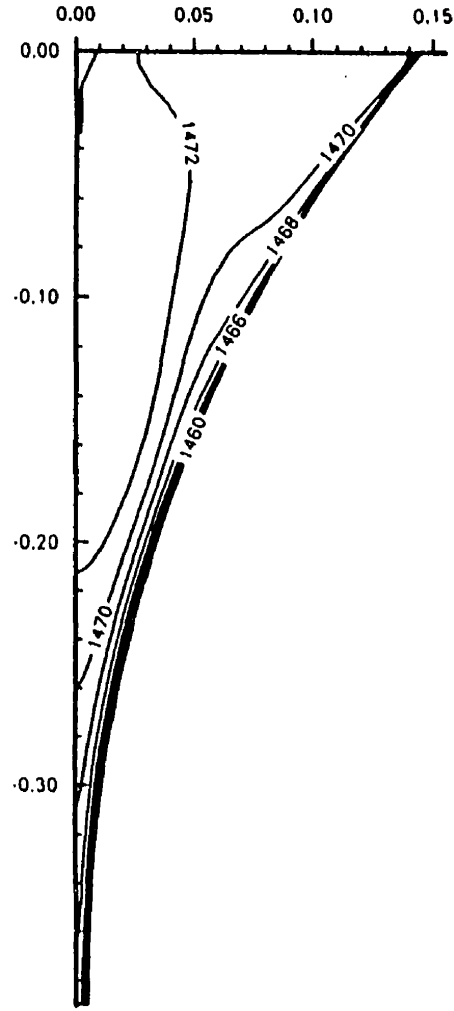


c)

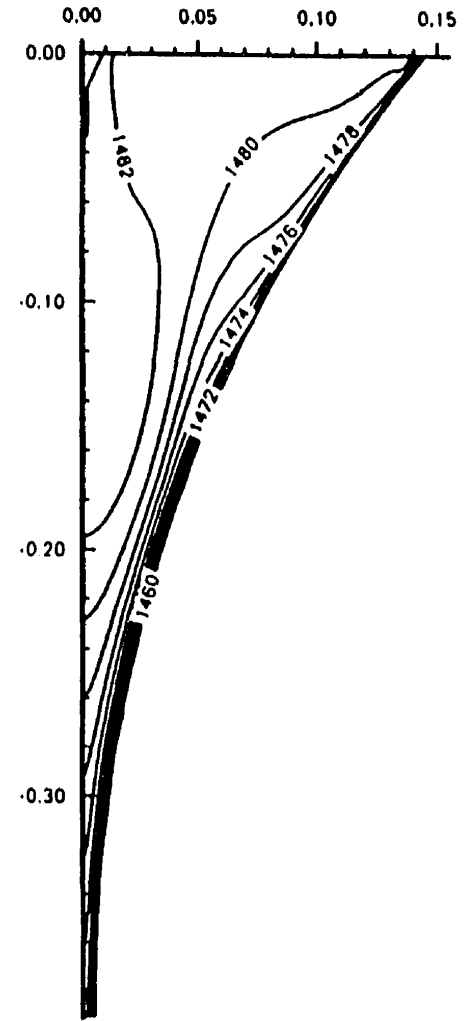
Fig. 6.13. Effect of the roll gap thickness on the turbulent kinetic energy for a constant roll speed , $u_r = 1 m/s$; (a) $t=4$ mm , (b) $t=10$ mm , (c) $t=20$ mm .



a)

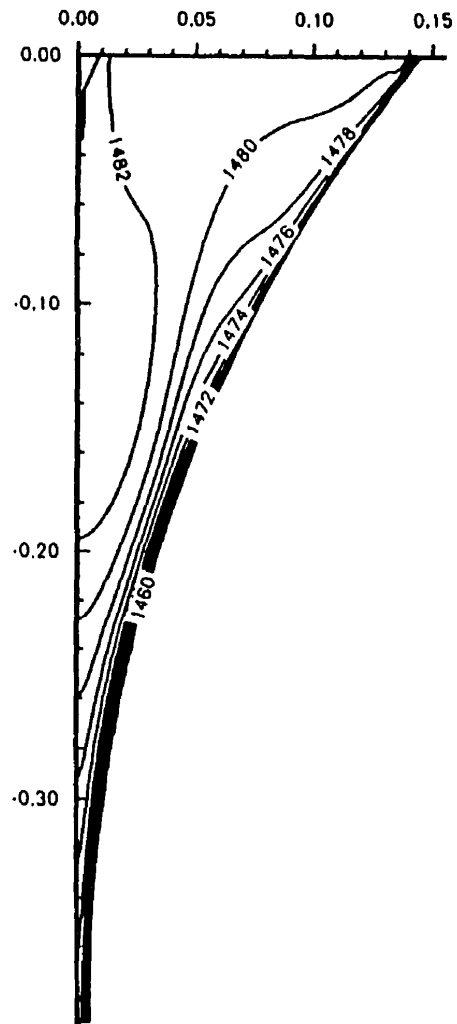


b)

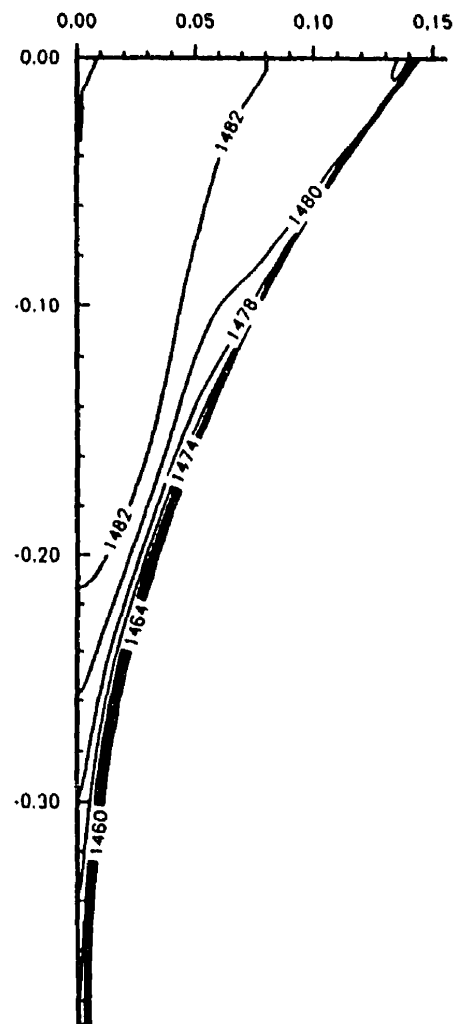


c)

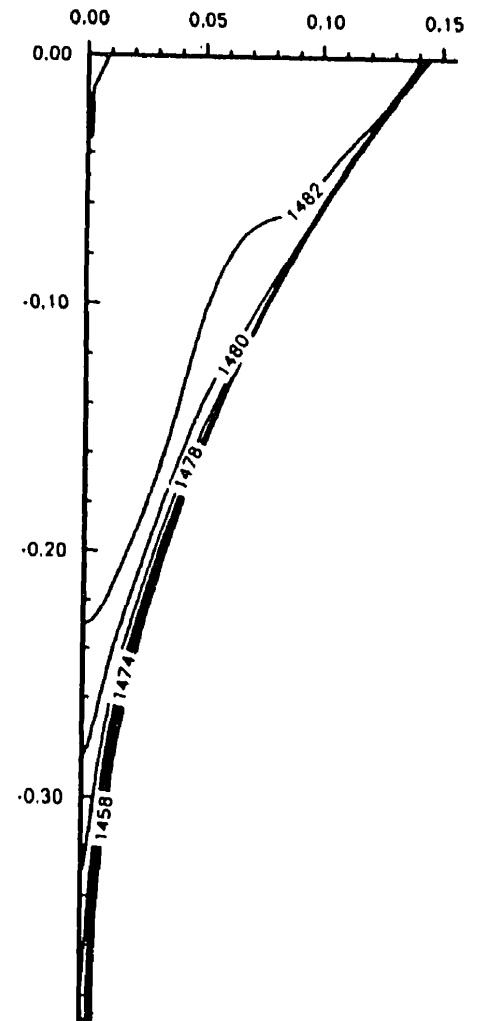
Fig. 6.14. Effect of the inlet superheat on the isotherm curves for $t=10$ mm and $u_r = 1$ m/s ; (a) $SH = 10^\circ C$, (b) $SH = 20^\circ C$, (c) $SH = 30^\circ C$.



a)



b)



c)

Fig. 6.15. Comparison of the temperature contours for different roll speeds, $t=10$ mm and $SH = 30^\circ C$; (a) $u_r = 1m/s$, (b) $u_r = 2m/s$, (c) $u_r = 3m/s$.

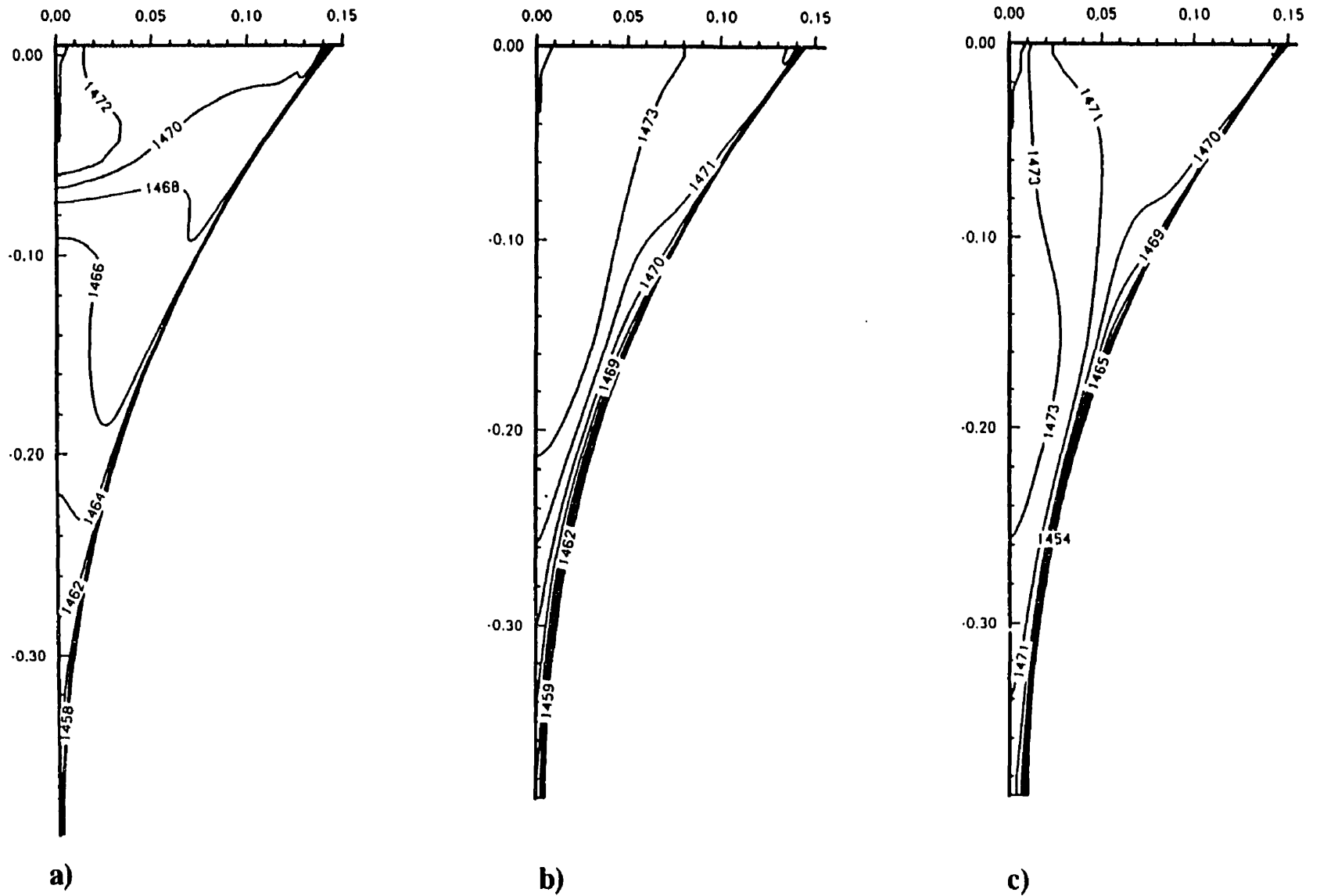


Fig. 6.16. Effect of the roll gap thickness on the temperature profiles for $u_r = 2$ m/s and $SH = 20^\circ C$; (a) $t=4$ mm, (b) $t=10$ mm, (c) $t=20$ mm.

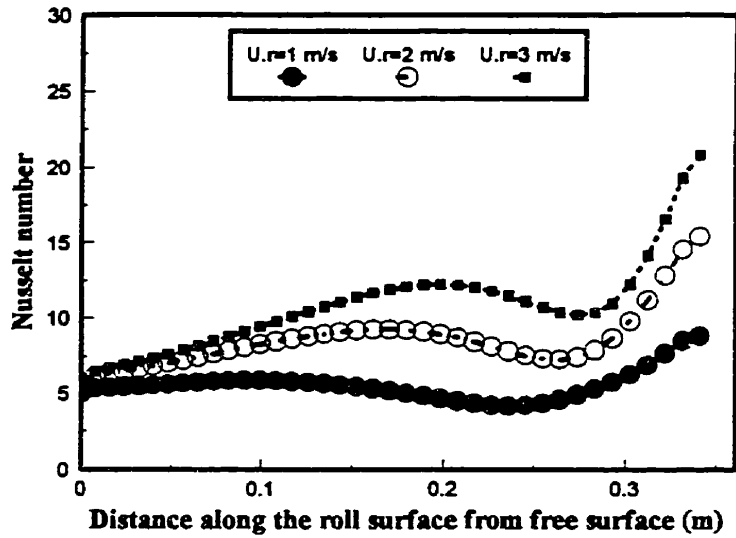


Fig. 6.17. Nusselt number distribution along the roll surface for $t=10$ mm, $\Delta T=10^\circ C$ and different roll speeds.

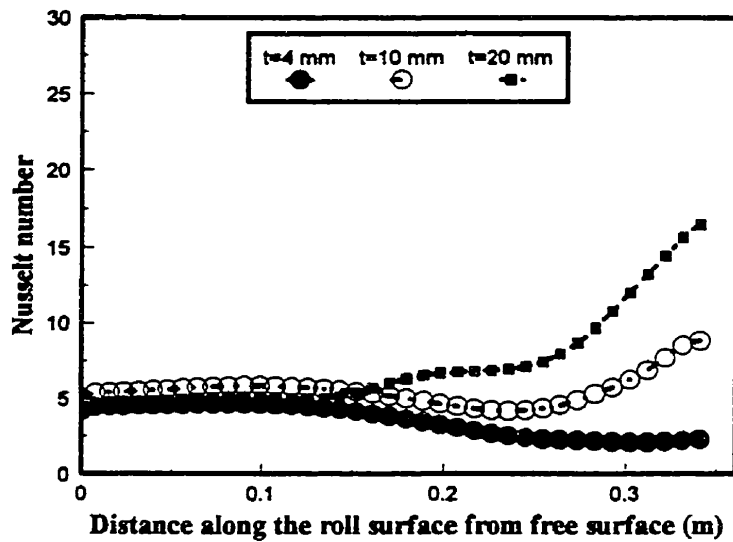


Fig. 6.18. Variation of the Nusselt number along the roll surface for $u_r = 1 m/s$ and different gap thicknesses.

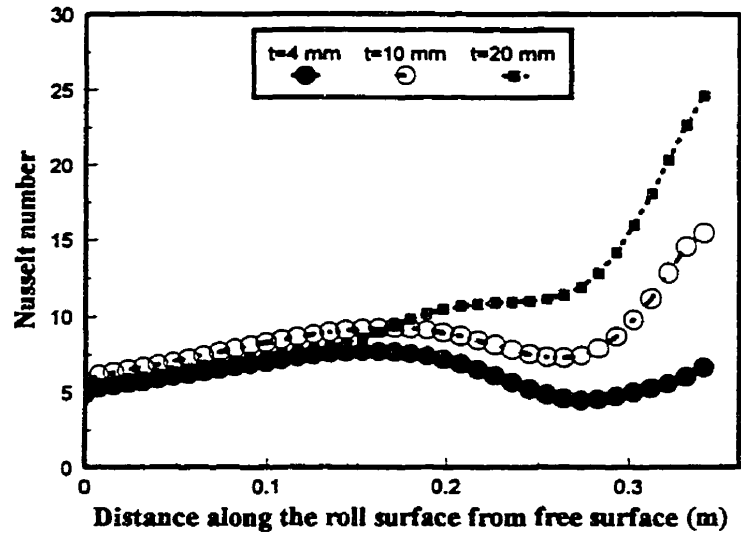


Fig. 6.19. Variation of the Nusselt number along the roll surface for $u_r = 2 \text{ m/s}$ and different gap thicknesses.

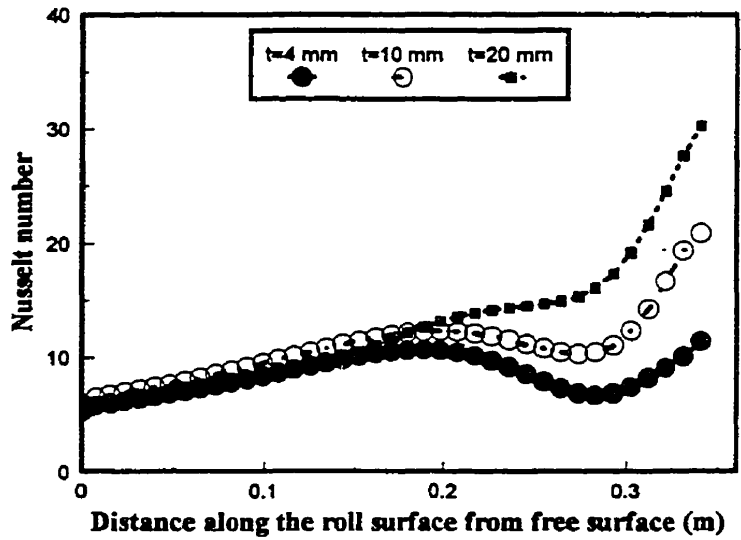


Fig. 6.20. Variation of the Nusselt number along the roll surface for $u_r = 3 \text{ m/s}$ and different gap thicknesses.

COUPLED TURBULENT FLOW, HEAT TRANSFER AND MACROSCOPIC SOLIDIFICATION IN A VERTICAL TWIN-ROLL THIN-STRIP CASTER

7.1 Introduction

The developments in continuous casting during the past two decades have been evolving towards casting systems which can commercially produce near-net-shape products such as thin slab, strip and thin strip. Twin-roll casting is seen as one of the feasible processes for near-net-shape casting to produce a thin strip directly from molten metal. The major problem in such processes is to produce a strip with precise thickness and desired physical properties. So, more precise and highly controlled casting techniques are now required for the practical production of thin strips. As mentioned in Chapter 6, the twin-roll casting process involves quite complicated phenomena which are poorly stable due to high sensitivity to the controlling of heat and mass flow within the mold as well as the development of solidifying shells on the roll. In other words, if solidification is completed before the liquid reaches the minimum clearance point between the rolls, then deformation of the solid will occur if operating with a fixed gap. Thus, the stable casting conditions can only be obtained if solidification is completed in the very vicinity of the kissing point between rolls, otherwise either a negative or a positive segregated central region is formed (Fig. 7.1). In case (c) no real casting would be possible because of immediate breakouts; and in case (a) the separating force would become too high and the rolls would automatically open, for protection of the mechanical parts. In addition, the

temperature across the width of the section should be kept constant to get a uniform shell thickness. Thus, without a uniform feeding and excellent temperature and composition control, it has been shown in many experimental findings that a perfect cast surface cannot be obtained.

Previous studies related to the modeling of the twin-roll casting processes were extensively reviewed in Chapter 6 and are not repeated here. The survey reveals that due to the complexities involving the operation of a twin-roll casting system and the process sensitivity to the solidification phenomena a mathematical model which can predict coupled turbulent fluid flow, heat transfer and solidification will play an important role in the successful development of such processes. The mathematical model introduced by Seyedein and Hasan (1996, 1997) was used in the previous chapter to numerically simulate the turbulent flow and forced convection heat transfer in the wedge-shaped cavity of a twin-roll caster. In that study the phase-change phenomena was not consider in the modeling, while in the present chapter the 2-D mathematical model of turbulent flow and heat transfer is further developed to take into account the macroscopic solidification. The objective of this work is to investigate the turbulent flow pattern and progress of mushy zone solidification in the wedge-shaped cavity of the twin-roll caster machine by varying various parameters affecting the solidification modeling. Specifically, this study is devoted to a twin roll process with a narrow nip thickness (roll gap) to be used for manufacturing thin-strip stainless steel products. The motivation is to computationally explore the effects of the Darcy coefficient and turbulent viscosity modification factor for the mushy region on the solidifying shell growth. The second objective of this study is to investigate the effect of parameters such as nozzle width and roll gap thickness on the flow, heat transfer and solidification involving the twin-roll casting processes.

7.2 Mathematical Modeling

A two-dimensional schematic diagram of a vertical twin-roll casting system was shown Fig. 6.1. The continuous casting mold is formed by two counter-rotating rolls, side

dams, the supplied liquid steel free surface and the strip. It is assumed that the molten steel is steadily fed to the caster through a slot nozzle at the free surface of the wedge-shaped pool. The numerical simulation of such processes for thin strip products involves various aspects of complexities, i.e. turbulent behavior of the liquid steel in the pool, mushy flow modeling in the presence of turbulence, and complex geometry treatment.

7.2.1 Turbulent Modeling

The development of a general turbulence model, having a wide range of applications, has been the subject of extensive research in turbulent modeling during the last two decades. One of the popular models of turbulence is the two-equation $k-\varepsilon$ model. This class of turbulent models has been proposed in a variety of forms. Among the various versions of the $k-\varepsilon$ models the one known as the low-Re $k-\varepsilon$ turbulence model and proposed by Launder and Sharma (1974), which was claimed to yield better results compared to the other similar models (Patel et al. 1985), was chosen for this study. The mathematical formulation of this model for a single phase fluid flow as well as its advantages especially for metallurgical applications were described in Chapter 6.

7.2.2 Solidification Modeling

Among the various methods for solidification modeling, the continuum model formulation for binary alloys, originally developed by Bennon and Incropera (1987) for the laminar flow problems, was modified and extended in the present study for the turbulent liquid steel flow in the twin roll process. A brief formulation of fluid flow and heat transfer using this solidification model along with turbulent modification, for a 2-D steady state problem in Cartesian coordinate systems is given below. The detail information about this modeling can be found in Chapter 3.

conservation of mass:

$$\nabla \cdot (\rho \vec{V}) = 0 \quad (7.1)$$

conservation of momentum:

$$\operatorname{div}(\rho \vec{V} u) = \operatorname{div}\left(\mu_{\text{eff}} \frac{\rho}{\rho_l} \operatorname{grad} u\right) - \frac{\partial P}{\partial x} - \frac{\mu_l}{K_p} \frac{\rho}{\rho_l} (u - u_s) + S_x \quad (7.2)$$

$$\operatorname{div}(\rho \vec{V} v) = \operatorname{div}\left(\mu_{\text{eff}} \frac{\rho}{\rho_l} \operatorname{grad} v\right) - \frac{\partial P}{\partial y} - \frac{\mu_l}{K_p} \frac{\rho}{\rho_l} (v - v_s) + S_y \quad (7.3)$$

In momentum equations K_p represent the permeability of the two-phase mushy zone and was assumed to vary with the liquid fraction in the mushy region and was calculated using the Carman-Koseny equation for permeability of a porous media as:

$$K_p = \frac{g_l^3}{D_1(1 - g_l)^2} \quad (7.4)$$

The value of D_1 used in Eq. (7.4) depends upon the specific structure of the mushy region and, at present, is a controversial issue so far as the numerical modeling of the mushy region solidification is concerned. As will be seen later, this parameter does affect the transport processes in the mushy region and is one of the variables studied in this work.

conservation of energy:

$$\operatorname{div}(\rho \vec{V} h) = \operatorname{div}\left(\frac{k_m^{\text{eff}}}{c_s} \operatorname{grad} h\right) + \operatorname{div}\left[\frac{k_m^{\text{eff}}}{c_s} \operatorname{grad} (h_s - h)\right] - \operatorname{div}[\rho(\vec{V} - \vec{V}_s)(h_l - h)] \quad (7.5)$$

In the above equations, ρ , \vec{V} , k_m^{eff} and h are mixture density, velocity, effective thermal conductivity and enthalpy, respectively, as expressed in Chapter 3.

After some algebraic manipulations for changing the mixture enthalpy in the energy equation to sensible energy, \bar{h} , and assuming $c_l = c_s$, the new form of the conservation of energy equation for a one-phase model becomes:

$$\operatorname{div}(\rho \vec{V} \bar{h}) = \operatorname{div}\left(\frac{k_m^{\text{eff}}}{c_s} \operatorname{grad} \bar{h}\right) + \operatorname{div}(\rho f_s \vec{V}_s L) \quad (7.6)$$

The effective viscosity, μ_{eff} , appearing in the momentum equations is the sum of molecular and turbulent viscosity, $\mu_{eff} = \mu_l + \mu_t$, in which the turbulent viscosity is:

$$\mu_t = \rho f_\mu c_\mu \frac{k^2}{\varepsilon} \quad (7.7)$$

The values of k and ε required for the calculation of turbulent viscosity can be obtained from the solutions of two additional partial differential equations as given in Chapter 6 (Eqs. 6.5 and 6.6).

7.2.3 Complex Geometry Treatment

Due to the vertical symmetry, only a half of the domain is modeled. In order to obtain accurate solutions of the transport equations involved, a boundary-fitted coordinate (BFC) scheme was used. In the BFC approach, the first step is to generate the grid layout in the physical domain in such a way that every nodal point in it coincides with a corresponding node in the computational domain. The typical grid structure which was presented in Fig. 6.1 (Chapter 6) was adopted in the present study. The grid clustering operation was carried out in order to get the grid refinement close to the roll surface where high gradients of the transport variables are expected. Using the new coordinate system (ξ, η) , the general form of the transformed governing equations becomes:

$$\begin{aligned} \frac{\partial(\rho U \Phi)}{\partial \xi} + \frac{\partial(\rho V \Phi)}{\partial \eta} = \frac{\partial}{\partial \xi} \left[\Gamma_\phi \left(\frac{\alpha}{J} \frac{\partial \Phi}{\partial \xi} - \frac{\beta}{J} \frac{\partial \Phi}{\partial \eta} \right) \right] \\ + \frac{\partial}{\partial \eta} \left[\Gamma_\phi \left(\frac{\gamma}{J} \frac{\partial \Phi}{\partial \eta} - \frac{\beta}{J} \frac{\partial \Phi}{\partial \xi} \right) \right] + JS_\phi(\xi, \eta) \end{aligned} \quad (7.8)$$

where the Jacobian of transformation J , metric coefficients α , β , and γ , contravariant velocity components U and V and also source terms, S_ϕ , are identical to those defined in Chapter 6 (Eqs. 6.23 through 6.29), except the source terms for momentum and energy equations which can be written as follows:

X-momentum ($\Phi = u$, $\Gamma_\Phi = \mu_e = \mu_l + \mu_t$):

$$S_u(\xi, \eta) = -\frac{1}{J} \left(y_\eta \frac{\partial P}{\partial \xi} - y_\xi \frac{\partial P}{\partial \eta} \right) + \frac{1}{J} \frac{\partial}{\partial \xi} \left[\frac{\mu_e y_\eta}{J} \left(\frac{\partial U}{\partial \xi} + \frac{\partial V}{\partial \eta} \right) - \mu_e \frac{\partial v}{\partial \eta} \right] + \frac{1}{J} \frac{\partial}{\partial \eta} \left[\frac{\mu_e y_\xi}{J} \left(\frac{\partial U}{\partial \xi} + \frac{\partial V}{\partial \eta} \right) + \mu_e \frac{\partial v}{\partial \xi} \right] - \frac{C_0(1-g_l)^2}{g_l^3 + q} (u_s - u) \quad (7.9)$$

Y-momentum ($\Phi = v$, $\Gamma_\Phi = \mu_e = \mu_l + \mu_t$):

$$S_v(\xi, \eta) = -\frac{1}{J} \left(x_\xi \frac{\partial P}{\partial \eta} - x_\eta \frac{\partial P}{\partial \xi} \right) + \frac{1}{J} \frac{\partial}{\partial \eta} \left[\frac{\mu_e x_\xi}{J} \left(\frac{\partial U}{\partial \xi} + \frac{\partial V}{\partial \eta} \right) - \mu_e \frac{\partial u}{\partial \xi} \right] + \frac{1}{J} \frac{\partial}{\partial \xi} \left[\frac{\mu_e x_\eta}{J} \left(\frac{\partial U}{\partial \xi} + \frac{\partial V}{\partial \eta} \right) + \mu_e \frac{\partial u}{\partial \eta} \right] - \frac{C_0(1-g_l)^2}{g_l^3 + q} (v_s - v) \quad (7.10)$$

Energy ($\Phi = h$, $\Gamma_\Phi = \frac{k_m^{\text{eff}}}{c_s}$):

$$S_h(\xi, \eta) = \frac{\partial(\rho U_s f_s L)}{\partial \xi} + \frac{\partial(\rho V_s f_s L)}{\partial \eta} \quad (7.11)$$

7.2.4 Boundary conditions

The boundary conditions which are considered for the fluid flow, turbulent quantities and energy equations are listed in Table 7.1. In this table, γ_r is the average heat transfer coefficient between the roll surface and the surrounding, and h_a represents the product of ambient temperature and the specific heat of steel. In the present study the values of γ_r were chosen to be equal to 10,000 and 8,000 $Wm^{-2}K^{-1}$ for 4 mm and 3 mm strip thicknesses, respectively.

Table 7.1. Summary of the adopted boundary conditions.

positions	velocity	turbulent quantities	energy
inlet	$u = u_{in},$ $v = 0$	$k = 0.01 \times u_{in}^2,$ $\varepsilon = c_{\mu} k_{in}^{3/2} / 0.05W$	$h = h_{in}$
outlet	$\beta \frac{\partial \Phi}{\partial \xi} - \gamma \frac{\partial \Phi}{\partial \eta} = 0$ $\Phi = u, v$	$\beta \frac{\partial \Phi}{\partial \xi} - \gamma \frac{\partial \Phi}{\partial \eta} = 0$ $\Phi = k, \varepsilon$	$\beta \frac{\partial \bar{h}}{\partial \xi} - \gamma \frac{\partial \bar{h}}{\partial \eta} = 0$
free surface	$u = 0$ $\beta \frac{\partial v}{\partial \xi} - \gamma \frac{\partial v}{\partial \eta} = 0$	$\beta \frac{\partial \Phi}{\partial \xi} - \gamma \frac{\partial \Phi}{\partial \eta} = 0$ $\Phi = k, \varepsilon$	$\beta \frac{\partial \bar{h}}{\partial \xi} - \gamma \frac{\partial \bar{h}}{\partial \eta} = 0$
symmetry plane	$v = 0,$ $\alpha \frac{\partial u}{\partial \xi} - \beta \frac{\partial u}{\partial \eta} = 0$	$\alpha \frac{\partial \Phi}{\partial \xi} - \beta \frac{\partial \Phi}{\partial \eta} = 0$ $\Phi = k, \varepsilon$	$\alpha \frac{\partial \bar{h}}{\partial \xi} - \beta \frac{\partial \bar{h}}{\partial \eta} = 0$
roll surface	$u = u_{roll} \cos \theta,$ $v = -u_{roll} \sin \theta,$	$k = \varepsilon = 0$	$\frac{\partial \bar{h}}{\partial n} = -\frac{\gamma_r}{K} (\bar{h}_s - h_a)$

7.3 Numerical Solution

The primitive form of the governing transport equations along with the boundary conditions were made discrete by the staggered-grid control-volume finite difference method. The well known SIMPLE algorithm of Patankar (1980) was employed to couple continuity and momentum equations. The non-linear discretized equations were solved iteratively using the line-by-line tri-diagonal matrix algorithm (TDMA), and the iteration loop was terminated if their maximum absolute residuals (normalized by the corresponding fluxes at the inlet) were less than 0.001.

The grid-independency of the solution results was verified by performing some numerical tests with different grid layouts. Three different grid numbers, i.e. 32×32 , 42×42 and 52×52 , were tested for a sample case with the roll gap thickness equal to 4 mm and roll velocity equal to 1 m/s. The variation of the velocity component in the x-direction and the turbulent kinetic energy at $x = 0.12m$ for three different grid distributions are shown in Figs. 7.2 and 7.3, respectively. Because of the insignificant difference in the results of the velocity and the turbulent kinetic energy obtained in 42×42 and 52×52 grid distributions, and for the sake of computational economy, most of the runs were performed with the 42×42 grid layout. To gain a better understanding of the effects of the process modeling parameters, a sensitivity study on the model was carried out. Specifically, the effects of the modeling parameters employed for the modeling of the mushy region, namely, the Darcy coefficient and the turbulent viscosity modification factor, on the model were analyzed. In addition, the geometrical parameters, such as the roll gap thickness and the inlet nozzle width, were investigated.

7.4 Results and Discussion

7.4.1 Darcy Coefficient Effect

The geometrical parameters of the simulated twin-roll caster and the transport properties of the molten stainless steel used are listed in Table 7.2. As mentioned in the mathematical formulation section, the fluid flow in the mushy region has been modeled assuming that the mushy region is a porous media with variable permeability. Upon application of Eq. (7.4) in the momentum equations, the final form of the Darcy source term becomes:

$$\text{Darcy Source Term} = \frac{C_0(1-g_i)^2}{g_i^3 + q_0} (u_i - u_s) \quad (7.12)$$

where C_0 is Darcy coefficient and q_0 is a small number to prevent division by zero in numerical calculation.

Table 7.2. Physical properties of stainless steel and the geometrical parameters used for the calculations.

variable	value	variable	value
viscosity	$0.007 \text{kgm}^{-1} \text{s}^{-1}$	roll diameter	1.2m
density	7000kgm^{-3}	pool depth	0.385m
specific heat	$700 \text{Jkg}^{-1} \text{K}^{-1}$	gap thickness	3 and 4 mm
thermal conductivity	$31 \text{Wm}^{-1} \text{K}^{-1}$	nozzle width	12 and 18 mm
latent heat of fusion	264kJkg^{-1}	roll speed	1m/s
liquidus temperature	1454°C	inlet temperature	1464°C
solidus temperature	1400°C		

Figures 7.4a-7.4f represent the effect of C_0 on the flow pattern for one-half of the vertical symmetry plane of the twin-roll caster's pool. In these figures, the roll gap thickness, roll speed and inlet nozzle width were kept constant at 4 mm, 1 m/s and 18 mm respectively but the value of C_0 was varied from 0 to 3200 in a geometrical fashion. In the vertical twin-roll casting process studied here, the inlet flow is driven by the ferrostatic pressure from an upstream tundish (not shown in the schematic diagram presented in Fig. 6.1), and it essentially acts as a plunging jet for the metal pool and tends to go downward along the symmetry plane towards the nip point (pool exit). On the other hand, the motion of the roll causes a shear dominated downward flow along the roll surface. Since the shear flow rate generated by the roll motion is high compared to the net out flow of the caster, it causes an upward flow across the symmetry plane to develop in order to satisfy the mass conservation law. The upward flow, generated due to the motion of the roll, resists the downward flow of the inlet stream. The collision of these two oppositely directed flows

results in a stagnation point under the nozzle's centerline. The position of the stagnation point was found to depend critically on the relative strengths of these two oppositely directed flows. Irrespective of the values of C_0 used in Figs. 7.4a-7.4c, it is seen that two asymmetrical counter rotating recirculation zones develop within the wedge-shaped pool. Figure 7.4a represents the flow pattern of the molten steel in the twin-roll casting process with $C_0 = 0$. The physical significance of this case is that the mushy region is assumed to behave as the liquid and the solidification phenomena does not affect the fluid flow there. Since in this case there exists no coupling between the energy and momentum equations, there is no change in the velocity in the mushy region due to the cooling of the melt below the liquidus temperature and the mushy region behaves similar to the purely liquid region. In the case of a non-zero C_0 , with the increase of the value of C_0 , the solid layer that develops on the roll surface moves with a velocity closer to the roll speed used, and as a result the discharge of the steel from the caster in the form of solid is also increased. This solid steel motion along the roll, especially at the region deeper than two-thirds of the pool depth, gets added to the shear flow induced by the motion of the solid layer and consequently produces a higher steel flow along the roll compared to the case of $C_0 = 0$. The presence of the upward flow along the symmetry plane, much deeper in the cases for non zero values of C_0 , can be attributed to the development of an additional downward mass flow of steel on the roll surface due to the solidification. Figures 7.4b-7.4f show the effect of increasing C_0 on the strength of the upward flow. As seen from these figures, an increase of C_0 from 400 to 3200 causes the solid layer velocity to approach the roll speed and also increases the strength of the upward flow, which in turn leads to a higher penetration depth of the pool from the bottom. All these effects are due to the enhancement of the Darcy source term in the momentum equations. It is to be noted that the differences in the strengths of the upward flows for the increasing values of C_0 gradually vanish at the shallower depth of the pool, which is due to the expansion of the mold cross sectional area as well as to the development of the thinner solid and mushy regions at the upper part of the pool.

Figures 7.5a-7.5f represent the solidus and liquidus contours in the twin-roll caster for various values of C_0 . In all of these figures, the shape of the liquidus curves which separate the region of the pure liquid from the mushy zone corresponds to the associated predicted flow patterns. The general trend of these figures is that the molten, hot metal flow from the entrance causes a high temperature region along the symmetry plane which is extended downstream up to the stagnation point. Under the stagnation point, the temperature field is influenced by the upward recirculation flow and a lower thermal zone having temperature levels less than the liquidus temperature develops there. The development of this low temperature zone is the result of the induced shear flow which is progressively cooled by traveling on the water-cooled roll surface. Figure 7.5a shows the liquidus and solidus lines for the case of $C_0 = 0$ in which there is no direct effect of solidification on the fluid flow. As seen from this figure, the liquid steel is penetrated downward along the roll surface up to a depth of about 0.2 meter, and the flow is stagnated there due to the inverse flow induced by the roll motion. A comparison between the results presented in Figs. 7.5b-7.5f for various non-zero values of C_0 , shows that the liquidus curves are distinct for these figures, while the solidus curves remain almost unchanged. The basic difference in the liquidus curves in these figures is the result of the variation of the liquid phase depth. An increase of the C_0 value results in the increase of the penetration depth of liquid phase. The deep penetration of hot metal for higher values of C_0 can be addressed to the role of the Darcy source term in the momentum equation. An increase in C_0 in the Darcy source term causes the fluid velocity in the mushy region to increase towards the roll speed and consequently there is an increase in the shear stress exerted on the interior layers of the fluid. Since the fluid flow close to the roll surface is dominated by the shear stress, the consequence of an increase in the shear stress appears as a deeper penetration of the inlet hot metal which is deflected towards the roll surface.

Figures 7.6a-7.6f provide the superheat contours in the wedge-shaped pool of the caster. In all of these cases, the high temperature gradient exists at the roll surface due to the high heat extraction rate at this region, and also a well mixed steel appears at the center of the pool due to the strong turbulent recirculatory motion of liquid steel. A better

mixing of the liquid metal for the higher values of C_0 can be attributed to the higher level of turbulence that develops at the center of the half-pool. This explanation can be supported by comparison of the turbulent viscosity contours presented in Figs. 7.7a-7.7c for three values of C_0 .

Figures 7.8 and 7.9 provide the effect of the C_0 value on the temperature profiles at two horizontal cross sections of the pool located at the depth of 12 and 25.5 cm, respectively, from the top surface. From these figures it can be seen that in a lower depth of the pool, all tested C_0 values display similar variations in temperature. For deeper cross sectional areas of the pool, where the fraction of the mushy region is considerable, there is a visible difference between the temperature profiles for the zero and non-zero values of C_0 . The temperature variations at the exit, horizontal cross-sectional plane of the pool for various C_0 's are presented in Fig. 7.10. This figure shows that with the increase of C_0 , the temperature of the solidified shell increases along with the accompanying reduction in the mushy layer temperature. A milder variation of temperature at the exit can be found for higher values of C_0 .

As mentioned earlier, the selection of a suitable value for C_0 , at present, is a controversial issue in the mushy fluid flow modeling studies. In the absence of any kind of experimental measurements of the thickness and/or temperature variations of the mushy region, it is truly difficult to recommend any suitable value of C_0 applicable for all casting conditions. In spite of this uncertainty, a value of 1600 for C_0 can be chosen for the coupled fluid flow and solidification studies in a twin-roll caster. This value of C_0 also corresponds to the value used by Minakawa et al. (1987) who estimated their value on the basis of the morphology of the porous media and the length of the secondary arm spacing. The latter was taken in the order of 10^{-2} cm.

7.4.2 Turbulent Viscosity Modification Effect

The next parameter which affects the modeling of mushy fluid solidification is the turbulent viscosity modification factor. Over the years various investigators who have modeled turbulent flow and solidification heat transfer problems have used various forms of this factor. All investigators agree that a modification of the turbulent eddy viscosity in the mushy region is necessary for damping the turbulent effect in the mushy region and that this damping factor should be based on the solid or liquid fraction there. Upon an application of the turbulent viscosity modification factor, the expression for the turbulent eddy viscosity becomes:

$$\mu_t = \rho c_\mu f_\mu f_m \frac{k^2}{\varepsilon} \quad (7.13)$$

where f_m is turbulent viscosity modification coefficient. In the present study, the following functions were selected along with the base case with no modification, i.e. $f_m=1$:

$$(a) \quad f_m = \sqrt{g_i}$$

$$(b) \quad f_m = g_i^2$$

It is noted that for studying the effects of the turbulent viscosity modification factor on the thermal and fluid flow fields, the value of C_0 was kept constant at 1600. Figures 7.11, 7.12 and 7.13 show the effect of f_m on the flow pattern, liquidus-solidus isotherms and superheat contours, respectively. The results presented in these figures show that the flow field is more sensitive to the examined turbulent viscosity modification factors. A comparison of the velocity vector plots in Figs. 7.11a-7.11c, predicted for different functional forms of f_m , shows that the application of the modification factor for the turbulent viscosity in the mushy region, which varies between 0 and 1, results in the weakening of the reversed flow at the center of the pool. The reason for this is that for a certain shear stress in the mushy region close to the roll surface, a decrease in the turbulent viscosity necessitates an increase in the velocity gradient in the mushy region especially close to the solid layer developed on the roll surface. Thus, the flow velocity in the mushy layer should decay from the roll speed to zero at a sharper rate with respect to

the thickness of the mushy layer when the turbulent viscosity modification factor is applied.

So far as the thermal field is concerned, Figs. 7.12(a-c) show that the extent of the mushy layer in the wedge-shaped pool decreases upon an application of any one of the two stated functions for f_m compared to that for $f_m = 1$. The reason for this being that by damping the turbulent viscosity in the mushy region, one increases the gradient for thermal transport there, and consequently the mushy layer becomes thinner. This is especially true close to the roll surface. An inspection of Figs. 7.12b and 7.12c shows that for $f_m = g_l^2$, the effect of modification intensifies and results in a thinner mushy zone compared to the use of the other modification function i.e., $f_m = \sqrt{g_l}$.

The superheat isotherms presented in Figs. 7.13a-7.13c show that for the cases when turbulent viscosity was dampened, the bulk temperature of the liquid phase at any cross section of the pool was higher than that for the case with no modification. It is worthy to mention here that this increase in the liquid temperature is as low as one degree Celsius or less and together with the reduction in the thickness of the mushy layer along the roll surface, one finds a logical agreement that the conservation of energy in the domain was correctly satisfied.

Figure 7.14 shows the temperature profiles at the exit of the pool for three different turbulent viscosity modification factors. In all the three cases studied, almost three quarters of the strip thickness was completely solidified. Although, there is an insignificant change in the thickness of the solid layer in these cases, along with the solid layer temperature differences one can compensate for the dissimilarity of the mushy layer temperatures at the exit. In general, while the modification of turbulent viscosity in the mushy zone has an insignificant effect on the thermal behavior of the twin-roll processes, it provides a more considerable effect on the fluid flow. To the best of the authors' knowledge, there is unfortunately no experimental data available for comparison with the predicted results, and there is no guidance in the literature for the selection of the appropriate modification factor in the mushy fluid flow modeling, related to coupled turbulent recirculatory flows and solidification heat transfer studies.

7.4.3 Casting Profile Effect

Figures 7.15a-7.15c show the velocity vectors, solidus and liquidus temperatures and temperature distributions in the liquid pool, respectively for the nozzle width of 12 *mm* and for a roll gap of 3 *mm*. Figures 7.16a-7.16c are similar plots as are Figs 7.15a-7.15c, but for a roll gap of 4 *mm*. A comparison of Figs. 7.15a and 7.16a shows that for the 4 *mm* roll gap, the inlet liquid metal jet penetrates a little deeper into the liquid metal pool compared to the caster with a 3 *mm* roll gap. Figures 7.15b-7.15c and Figs. 7.16b-7.16c show that the extent of the liquid region for the 4 *mm* roll gap is bigger compared to the caster with a 3 *mm* roll gap. The above results are expected from physical reasonings. Since, during computations at a steady state, the inlet metal flow rate at the nozzle was balanced with the outlet flow through the roll gap for a fixed roll speed and width of the caster, the bigger the roll gap, the larger the inlet flow and higher the enthalpy of the liquid metal entering the cavity between the cooled rolls. The deeper penetration of the jet and higher energy level in the cavity for a bigger roll gap is the manifestation of the above fact. A comparison of Figs. 7.16a-7.16c with the corresponding Figs. 7.11a, 7.12a and 7.13a shows that for a fixed roll gap, the larger the width of the inlet nozzle, the lesser the penetration of the inlet jet and the smaller the extent of the liquid zone. The limited parametric changes carried out in this study, related to the roll gap and nozzle width, did not show any appreciable effect on the solidified shell profile along the roll.

7.5 CONCLUDING REMARKS

Basic phenomena of the vertical twin-roll thin-strip casting process for stainless steel have been investigated through numerical modeling of the coupled turbulent flow, heat transfer and macroscopic solidification in the wedge-shaped cavity of the caster. The

influence of the macroscopic solidification parameters, namely, the Darcy coefficient and the turbulent eddy viscosity damping factor for the mushy region (located between the solidus and liquidus temperatures), on the velocity and temperature fields, turbulent viscosity distributions and extents of the mushy and solid regions is primarily investigated. This study shows that irrespective of the values of the Darcy coefficient and the turbulent damping factor used in the model, two asymmetrical counter rotating recirculation zones develop within the wedge-shaped pool. The changing of the Darcy coefficient in the range 800 to 3200 did not show any noticeable influence on the transport processes in the caster. On the basis of the present investigation, we recommend a value of 1600 for the Darcy coefficient for studying mushy zone solidification in a twin-roll caster and similar systems. Considering the fact that the mushy region is a mixture of solid and liquid steel, sensitivity studies were carried out on the model using three turbulent eddy damping factors, two of which were dependent on the liquid fraction. The three factors studied did not show any significant effect on the solidified shell thickness but did show a noticeable influence on the velocity and temperature distributions in the liquid and mushy regions. With regard to the selection of this factor, further investigations are warranted. However, for engineering calculations and design any of the three examined damping functions can be selected. For a fixed width of the nozzle, an increase in the roll gap increased the penetration depth of the plunging inlet jet into the liquid metal pool of the caster but decreased the extent of the mushy region, while the solidified shell profile remained insensitive to the change of the roll gap. For a fixed roll gap, an increase in the width of the nozzle decreased the penetration depth of the inlet liquid metal jet but increased the extent of the mushy region, while the solidified shell thickness remained practically unaffected.

NOMENCLATURE

Symbol	Description
a_p, a_{nb}, b	coefficients in the discretized governing equations
C_0	Darcy coefficient
c_1, c_2, c_μ	empirical constants for low Reynolds turbulent models
c_l	liquid specific heat
c_s	solid specific heat
D_1	Darcy coefficient
D_k	extra dissipation term in k -equation
E_ε	extra generation term in ε -equation
f_1, f_2, f_μ	empirical constants for low Reynolds turbulent models
f_m	turbulent viscosity modification factor
g_l, g_s	liquid and solid fractions, respectively
G	turbulent kinetic energy generation in k -equation
\bar{h}	sensible heat
h_l	liquid enthalpy
h_s	solid enthalpy
J	Jacobian of the transformation
k	turbulent kinetic energy
k_l, k_s	liquid and solid thermal conductivities, respectively
k_t	turbulent thermal conductivity
k_m^{eff}	mixture effective thermal conductivity
k_l^{eff}	effective thermal conductivity of liquid
K_p	permeability
P	Pressure

Pr	laminar Prandtl number
Re_t	turbulent Reynolds number based on the turbulent quantities
S_Φ	source term associated with Φ
T	temperature
T_{in}	inlet temperature
T_l	liquidus temperature
T_s	solidus temperature
u_i	velocity component in the i-th direction; corresponding to u , v and w
u_{in}	inlet velocity
u_l, u_s	liquid and solid speeds, respectively
W	nozzle width
$x_\xi, x_\eta, y_\xi, y_\eta$	metric derivatives

Greek Symbols

α, β, γ	geometric relations between coordinate systems
ε	turbulent kinetic energy dissipation rate
γ_r	convective heat transfer coefficient
Γ_Φ	diffusion coefficient associated with Φ value
μ	laminar viscosity
μ_e	effective viscosity equal to $\mu + \mu_t$
μ_t	turbulent viscosity
Φ	generalized dependent variable
ρ	mass density
σ_l, σ_t	laminar and turbulent Prandtl numbers
$\sigma_k, \sigma_\varepsilon$	empirical constants in turbulent model equations
ξ, η	axes of nonorthogonal curvilinear coordinate system

REFERENCES

- Bennon W. D. and Incropera F. P., A continuum model for momentum, heat and species transport in binary solid-liquid phase change systems-I. model formulation, *Int. J. Heat Mass Transfer*, Vol. 30, No. 10, pp. 2161-2170, (1987).
- Launder B. E. and Sharma B. I., Application of the energy dissipation model of turbulence to the calculation of flow near a spinning disc, *Letters in Heat and Mass Transfer*, Vol. 1, pp. 131-138, (1974).
- Minakawa S., Samarasekera I. V. and Weinberg F., Centerline porosity in plate castings, *Metall. Trans. B*, Vol. 16B, pp. 245-255, (1987).
- Patankar S.V., *Numerical Heat Transfer and Fluid Flow*, Hemisphere/McGraw-Hill, Washington, (1980).
- Patel V. C., Rodi W. and Scheuerer J., Turbulence models for near-wall and low-Reynolds-number flows: a review, *AIAA Journal*, Vol. 23, No. 9, pp. 1308-1319, (1985).
- Seyedein S. H. and Hasan M., A numerical study of turbulent transport phenomena and superheat dissipation in a Twin-Roll Caster, in *Computational Fluid Dynamics and Heat/Mass Transfer Modeling in the Metallurgical Industry, the proceedings of the 35th Annual Conference of Metallurgists of CIM*, pp. 187-202, (1996).
- Seyedein S. H. and Hasan M., Numerical simulation of turbulent flow and heat transfer in the wedge-shaped liquid metal pool of a twin-roll caster, *Numerical Heat Transfer: Part A*, Vol. 31, pp. 393-410, (1997).

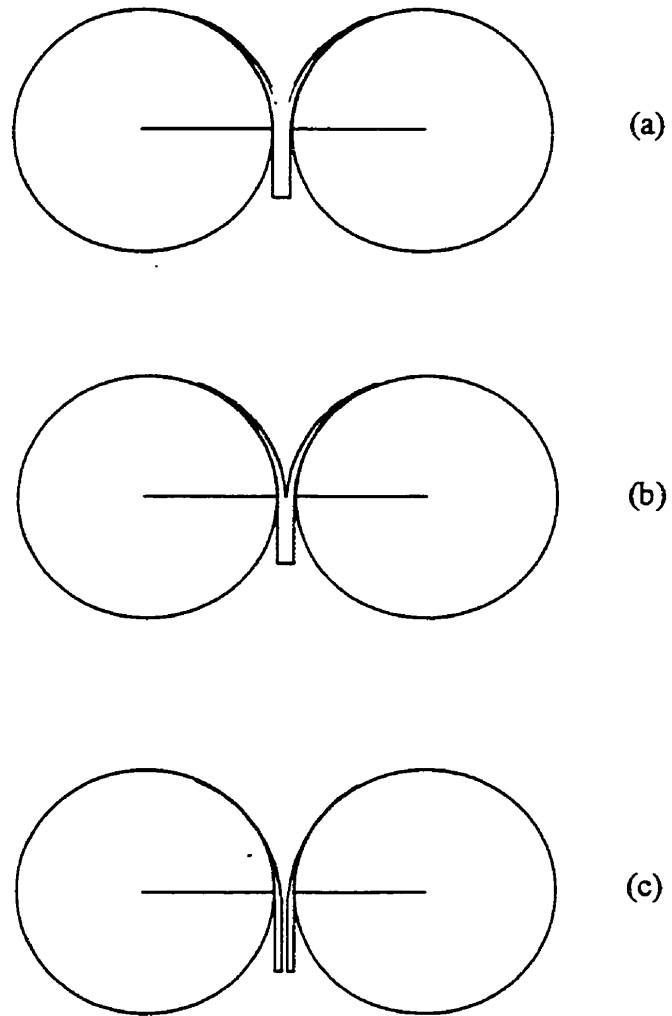


Fig. 7.1. Various conditions for solidification progressing in a twin-roll casting machine; (a) unstable and exerts mechanical force on the rolls, (b) stable, (c) unstable and leads to breakout.

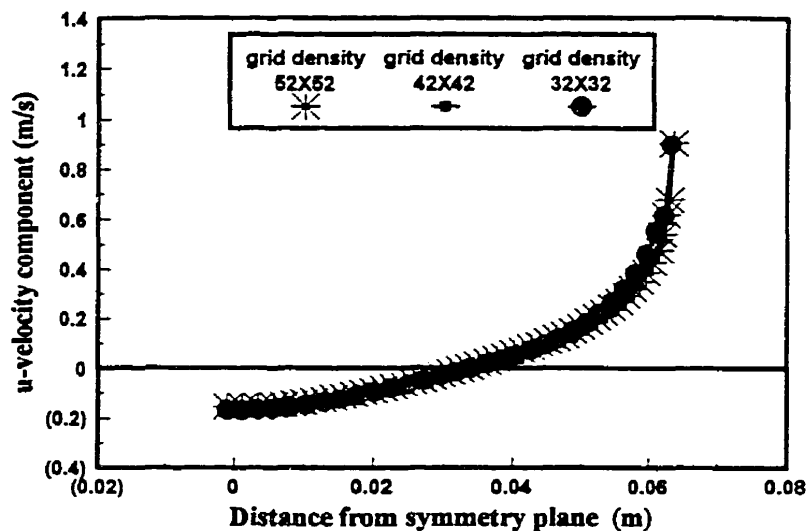


Fig. 7.2. Effect of grid number on u-component velocity profile at a depth of 0.12 m across the cross-section of the cavity for $t=4$ mm and $u_r = 1m/s$.

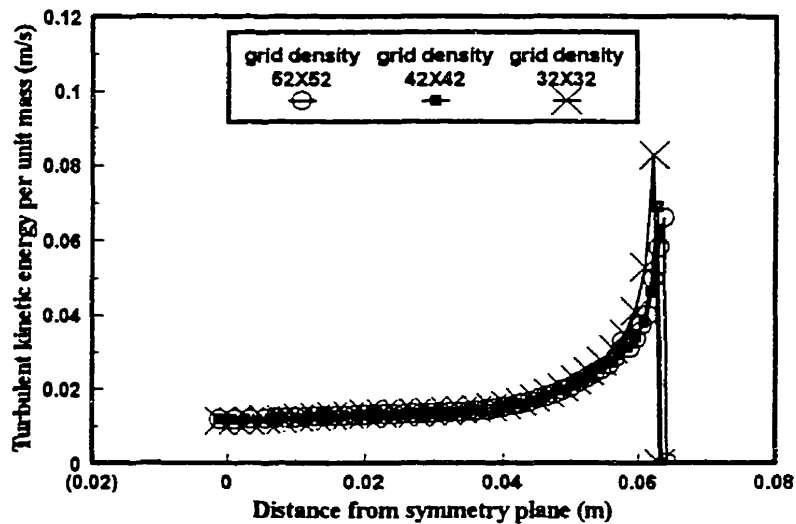


Fig. 7.3. Effect of grid number on turbulent kinetic energy profile at a depth of 0.12 m across the cross-section of the cavity for $t=4$ mm and $u_r = 1m/s$.

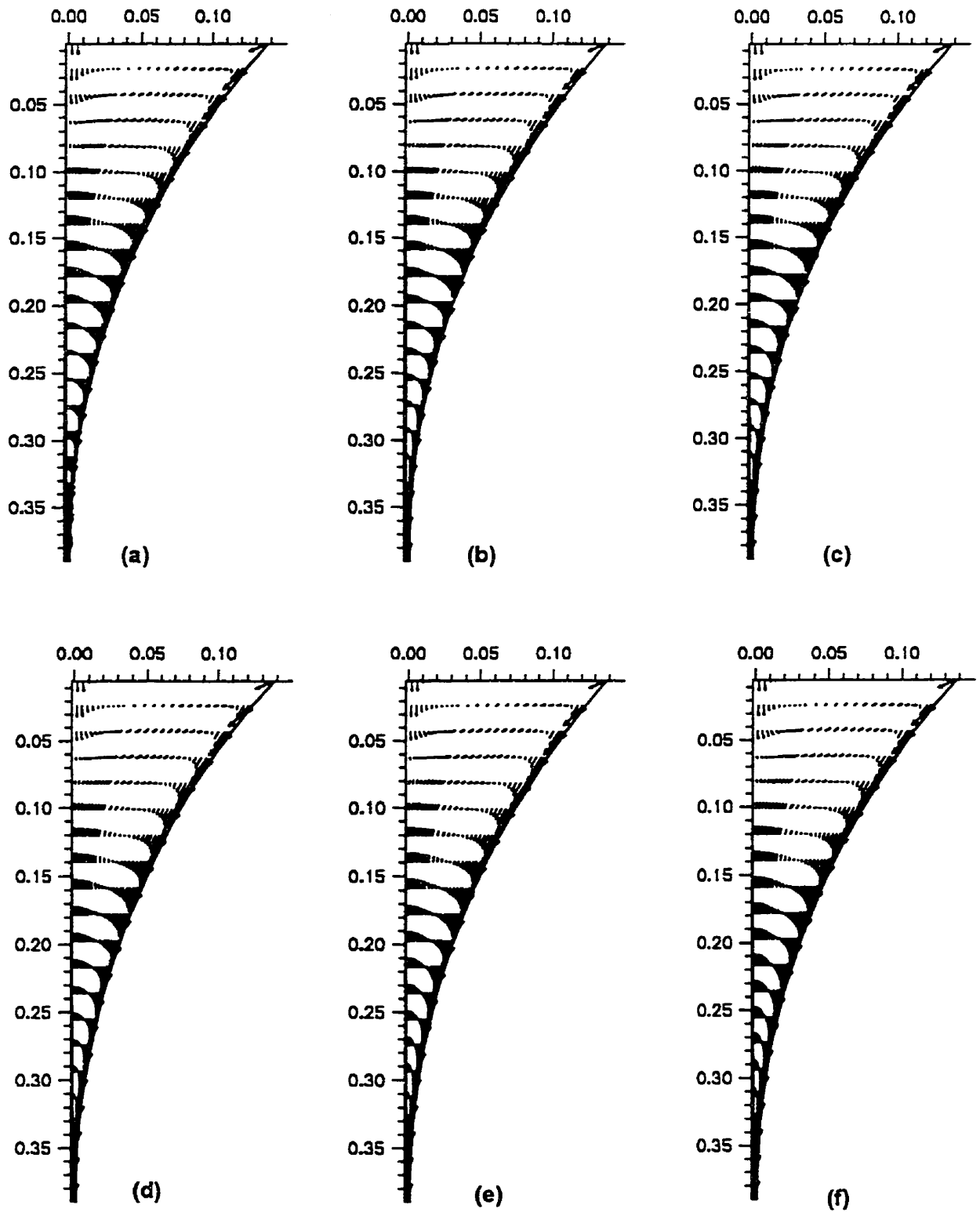


Fig. 7.4. Effect of C_0 value on the velocity field for $u_r = 1m/s$ and $t=4$ mm ; (a) $C_0 = 0$, (b) $C_0 = 200$, (c) $C_0 = 400$, (d) $C_0 = 800$, (e) $C_0 = 1600$, (f) $C_0 = 3200$.

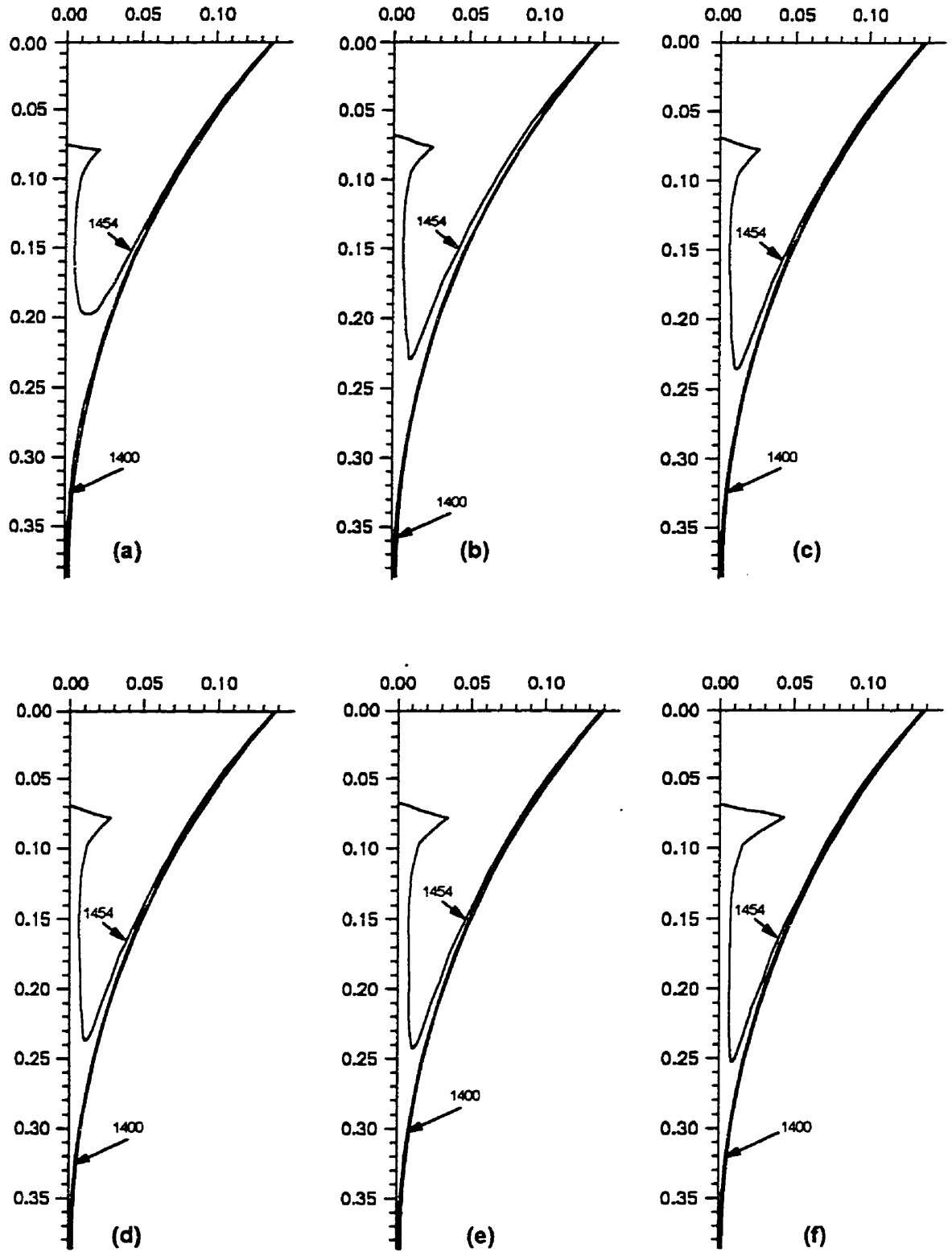


Fig. 7.5. Effect of C_0 value on the solidus and liquidus contours for $u_r = 1m/s$ and $t=4$ mm; (a) $C_0 = 0$, (b) $C_0 = 200$, (c) $C_0 = 400$, (d) $C_0 = 800$, (e) $C_0 = 1600$, (f) $C_0 = 3200$.

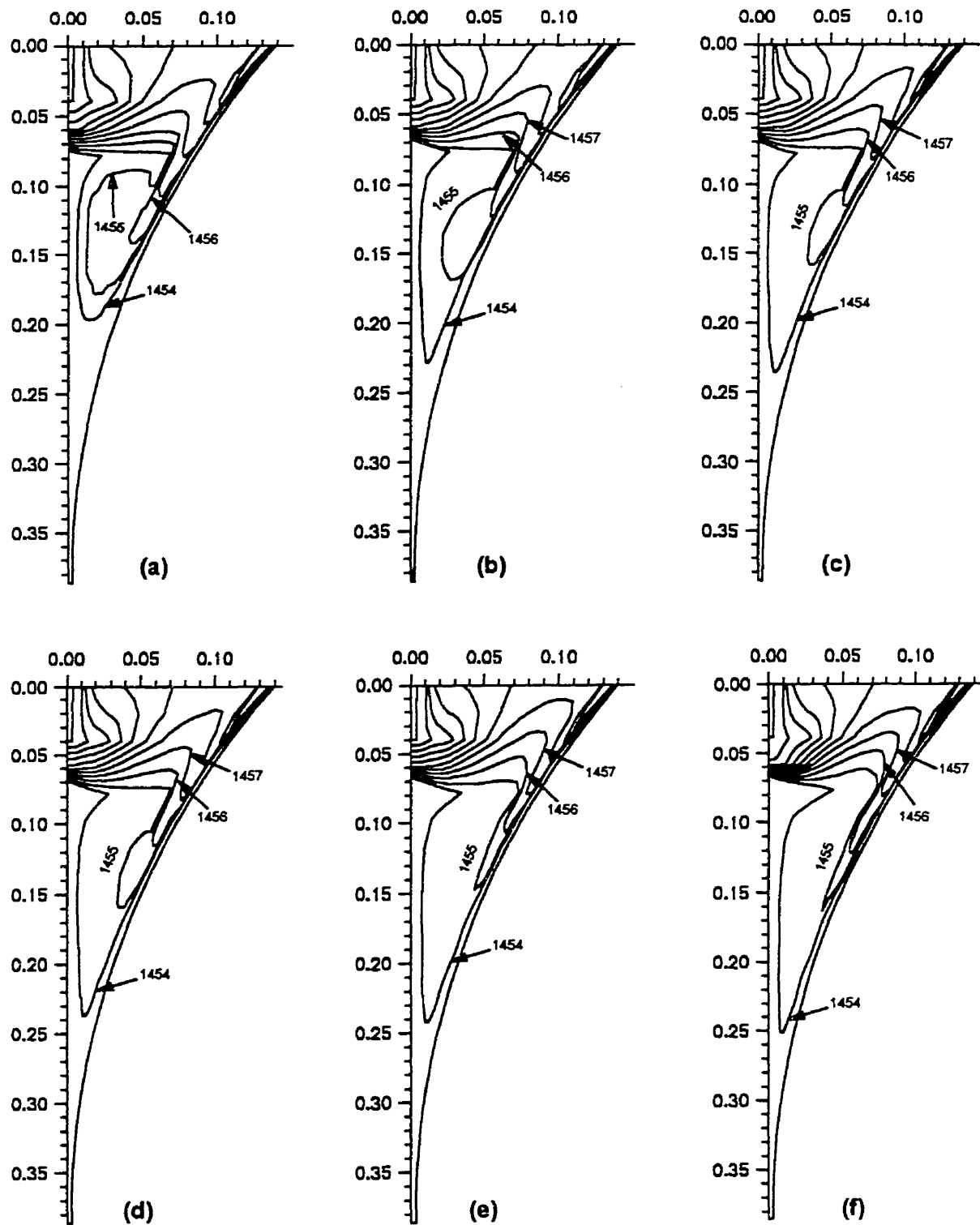


Fig. 7.6. Effect of C_0 value on the superheat isotherms for $u_r = 1\text{ m/s}$ and $t = 4\text{ mm}$; (a) $C_0 = 0$, (b) $C_0 = 200$, (c) $C_0 = 400$, (d) $C_0 = 800$, (e) $C_0 = 1600$, (f) $C_0 = 3200$.

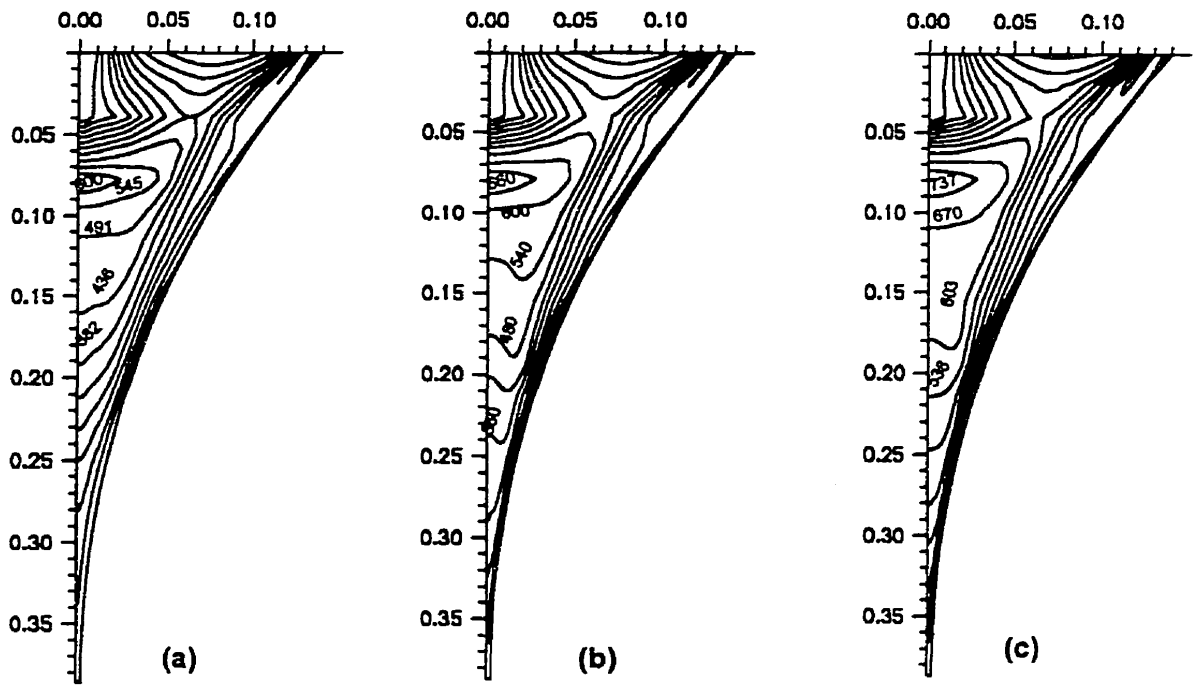


Fig. 7.7. Comparison of the non-dimensional turbulent viscosity contours for $t=4$ mm, $u_r = 1\text{m/s}$, and different C_0 value; (a) $C_0 = 0$, (b) $C_0 = 1600$, (c) $C_0 = 3200$.

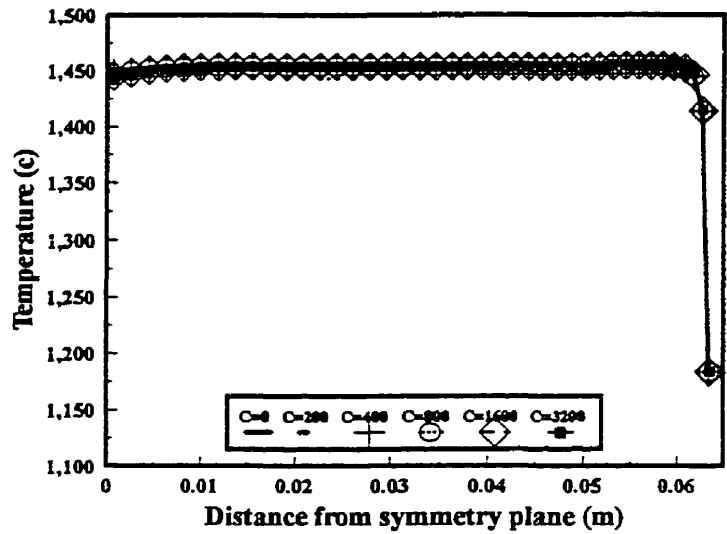


Fig. 7.8. Effect of C_0 value on the temperature profile on a horizontal cross-sectional plane at a depth of 0.12 m from the top.

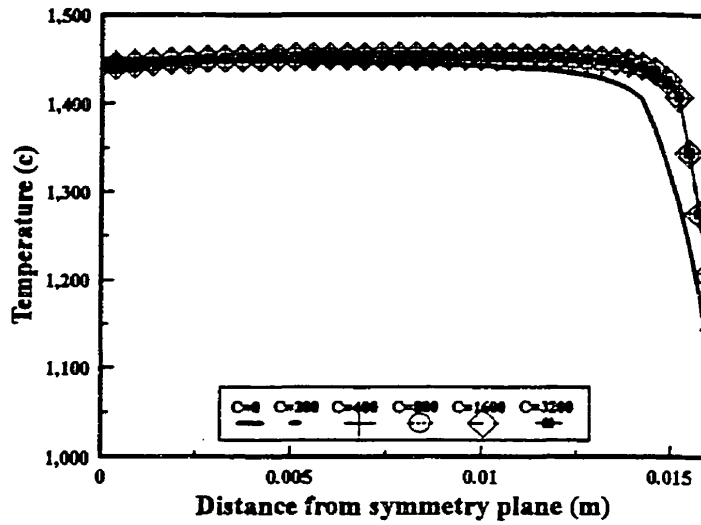


Fig. 7.9. Effect of C_0 value on the temperature profile on a horizontal cross-sectional plane at a depth of 0.25 m from the top.

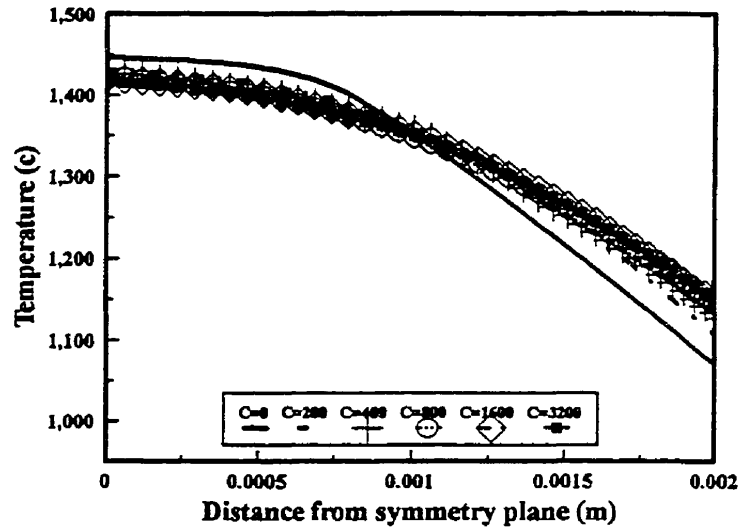


Fig. 7.10. Effect of C_0 value on the temperature profile on a horizontal cross-sectional plane at exit (depth of 0.385 m from the top).

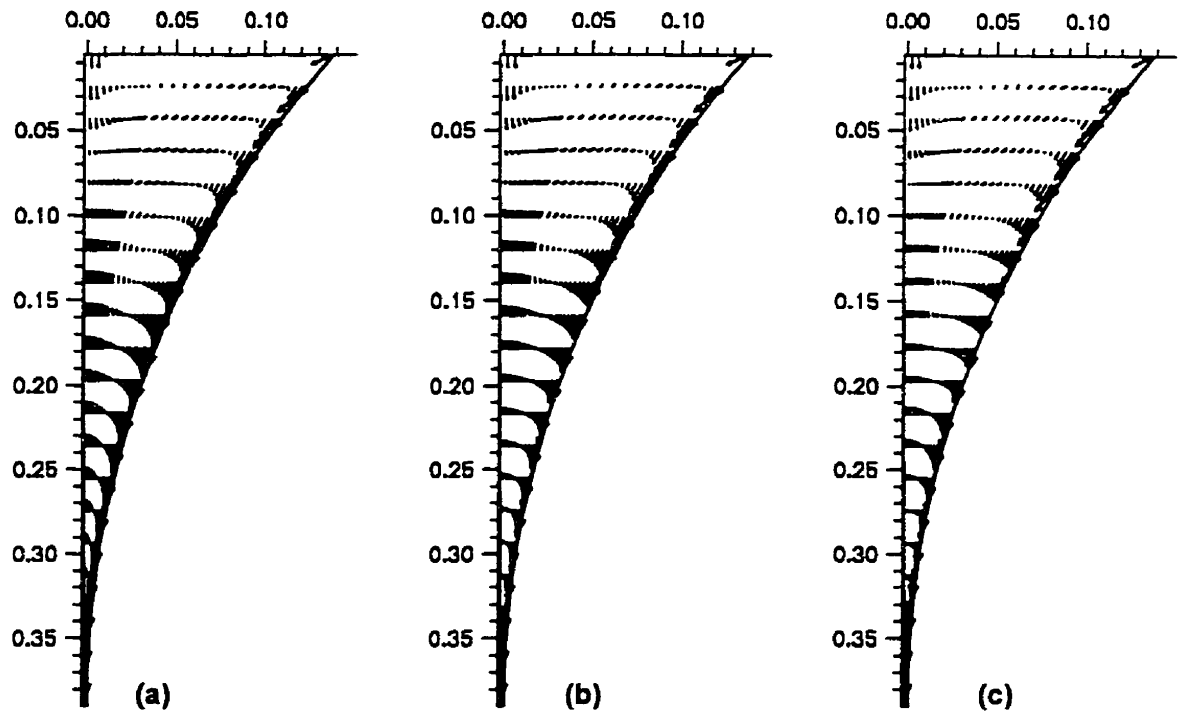


Fig. 7.11. Effect of various turbulent viscosity modification factors on the velocity distribution for $C_0 = 1600$; (a) $f_m = 1$, (b) $f_m = \sqrt{g_i}$, (c) $f_m = g_i^2$.

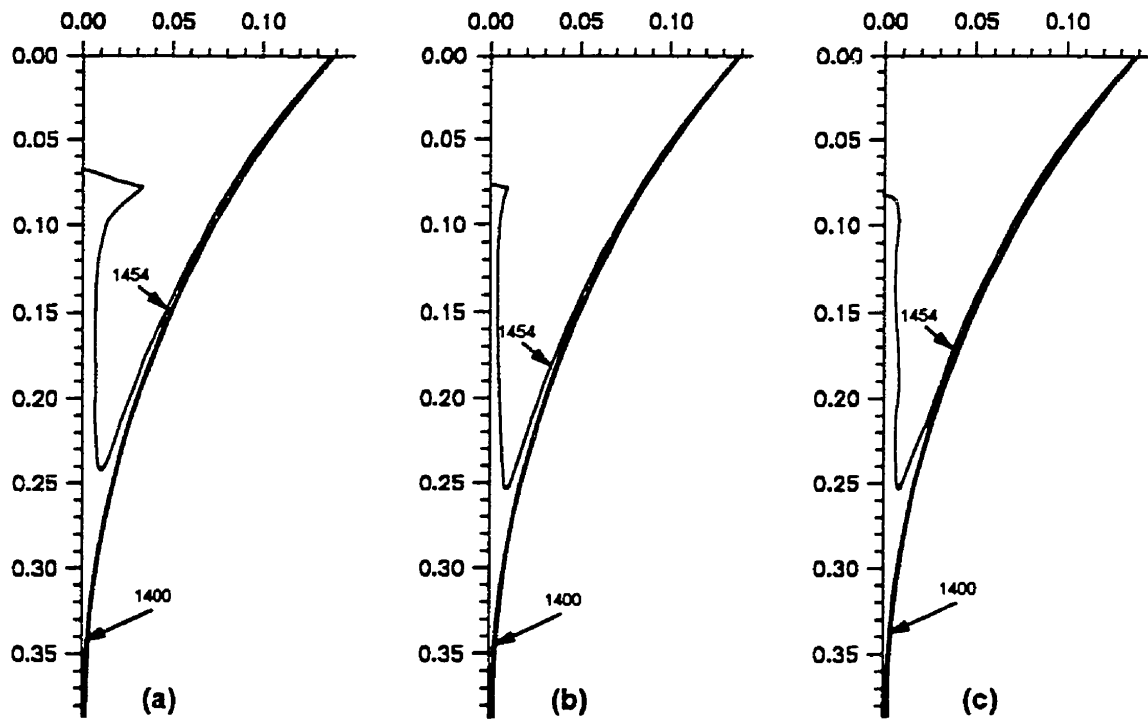


Fig. 7.12. Effect of various turbulent viscosity modification on liquidus and solidus temperature profiles for $C_0 = 1600$; (a) $f_m = 1$, (b) $f_m = \sqrt{g_i}$, (c) $f_m = g_i^2$.

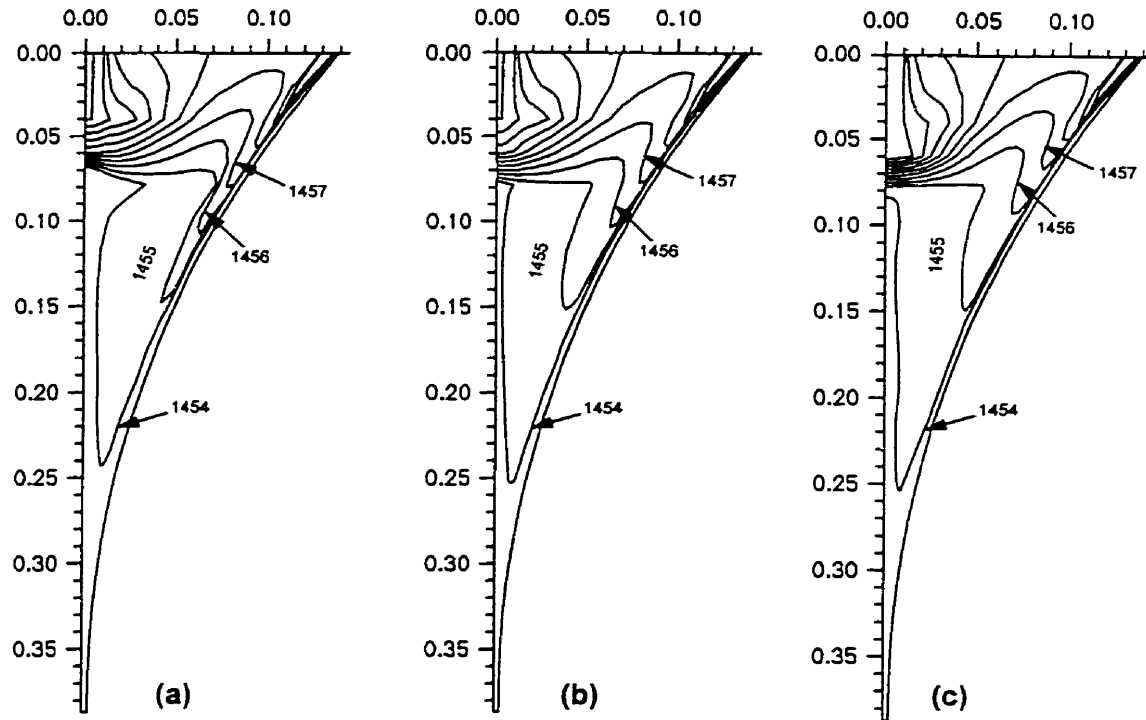


Fig. 7.13. Effect of various turbulent viscosity modification factors on temperature distributions for $C_0 = 1600$; (a) $f_m = 1$, (b) $f_m = \sqrt{g_i}$, (c) $f_m = g_i^2$.

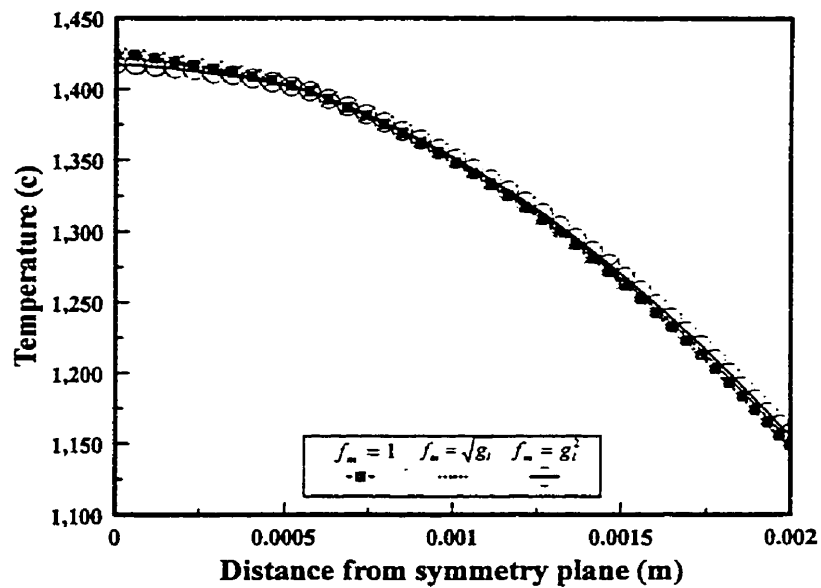


Fig. 7.14. Effect of various turbulent viscosity modification factors on the temperature profile on a horizontal cross-sectional plane at exit (depth of 0.385 m from the top).

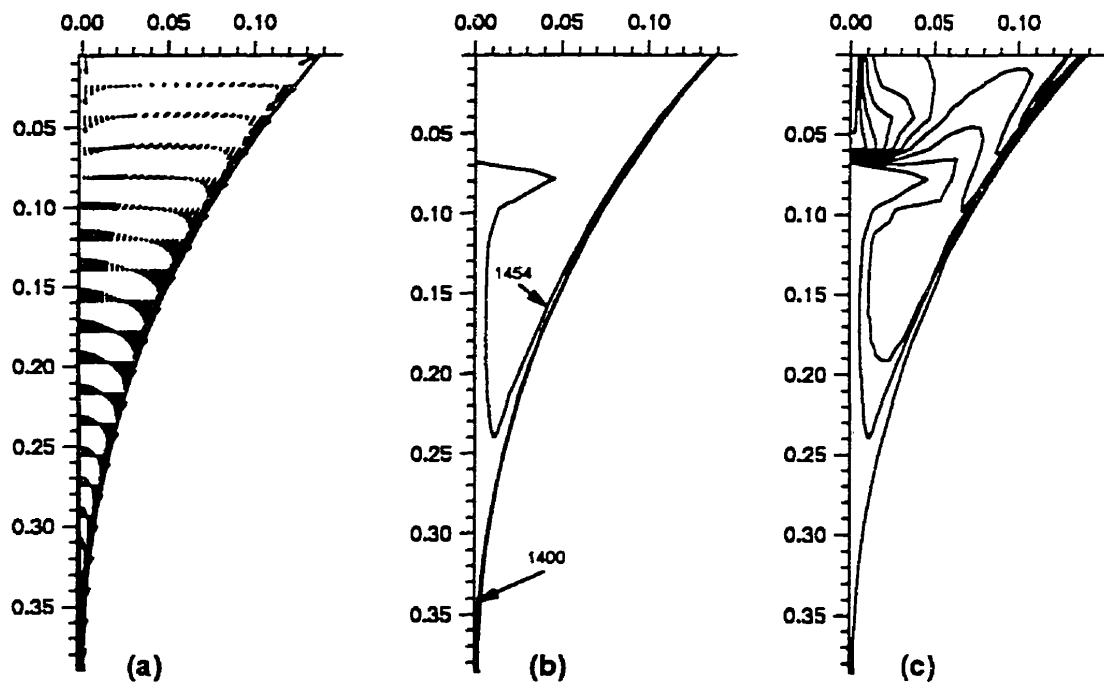


Fig. 7.15. Predicted results for a nozzle width of 12 mm, roll-gap of 3 mm, $C_0 = 1600$ and $f_m = 1$; (a) velocity vectors, (b) liquidus and solidus temperatures, (c) temperature contours.

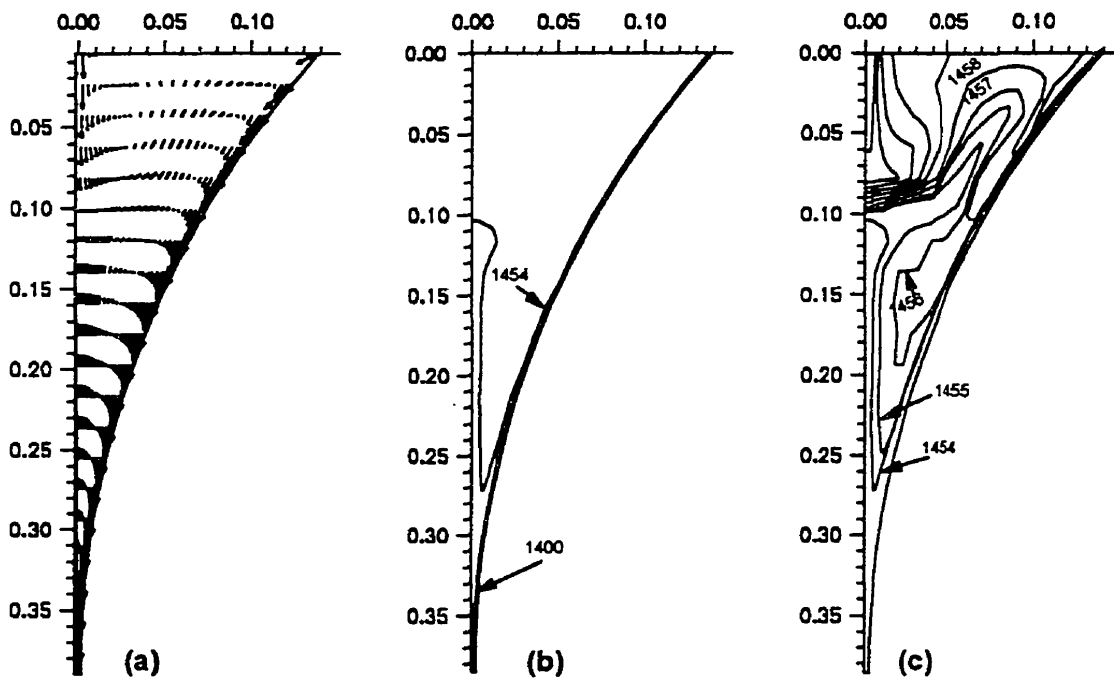


Fig. 7.16. Predicted results for a nozzle width of 12 mm, roll-gap of 3 mm, $C_0 = 1600$ and $f_m = 1$; (a) velocity vectors, (b) liquidus and solidus temperatures, (c) temperature contours.

SUMMARY AND CONCLUDING REMARKS

8.1 Conclusions

The fundamental research carried out in the present work is concerned with the mathematical modelling of transport phenomena in continuous slab casting and thin-strip twin-roll casting processes. The part related to the former process, comprises four chapters while the part concerning the latter process consists of two chapters. The results of these six original chapters are summarised and some key conclusions are presented here:

1. A three-dimensional control volume based finite-difference model, along with the associated computer code, have been developed to obtain the numerical solution of the coupled turbulent flow, heat transfer and macroscopic solidification in the mold and submold regions of an industrial size continuous caster for steel slabs. To investigate the turbulence effects in the process, a low Reynolds number $k - \epsilon$ model was employed in the mathematical formulation. The mushy region fluid flow and solidification was modeled using an enthalpy-porosity scheme. Numerical accuracy of the model was tested by comparison of the predicted solid shell with the available experimentally measured solidified shell thickness for a slab caster. The comparison between results obtained by the model and published experimental data, indicated a very good capability of the code in simulation of continuous slab casters. The model was then used to investigate the effect of primary operating parameters such as casting speed, delivered superheat and submergence depth of the nozzle on flow pattern, shell thickness and growth rate of the mushy region, and temperature and turbulent viscosity distributions in the liquid and mushy regions within the caster. The model prediction showed that most of the inlet superheat is

removed in or just below the mold. The growth rate of the solid shell and mushy region near the center of the wide face was found to be higher compared to the edges and the narrow face. This resulted in a nonuniform solid shell growth and mushy layer development in the mold region. It was also seen that, except for the vicinity of the jet impingement region, the inlet superheat has minimal effect on the growth rate of the solid shell and mushy layer while the casting speed has the most important effect. The output of this simulation study clearly signified the importance and need for a three-dimensional, conjugate turbulent flow, heat transfer and solidification modeling study for a continuous-slab casting process. Prior modeling studies related to continuous casting processes, which have employed either *ad hoc* effective thermal conductivity or *ad hoc* effective viscosity approach or have uncoupled the process of solidification from heat transfer and fluid flow, cannot provide realistic results, particularly for a slab caster.

2. Following the parametric study on the primary casting conditions, the effects of mold heat extraction rates on a continuous stainless steel slab casting process were numerically investigated using the validated code developed in the previous part of this study. Three different surface boundary conditions for the mold region involving two constant mold heat transfer coefficients and an empirical heat flow relationship were examined. Numerical accuracy of the model was tested by comparing the predicted solidified shell thickness with the known published experimentally measured data obtained through a radioactive gold tracer technique for a stainless-steel slab caster. A very good agreement was obtained between the theoretically predicted and experimentally measured solid shell thickness. Concerning the thermal fields and solid shell profiles, the predicted results showed a significant difference for various thermal boundary conditions in the mold. Thus, the assignment of a correct (preferably experimental) mold heat flux distribution profile is important to study the initial development of the solid shell thickness in the mold.

3. Next, the three-dimensional control volume based finite-difference computer code

was further developed to take into account the effect of magnetohydrodynamics phenomena in the slab casting process. In this regard, a solution scheme for the Maxwell's equations was incorporated into the program. The usefulness of five different configurations of the in-mold electromagnetic braking systems for a continuous slab casting process was investigated and their effects, specifically on the flow pattern in the mold, were documented in this section. In general, it was proved that the EMBR systems can be successfully used to control the molten steel flow in the mold and prevent the so-called impingement flow on the narrow face of the slab. The predicted results showed that the length and strength of the upper and lower recirculation loops may be changed by the application of DC electromagnetic fields. The magnetic field located at the meniscus suppressed the upper recirculation loop and led to the reduction of the meniscus-averaged temperature. However, the magnetic field located under the nozzle reduced the downward flow close to the narrow face and directed most of the flow to be circulated in the upper part of the mold and thereby increased the average temperature at the meniscus. The solution of the inclusion concentration (mass fraction) equation also showed that the removal of the inclusions can be accelerated by suitably imposing electromagnetic field in the mold, which can be attributed to the reduction of the downward velocity of the liquid steel due to braking effect. Moreover, the model predicted that the minimum thickness of the slab at the exit of the mold increases upon imposition of the electromagnetic field on the caster mold. Thus the proper use of EMF should enable the steel industries to increase the casting speed and hence the production level. Among the various EMBR devices studied here, one having two magnetic fields covering the entire width of the strand, one located at the meniscus and another under the nozzle, showed better controllability of fluid flow in the mold. The performance of this type of EMBR increases in the newly proposed EMBR system in which two magnetic fields, one acting at the top and other acting at the bottom can be set independently with unequal magnetic flux densities.

4. In terms of gas injection study in the continuous slab casting processes, the three-dimensional mathematical model developed in the previous parts was further advanced by incorporating the gas dispersion model into the program. The coupling of the solidification with the other transport phenomena in this numerical simulation made it possible to study the entrapment of the gas bubbles in the solidifying shell. A good agreement was obtained with regard to fluid flow and gas distribution predicted by the present model and those available in the literature. Other aspects of the code were validated in the previous parts of this study through comparison with the available data. The parameters studied in this part were gas injection rate at the inlet and gas bubble size. The results showed that the flow discharged from the nozzle port immediately deflects upward and changes the size of the upper recirculation loop. The injection of the gas in the studied conditions caused a reverse flow at the meniscus close to the narrow face and generated a stagnation region at the free surface. The results also showed that the stagnation region at the meniscus shifts towards the center of slab for higher bubble sizes. Increasing the gas injection rate intensified the changes in the flow pattern and increased the average meniscus velocity which may drag the inclusions or powder from the meniscus inward into the caster. The gas bubbles with smaller sizes were found to travel deeper towards the narrow face of the slab and spread wider in the mold. The gas entrapment study also indicated that for 11% gas injection rate at the inlet and 1 mm bubble size, almost the entire width of the slab shows gas entrapment with the level 0.1% and greater, while for 3 mm bubble size only a small area of wide face close to the center of the slab shows a similar entrapment.

5. In terms of thin-strip twin-roll casting processes, first a thermal fluid flow model was developed to study the coupled turbulent flow and heat transfer in an arbitrary geometry to predict mean flow, turbulent characteristics and heat transfer in the wedge-shaped liquid steel pool of a twin-roll continuous steel strip caster. To take into account the effect of turbulent phenomena in the mathematical formulation, the Launder and Sharma version of low-Re $k - \epsilon$ turbulent model was adopted. In order to tackle the arbitrary

geometry, a non-orthogonal body-fitted coordinate transformation technique was employed. The transformed curvilinear conservation equations for mass, momentum, energy and turbulent quantities were written in terms of physical variables and solved using a control-volume finite difference method on a staggered grid arrangement. A special feature of the present numerical scheme was the improvement of the body-fitted coordinate technique through finding the location of main grid points, as well as control volume faces directly through grid generation technique, which eliminated further interpolation in the calculation of metric coefficients and jacobian required in the discretized equations. The results showed that, for the range of parameters typically expected from an industrially operating caster, two recirculation zones develop in the liquid pool. For a higher roll gap thickness, the two recirculation zones were almost of equal size but for a small roll gap, the recirculation zone developed near the inlet jet was much smaller compared to the one that developed due the motion of the roll. For high casting speeds, a high level of turbulence generated at the free surface of the liquid pool, which might lead to the formation of surface waves and eventually yield poor quality products. For a fixed casting speed, the local Nusselt number profile versus distance along the roll surface showed two distinct positive upward slop changes: one near the middle of the roll surface and the other near the roll nip. The first positive change in slope was due to the jet impingement from the return flow of the incoming inlet jet on the melt shear layer carried by the rotating roll. The second rapid change was due to the progressive thinning of the thermal boundary-layer at the roll, caused by the increased turbulent convective flow as a result of the reduction in cross-sectional area of the flow in the downstream section of the wedge-shaped cavity.

6. The thermal fluid flow model used in the previous part was further developed to a fully coupled turbulent flow and macroscopic solidification model to study the basic transport phenomena in the vertical twin-roll thin-strip caster for stainless steel. The influence of the macroscopic solidification parameters, namely, the D'arcy coefficient and the turbulent eddy viscosity damping factor for the mushy region (located between the solidus and liquidus temperatures), on the velocity and temperature fields, turbulent viscosity

distributions and extents of the mushy and solid regions, was primarily investigated. On the basis of the present investigation, a value of 1600 for the Darcy coefficient was recommended for studying mushy zone solidification in a twin-roll caster and similar systems. Considering the fact that the mushy region is a mixture of solid and liquid steel, sensitivity studies were carried out on the model using three turbulent eddy damping factors, two of which were dependent on the liquid fraction. The three factors studied did not show any significant effect on the solidified shell thickness but did show a noticeable influence on the velocity and temperature distributions in the liquid and mushy regions. With regard to the selection of this factor, further investigations are warranted. However, for engineering calculations and design, any of the three examined damping functions can be selected. For a fixed heat extraction rate, with the variation of casting parameters, namely the roll gap thickness and nozzle opening, the penetration depth of the plunging inlet jet into the liquid metal pool of the caster as well as the extent of the mushy region were changed but the solidified shell thickness remained practically unaffected.

8.2 Contributions to Knowledge

1. Development from scratch of a general 3-D CFD code for the numerical simulation of coupled turbulent flow, heat transfer, macroscopic solidification. The code was further advanced to model the electromagnetic flow control and gas bubble dispersion in the presence of solidification.
2. Three-dimensional numerical simulation of coupled turbulent flow and macroscopic solidification study for a slab has been carried out for the first time.
3. Realistic simulation of various commercially used MHD flow control devices for continuous casting processes. The model is specifically advanced by considering simultaneously the turbulent phenomena, solidification and magnetic field effects in the simulation. The study of the effects of various MHD flow control devices on the flow field and solidification and clarification of their usefulness can be considered as a contribution to knowledge.

4. A new magnetic flow control device has been proposed which should significantly improve the performance of a continuous casting process by suitably controlling the flow field in the mold.

5. Realistic simulation of argon gas bubble dispersion blown into the continuous casting mold. The model was specifically used to study the effects of bubbles injection on the flow pattern and their entrapments in the solidifying shell.

6. Development of an advanced two-dimensional mathematical model based on fully coupled turbulent flow and macroscopic solidification and using an optimised boundary-fitted coordinate technique for the simulation of a thin-strip, twin-roll casting process.

8.3 Recommendations for Future Work

1. Develop a 3-D simulation model for predicting macrosegregation in a continuous slab caster through the implementation of the solute transport equation into the present model.

2. Combine the macroscopic and microscopic models to predict solutes' segregation and grain growth for both continuous slab casting and thin-strip twin-roll casting systems.

3. Realistically model the effect of electromagnetic stirring in the continuous casting operation and determine the impact of electromagnetic stirring on the macrosegregation phenomena.

4. Adopt the present model to study the electromagnetic casting of aluminium by taking into account the free surface fluctuation at the top.

5. A numerical study of the twin-roll casting operation in which the molten metal is confined with the electromagnetic side dams instead of direct contact with the solid side wall dams would be an innovative undertaking.

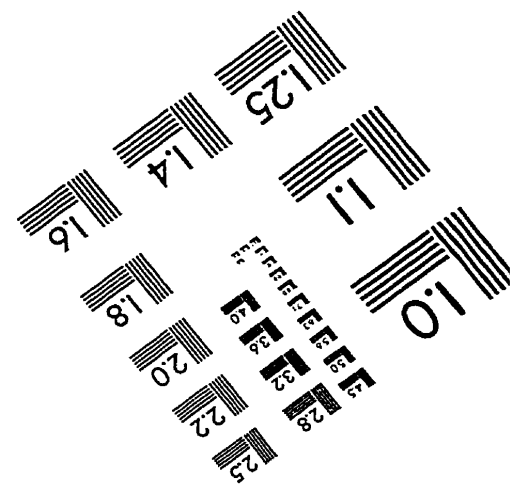
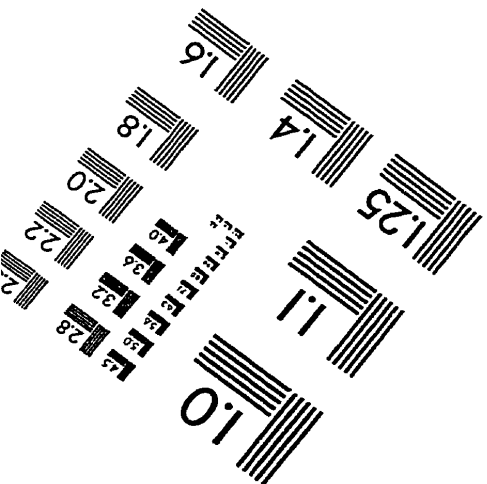
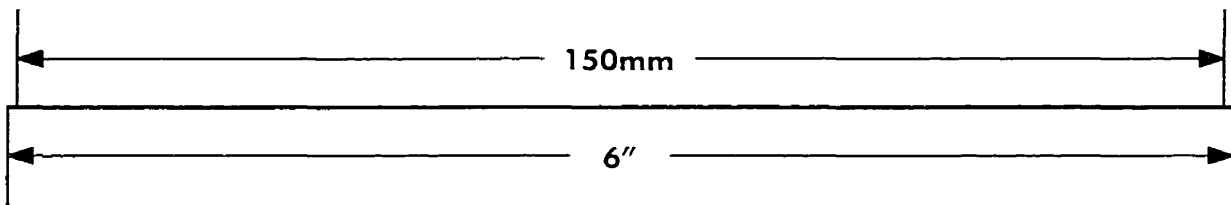
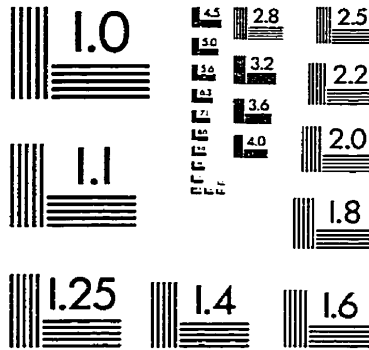
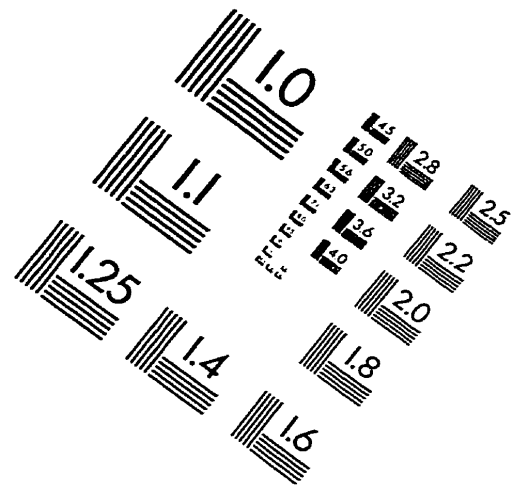
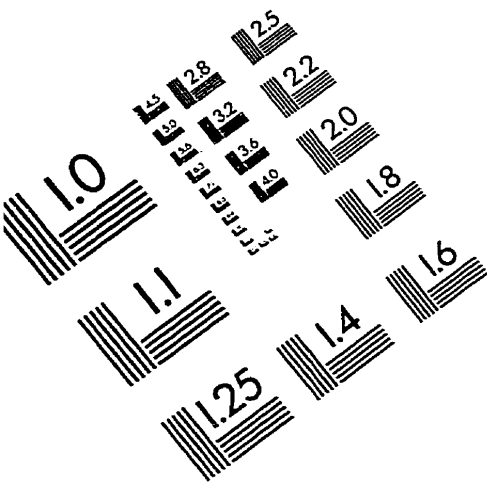
6. A model which can take into account the start-up conditions both for the slab and twin-roll casting processes would be useful.

7. An accurate 3-D numerical study of a thin-strip twin-roll casting process would be a challenging undertaking.

8. The effect of mold taper and mold oscillation on the transport phenomena for the slab caster should be clarified.

9. The present model should be extended to accommodate the deformable top free surface for both continuous steel slab and thin-strip twin-roll casters.

IMAGE EVALUATION TEST TARGET (QA-3)



APPLIED IMAGE, Inc
 1653 East Main Street
 Rochester, NY 14609 USA
 Phone: 716/482-0300
 Fax: 716/288-5989

© 1993, Applied Image, Inc., All Rights Reserved